EURASIP Journal on Wireless Communications and Networking

Advances in Propagation Modeling for Wireless Systems

Guest Editors: Claude Oestges, Michael Jensen, Persefoni Kyritsi, Mansoor Shafi, and Jun-ichi Takada

Advances in Propagation Modeling for Wireless Systems

EURASIP Journal on
Wireless Communications and Networking

Advances in Propagation Modeling for Wireless Systems

Guest Editors: Claude Oestges, Michael Jensen, Persefoni Kyritsi, Mansoor Shafi, and Jun-ichi Takada

This is a special issue published in volume 2009 of "EURASIP Journal on Wireless Communications and Networking."

Contents

Hindawi Publishing Corporation
EURASIP Journal on Wireless Communications and Networking
Volume 2009, Article ID 415736, 2 pages
doi:10.1155/2009/415736

Editorial

Advances in Propagation Modeling for Wireless Systems

Claude Oestges,[1] Michael Jensen,[2] Persefoni Kyritsi,[3] Mansoor Shafi,[4] and Jun-ichi Takada[5]

[1] *Microwave Laboratory, Université catholique de Louvain, 1348 Louvain-la-Neuve, Belgium*
[2] *Department of Electrical and Computer Engineering, Brigham Young University, Provo, UT 84602, USA*
[3] *Antennas, Propagation and Radio Networking Section, Aalborg University, 9100 Aalborg, Denmark*
[4] *Telecom New Zealand, P. O. Box 293, Wellington, New Zealand*
[5] *Department of International Development Engineering, Graduate School of Science and Engineering, Tokyo Institute of Technology, Meguro-ku, Tokyo 152-8550, Japan*

Correspondence should be addressed to Claude Oestges, claude.oestges@uclouvain.be

Received 18 March 2009; Accepted 18 March 2009

Advanced wireless systems face an ever-increasing number of challenges, such as the limited availability of the radio frequency spectrum and the demand for faster data transmissions, better quality of service, and higher network capacity. Yet, the true challenge faced by new communication technologies is to achieve the expected performance in real-world wireless channels. System designers classically focus on the impact of the radio channel on the received signals and use propagation models for testing and evaluating receiver designs and transmission schemes. The needs for such models evolve as new applications emerge with different bandwidths, terminal mobility, higher carrier frequencies, new antennas, and so forth. Furthermore, channel characterization also yields the fundamental ties to classical electromagnetics and physics as well as the answers to some crucial questions in communication and information theory. In particular, it is of outstanding importance for designing transmission schemes which are efficient in terms of power or spectrum management. Advanced channel modeling is also recognized as a major topic by two on-going research programs in Europe: the Network of Excellence in Communications NEWCOM++ and the European COST 2100 Action "Pervasive Mobile & Ambient Wireless Communications." While the former only includes a number of European partners (see http://www.newcom-project.eu/), the latter is a large network of coordinated national research projects in the fields of interest to participants coming from different EU and non-EU countries (see http://www.cost2100.org/).

The objective of this special issue, published following an initiative by NEWCOM++ and COST 2100 partners, is to highlight the most recent advances in the area of propagation measurement and modeling. We received 25 high-quality submissions, which were peer-reviewed by experts in the field, and we selected 9 papers for inclusion in this special issue. These articles cover the gamut from electromagnetic models to experimental characterizations of complex environments as well as the measurement-based parameterization and analysis of geometry-based stochastic models.

Three papers deal with the modeling of complex media or environments. One of the challenges of emerging or future technologies is indeed the large variety of application scenarios, for which classical models might not apply. Furthermore, more and more techniques rely on adaptive and/or multiple antenna signal processing, so that the dynamic and spatial behaviors of the propagation channel should be covered as well.

The paper by Molina-Garcia-Pardo et al. proposes the experimental characterization and modeling of propagation in tunnels, at various frequencies in the 2.8–5 GHz band. Path loss, large-scale correlation, and fading statistics are derived from measurements conducted by means of a vector network analyzer. It is shown that the tunnel behaves as a low-loss waveguide, and the fading is strongly dependent on the distance. An extension to a multiple-input multiple-output (MIMO) channel model is also presented.

The paper by Moraitis et al. presents experimental results related to the propagation inside a passenger aircraft, at various frequencies between 1.8 and 2.45 GHz. Empirical

formulas are inferred for the path loss, slow- and fast-fading, and interference modeling. A comparison with a physical-optics-based ray-tracing model is also successfully conducted.

The paper by Cheffena and Ekman combines fading measurements from 2.45 up to 60 GHz with wind speed data to study the dynamic effects of swaying vegetation on radiowave propagation. A simulation model based on a multiple mass-spring system is developed and empirically validated. The outputs of the model are the fading first- and second-order statistics.

Two papers cover the area of physical models. Physical models traditionally consist of electromagnetic theory combined with engineering expertise that allows making reasonable assumptions about the propagation mechanisms involved. Provided that the correct propagation phenomena are identified, such theoretical models are capable of making very accurate predictions in a deterministic manner. The output being specific to particular locations rather than being an average value, the model can be applied to very wide ranges of system and environment parameters, certainly well beyond the range within which measurements have been made. The two drawbacks of such models are the computational effort and the required accuracy of the geometrical and electrical properties of the environment. These two issues are dealt with by the following papers.

The paper by Jemai and Kürner investigates the performance boundaries of a calibrated ray-tracing model in indoor scenarios. It is indeed well known that the precision of ray-tracing tools is limited by the accuracy of the environmental description. The proposed approach improves the prediction accuracy by means of a calibration procedure, whose sensitivity is further analyzed in the paper.

The paper by Valcarce et al. applies a finite-difference time-domain (FDTD) method in the framework of WiMAX femtocells. Two optimization methods are proposed to tackle the issue of computational complexity. Calibration is also carried out. The paper eventually presents mobile WiMAX system-level simulations that make use of the developed model.

Finally, the last set of papers deals with geometry-based models for MIMO systems. In geometrical channel models, the channel impulse response is related to the location of scatterers, the location of which is chosen stochastically. A further important generalization is the existence of multiple clusters of scatterers. Geometry-based models emulate the physical reality and thus reproduce many effects implicitly: small-scale fading, correlation of the signals at different antenna elements, and even large-scale changes of delays and directions. Due to the close relationship with physical reality, it is also relatively easy to parameterize that model, for example, from measurement results. In a first step, the matrix impulse responses are measured with a channel sounder. High-resolution algorithms are then employed to extract the required information.

Two papers deal with multipath clustering. The paper by Czink et al. presents the so-called Random-Cluster Model, which is a stochastic time-variant frequency-selective MIMO channel model directly parameterized from experimental data. A fully automated clustering algorithm is used to identify multipath clusters which define the model. The approach is then validated based on different metrics applied to indoor data.

The paper by Materum et al. presents a methodology to identify multipath clusters in an automatic way. The approach is then applied to the clustering at the mobile station in small urban macrocell at 4.5 GHz. Each identified cluster is manually confronted with its physical counterpart, and conclusive results are drawn on the various propagation mechanisms.

The last paper on geometry-based modeling by Zhang et al. investigates several possible simplifications of geometry-based models in view of reducing their complexity without compromising their accuracy. The analysis relies on simulation and experimental results and a number of metrics.

Finally, the paper by Sivasondhivat et al. focuses on the modeling of the double-directional power spectrum in urban macrocells when considering dual-polarized MIMO transmissions. In particular, the separability of the power spectrum between the base station and the mobile is investigated, and a model is proposed and validated, based on the sum of polarization pairwise Kronecker product approximation.

Acknowledgments

We would like to take this opportunity to express our sincere thanks to the authors for contributing to this special issue and to the reviewers for providing prompt and detailed remarks that helped improve the quality of the manuscripts. We also wish to thank the Editor-in-Chief and the editorial office for their support through the entire editing process. Finally, C. Oestges acknowledges the contribution of the European Commission through the FP7 research program (European Network of Excellence NEWCOM++, which started in January 2008 for a period of 3 years). C. Oestges and J-i. Takada are also members of the European COST 2100 Action.

Claude Oestges
Michael Jensen
Persefoni Kyritsi
Mansoor Shafi
Jun-ichi Takada

Hindawi Publishing Corporation
EURASIP Journal on Wireless Communications and Networking
Volume 2009, Article ID 560571, 9 pages
doi:10.1155/2009/560571

Research Article

Propagation in Tunnels: Experimental Investigations and Channel Modeling in a Wide Frequency Band for MIMO Applications

J.-M. Molina-Garcia-Pardo,[1] M. Lienard,[2] and P. Degauque[2]

[1] *Departamento de Tecnología de la Información y la Comunicación, Technical University of Cartagena, 30202 Cartagena, Spain*
[2] *Télécommunications, Interférences et Compatibilité Electromagnétique (TELICE), Institut d'Electronique, Microélectronique et Nanotechnologie (IEMN), University of Lille, 59655 Villeneuve D'Ascq, France*

Correspondence should be addressed to J.-M. Molina-Garcia-Pardo, josemaria.molina@upct.es

Received 25 July 2008; Accepted 10 February 2009

Recommended by Jun-ichi Takada

The analysis of the electromagnetic field statistics in an arched tunnel is presented. The investigation is based on experimental data obtained during extensive measurement campaigns in a frequency band extending from 2.8 GHz up to 5 GHz and for a range varying between 50 m and 500 m. Simple channel models that can be used for simulating MIMO links are also proposed.

1. Introduction

Narrowband wireless communications in confined environments, such as tunnels, have been widely studied for years, and a lot of experimental results have been presented in the literature in environmental categories ranging from mine galleries and underground old quarries to road and railway tunnels [1–4].

However, in most cases, measurements dealt with channel characterization for few discrete frequencies, often around 900 MHz and 1800 MHz. For example, in [5, 6] Zhang et al. report statistical narrowband and wideband measurement results. In [7], results on planning of the Global System for Mobile Communication for Railway (GMS-R) are presented. In [8], simulations and measurements are also described in the same GSM frequency band. In [9], the prediction of received power in the out-of-zone of a dedicated short range communications (DSRC) system operating inside a typical arched highway tunnel is discussed, and in this case the channel impulse response was measured with a sounder at 5.2 GHz whose bandwidth is on the order of 100 MHz. Recently, in [10], measurement campaigns have been performed in underground mines in the 2–5 GHz band but the results cannot be extrapolated to road and railway tunnels since the topology is quite different. In a mine gallery, roughness is very important, the typical width is 3 m, the geometry of the cross-section is not well defined and lastly, there are often many changes in the tunnel direction.

Furthermore, to increase the channel capacity in tunnels, space diversity both at the mobile and at the fixed base station can be introduced. However, good performances of multiple input multiple output (MIMO) techniques can be obtained under the condition of a small correlation between paths relating each transmitting and receiving antennas. This decorrelation is usually ensured by the multiple reflections on randomly distributed obstacles, giving often rise to a wide spread in the direction of arrival of the rays. On the contrary, a tunnel plays the role of an oversized waveguide and decorrelation can be due to the superposition of the numerous hybrid modes supported by the structure [11]. Experimental results at 900 MHz for a $(4, 4)$ MIMO configuration, are described in [12]. This paper shows that the antenna arrays must be put in the transverse plane of the tunnel to minimize the coupling between elements.

The objective of this work is thus to extend the previous approaches by investigating the statistics of the electric field

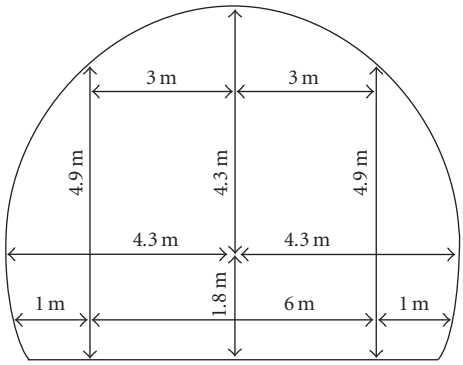

Figure 1: Cross-section of the tunnel.

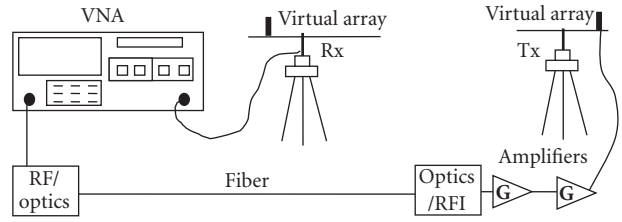

Figure 2: Principle of the channel sounder setup.

distribution in the 2.8–5 GHz frequency range in a tunnel environment for MIMO applications. Empirical formulas based on the experimental results are also proposed.

We proceed in two steps: (1) determination of the mean path loss and of the statistical distribution of the average field which can be received by the various antennas of an MIMO system. This first approach can thus be used to determine the average power related to the **H** matrix of an MIMO link, (2) field distribution and correlation in a transverse plane.

The paper is distributed as follows. Section 2 explains the experiments in detail and more specifically the environment and methodology of the measurements that has been followed. Section 3 investigates path loss and axial correlation while, in Section 4, field statistics in the transverse plane are analyzed. Section 5 deals with the transverse spatial correlation and Section 6 presents the principle of modeling the MIMO channel and gives an example of application. Finally, Section 7 summarizes the contributions of the present work and gives conclusions.

2. Environment, Measurement Equipment, and Methodology

2.1. Description of the Environment. The measurement campaign was performed in a 2-way tunnel, situated in the French Massif Central mountains. This straight tunnel, 3.4 km long, has a semicircular shape, as shown in Figure 1. The diameter of the cylindrical part is 8.6 m and the maximum height of the tunnel is 6.1 m. The tunnel was empty with no pipes, cables, or lights. However, every 100 m there are small safety zones, 1 m wide and few meters long, where an extinguisher is hung. It is difficult to estimate the roughness accurately but it is on the order of a centimetre. The tunnel was closed to traffic during the experiments, to make measurements in stationary conditions.

2.2. Measurement Equipment. Since we want to explore the channel response in a very wide frequency band (2.8–5 GHz), we have chosen to make measurements in the frequency domain rather than in the time domain, so as to get better accurate results. The complex channel transfer function between the transmitting (Tx) and receiving (Rx) antennas has thus been obtained by measuring the S_{21} parameter with a vector network analyzer (VNA Agilent E5071B). The Rx antenna is directly connected to one port of the VNA using a low attenuation coaxial cable, 4 m long, a 30 dB low-noise amplifier being inserted or not, depending on the received power. Using a coaxial cable to connect the Tx antenna to the other port of the VNA would lead to prohibitive attenuation, the maximum distance between Tx and Rx being 500 m. The signal of the Tx port of the VNA is thus converted to an optical signal which is sent through fibre optics, converted back to radio frequency and amplified. The signal feeding the vertical biconical transmitting (Tx) antenna has a power of 1 W. The phase stability of the fibre optics link has been checked and the calibration of the VNA takes amplifiers, cables, and optic coupler into account. The block diagram of the channel sounder is depicted in Figure 2.

The wideband biconical antennas (Electrometrics EM-6116) used in this experiment have nearly a flat gain, between 2 and 10 GHz. Indeed, the frequency response of the two antennas has been measured in an anechoic chamber, and the variation of the antenna gain was found to be less than 2 dB in our frequency range. Nevertheless, we have subtracted the antenna effect in the measurements, as it will be explained in Section 3.

It must also be emphasized that, in general, the radiation pattern of wideband antennas is also frequency dependent. This is not a critical point in our case since, in a tunnel, only waves impinging the tunnel walls with a grazing angle of incidence contribute to the total received power significantly. This means that, whatever the frequency, the angular spread of the received rays remains much smaller than the 3 dB beam width of the main antenna lobe in the E plane, equal to about 80°, the antenna being nearly omnidirectional in the H plane.

Since the channel transfer function may also strongly depend on the position of the antennas in the transverse plane of the tunnel, both Tx and Rx antennas were mounted on rails. The position mechanical systems are remote controlled, optic fibres connecting the step by step motors to the control unit.

2.3. Methodology. The channel frequency response has been measured for 1601 frequency points, equally spaced between 2.8 and 5 GHz, leading to a frequency step of 1.37 MHz.

The rails supporting the Tx and Rx antennas were put at a height of 1 m and centred on the same lane of this 2-lane tunnel. For each successive axial distance d, both

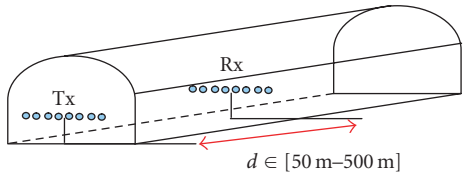

Figure 3: Configuration of the wideband MIMO measurements.

Table 1: Equipment characteristics and measurement parameters.

Frequency band	2.8–5 GHz
Number of frequency points	1601
Antenna	Biconical antenna (Electrometrics EM-6116)
Transmitter power	20 dBm
Dynamic range	>100 dB
Position in the transverse plane	12 positions every 3 cm ($\lambda/2$ at 5 GHz)
Positions along the longitudinal axis	From 50 m to 202 m every 4 m From 202 m to 500 m every 6 m
Number of acquisitions at each position	5

the Tx and Rx antennas were moved in the transverse plane on a distance of 33 cm, with a spatial step of 3 cm, corresponding to half a wavelength at 5 GHz. A $(12, 12)$ transfer matrix is thus obtained, the configuration of the measurements being schematically described in Figrue 3. Fine spatial sampling was chosen for measurements in the transverse plane because, as recalled in the introduction, antenna arrays for MIMO applications have to be put in this plane to minimize correlation between array elements.

Due to the limited time available for such an experiment and to operational constraints, it was not possible to extensively repeat such measurements for very small steps along the tunnel axis. In the experiments described in this paper, the axial step was chosen equal to 4 m when $50\,\text{m} < d < 202\,\text{m}$ and to 6 m when $202\,\text{m} < d < 500\,\text{m}$. This is not critical because we are interested, in the axial direction, by the mean path loss and by the large-scale fluctuation of the average power received in the transverse plane. At each Tx and Rx position, 5 successive recordings of field variation versus frequency are stored and averaged.

It must be noted that in the case of a single input single output (SISO) link, a number of papers have already been published on the small-scale variation of a narrowband signal along the tunnel axis. For example, [13] describes results of experiments carried out in a wide tunnel at a frequency of 900 MHz. A summary of the measurement parameters and equipment characteristics is summarized in Table 1.

3. Path Loss and Correlation Along the Longitudinal Axis

3.1. Path Loss. The path loss is deduced from the measurement of the $S_{21}(f, d)$ scattering parameter. However, as briefly mentioned in the previous section, it can be more interesting to subtract the effects of the variation of the antenna characteristics with frequency by introducing a correction factor $C(f)$. We have thus made preliminary measurements by putting the two biconical antennas, 1 m apart, in an anechoic room. Let $S_{21}^{\text{anech}}(f)$ be the scattering parameter measured in this configuration. The correction factor is thus given by $C(f) = |S_{21}^{\text{anech}}(f)| - \langle |S_{21}^{\text{anech}}(f)| \rangle$, where $\langle x \rangle$ means the average of x over the frequency band.

The path loss in tunnel, taking this correction into account, is given by

$$\text{PL}(f, d) = -20 \cdot \log_{10}(|S_{21}(f, d)|) - (-20 \cdot \log_{10} C(f)). \tag{1}$$

Figure 4 shows the variation of $\text{PL}(f, d)$ versus frequency, for $d = 50\,\text{m}$. The fluctuation of the field amplitude is due to the combination in phase or out of phase of the various modes excited by the transmitting antenna, the phase of the propagation constant depending on frequency but also on the order of the hybrid modes propagating in the tunnel. To extract the variation of the mean path loss versus frequency, it is interesting to average such curves, obtained at any distance d, for the various transverse positions of the antennas. Furthermore, one can also average over few frequencies, considering a frequency bandwidth smaller than the channel coherence bandwidth. In this example, the coherence bandwidth being on the order of 10 MHz, $\text{PL}(f, d)$ was averaged over 7 frequencies around f, the frequency step being 1.37 MHz, and over the 144 successive combinations of the transverse positions of the Tx and Rx antennas. The average value $\langle \text{PL}(f, d) \rangle$ is also plotted in Figure 4.

The curves "measurements" in Figure 5 represent the variation of $\langle \text{PL}(f, d) \rangle$ versus axial distance at 3 and 5 GHz. The path loss, at 3 GHz, corresponding to free-space conditions, has been also plotted. We see that, in this frequency range, the path loss is only slightly dependent on frequency.

To deduce from these curves a simple theoretical model of the mean path loss $\overline{\text{PL}}(f, d)$, these curves must be smoothed again by introducing a running mean over the axial distance. To get a very simple approximate analytical expression of $\overline{\text{PL}}(f, d)$, it is assumed that $\overline{\text{PL}}(f, d)$ is the product of two functions, one depending on f and one depending on d [14].

Furthermore, it is usually expressed in terms of two path loss exponents, $n_{\text{PL}_0\text{-}f}$ and $n_{\text{PL}_0\text{-}d}$ which indicate the rate at which the path loss decreases with frequency and distance, respectively, [15]. This leads to

$$\begin{aligned}\overline{\text{PL}}(f, d) = {} & (\text{PL}_0 + 10 \cdot n_{\text{PL}_0\text{-}f} \log_{10}(f(\text{GHz}))) \\ & + 10 n_{\text{PL}_0\text{-}d} \log_{10}(d).\end{aligned} \tag{2}$$

The constant PL_0 and the path loss exponents have been determined by minimizing the mean square error between

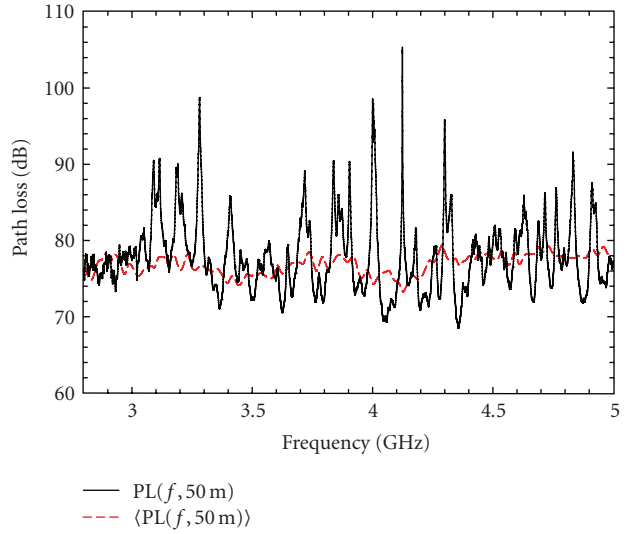

FIGURE 4: Path loss PL(f,d) between two antennas for $d = 50$ m and path loss $\langle \mathrm{PL}(f,d)\rangle$ averaged over the transverse positions of the antennas and over 7 frequencies in a 10 MHz band.

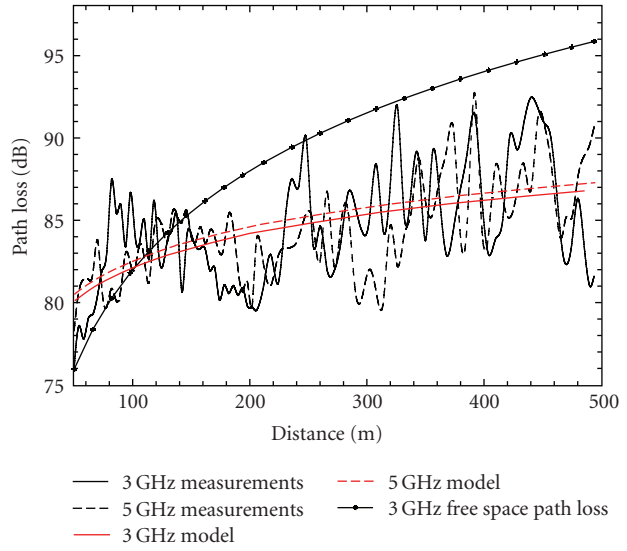

FIGURE 5: Average path loss (curves "measurements") and mean path loss deduced from the model (curves "model") at 3 and 5 GHz.

the measurements and the model. The following values were found: $\mathrm{PL}_0 = 86$ dB, $n_{\mathrm{PL}_0\text{-}f} = 0.82$, and $n_{\mathrm{PL}_0\text{-}d} = 0.57$. The corresponding curves for 3 and 5 GHz have also been plotted in Figure 5. It must be outlined that all these values were deduced from measurements between 50 and 500 m and consequently, they are valid only in this range of axial distance.

It can be interesting to compare this value of $n_{\mathrm{PL}_0\text{-}d}$ to those already published in the literature and corresponding to attenuation factors measured for ultra-wideband systems in indoor environments. However, in this case, the range is much smaller, typically below 50 m. In line of sight (LOS) conditions, values from 1.3 to 1.7 were reported by [16, 17],

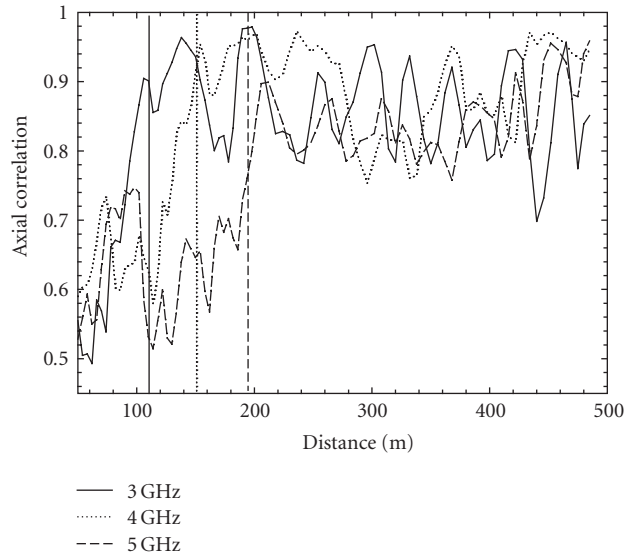

FIGURE 6: Axial correlation between receiving arrays 4 m (for 50 m $< d <$ 202 m) or 6 m (for 202 m $< d <$ 500 m) apart for three frequencies and their corresponding breakpoints.

while for non-LOS, $n_{\mathrm{PL}_0\text{-}d}$ may reach 2 to 4 as mentioned in [18, 19]. The small value that we have obtained comes from the guiding effect of the tunnel.

The comparison between $\langle \mathrm{PL}(f,d)\rangle$ and the predicted path loss $\overline{\mathrm{PL}}(f,d)$ shows that the difference in their values is characterized by a standard deviation $\sigma_{\mathrm{PL}} = 2.7$ dB. $\langle \mathrm{PL}(f,d)\rangle$ can thus be modeled by (2) and by adding a random variable $X_{\sigma_{\mathrm{PL}}}$ with zero mean and standard deviation σ_{PL}:

$$\langle \mathrm{PL}(f,d)\rangle_{\mathrm{model}} = \overline{\mathrm{PL}}(f,d) + X_{\sigma_{\mathrm{PL}}}. \quad (3)$$

3.2. Axial Correlation. One can expect that the variation of the average received power between one transverse plane and another will depend on the distance d, high-order propagating modes suffering important attenuation at large distances. To study this point, we have calculated, for a given frequency, the amplitude ρ_{axial} of the complex correlation coefficient between the (12, 12) transfer matrix elements measured at a distance d and the matrix elements measured at the distance $d + \Delta d$, d varying between 50 m and 500 m. Let us recall that the step Δd is equal 4 m while 50 m $< d <$ 202 m and 6 m when 202 m $< d <$ 500 m.

Curves in Figure 6 give the variation of ρ_{axial} for three frequencies: 3, 4, and 5 GHz. As one can expect from the modal theory, the correlation is an increasing function of distance. At 3 GHz, for example, the correlation between 2 receiving arrays, 4 m apart, varies from 0.6 at 50 m, to reach an average value of 0.9 at a distance of 200 m. If we now compare results obtained at 3 and 5 GHz, we see that the correlation increases less rapidly at 5 GHz, because high-order modes suffer less attenuation. By examining the shape of these curves, we observe two regions: the first one, at short distance from the transmitter, where the correlation increases nearly linearly, and the other where the average value of the

correlation does not vary appreciably. A two-slope model seems thus well suited to fit the average variation of the correlation function.

In Figure 6, the three vertical lines correspond to the positions of the breakpoint between the two slopes, for the three frequencies, respectively. This breakpoint thus occurs at distance $d_{\text{breakpoint\_axial}}$ from the transmitter and by plotting all curves for frequencies between 2.8 and 5 GHz, the following empirical formula giving has been obtained:

$$10\log_{10}(d_{\text{breakpoint\_axial}}) = 16.8 + 1.2f\ (\text{GHz}). \tag{4}$$

At the breakpoint and beyond this distance, the average correlation between the fields received by the array elements, 6 m apart, is equal to $\rho_{\text{breakpoint}} = 0.88$, with a standard deviation $\sigma_{\rho\_\text{axial}} = 0.06$, this result remaining valid in all the frequency range. In the first zone, that is, for $d < d_{\text{breakpoint\_axial}}$, the average variation of ρ_{axial} is modelled by

$$\langle\rho_{\text{axial}}\rangle = \rho_{\text{breakpoint}} + 0.06(d_{\text{breakpoint\_axial}} - d) \tag{5}$$

the standard deviation $\sigma_{\rho\_\text{axial}}$ being also equal to 0.06.

This leads to the following expression for modeling the variation of the correlation coefficient along the tunnel axis:

$$\rho_{\text{axial,model}} = \langle\rho_{\text{axial}}\rangle + X_{\rho\_\text{axial}}. \tag{6}$$

4. Field Distribution in the Transverse Plane

4.1. Field Distribution Function. In the transverse plane, the field distribution was first studied by considering, for a given axial distance d, the 12×12 possible combinations of the Tx and Rx antennas, and 7 close frequencies, within a 10 MHz band, as earlier explained. This has been done for various frequency bands between 2.8 and 5 GHz. We have compared the measured data to those given by a Rayleigh, Weibull, Rician, Nakagami and Lognormal distribution, and then using the Kolmogorov-Smirnov [20] test to decide what distribution best fits the experimental results. A Rice distribution appears to be the optimum one, whatever the frequency. The mathematical expression of its probability density function (PDF) is given by

$$f(x \mid \nu, \sigma_{\text{RICE}}) = \frac{x}{\sigma^2_{\text{RICE}}} \exp\left(\frac{-(x^2+\nu^2)}{2\sigma^2_{\text{RICE}}}\right) I_0\left(\frac{x\nu}{\sigma^2_{\text{RICE}}}\right). \tag{7}$$

In this formula, $I_0(\cdot)$ is the modified Bessel function of the first kind with order zero and ν and σ_{RICE} are parameters to be adjusted. The first order moment is expressed as

$$E(x) = \sqrt{\frac{\pi}{2}}\sigma_{\text{RICE}} L_{1/2}\left(-\frac{\nu^2}{2\sigma^2_{\text{RICE}}}\right) = \sqrt{\frac{\pi}{2}}\sigma_{\text{RICE}} L_{1/2}(-K), \tag{8}$$

$L_{1/2}$ being a Laguerre polynomial.

Before explaining how the two parameters of the Rice distribution have been found, let us recall that, in the mobile communication area, a Rice distribution usually characterizes the field distribution in line of sight (LOS) conditions and in presence of a multipath propagation. Usually a K factor is introduced and defined as the ratio of signal power in dominant component, corresponding to the power of the direct ray, over the scattered, reflected power. One can follow the same approach by defining a K factor in a given receiving zone which is, in our case, defined by the segment 33 cm long in the transverse plane of the tunnel, along which measurements were carried out.

4.2. Ricean K Factor. Knowing the (12, 12) matrix whose elements are the S_{21} complex values for successive positions of the Tx and Rx antennas in the transverse plane, one can calculate K at a distance d and a frequency f, from the following expression:

$$K = \frac{|\langle S_{21}\rangle|^2}{\left\langle |S_{21} - \langle S_{21}\rangle|^2 \right\rangle}. \tag{9}$$

It must be clearly outlined that, in a tunnel, the K factor cannot be easily interpreted. Indeed, there is no contribution of random components to the received power, the position of the 4 reflecting walls being invariant. K could be related to richness in terms of propagation modes having a significant power in the receiving transverse plane, a high number of modes giving rise to a high fluctuating field. However, quantifying the relationship between K and mode richness is not easy since the field fluctuation depends not only on the amplitude of the modes but also on their relative phase velocity. In a tunnel, one can conclude that K just gives an indication on the relative range of variation of the received power in a given zone.

Curves in Figure 7 have been plotted for 2 frequencies: 3 and 5 GHz. In the transverse zone of investigation (33 cm), for distances smaller than 200 m, the K factor is below -15 dB, which means that the received power strongly varies in the transverse plan, nearly following a Rayleigh distribution. However, K increases with distance and reaches 0 dB or more beyond 400 m, the constant part of the distribution becoming equal to or greater than the random part.

This increase of K is due to the fact that the contribution of high-order modes becomes less important leading to less fluctuation of the transverse field. The same interpretation based on the modes can be made to interpret the influence of frequency on the K values. The variation of K is of course related to the variation of the correlation coefficient along the tunnel axis, as described in the previous section.

By following the same approach as for the path loss, described in Section 3, and thus by averaging K over groups of 7 frequencies and over 144 successive combinations of the transverse positions of the transverse positions of the Tx and Rx antennas, an empirical expression of the average K factor in terms of frequency and distance can be found. It is given by

$$\overline{K} = (K_0 + 10 \cdot n_{K_0}\log_{10}(f(\text{GHz}))) + 10 \cdot (n_0 + 10 \cdot n_{n_0}\log_{10}(f(\text{GHz})))\log_{10}(d). \tag{10}$$

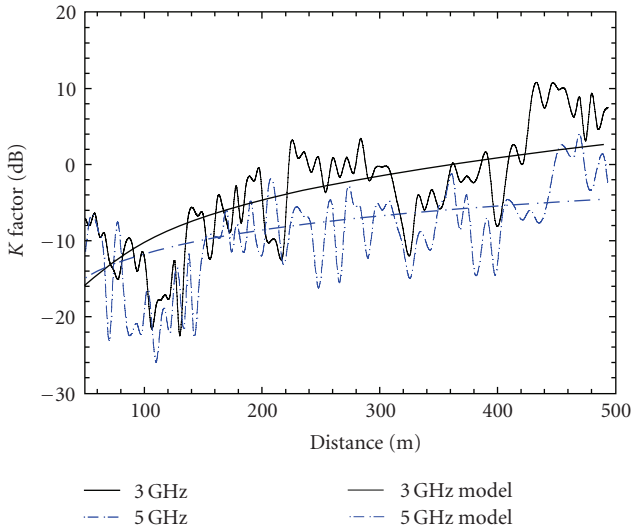

Figure 7: Variation of the K factor at 3 and 5 GHz, versus distance, and deduced from measurements. Its average variation calculated from an empirical mathematical expression is also plotted.

Table 2: Parameters to be introduced in (10) for modeling the variation of the K factor.

	K_0	n_{K_0}	n_0	n_{n_0}	σ_K
Values	−79	6.73	3.6	−0.37	4.9

The best fit between the results given by (10) and those extracted from the measurements was obtained for the values of the parameters given in Table 2. The standard deviation between (10) and the measured K is given by σ_K.

The curves labelled "model" in Figure 7 have been obtained by applying (10) and the above values for the parameters.

Let X be a random variable of zero mean. To completely describe the model, we can add to $\overline{K}$ such a random variable with a standard deviation of σ_K and labeled X_{σ_K}:

$$K_{\text{model}} = \overline{K} + X_{\sigma_K}. \tag{11}$$

4.3. Determination of the Ricean Parameters and Modeling of the Field Variation in the Transverse Plane. $\overline{K}$ is related to the field distribution parameters of the Rice distribution by

$$\overline{K} = \frac{\nu^2}{2\sigma^2_{\text{RICE}}}. \tag{12}$$

The mean value of $\overline{K}$ is deduced from (10) for a given frequency and distance, and by assuming a mean value of 1 of the amplitude of the field distribution $E(x) = 1$, the field distribution parameters ν and σ_{RICE} can be calculated. Note that mean value of the field would be determined by the large-scale fading, and fast variations around the mean value by the Rice distribution. Therefore, σ_{RICE} can be computed using (8) and (12):

$$\sigma_{\text{RICE}} = \sqrt{\frac{2}{\pi}}\frac{1}{L_{1/2}(-\overline{K})}. \tag{13}$$

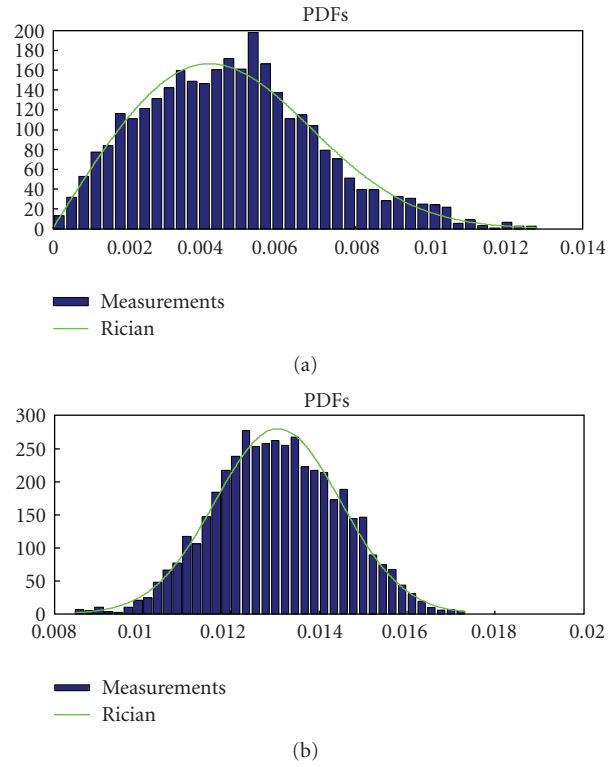

Figure 8: PDFs of the field amplitude in a transverse plane either deduced from measurements or calculated assuming a Rice distribution: (a) $d = 50$ m and $f = 5$ GHz, (b) $d = 500$ m and $f = 3$ GHz.

By knowing σ_{RICE}, ν is immediately deduced from (12). As an example, curves (a) and (b) in Figure 8 compare the PDFs deduced from the measurements to those assuming a Rice distribution, for $d = 50$ m and $f = 5$ GHz, and $d = 500$ m and $f = 3$ GHz, respectively. We see the rather good agreement between measurements and the empirical formulation; the confidence level of the Smirnoff-Kolmogorov test remaining below 0.05.

5. Transverse Spatial Correlation

The knowledge of the spatial correlation in the transverse plane is of special interest for MIMO systems. It is assumed, for simplicity, that the correlations at the transmitter and at the receiver are separable [21]. Furthermore, since the Rx and Tx antenna arrays are situated in the same transverse zone of the tunnel, one can expect that the correlation statistics are the same for the Tx site and for the Rx site and thus, in the following, they are not differentiated.

For each axial distance d, and for each frequency f, the amplitude of the complex correlation function ρ_{trans} was deduced from the 12×12 channel matrix, whose elements are associated to the successive positions of the Tx and Rx antennas in the transverse plane. Let s be the spacing between two receiving points. Figure 9 shows, for $f = 3$ GHz, the variation of ρ_{trans} versus the axial distanceand for different values of s: 3, 9, 21, and 33 cm.

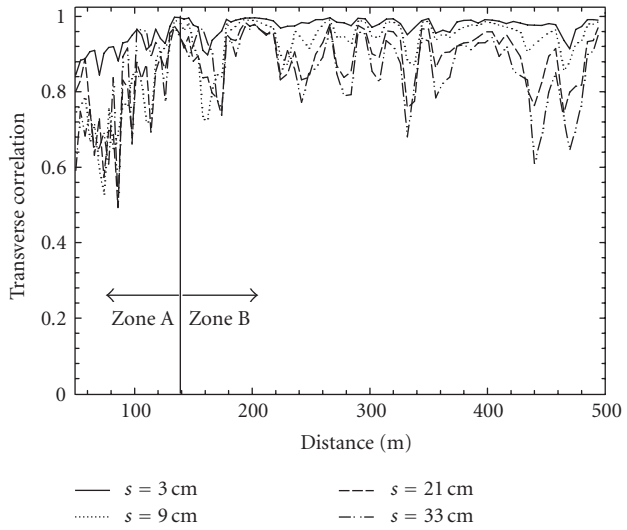

FIGURE 9: Transverse correlation at 3 GHz versus axial distance and for different spacing in the transverse plane.

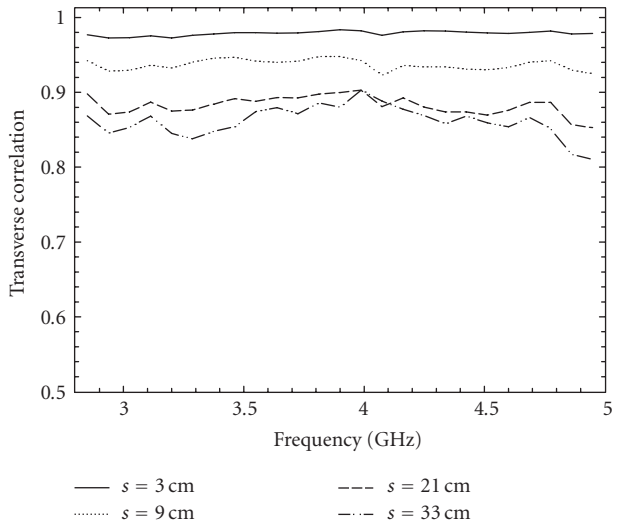

FIGURE 10: Average correlation in zone B, versus frequency, and for four antenna spacing.

ρ_{trans} is of course a decreasing function of the antenna spacing. Furthermore, for a given spacing, the correlation in the transverse plane increases when the axial distance increases, at least until the end of a zone, named A in Figure 9, occurring at a point called "breakpoint trans." This remark is connected to the comments made in Section 4 concerning the axial correlation, where we have outlined that, when the axial distance increases, the high-order modes are more and more attenuated, leading to a less fluctuating electromagnetic field. Beyond the "breakpoint trans" (zone B in Figure 9), ρ_{trans} keeps an average high value, even if local decreases are observed. The local decreases can be explained by the field pattern in the transverse plane of the tunnel. Indeed, this pattern does not present translation symmetry since it results from the combining of many modes, both in amplitude and in phase.

By analyzing results in the whole frequency range, it appears that the width of zone A slightly increases with frequency, as it occurred in the case of the longitudinal correlation (Section 4). Again, using all measured frequencies, an empirical formula giving the position of the "breakpoint_trans" point is given by

$$10\log_{10}\left(d_{\text{breakpoint\_trans}}\right) = 16 + 1.7f\,(\text{GHz}). \tag{14}$$

In zone B, one can calculate the mean value $\rho_{\text{trans}}(s, \text{zone } B, f)$ by averaging $\rho_{\text{trans}}(s, d, f)$ over the axial distance d. The results are the curves plotted in Figure 10, versus frequency and for different values of s: 3, 9, 21, and 33 cm.

It appears that $\rho_{\text{trans}}(s, \text{zone } B, f)$ is nearly frequency independent and that an empirical formula fitting the experimental results can be obtained:

$$\rho_{\text{trans}}(s, \text{zone } B) = 0.98 - 0.0042s\,(\text{cm}). \tag{15}$$

The difference between (15) and the measured correlation is a random variable of zero mean and standard deviation $\sigma_{\rho\_\text{trans}}$:

$$\sigma_{\rho\_\text{trans}}(s, \text{zone } B) = 0.02 + 0.0025s\,(\text{cm}). \tag{16}$$

The modeling of the ρ_{trans} in zone A assumes an average linear variation with distance. The adequate formula in this zone is

$$\rho_{\text{trans}}(s, d, f) = \rho_{\text{trans}}(s, \text{zone } B) + 0.04\left(d_{\text{breakpoint\_trans}} - d\right). \tag{17}$$

In this formula, the implicit dependence on frequency comes from the value of $d_{\text{breakpoint\_trans}}$. The standard deviation around this value is nearly frequency independent and is modeled by

$$\sigma_{\rho_{\text{trans}}}(s) = 0.0324 + 0.0033s\,(\text{cm}). \tag{18}$$

Finally, for a given antenna spacing, the correlation between two antenna elements is modeled by

$$\rho_{\text{trans,model}} = \rho_{\text{trans}} + X_{\sigma\rho\_\text{trans}}. \tag{19}$$

6. Full Model

The previous sections have proposed empirical formulas, based on experimental results, to model the path loss and the field fluctuation and correlation in a transverse plane. These formulas can be applied to randomly generate the transfer matrices $\mathbf{H}$ of an MIMO link in a straight tunnel having an arched cross-section, which is the shape of most road and railway tunnels. The transmitting and receiving arrays are supposed to be linear arrays, whose axes are horizontal and situated in the transverse plane of the tunnel, this configuration being quite usual. An approach based on the Kronecker model [21] was chosen for its simplicity.

To determine the various elements of **H**, the following steps can be followed:

(1) define the system parameters, such as frequency, distance between the transmitter and the receiver, number of array elements at the transmitter and at the receiver, element spacing and number of snapshots, corresponding to the number of realizations to be simulated;

(2) determine a value for the path loss $\mathrm{PL}(f,d)$ using (3);

(3) compute a K factor from (11). We recall that in (3) and in (11), the value given by the model is the sum of two terms: a deterministic one plus a random variable whose standard deviation is known;

(4) knowing K and $\mathrm{PL}(f,d)$, the elements of a $\mathbf{G}_{\mathrm{trans}}$ matrix, having the same size as **H**, are randomly chosen in a normalized Ricean distribution;

(5) as mentioned in Section 4, it was assumed that the correlations between either the transmitting elements or the receiving elements follow the same distribution. The terms of the correlation matrices at the transmitting and receiving sites, R_{Rx} and R_{Tx}, are thus deduced from (19).

The Kronecker model leads to

$$\mathbf{H} = \mathrm{PL}(f,d)\mathbf{R}_{\mathrm{Rx}}^{1/2}\mathbf{G}_{\mathrm{trans}}\left(\mathbf{R}_{\mathrm{Tx}}^{1/2}\right)^{T}. \tag{20}$$

To give an example of application of this formula, let us consider a 4×4 MIMO system at 4 GHz, an array element spacing of 0.8λ (6 cm at 4 GHz) and a distance d between the transmitter and the receiver of 250 m.

The channel capacity of a MIMO system for a given channel realization **H** can be computed as [22]

$$C = \log_2\left(\det\left|\mathbf{I}_N + \frac{\mathrm{SNR}}{M}\mathbf{H}\mathbf{H}^{\dagger}\right|\right), \tag{21}$$

where $\mathbf{I}_N$ is the $N \times N$ identity matrix, $(\,)^{\dagger}$ is the transpose conjugate operation and SNR is the signal-to-noise ratio at the receiver. The channel capacity C was calculated by assuming a fixed SNR equal to 10 dB. A constant SNR was chosen because we want to emphasize the influence of correlation and field distribution in the transverse plane. To compute the capacity assuming a fixed transmitting power, the contribution of the path loss must be added, which is straightforward.

The model was applied by considering 1000 realizations and the cumulative probability density function of the capacity is plotted in Figure 11 (curve "model"). To be able to compare this distribution to experimental results, a large number of measured values are needed. To increase this number we have thus calculated the capacity not only at 4 GHz, but also for all frequencies within a 100 MHz band around 4 GHz. We see in Figure 11, the rather good agreement between results deduced from the experiments (curve "measurements") and those given by the model.

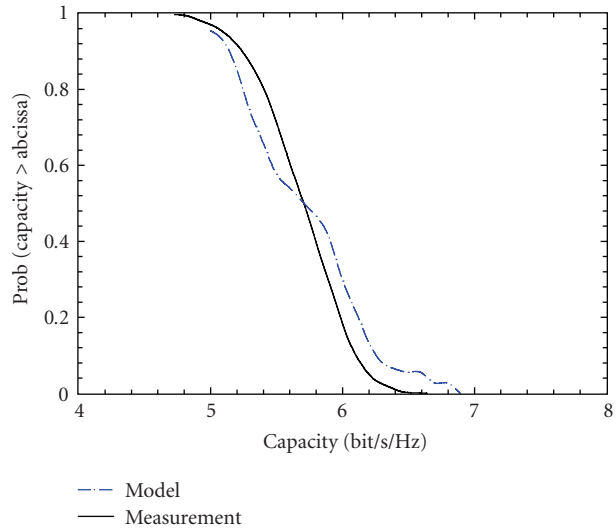

Figure 11: Application of the MIMO model for a 4×4 MIMO system, for a frequency of 4 GHz and for a distance of 250 m.

7. Conclusion

The statistics of the electromagnetic field variation in a tunnel has been deduced from measurements made in an arched tunnel, which is the usual shape of road and railway tunnels, and in a frequency range extending from 2.8 to 5 GHz. Both the methodology of the experiments and the analysis were aimed at predicting the performance of an MIMO link in a wide frequency band.

It was shown, by subtracting the antenna effect, that the path loss is not strongly dependent on frequency and that the attenuation constant keeps small values, the tunnel behaving as a low-loss guiding structure. Along the investigated transverse axis of the tunnel, over 33 cm long, the small-scale fading follows a Ricean distribution. However, for distances between the transmitting and receiving antennas up to 200 m, the K factor is below -15 dB, meaning that the field is nearly Rayleigh distributed. It also appeared that K is an increasing function of distance, reaching 0 dB at about 400 m.

Empirical formulas to model the main propagation characteristics were proposed and applied to generate transfer matrices of an MIMO link.

Acknowledgments

This work has been supported by the European FEDER funds, the Region Nord-Pas de Calais, and the French ministry of research, in the frame of the CISIT project.

References

[1] Y. Yamaguchi, T. Abe, and T. Sekiguchi, "Radio wave propagation loss in the VHF to microwave region due to vehicles in tunnels," *IEEE Transactions on Electromagnetic Compatibility*, vol. 13, no. 1, pp. 87–91, 1989.

[2] M. Lienard and P. Degauque, "Natural wave propagation in mine environments," *IEEE Transactions on Antennas and Propagation*, vol. 48, no. 9, pp. 1326–1339, 2000.

[3] D. Didascalou, J. Maurer, and W. Wiesbeck, "Subway tunnel guided electromagnetic wave propagation at mobile communications frequencies," *IEEE Transactions on Antennas and Propagation*, vol. 49, no. 11, pp. 1590–1596, 2001.

[4] X. Yang and Y. Lu, "Research on propagation characteristics of millimeter wave in tunnels," *International Journal of Infrared and Millimeter Waves*, vol. 28, no. 10, pp. 901–909, 2007.

[5] Y. P. Zhang and Y. Hwang, "Characterization of UHF radio propagation channels in tunnel environments for microcellular and personal communications," *IEEE Transactions on Vehicular Technology*, vol. 47, no. 1, pp. 283–296, 1998.

[6] Y. P. Zhang, G. X. Zheng, and J. H. Sheng, "Radio propagation at 900 MHz in underground coal mines," *IEEE Transactions on Antennas and Propagation*, vol. 49, no. 5, pp. 757–762, 2001.

[7] C. Briso-Rodriguez, J. M. Cruz, and J. I. Alonso, "Measurements and modeling of distributed antenna systems in railway tunnels," *IEEE Transactions on Vehicular Technology*, vol. 56, no. 5, part 2, pp. 2870–2879, 2007.

[8] T.-S. Wang and C.-F. Yang, "Simulations and measurements of wave propagations in curved road tunnels for signals from GSM base stations," *IEEE Transactions on Antennas and Propagation*, vol. 54, no. 9, pp. 2577–2584, 2006.

[9] G. S. Ching, M. Ghoraishi, N. Lertsirisopon, et al., "Analysis of DSRC service over-reach inside an arched tunnel," *IEEE Journal on Selected Areas in Communications*, vol. 25, no. 8, pp. 1517–1525, 2007.

[10] M. Boutin, A. Benzakour, C. L. Despins, and S. Affes, "Radio wave characterization and modeling in underground mine tunnels," *IEEE Transactions on Antennas and Propagation*, vol. 56, no. 2, pp. 540–549, 2008.

[11] J.-M. Molina-Garcia-Pardo, M. Lienard, P. Degauque, D. G. Dudley, and L. Juan-Llàcer, "Interpretation of MIMO channel characteristics in rectangular tunnels from modal theory," *IEEE Transactions on Vehicular Technology*, vol. 57, no. 3, pp. 1974–1979, 2008.

[12] M. Liénard, P. Degauque, J. Baudet, and D. Degardin, "Investigation on MIMO channels in subway tunnels," *IEEE Journal on Selected Areas in Communications*, vol. 21, no. 3, pp. 332–339, 2003.

[13] M. Lienard and P. Degauque, "Propagation in wide tunnels at 2 GHz: a statistical analysis," *IEEE Transactions on Vehicular Technology*, vol. 47, no. 4, pp. 1322–1328, 1998.

[14] A. F. Molisch, "Ultrawideband propagation channels-theory, measurement, and modeling," *IEEE Transactions on Vehicular Technology*, vol. 54, no. 5, pp. 1528–1545, 2005.

[15] T. S. Rappaport, *Wireless Communications*, Prentice-Hall, Englewood Cliffs, NJ, USA, 1996.

[16] S. S. Ghassemzadeh, R. Jana, C. W. Rice, W. Turin, and V. Tarokh, "Measurement and modeling of an ultra-wide bandwidth indoor channel," *IEEE Transactions on Communications*, vol. 52, no. 10, pp. 1786–1796, 2004.

[17] J. Keignart and N. Daniele, "Channel sounding and modeling for indoor UWB communications," in *Proceedings of International Workshop on Ultra Wideband Systems (IWUWBS '03)*, Oulu, Finland, June 2003.

[18] D. Cassioli, M. Z. Win, and A. F. Molisch, "The ultra-wide bandwidth indoor channel: from statistical model to simulations," *IEEE Journal on Selected Areas in Communications*, vol. 20, no. 6, pp. 1247–1257, 2002.

[19] V. Hovinen, M. Hämäläinen, R. Tesi, L. Hentilä, and N. Laine, "A proposal for a selection of indoor UWB path loss model," Tech. Rep. IEEE P802.15-02/280-SG3a, Wisair, Tel Aviv, Israel, July 2002, http://grouper.ieee.org/groups/802/15/pub/2002/Jul02.

[20] A. Papoulis and S. U. Pillai, *Probability, Random Variables and Stochastic Processes*, McGraw-Hill, Boston, Mass, USA, 4th edition, 2002.

[21] J. P. Kermoal, L. Schumacher, K. I. Pedersen, P. E. Mogensen, and F. Frederiksen, "A stochastic MIMO radio channel model with experimental validation," *IEEE Journal on Selected Areas in Communications*, vol. 20, no. 6, pp. 1211–1226, 2002.

[22] G. J. Foschini and M. J. Gans, "On limits of wireless communications in a fading environment when using multiple antennas," *Wireless Personal Communications*, vol. 6, no. 3, pp. 311–335, 1998.

Hindawi Publishing Corporation
EURASIP Journal on Wireless Communications and Networking
Volume 2009, Article ID 784905, 13 pages
doi:10.1155/2009/784905

Research Article

Propagation Measurements and Comparison with EM Techniques for In-Cabin Wireless Networks

Nektarios Moraitis,[1] Philip Constantinou,[1] Fernando Perez Fontan,[2] and Pavel Valtr[2]

[1] *Mobile Radiocommunications Laboratory, National Technical University of Athens, 9 Heroon Polytechniou str., Zografou, 15773, Athens, Greece*
[2] *Department of Signal Theory and Communications, ETSI Telecommunicacion, University of Vigo, 36200, Vigo, Spain*

Correspondence should be addressed to Fernando Perez Fontan, fpfontan@tsc.uvigo.es

Received 2 September 2008; Revised 20 January 2009; Accepted 16 March 2009

Recommended by Claude Oestges

This paper presents results of a narrowband measurement campaign conducted inside a Boeing 737–400 aircraft, the objective being the development of a propagation prediction model which can be used in the deployment of in-cabin wireless networks. The measurements were conducted at three different frequency bands: 1.8, 2.1, and 2.45 GHz, representative of several wireless services. Both a simple, empirical, inverse distance power law and a deterministic, site-specific model were investigated. Parameters for the empirical model were extracted from the measurements at different locations inside the cabin: aisle and seats. Additionally, a statistical characterization of the multipath scenario created by the transmitted signal and the various cabin elements is presented. The deterministic model, based on Physical Optics (PO) techniques, provides a reasonable match with the empirical results. Finally, measurements and modeling results are provided for the penetration loss into the cabin (or out of the cabin), representative of interference scenarios.

1. Introduction

Airplanes seem to be the last remaining frontier where wireless communications and Internet access are still not available [1]. Airlines are increasingly interested in providing passengers with in-flight wireless services allowing a similar entertainment or business experience as their terrestrial counterparts [2]. The so-called "in-cabin wireless networks" will allow the passengers to use their own personal equipment such as mobile phones, laptops, or PDAs while the aircraft is en-route. The typical onboard infrastructure contains an in-cabin wireless access point, a service integrator/server and an aircraft-to-satellite link, in order to connect the in-cabin network to the terrestrial backbone network through a satellite, as shown in Figure 1.

To succeed in the implementation of such wireless communication systems inside aircraft, and to assess their expected performance, it is necessary to have at our disposal an in-depth and thorough characterization of the in-cabin channel. Furthermore, to avoid interference from outside networks, or interfering with external networks, it is essential to assess and limit the attenuation introduced by the body of the aircraft.

Up to now, only few measurement campaigns have been conducted in this type of scenarios, for example, [2] and [3], at very specific frequency bands. Scarce deterministic prediction and capacity planning studies [4–8] have been carried out. Simple empirical, regression-based models have been developed in [9]. As for deterministic models, they have been mainly based on (Uniform Theory of Diffraction) UTD techniques [6]. Some of the references also provide presence of passenger effects [10] and wideband measurements, that is, delays spread, not considered in this paper. Some of these studies have been performed in relation to the use of Ultra-wideband (UWB) systems [10, 11], a technique likely to be used in Wireless Personal Area Networks (WPAN) for linking computers and peripherals at very short distances.

A major concern in the use of wireless *passenger-carried electronic devices* (PEDs) aboard aircraft is their electromagnetic compatibility (EMC) with aircraft electronic systems.

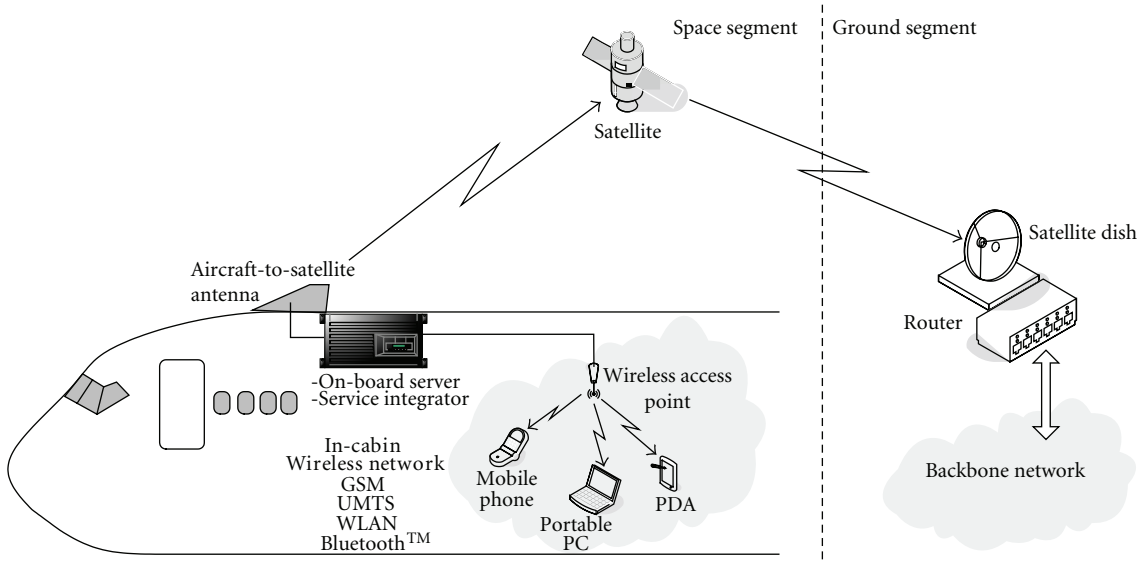

Figure 1: In-cabin wireless network infrastructure.

Intentional PED emitters are protected by frequency separation regulated by the International Telecommunication Union (ITU). Therefore, any intentional emission from an arbitrary PED is out of band for any aircraft NAV/COM system today [1]. Due to frequency separation WLAN 802.11b should not be a candidate to interfere with sensitive aircraft navigation and communication systems. WLAN is out of band to any current aircraft navigation or communication system. Consequently, Bluetooth, for example, currently is exempt from restrictions on wireless emitters inside the cabin [12]. Intentional emitters can be allowed aboard aircraft according to RTCA/DO233 recommendations if their safe use is demonstrated [13]. For A340-600 the safe use and compatibility of WLAN has been demonstrated in the aircraft environment at a power level artificially increased 250 times. Bluetooth has been investigated by Intel [14]. Lufthansa already provides a certified wireless service in the cabin in combination with portable electronic devices. During tests conducted thus far, even nonessential systems such as in-flight entertainment that are qualified to low susceptibility levels have not been observed to be disturbed [1]. From a technical point of view there is no general objection to the use of these services.

The first goal of this paper is to describe the narrowband measurement campaign performed and provide an adequate channel characterization of the in-cabin environment for personal wireless communications at GSM, UMTS, and ISM bands. This paper provides an empirical in-cabin path loss model together with a statistical characterization of the multipath environment, that is, the spatial distribution of the received signal, that is, a standing wave, complementing the results provided in the aforementioned papers. Our results refer to the aisle as well as the passenger seats. The *insertion loss* caused by the seat backrests is also defined and quantified. Additionally, *entry loss* measurements were conducted to evaluate the outdoor-to-indoor attenuation introduced by the body of the aircraft at different seats along its length.

The reported measurements were performed inside a Boeing 737–400 aircraft at three different frequency bands:

(i) 1.8 GHz representative of GSM services,

(ii) 2.1 GHz for UMTS networks,

(iii) 2.45 GHz for WLAN and Bluetooth links.

The measurements have been performed using standard antennas. An alternative to providing in-cabin coverage is using *radiating cables*, also called *leaky feeders*, laid along the roof of the cabin [3].

The second target was to develop a simple, site-specific model for in-cabin and outdoor-indoor propagation based on Physical Optics (PO) techniques. The approach followed, and the comparisons between predictions and measurements are presented in some detail. The main purpose of developing an EM based, site-specific tool is the need to extend the modeling to all possible types of aircraft. The reported measurements have been performed in a medium-sized plane. Consequently, the empirical models derived for this aircraft will not be usable in much larger airplanes, with a much larger size, and different configuration: distribution of seats, and so forth. However, once an EM model is properly validated and fine-tuned, it will be possible to use it in any new aircraft configuration, and especially, at different frequency bands that need analysis. Thus, the contribution made in this paper is expected to be of immediate practical interest.

The remainder of this paper is organized as follows. Section 2 presents the experimental setup for the in-cabin and outdoor-to-cabin measurements, a detailed description of the aircraft, and the measurement procedure are discussed. In Section 3, we show the empirical path loss model and corresponding extracted parameters from the measurement

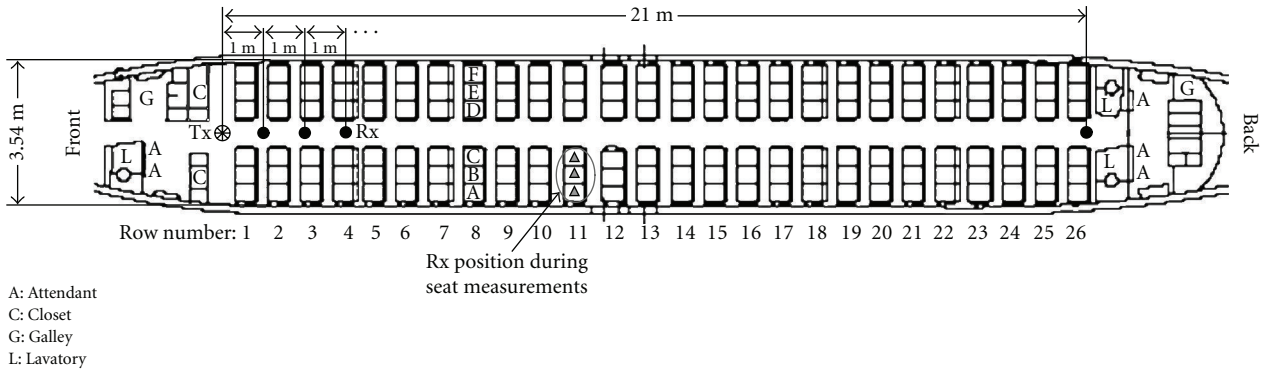

Figure 2: Ground plan of the measurement environment.

data, moreover, the fading statistics of the in-cabin radio channel are given. Additionally, the entry losses into the cabin for different locations along the length of the aircraft have also been extracted. Section 4, discusses the physical, PO-based model developed together with implementation details. A comparison between measurements and predictions is presented both for the in-cabin and penetration cases. Finally, Section 5 is devoted to summarizing the work presented in the preceding sections.

2. Experimental Setup

2.1. Measurement Environment. The Boeing 737–400 [15] is a short-haul aircraft with a seating capacity of 156 passengers, all in economy class configuration, arranged in 26 rows. The aircraft dimensions are overall aircraft length 38.4 m, height 11.15 m, maximum cabin width and height 3.54 m and 2.2 m, respectively, and length of the passengers area 22 m. Seats are called A, B, and C from window to aisle on the left side of the aisle facing the direction of flight, and D, E, and F from aisle to window on the right side of the aisle. The aisle width is 0.5 m. The seat height is 1.15 m above the floor and the distance between the seat centers is 43 cm. The distance between rows is 81 cm. The seats have textile covers. The passenger luggage compartments are located 1.68 m above the floor, 1.16 m apart, and 45 cm over the passenger heads. The ground plan of the measurement environment is shown in Figure 2.

2.2. Measurment Setup. The measurements were made by transmitting a continuous wave (CW) signal, at the three aforementioned frequency bands, from a fixed transmitter to a fixed receiver, and recording the signal level. The measurement setup is sketched in Figure 3. The transmitter output power was 0 dBm and antenna utilized at 1.8 GHz was a vertically polarized patch with a 7.5 dBi gain. The vertical and horizontal 3-dB beamwidths were 70° and 75°, respectively. For the measurements at 2.1 and 2.45 GHz a discone antenna with a semispherical gain of 0 dBi was used. The receive hardware was placed on a trolley, which was stationary at each measurement position. After amplification, the received signal was fed to a spectrum analyzer which was used as a receiver using the zero-span setting. The auxiliary video output of the spectrum analyzer was then sampled at 1 kHz and the values were stored to a portable PC. At the receive side, a vertically polarized omnidirectional antenna was used having a gain of between 0.75 and 1.64 dBi, depending on the frequency. The transmitter and receiver characteristics are summarized in Table 1.

Table 1: Transmitter and receiver characteristics.

Transmitter			
Frequency	1.8 GHz	2.1 GHz	2.45 GHz
Power output		0 dBm	
Antenna gain	7.5 dBi	0 dBi	0 dBi
EIRP	7.5 dBm	0 dBm	0 dBm
Receiver			
Receiver sensitivity		−90 dBm	
Antenna gain	1.64 dBi	1.63 dBi	0.75 dBi
LNA gain	26.3 dB	28.1 dB	26.2 dB
Total loss	3.7 dB	4.7 dB	5.3 dB
Total measurable path loss	122 dB	115 dB	112 dB

2.3. Measurement Procedure. Different sets of measurements were conducted inside the aircraft. In the first, the received power was measured at different points along the aisle as well as at the passenger seats in order to identify the decay rate of the average received power with increasing distances from the transmitter. Additionally, a statistical characterization of the multipath scenario, that is, its spatial variations, was also performed. Finally, the measurements have been compared with predictions carried out with a deterministic model.

During the measurements, the aircraft was in parked position and the cabin had no passengers. Under these conditions, the channel can be regarded as stationary or, at least, quasistationary. Small time variations were observed barely exceeding a standard deviation of one dB, due to the presence of the people involved in the measurements.

While performing the measurements along the aisle, the transmit and receive antennas were at 1.8 and 1.7 m above the floor, respectively, and were always aligned to point at each other, thus preserving the line-of-sight (LoS) condition. The

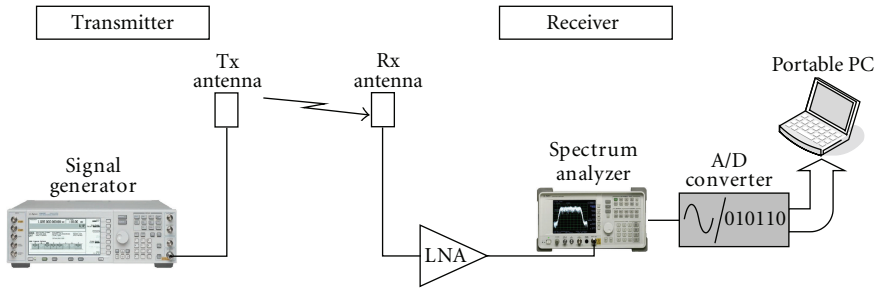

Figure 3: Measurement system setup.

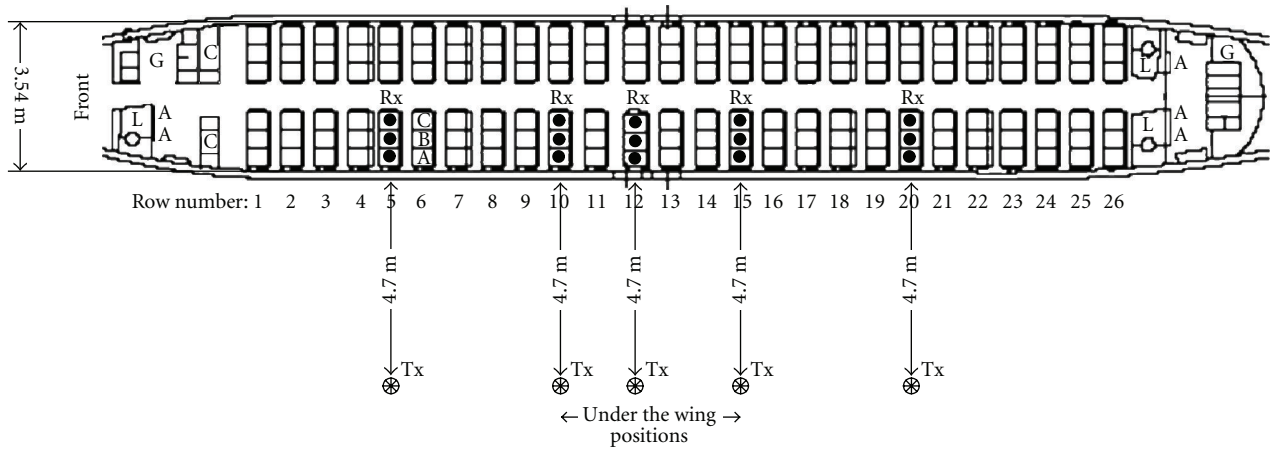

Figure 4: Ground plan of the attenuation measurement procedure.

transmitter was placed at the beginning of the aisle (Figure 2) and recordings were performed starting with the receiver located 1 m away from the transmitter up to 21 m in steps of 1 m, as indicated in Figure 2. At each position, the receive antenna was shifted by $\pm 4\lambda$ with respect to the nominal measurement position in steps of λ (in all, 9 recordings), so as to obtain uncorrelated measurements. It should be pointed out that the spatial variations thus observed, due to a spatial standing wave generated by the multipath, are much stronger than the time variations mentioned above.

Then, the nine recordings were averaged [16]. Each recording lasted 10 seconds so that a total of 90 k samples (9×10 s $\times$ 1000 samples/s) were used to calculate the *local mean* of the received power at each nominal measurement position. From the local mean the average path loss (dB) was calculated.

Similar measurements were also conducted at the seats. The measurements were taken at every seat from row 2 up to row 26, and at each of the three frequency bands. The transmitter was located at the same position as that given in Figure 2, at 1.8 m above the floor and the receiver was placed at each seat with the antenna a few centimeters below the head of the backrest (approximately 1.10–1.12 m above the cabin floor). Hence, the passenger seat intercepted the direct path between the transmitter and receiver, giving rise to an obstructed line-of-sight (OLoS) condition. Each recording, again, lasted 10 seconds, that is, 10 k samples which were averaged to find the mean power (*local mean*) at each passenger seat. In all, 150 sets of power recordings, corresponding to all the measurement seats, were collected (25 rows $\times$ 6 seats/row).

A final measurement set was gathered for evaluating the attenuation (*entry loss*) due to the fuselage in an outdoor-to-indoor configuration, typical of interference paths between the in-cabin network and outside networks. Attenuation measurements were taken at five different positions along the aircraft's length. The horizontal separation between the transmitter and the aircraft was always kept at 4.7 m. Attenuation measurements were taken at rows 5, 10, 12, 15, and 20. The measurements corresponding to rows 10, 12, and 15 were performed with the transmitter shaded by the wing, as shown in Figure 4. These measurements were performed with the transmitter outside the aircraft at the height of 1.65m above the ground.

The receiver was placed at the seats A, B, and C in order to collect the measurements as indicated in Figures 4 and 5. The receiver height was approximately 1.10–1.12 m above the floor. Each measurement lasted 10 seconds and, again, 10 k power samples were collected from which the average received power was computed. The average path loss was then calculated for each seat. From the actual geometry of the link, we calculated the distance between the transmitter and the receiver at each position.

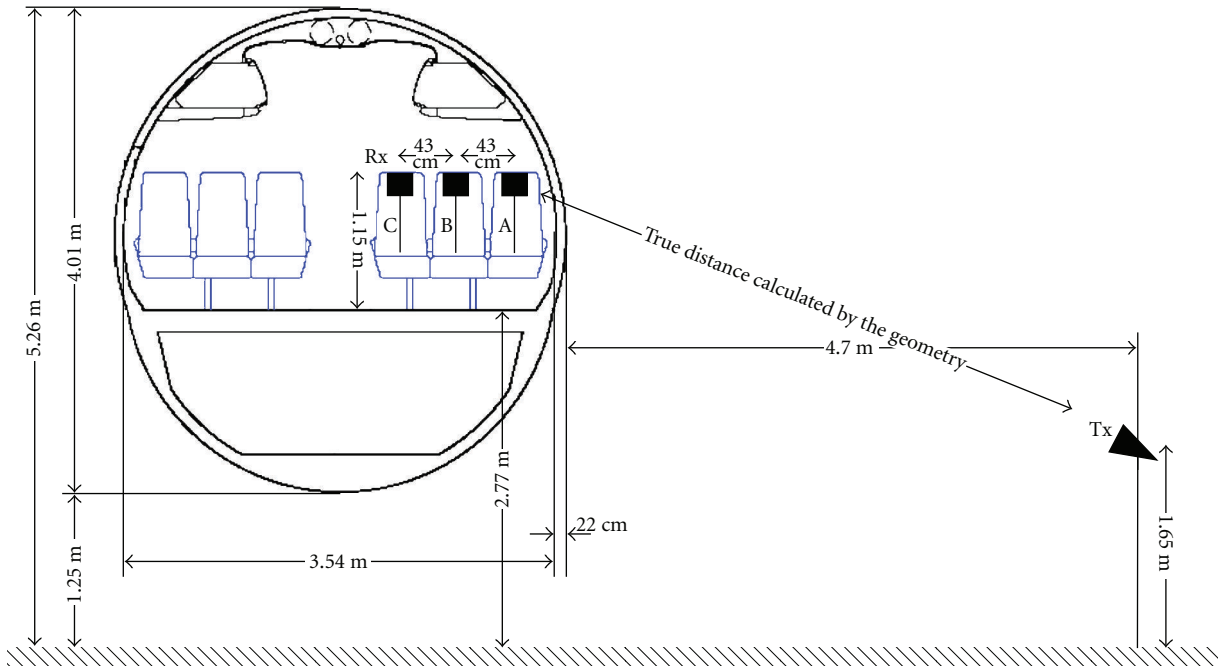

Figure 5: Cross-section of the attenuation measurement configuration.

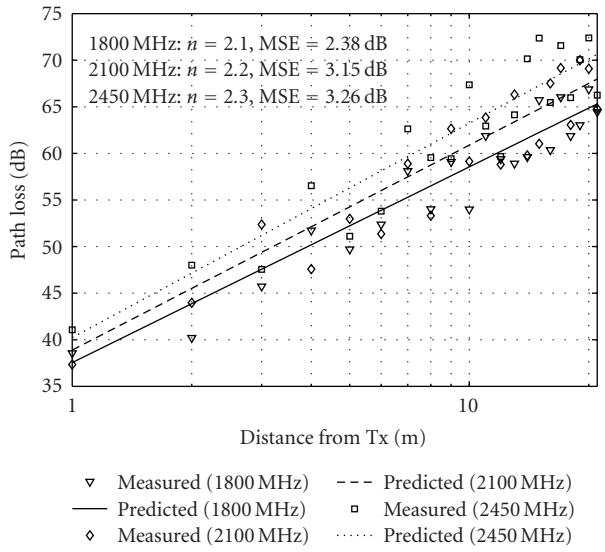

Figure 6: Path loss model results at the three frequency bands along the aisle of the aircraft.

3. Measurement Results

3.1. Path Loss Modeling. A model to predict the path loss inside the aircraft cabin, along the aisle, can be formulated using the following relationship [17]:

$$\overline{PL}(d) = FSL(d_0) + 10n \log_{10}\left(\frac{d}{d_0}\right)(\text{dB}), \qquad (1)$$

where $\overline{PL}(d)$ is the average path loss value (dB) at a distance d (m) from the transmitter to the receiver, $FSL(d_0)$ is the free-space path loss (dB) at a reference distance d_0, and n is the path loss exponent (decay rate) that characterizes how fast the path loss increases with increasing transmitter-receiver separation. This model is quite standard in indoor propagation studies and corresponds, in linear units, to a power law of exponent n with the inverse of the path length. What needs to be worked out is the adequate parameter, n, for the specific case of in-cabin propagation, where wave-guide effects may be present.

In our case, the reference distance, d_0, was set to 1 m, therefore, the free-space path loss is 37.5, 38.9, and 40.2 dB for 1.8, 2.1, and 2.45 GHz, respectively. Taking into account the model in (1), when performing the measurement analysis, the path loss parameter (decay rate) n was found to be 2.1 at 1.8 GHz, 2.2 at 2.1 GHz and 2.3 at 2.45 GHz. The mean square error (MSE) between the measured and the predicted values was found to be 2.38, 3.15, and 3.26 dB, respectively. A comparison between the measured and the model results is presented in Figure 6 for the three bands. Given the small MSE values observed, it can be concluded that the model describes the propagation environment along the aisle with great accuracy.

Due to the specific aircraft structure (tunnel-like), path loss exponents lower than 2, indicating the presence of clear wave-guiding effects, could have been expected. In our case, the decay factor was found to be slightly greater than 2. This can be attributed to the heavy cluttered environment in the cabin. The waveguide effect is counterbalanced as the aircraft interior is comprised of materials that do not enhance the wave-guide propagation phenomenon; the floor is covered with a thick carpet while the seats are made of a non-reflective textile. Moreover, the gaps between rows of seats trap the transmitted rays, and hence, the wall-reflected power cannot fully arrive at the receiver.

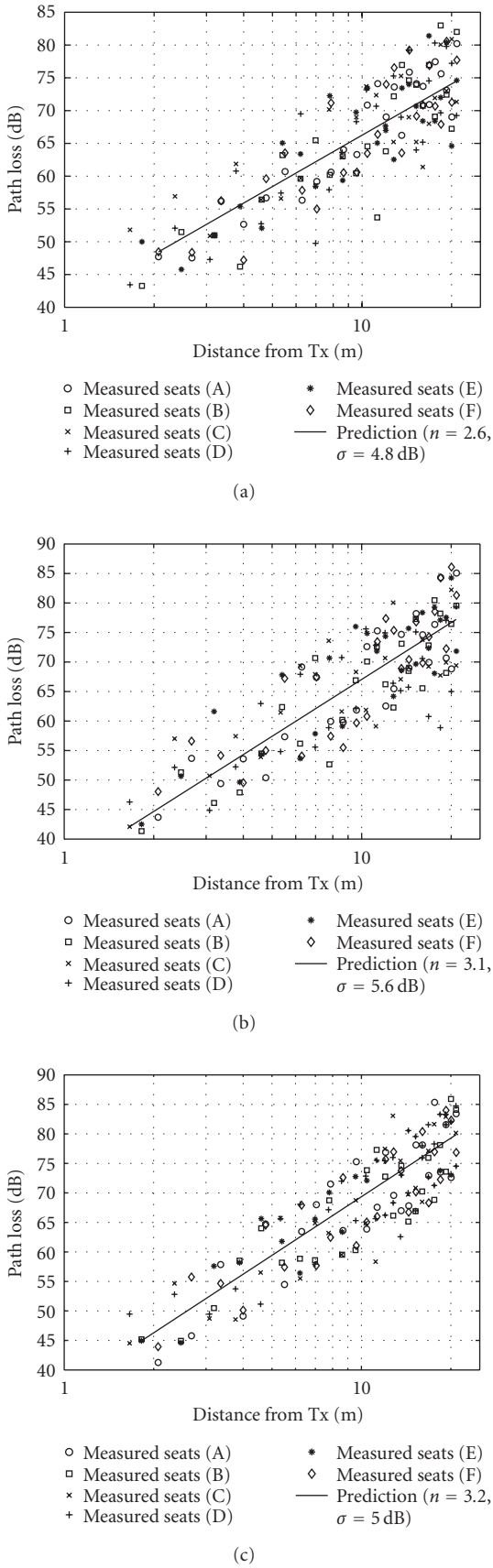

Figure 7: Path loss model results at the seats of the aircraft at: (a) 1.8 GHz, (b) 2.1 GHz, and (c) 2.45 GHz.

To describe the path loss at the seats where OLoS conditions exist, we can utilize (1) but the power decay factor is expected to be greater than 2. Applying (1) to the measured path loss at the passenger seats, the path loss exponent was found to be between 2.0 and 3.1 at 1.8 GHz, 2.5 and 3.4 at 2.1 GHz and between 2.5 and 3.9 at 2.45 GHz. The overall mean square error (MSE) between the measured and the predicted values was found to be 4.8, 5.6, and 5.0 dB, respectively.

From an ensemble study of all 150 seats, the average path loss factor, n, was found to be 2.6, 3.1, and 3.2 at 1.8, 2.1 and 2.45 GHz, respectively. A comparison between the measurements and the model at all the seats is presented in Figure 7 for the three frequencies. The small MSE values observed indicate that the model describes the in-cabin propagation environment with great accuracy, both at the corridor and seats.

From the measurements at the seats, we can define the *average seat insertion loss* due to the backrests. For performing such calculation, the free-space loss FSL_i at each seat (150 of them) was carried out taking into account the actual Tx-Rx linear distance d_i. The average insertion loss was calculated using

$$\overline{L}_{seat} = \frac{1}{N}\sum_{i=1}^{N}\left(\overline{PL}_i^{\text{meas}} - FSL_i\right)(\text{dB}), \tag{2}$$

where FSL_i is the free-space loss at the ith seat, $\overline{PL}_i^{\text{meas}}$ is the average measured path loss at the i-th passenger seat and N is total number of measurement seats (N = 150). According to the above expression, the average passenger seat backrest insertion loss was 7.7 dB at 1.8 GHz, 8.1 dB at 2.1 GHz, and 9.6 dB at 2.45 GHz, respectively.

3.2. Fading Statistics (Spatial Variability of the Channel due to Multipath). As said in Section 2.3, the channel is practically stationary, in time, while there are very marked spatial variations due to multipath. In the measurements, it was found that the channel response remained practically constant for periods of over 7 seconds (the envelope autocorrelation function remained invariant over time at a level above 0.9), for the whole ensemble of measurement locations (aisle and seats), and of all three frequency bands.

Using the local mean of the received power as a reference, the ensemble of fade depths for a specific location was calculated as [16]

$$F_k = P_k - \overline{P}(\text{dB}), \tag{3}$$

where F_k is the k-th fade depth (in dB), P_k is the kth received power sample and $\overline{P}$ is the measured local mean power, both in dB. From these fade depths, the average (M), standard deviation (Σ), 90% percentile, minimum value, and dynamic range (DR) were calculated for each one of the measured locations along the aisle and at the seats. Note that one location along the corridor is actually represented by a set of nine points, including the nominal location, in a $\pm 4\lambda$ line.

Table 2, summarizes these statistical results at five different locations along the aisle at the three measurement frequencies. Additionally, Table 3 presents the average statistics for all 150 passenger seats at the three frequencies.

Table 2: Fading statistics along the aisle of the Boeing 737–400.

f [GHz]	$d_{\text{Tx-Rx}}$ [m]	$\overline{P}$ [dBm]	$\overline{PL}$ [dB]	M [dB]	Σ [dB]	90% [dB]	$\min\{F_i\}$ [dB]	DR [dB]	K-factor [dB]
1.8	1	−6.7	38.5	−0.25	1.07	1.37	−3.7	4.9	13.6
	5	−8.4	40.1	−0.28	1.14	1.40	−4.3	5.9	13.1
	10	−13.9	45.6	−0.30	1.21	1.47	−4.7	6.3	12.7
	15	−19.9	51.7	−0.32	1.15	1.50	−4.5	6.9	12.2
	20	−17.9	49.6	−0.35	1.33	1.55	−5.2	7.0	11.3
		Overall average		−0.30	1.18	1.46	−4.5	6.2	12.6
2.1	1	−12.3	37.3	−0.30	1.13	1.41	−4.3	5.6	13.5
	5	−18.9	44.0	−0.32	1.21	1.47	−4.7	6.3	12.9
	10	−27.3	52.4	−0.36	1.33	1.52	−5.1	6.7	12.3
	15	−22.6	47.6	−0.38	1.36	1.57	−5.5	7.3	11.8
	20	−27.9	53.0	−0.40	1.41	1.63	−5.8	7.8	11.2
		Overall average		−0.35	1.29	1.52	−5.1	6.7	12.3
2.45	1	−19.4	41.1	−0.32	1.22	1.48	−4.9	6.0	13.8
	5	−26.4	48.0	−0.34	1.33	1.53	−5.5	6.7	12.5
	10	−25.9	47.6	−0.37	1.36	1.59	−6.0	7.7	12.0
	15	−34.9	56.5	−0.40	1.44	1.62	−6.2	7.8	11.5
	20	−29.5	51.1	−0.42	1.51	1.68	−6.3	8.1	10.9
		Overall average		−0.37	1.37	1.58	−5.8	7.2	12.1

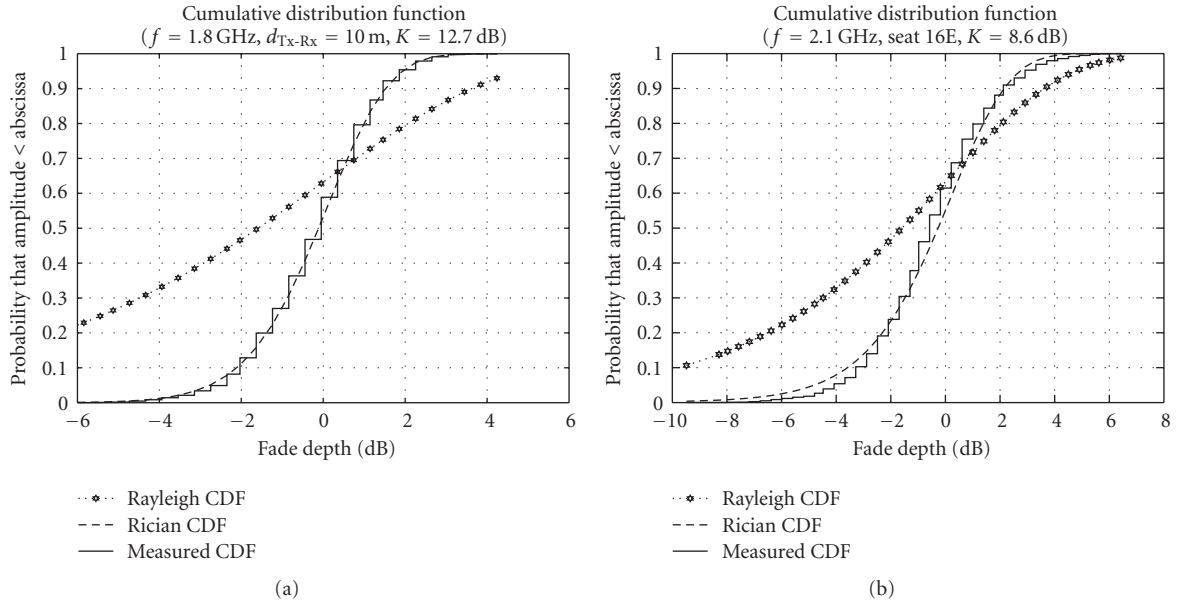

Figure 8: Indicative cumulative distribution functions: (a) at the corridor of the aircraft, and (b) at the seats of the aircraft.

Cumulative distribution functions (CDFs) for the envelope of the received signal (in linear units) were computed for each receive antenna location. In all cases, it was found that the spatial fading statistics corresponded very well with a Rice distribution with average K parameter (direct-to-multipath power ratio) between 12.1 and 12.6 dB in the aisle, and between 7.3 and 8.1 dB at the seats. The Cramer-von-Mises criterion was used to estimate the goodness-of-fit [18] to the Rice distribution.

Example CDFs are presented in Figure 8 for both the aisle and the seats of the aircraft. The Rayleigh CDF is also shown for comparison. It can be observed how the K-factors are lower at the seats than along the aisle. This is due to obstruction of the direct ray by the backrests of the various seats.

Along the aisle, from the extracted results, only a slight increase in the dynamic range of the fades (also confirmed by the other parameters) was observed as the distance between the receiver and the transmitter was increased. However, overall, the fading statistics can be regarded as range independent. Thus, the K-factor only decreased with increasing distance by approximately 2 dB between first and the last sections of the measured data (Table 2).

Table 3: Average fading statistics for ensemble of seats.

Frequency	1.8 GHz	2.1 GHz	2.45 GHz
$\overline{P}$[dBm]	−33.8	−41.0	−45.8
$\overline{PL}$[dB]	65.6	66.0	67.5
M [dB]	−1.4	−1.7	−1.8
Σ [dB]	2.6	2.8	2.7
90% [dB]	2.9	3.1	2.8
min$\{F_i\}$ [dB]	−11.0	−13.5	−14.7
DR [dB]	12.6	15.7	16.3
K-factor [dB]	8.1	7.5	7.3

On the other hand, the fade dynamic range, DR, increases, also confirmed by the other statistics (M, Σ, and 90% percentile), at the seats in comparison with the results along the aisle, see Tables 2 and 3. The lower K-ratios at the seats, are due to the OLoS propagation condition due to the obstruction of the direct path. The received signal envelope though, still follows quite well a Rice distribution, see Figure 8(b).

From the above discussion, it is possible to complete the model in (1). This model describes the average of the path loss at distance d. However, a three-stage model is usually assumed when describing the actual loss [19], which includes a distance dependent term, that in (1), slow variations due to shadowing and faster (in time and space) variations due to multipath. In our case, the new expression for (1) becomes

$$PL(d) = \overline{PL}(d) + X(0,\sigma_L) + Y + Z$$
$$= FSL(d_0) + 10n\log 10\left(\frac{d}{d_0}\right) + X(0,\sigma_L) + Y + Z\,(\text{dB}), \quad (4)$$

where $PL(d)$ represents the path loss at one particular point and time which is given by the sum of an average, distance-dependent term, $\overline{PL}(d)$, a spatially slowly varying term, $X(0,\sigma_L)$, which can be modelled as a zero-mean Gaussian term with a standard deviation or location variability, σ_L, which can be equated to the MSE of the fittings in Section 3.1, that is, 2.38, 3.15, and 3.26 dB, for the aisle paths at the three frequencies of interest, and 4.8, 5.6, and 5.0 dB for the seats. The last two terms, Y and Z, would be the space and time variability terms due to multipath. In this section we have characterized Y in linear units as Rice distributed. The time variations, as said, are negligible in this case.

It should be pointed out that the measurements performed provide a limited accuracy when used for extracting passenger seat model parameters. This has been due to the fact that the measurements were taken at only one position per measurement location, that is, no spatial averaging has been carried out. However, in the time domain, variations due to the quasistatic nature of the channel have been smoothed out through time averaging of ten consecutive snapshots.

3.3. Indoor-Outdoor Penetration Loss. To evaluate the loss caused by the fuselage, including its openings (windows, etc.) to indoor-to-outdoor paths, we compared the free-space loss for the true distance, d_i, between a transmitter situated outside the aircraft and a receiver placed at seats A, B, and C, as indicated in Figure 5. Distance d_i could easily be calculated using simple geometry. The attenuation for each row was calculated by averaging the measurements at seats A, B, and C according to

$$\overline{EL}_i = \overline{PL}_i^{\text{meas}} - \overline{FSL}_i\ (\text{dB}) \quad (5)$$

where $\overline{EL}_i$ is the average entry loss for row i, $\overline{FSL}_i$ is the average free-space loss for row i, and $\overline{PL}_i^{\text{meas}}$ is the average measured path loss. The data processing here also includes the averaging over all tree seats, A, B, and C, of the same row. The entry loss results are summarized in Table 4 for each frequency band. There is a clear increase in the attenuation values especially for rows 10, 12, and 15, for which the transmitter was located under the wing. On average, the attenuation was approximately 4.8 dB larger.

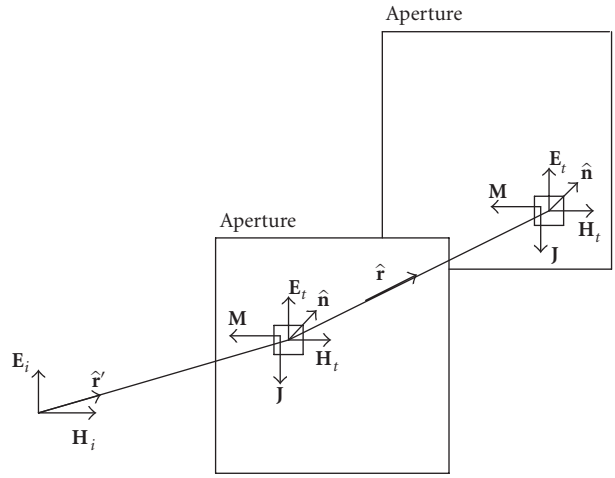

Figure 9: Basic outline of the physical optics calculation.

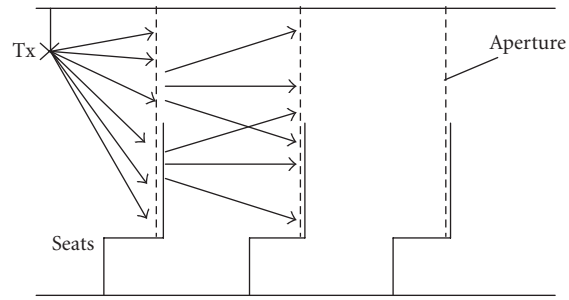

Figure 10: Schematic diagram of the modeling approach employed.

4. Comparison With EM Techniques

4.1. Physical Optics Basics. In this section, a comparison between the above measurements and simple electromagnetic modeling results based on the application of PO techniques is presented. First, we briefly describe the implementation used and, then, present the obtained results.

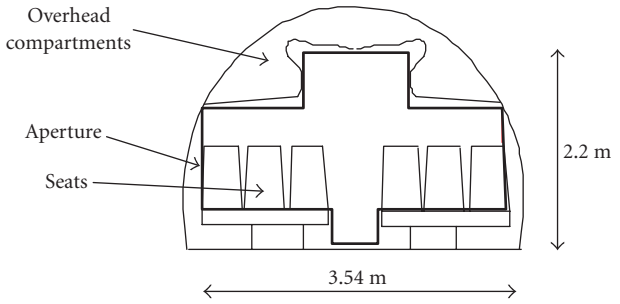

Figure 11: Cross-section of the cabin.

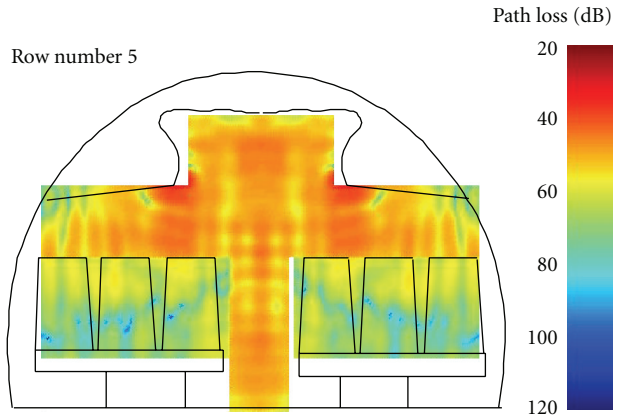

Figure 12: Example of PO results (path loss in dB) for row 5.

Table 4: Measured attenuation introduced by the haul of the aircraft.

Frequency [GHz]	Row	$\overline{d}_{\text{Tx-Rx}}$[m]	$\overline{P}_i$[dBm]	$\overline{PL}_i^{\text{meas}}$[dB]	$\overline{FSL}_i$[dB]	$\overline{EL}_i$[dB]
1.8	5	5.93	−13.25	63.91	53.0	10.9
	10	5.92	−18.14	68.80	53.0	15.8
	12	5.95	−18.29	69.32	53.0	16.0
	15	5.93	−17.87	68.53	53.0	15.5
	20	5.94	−12.91	63.57	53.0	10.6
2.1	5	5.93	−23.61	66.91	54.3	12.6
	10	5.92	−28.86	72.16	54.3	17.8
	12	5.95	−28.24	71.54	54.3	17.2
	15	5.93	−28.42	71.72	54.3	17.4
	20	5.94	−23.67	66.97	54.3	12.6
2.45	5	5.93	−29.84	69.29	55.5	13.8
	10	5.92	−34.26	73.71	55.5	18.2
	12	5.95	−34.77	74.22	55.5	18.7
	15	5.93	−34.53	73.98	55.5	18.5
	20	5.94	−29.93	69.38	55.5	13.9

PO uses the concept of (equivalent) surface currents over the surface of an object or an aperture. The currents result from the overall tangential part of the incident electric and magnetic field intensity vectors. The resulting reradiated field is obtained by integrating the surface current densities over the scattering object surface [20] or, alternatively, aperture. Here, only the basic PO formulas will be presented, more details on the numerical implementation of the method can be found in [21]. It must be borne in mind that the propagation along the aircraft cabin can be calculated by considering the radiation of successive apertures. In addition, wall scattering effects can also be taken into account using PO.

The principle for the calculation of the received field strength originating at an aperture is outlined in Figure 9. The figure can be interpreted as a point source (antenna) followed by a concatenation of two apertures, each corresponding to planes where the field strength is calculated. These apertures can be taken to be along the cabin length and have the same shape as its cross-section. The apertures have to be tightly sampled in a regular mesh with a sub-lambda step. Here, for the tests carried out at 2.1 GHz ($\lambda = 0.1429$), the step size was 2 cm (14 samples per wave length).

First, the surface of all apertures has to be discretized, then the tangential components, $\mathbf{E}_t$ and $\mathbf{H}_t$, of the incident electric and magnetic fields, $\mathbf{E}_i$ and $\mathbf{H}_i$, are calculated at all points of the first aperture as

$$\begin{aligned} \mathbf{E}_t &= \hat{\mathbf{n}} \times [(\mathbf{E}_i + R\mathbf{E}_i) \times \hat{\mathbf{n}}], \\ \mathbf{H}_t &= \hat{\mathbf{n}} \times [(\mathbf{H}_i + R\mathbf{H}_i) \times \hat{\mathbf{n}}], \end{aligned} \tag{6}$$

where R is the reflection coefficient which is dependent on the incidence angle and the electrical parameters of the object (R is zero in the case of an aperture), and the vector cross-product with the normal to the surface, $\mathbf{n}$, represents the calculation of the tangential component.

The electric and magnetic current densities, $\mathbf{J}$ and $\mathbf{M}$, are calculated as

$$\mathbf{J} = \hat{\mathbf{n}} \times \mathbf{H}_t, \qquad \mathbf{M} = -\hat{\mathbf{n}} \times \mathbf{E}_t. \tag{7}$$

The reradiated fields, $\mathbf{E}_r$ and $\mathbf{H}_r$, at each point of the following aperture are calculated as

$$\begin{aligned} \mathbf{E}_r &= \frac{1}{4\pi} \iint_S (\hat{\mathbf{r}} \times \mathbf{M}) \frac{1 + jk_0|\mathbf{r}|}{|\mathbf{r}|} e^{-jk_0|\mathbf{r}|} dS, \\ \mathbf{H}_r &= -\frac{1}{4\pi} \iint_S (\hat{\mathbf{r}} \times \mathbf{J}) \frac{1 + jk_0|\mathbf{r}|}{|\mathbf{r}|} e^{-jk_0|\mathbf{r}|} dS, \end{aligned} \tag{8}$$

where $\mathbf{r}$ is the vector from each elementary area, dS, at the previous aperture to the point at the following aperture and k_0 is the wave number. The total electric and magnetic field, $\mathbf{E}$ and $\mathbf{H}$, at a given calculation point of the aperture is obtained as

$$\mathbf{E} = \mathbf{E}_r + Z_0 \cdot (\mathbf{H}_r \times \hat{\mathbf{r}}), \qquad \mathbf{H} = \mathbf{H}_r + \frac{1}{Z_0} \cdot (\hat{\mathbf{r}} \times \mathbf{E}_r). \tag{9}$$

4.2. In-Cabin Propagation. The in-cabin propagation scenario has a complex geometry, including multiple diffractions by, and multiple transmissions though, the seat backrests, and multiple reflections off the walls. Therefore, to physically model the wave propagation phenomenon within the cabin, a simplified numerical approach was attempted.

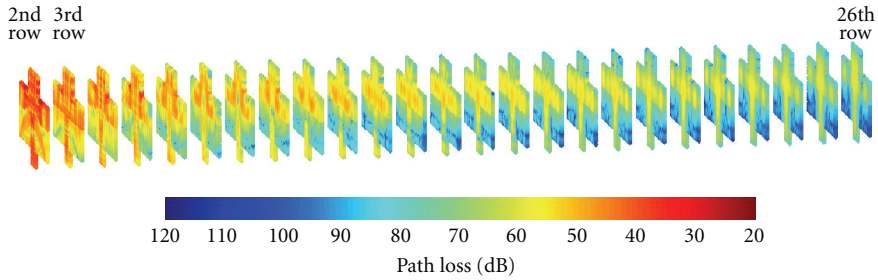

Figure 13: Example of PO results (path loss in dB) for all rows.

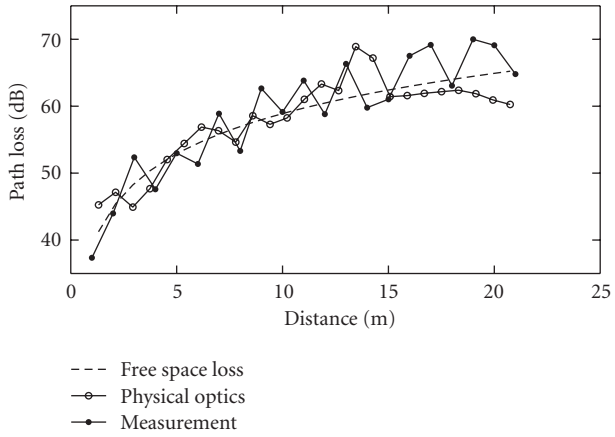

Figure 14: Comparison of simulated and measured values, aisle.

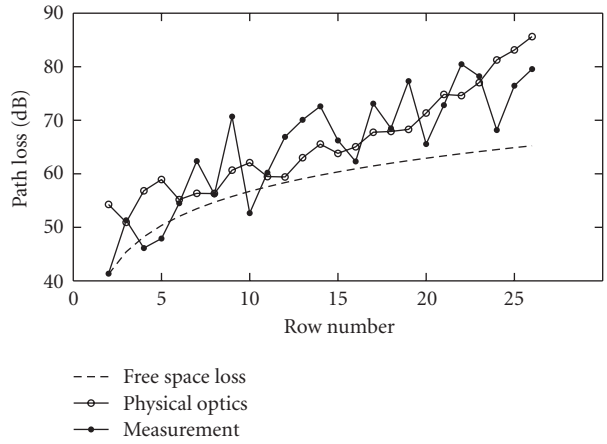

Figure 16: Comparison of simulated and measured values, B seat.

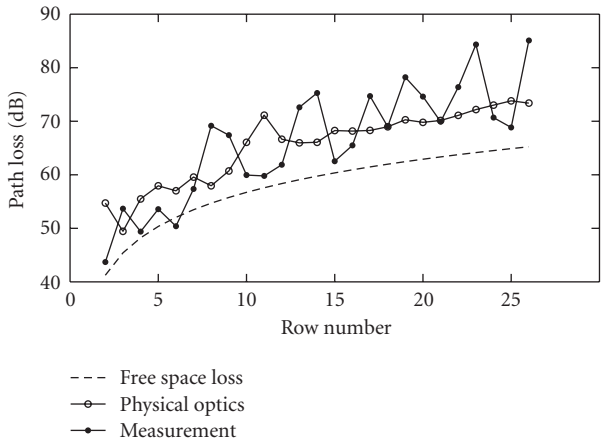

Figure 15: Comparison of simulated and measured values, A seat.

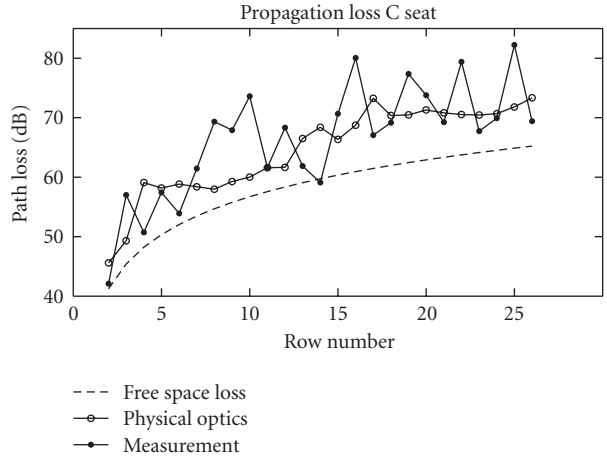

Figure 17: Comparison of simulated and measured values, C seat.

Due to the nature of the in-cabin problem, which can be decomposed into multiple screens, PO was chosen as the most suitable approach.

The field was calculated over subsequent apertures formed by the space of the cabin above the seats, by seat backrests and by the walls, the ceiling and the floor of the cabin. The field over the aperture in each row of seats is reradiated onward to obtain the field over the next aperture. This procedure is repeated for all rows. Figure 10 illustrates this approach in a schematic form. Figure 11 shows the actual cross-section of the cabin. Figures 12 and 13 show examples of obtained path loss maps. In Figure 12 the assumed simplified shape of the cabin cross-section is shown where perpendicular surfaces are considered in lieu of the actual curved ones.

The field over each subsequent aperture is calculated as a sum of the field reradiated directly from previous aperture and the contributions coming from reflections off

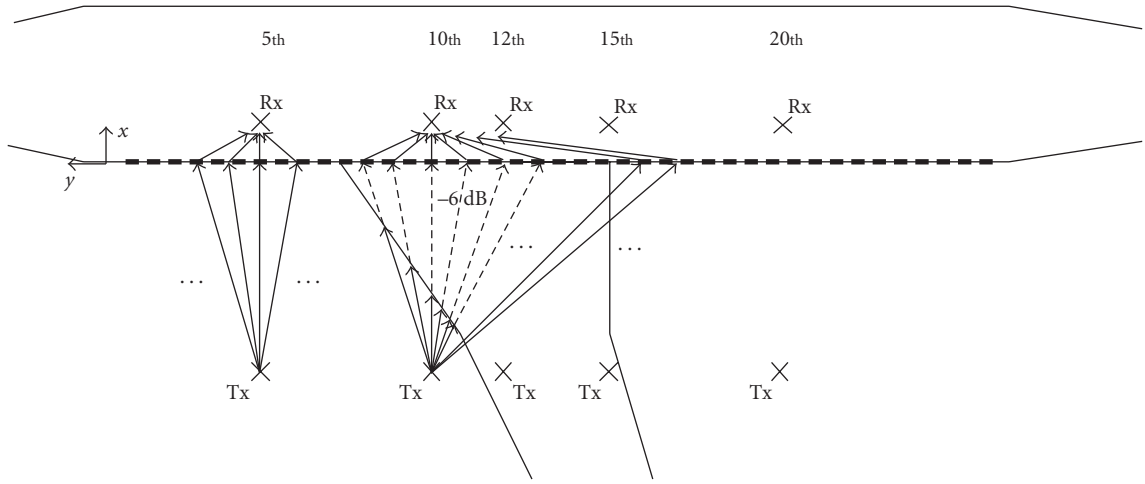

Figure 18: Received power level calculation

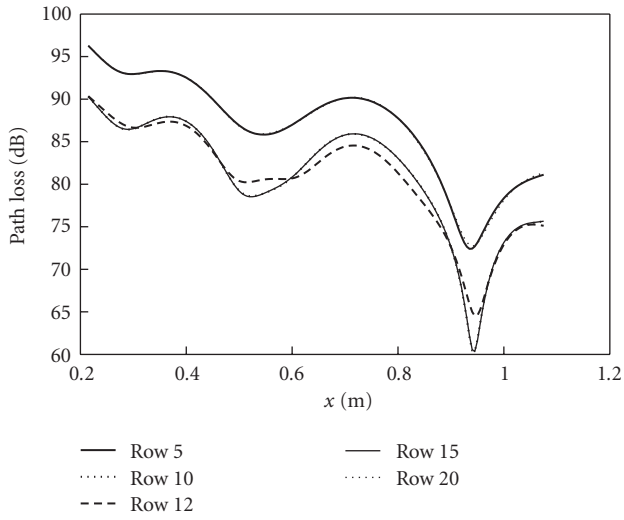

Figure 19: Propagation loss inside the cabin as a function of distance from the window.

the walls, ceiling and the floor. In all cases PO techniques were assumed.

For verifying the accuracy of the model, a vertically polarized transmitter was set in the centre of the modelled cabin at a height of 1.8 m and the frequency was 2.1 GHz. The relative permittivity and conductivity for calculating the wall reflection coefficient was $\varepsilon_r = 4$ and $\sigma = 0.03$ S/m, respectively. An additional attenuation term was added to the part of the apertures corresponding to the backrests, to account for the transmission loss. The calculation of this loss was performed assuming a 10 cm thick dielectric slab of conductivity $\sigma = 0.1$ S/m.

Figure 14 shows a comparison between the simulated and measured path loss values as the receiver is moved along the aisle at the height of 1.7 m. Figures 15, 16, and 17 show the simulated path loss at positions of the receiver 1.15 m above the floor for each seat as a function of the seat row number. The simulation results at each position have been calculated using a similar averaging process about the nominal prediction point as for the measurements. Because of the symmetry, only one side of the cabin with seats A, B, and C is shown. Note in Figure 12 the strong spatial variability of the predicted field strength. The discrepancies between measurements and predictions may be due to additional scattering effects not considered in the EM simulations. However, the simulations differ from the measurements by no more than 10 dB.

Although the simulation procedure is quite complex, several simplifications have been made. The apertures are made up of sections of rectangular shape which do not quite correspond to real cabin cross-sections. No scattering from the back and front of the cabin has been considered.

Further improvements towards a more realistic simulation of the propagation channel would mean to include additional attenuation terms due to passenger bodies, which could be modeled as lossy dielectric cuboids.

4.3. Outdoor-to-Indoor Propagation: Entry Loss. Also the outdoor-to-indoor case has been simulated. For a given point inside the cabin, the resulting received signal strength was calculated as a sum of the contributions from all 26 windows on the external transmitter side of the aircraft. The windows were treated as reradiation apertures using the same approach as above. The real propagation scenario shown in Figures 4 and 5 is translated into that shown in Figure 18 where the simulation approach followed is depicted.

In the case of the rows 10, 12, and 15, the contribution from each of the windows above the wing was reduced by 6 dB to account for the diffraction losses due to the shadowing by the wing. This diffraction loss introduced corresponds to that for grazing incidence on a knife-edge. From the measurements (Section 3.3) on average, the excess attenuation observed at those seats for which the transmitter was below the wing was approximately 4.8 dB larger.

Figure 19 shows the evolution of the propagation loss at 2.1 GHz as a function of the distance from the window inside the cabin for the 5th, 10th, 12th, 15th , and 20th rows.

The measured propagation losses in Table 4 are within the range of the simulated values, although the simulations show higher propagation loss as the distance from the window increases.

5. Conclusion

This paper presented propagation measurements and channel characterization conducted inside a Boeing 737–400. The objective was to understand the propagation mechanisms involved in the setting up of in-cabin wireless networks. The measurements were conducted in the aisle as well as at the seats at three different frequency bands (1.8, 2.1, and 2.45 GHz) representative of various different services. It has been shown how the path loss is distance dependent with additional random variations due to shadowing and multipath. Furthermore, it has been shown how the propagation exponent for aisle paths barely exceeds a value of two, close to the free-space law. This means that the expected waveguide effect which would lead to exponents below two is attenuated due to the seat rests and to the materials used that prevent the generation of strong multipath. For the seat paths, the attenuation law may be larger than three, in some cases. The spatial variations have been split into slow and fast. The slow variations can be characterized by their standard deviations, which are in the order of 3 dB for aisle paths while, for seat paths are larger, in the order of 5 dB. The faster variations have been quantified and characterized by means of Rice distributions. For interference paths between in-cabin and external networks, the excess loss with respect to free-space has been quantified, being in the order of approximately 10 to 14 dB, increasing with frequency.

The disadvantage of empirically derived models is that they are not suitable for aircraft very different from those where the measurements have been performed. The need for a generalization of results has led us to study a physical, site-specific approach. A model based on Physical (PO) techniques has been presented. Comparisons between measurement and predictions have shown a fairly good agreement. The slow received signal variations in the measurements seem to be slightly larger than in the predictions. Thin can be attributed to propagation mechanisms not considered in the modeling. Still, EM, site-specific models can provide a flexible way of producing acceptably accurate perditions for all possible aircraft configurations without the need to perform new measurements.

Acknowledgments

The authors would like to thank the Olympic Airlines Technical Base in Athens International Airport Eleftherios Venizelos. This research has been partly carried out in the framework of the European Network of Excellence SatNEx 2.

References

[1] A. Jahn, M. Holzbock, J. Müller, et al., "Evolution of aeronautical communications for personal and multimedia services," *IEEE Communications Magazine*, vol. 41, no. 7, pp. 36–43, 2003.

[2] N. R. Díaz and J. E. J. Esquitino, "Wideband channel characterization for wireless communications inside a short haul aircraft," in *Proceedings of the IEEE Vehicular Technology Conference (VTC '04)*, vol. 1, pp. 223–228, Milan, Italy, May 2004.

[3] N. R. Díaz, "Narrowband measurements in an airbus A319 for in-cabin wireless personal communications via satellite," in *Proceedings of the Advanced Satellite Mobile Systems (ASMS '03)*, pp. 226–233, Frascati, Italy, July 2003.

[4] G. Hankins, L. Vahala, and J. H. Beggs, "Propagation prediction inside a B767 in the 2.4 GHz and 5 GHz radio bands," in *Proceedings of the IEEE International Symposium on Antennas and Propagation Society*, vol. 1A, pp. 791–794, Chicago, Ill, USA, July 2005.

[5] G. Hankins, L. Vahala, and J. H. Beggs, "Electromagnetic propagation prediction inside aircraft cabins," in *Proceedings of the IEEE International Symposium on Antennas and Propagation Society*, vol. 3, pp. 2227–2230, Monterey, Calif, USA, June 2004.

[6] N. R. Díaz, B. S. Pérez, and F. P. Fontán, "Deterministic propagation modelling inside aircraft cabins," in *Proceedings of the 5th International Conference on ITS Telecommunications (ITST '05)*, Brest, France, June 2005.

[7] C. P. Niebla, "Topology and capacity planning for wireless heterogenous networks in aircraft cabins," in *Proceedings of the 16th IEEE International Symposium on Personal, Indoor and Mobile Radio Communications (PIMRC '05)*, pp. 2088–2092, Berlin, Germany, September 2005.

[8] C. P. Niebla, "Coverage and capacity planning for aircraft in-cabin wireless heterogeneous networks," in *Proceedings of the 58th IEEE Vehicular Technology Conference (VTC '03)*, pp. 1658–1662, Orlando, Fla, USA, October 2003.

[9] A. Kaouris, M. Zaras, M. Revithi, N. Moraitis, and P. Constantinou, "Propagation measurements inside a B737 aircraft for in-cabin wireless networks," in *Proceedings of the IEEE Vehicular Technology Conference (VTC '08)*, pp. 2932–2936, Singapore, May 2008.

[10] J. Chuang, N. Xin, H. Huang, S. Chiu, and D. G. Michelson, "UWB radiowave propagation within the passenger cabin of a Boeing 737-200 aircraft," in *Proceedings of the IEEE Vehicular Technology Conference (VTC '07)*, pp. 496–500, Dublin, Ireland, April 2007.

[11] I. Schmidt, J. Jemai, R. Piesiewicz, et al., "UWB propagation channels within an aircraft and an office building environment," in *Proceedings of the IEEE International Symposium on Antennas and Propagation and USNC/URSI National Radio Science Meeting (APSURSI '08)*, pp. 1–4, San Diego, Calif, USA, July 2008.

[12] RTCA/DO233, "Portable Electronic Devices Carried on Board Aircraft," August 1996.

[13] J. L. Schiffer and A. E. Waltho, "Intel Safety Evaluation of Bluetooth Class ISM Band Transmitters on Board Commercial Aircraft," Revision 2, December 2000.

[14] JAA TGL Leaflet No. 29, "Guidance concerning the use of portable electronic devices on board aircraft," October 2001.

[15] The Boeing, 2007, http://www.boeing.com.

[16] R. A. Valenzuela, O. Landron, and D. L. Jacobs, "Estimating local mean signal strength of indoor multipath propagation," *IEEE Transactions on Vehicular Technology*, vol. 46, no. 1, pp. 203–212, 1997.

[17] T. S. Rappaport, *Wireless Communications: Principles and Practice*, Prentice-Hall, Englewood Cliffs, NJ, USA, 1996.

[18] L. Dossi, G. Tartara, and F. Tallone, "Statistical analysis of measured impulse response functions of 2.0 GHz indoor radio channels," *IEEE Journal on Selected Areas in Communications*, vol. 14, no. 3, pp. 405–410, 1996.

[19] W. C. Y. Lee, *Mobile Communications Design Fundamentals*, Wiley Series in Telecommunications and Signal Processing, John Wiley & Sons, Chichester, UK, 1993.

[20] C. A. Balanis, *Advanced Engineering Electromagnetics*, John Wiley & Sons, New York, NY, USA, 1989.

[21] L. Diaz and T. Milligan, *Antenna Engineering Using Physical Optics: Practical CAD Techniques and Software*, Artech House, Boston, Mass, USA, 1996.

Hindawi Publishing Corporation
EURASIP Journal on Wireless Communications and Networking
Volume 2009, Article ID 306876, 11 pages
doi:10.1155/2009/306876

Research Article

Dynamic Model of Signal Fading due to Swaying Vegetation

Michael Cheffena[1] and Torbjörn Ekman[2]

[1] *University Graduate Center (UNIK), P.O. Box 70, 2027 Kjeller, Norway*
[2] *Department of Electronics and Telecommunications, Norwegian University of Science and Technology, 7491 Trondheim, Norway*

Correspondence should be addressed to Michael Cheffena, cheffena@yahoo.com

Received 31 July 2008; Revised 1 December 2008; Accepted 18 February 2009

Recommended by Michael A. Jensen

In this contribution, we use fading measurements at 2.45, 5.25, 29, and 60 GHz, and wind speed data, to study the dynamic effects of vegetation on propagating radiowaves. A new simulation model for generating signal fading due to a swaying tree has been developed by utilizing a multiple mass-spring system to represent a tree and a turbulent wind model. The model is validated in terms of the cumulative distribution function (CDF), autocorrelation function (ACF), level crossing rate (LCR), and average fade duration (AFD) using measurements. The agreements found between the measured and simulated first- and second-order statistics of the received signals through vegetation are satisfactory. In addition, Ricean K-factors for different wind speeds are estimated from measurements. Generally, the new model has similar dynamical and statistical characteristics as those observed in measurements and can thus be used for synthesizing signal fading due to a swaying tree. The synthesized fading can be used for simulating different capacity enhancing techniques such as adaptive coding and modulation and other fade mitigation techniques.

1. Introduction

In a given environment, radiowaves are subjected to different propagation degradations. Among them, vegetation movement due to wind can both attenuate and cause a fading effect to the propagating signal. Operators cannot guarantee a clear line-of-sight (LOS) to wireless customers as vegetation in the surrounding area may grow or expand over the years and obstruct the path. Fade mitigation techniques (FMTs) such as adaptive coding and modulation can be used to counteract the signal fading caused by swaying vegetation. For example, during windy conditions (high signal fading), power efficient modulation schemes such as BPSK and QPSK (which are less sensitive to propagation impairments compared to high-order modulation schemes) can be used to increase the link availability, while spectral efficient modulation schemes such as 16 QAM and 64 QAM can be applied during calm wind conditions (less signal fading) [1]. An extra coding information can also be added to the channel so that errors can be detected and corrected by the receiver. FMTs need to track the channel variations and adjust their parameters (modulation order, coding rate, etc.) to the current channel conditions. In order to design, optimize, and test FMT, data collected from propagation measurements are needed. However, such data may not be available at the preferred frequency, wind speed conditions, and so forth. Alternatively, time series generated from simulation models can be used. In this case, the simulated time series need to have similar dynamical and statistical characteristics as those obtained from measurements [1].

The signal attenuation depends on a range of factors such as tree type, whether trees are in leaf or without leaf, whether trees are dry or wet, frequency, and path length through foliage [2, 3]. For frequencies above 20 GHz, leaves and needles have large dimensions compared to the wavelength, and can significantly affect the propagation conditions. The ITU-R P.833 [4] provides a model for predicting the mean signal attenuation though vegetation. The temporal variations of the relative phase of multipath components due to movement of the tree result in fading of the received signal as reported in, for example, [5–10]. The severity of the fading depends on the rate of phase changes which further depends on the movement of the tree components. Therefore, for accurate prediction of the channel characteristics, the motion of trees under the influence of wind should be taken into account. This requires the knowledge of wind dynamics and

the complex response of a tree to induced wind force. In our previous work, a heuristic approach was used to model the dynamic effects of vegetation [10]. In this paper, we develop a theoretical model based on the motion of trees under the influence of wind, and is validated in terms of first- and second-order statistics using available measurements.

The paper begins in Section 2 by giving a brief description of the measurement setup for measuring signal fading after propagating through vegetation and for measuring meteorological data (wind speed and precipitation). Section 3 discusses the wind speed dynamics. The motion of trees and their dynamic effects on propagating radiowaves as well as the validation of the proposed simulation model are dealt with in Section 4. Finally, conclusions are presented in Section 5.

2. Measurement Setup

To characterize the influence of vegetation on radiowaves, measurements were performed in [7] for a broad range of frequencies, including 2.45, 5.25, 29, and 60 GHz, in various foliage and weather conditions. A sampling rate of 500 Hz was used to collect the radio frequency (RF) signals using a spectrum analyzer, multimeter, and a computer with General Purpose Interface Bus (GPIB) interface. In order to understand the behavior of radiowaves propagating through vegetation under different weather conditions, meteorological measurements including wind speed and precipitation were also performed in [7]. The wind speed was recorded every 5 seconds, and the precipitation data every 10 seconds.

The measurements were taken at two different locations, referred to as Site 1 and Site 2. The trees at Site 1 were deciduous trees, and were considered both when the trees were in full leaf and when they were without leaf. Site 2 was populated by several coniferous trees which made a wall of trees. Table 1 gives a general site information. A detailed description of the measurements can be found in [7]. An example of received signal at 29 GHz after propagating through dry leaved deciduous trees (Site 1) is shown in Figure 1, and the corresponding measured wind speed is shown in Figure 2. These figures indicate a strong dependency of the signal variation transmitted through vegetation on the wind speed. For a closer look, Figures 3 and 4 show examples of typical measured signals during low (1 to 3 m/s) and high (≥4.5 m/s) wind speed conditions for leaved dry deciduous trees (Site 1) at 29 GHz. As expected, we can observe that the signal variation increases with increasing wind speed. Accurate modeling of the channel is needed when designing mitigation techniques for the fast and deep signal variations are like the ones shown in Figures 1 and 4. In order to do this, a good knowledge of wind dynamics and trees motions due to wind is required.

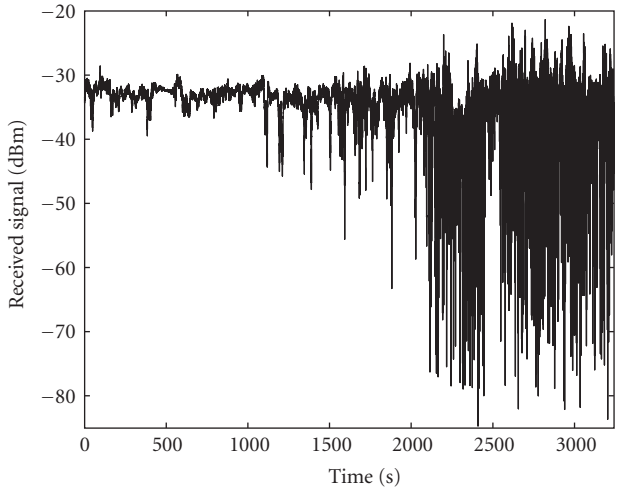

Figure 1: Measured signal fading after propagating through dry leaved deciduous trees (Site 1) at 29 GHz. A sampling rate of 500 Hz was used to collect the signal.

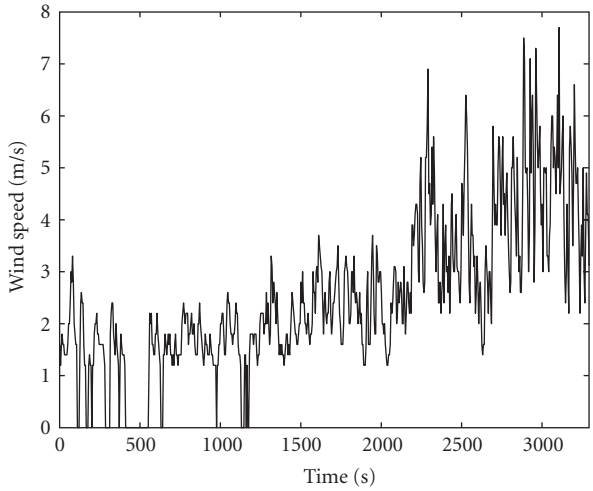

Figure 2: Measured wind speed for the corresponding signal fading shown in Figure 1. The wind speed was measured every 5 seconds.

3. Wind Dynamics

Trees sway mostly due to wind. Understanding the dynamic characteristics of wind is therefore essential when describing the complex response of a tree to induced wind force and their dynamic effects on propagating radiowaves. The turbulent wind speed power spectrum can be represented by a Von Karman power spectrum [11], and it can be simulated by passing white noise through a shaping filter with transfer function given by [12, 13]

$$H_F(s) = \frac{K_F}{(1 + sT_F)^{5/6}}, \tag{1}$$

where K_F and T_F are the gain and time constant of the shaping filter, respectively. A close approximation of the 5/6-order filter in (1) by a rational transfer function is given by [12]

$$H_F(s) = K_F \frac{(g_1 T_F s + 1)}{(T_F s + 1)(g_2 T_F s + 1)}, \tag{2}$$

Table 1: Site description [7].

Site	Path length	Foliage depth	Description
Site 1	63.9 m	14.3 m	3 foliated maple trees
		7.6 m	1 foliated flowering crab tree
Site 2	110 m	25 m	Several spruce and one pine tree creating a wall

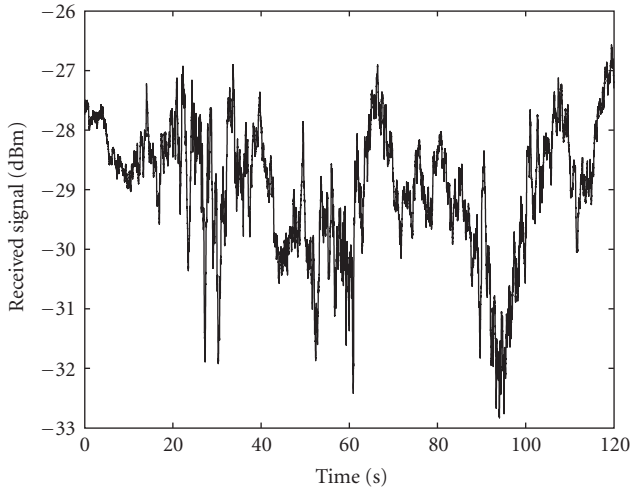

Figure 3: Typical measured signal at 29 GHz for leaved dry deciduous trees (Site 1) during low-wind speed conditions (1 to 3 m/s). A sampling rate of 500 Hz was used to collect the signal.

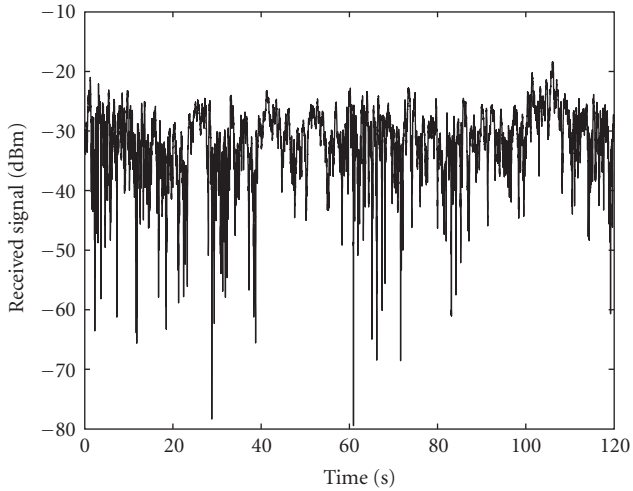

Figure 4: Typical measured signal at 29 GHz for leaved dry deciduous trees (Site 1) during high-wind speed conditions (≥4.5 m/s). A sampling rate of 500 Hz was used to collect the signal.

where $g_1 = 0.4$ and $g_2 = 0.25$. T_f and K_F are defined as

$$T_F = \frac{L_r}{w_m}, \tag{3}$$

$$K_F \approx \sqrt{\frac{2\pi}{B(1/2, 1/3)} \frac{T_F}{T_s}}, \tag{4}$$

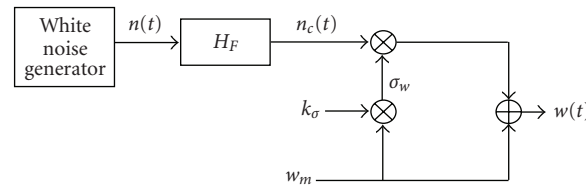

Figure 5: Model for simulating wind speed. $n(t)$ is a white Gaussian noise with zero mean and unite variance, H_F is the low-pass filter defined in (2), $n_c(t)$ is a colored noise, k_σ is a model parameter (see Table 2), w_m is the mean wind speed, $\sigma_w = w_m k_\sigma$, and $w(t)$ is the resulting wind speed.

Table 2: k_σ values for different terrain types at 10 meter height [14].

Type	Coastal	Lakes	Open	Built-up areas	City centers
k_σ	0.123	0.145	0.189	0.285	0.434

where w_m is the mean wind speed and L_r is the turbulence length scale that corresponds to the site roughness. The turbulence length can be calculated from the height, h, above the ground, expressed as $L_r = 6.5h$ [14]. T_s is the sampling period and B designates the beta function, and is given by

$$B(u, y) = \int_0^1 z^{u-1}(1-z)^{y-1} dz. \tag{5}$$

Figure 5 shows the model for simulating wind speed. In the model, a white Gaussian noise $n(t)$ (where t is the time) with zero mean and unite variance is transformed into colored noise $n_c(t)$ by smoothing it with the filter given in (2). The static gain K_F defined in (4) ensures that the resulting colored noise $n_c(t)$ has a unit variance. The wind speed $w(t)$ is then obtained by multiplying $n_c(t)$ by the standard deviation of the turbulent wind σ_w and adding the mean wind speed w_m. k_σ is a constant which depends on the type of the terrain [14]; see Table 2. This wind model is used in Section 4.1 to describe the displacement of tree due to induced wind force.

4. The Dynamic Effects of Vegetation on Radiowaves

4.1. The Motion of Trees. A tree is a complex structure consisting of a trunk, branches, subbranches, and leaves. The tree responds in a complex way to induced wind forces, with each branch swaying and dynamically interacting with other branches and the trunk. During windy conditions, first-order branches sway over the swaying trunk, and second-order branches sway over the swaying first-order branches. Generally, smaller branches sway over swaying

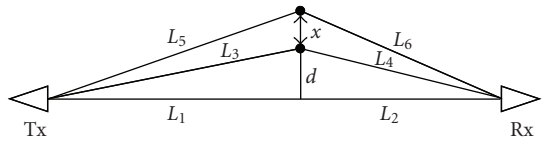

Figure 6: Path length difference. L_1+L_2 is the path length of the LOS component, $L_3 + L_4$ is the path length of the multipath component at rest, $L_5 + L_6$ is the path length of the multipath component when displaced, x is the displacement, d is the distance from the LOS path to the position of a tree component. Tx and Rx are the transmitting and receiving antennas.

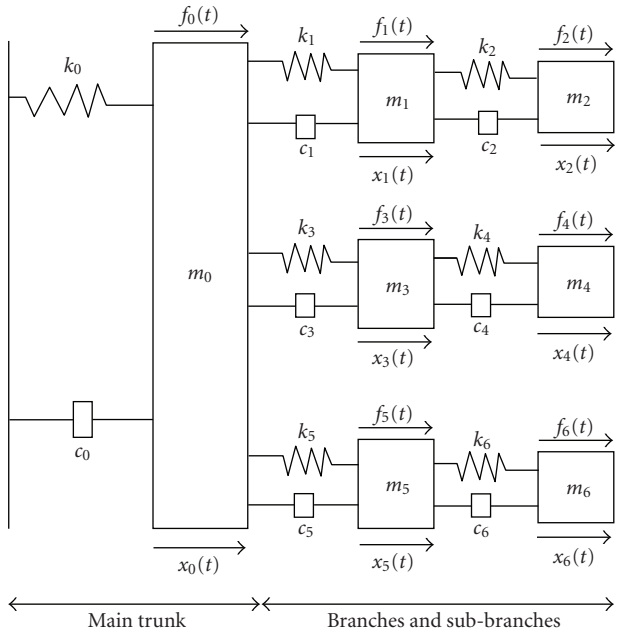

Figure 7: Dynamic representation of a tree. m_i, k_i, c_i, $f_i(t)$, and $x_i(t)$ are the mass, spring constant, damping factor, time varying wind force, and time varying displacement of tree component i, respectively.

larger branches, and leaves vibrate over swaying smaller branches. The overall effect minimizes the dynamic sway of the tree by creating a broad range of frequencies and prevents the tree from failure [15]. Radiowaves scattered from these swaying tree components have a time varying phase changes due to periodic changes of the path length which results in fading of the received signal. Figure 6 illustrates the path length difference due to displacement of a tree component from rest, and is given by (see Appendix A)

$$\Delta L \approx x\frac{d(L_1 + L_2)}{L_1 L_2}, \tag{6}$$

where $L_1 + L_2$ is the path length of the LOS component. L_1 is the distance from the transmitter to a point parallel to a position of a tree component, d is the distance from the point to the position of a tree component, L_2 is the distance from the point parallel to a position of a tree component to the receiver, and x is the displacement.

A dynamic structure model of tree was reported in [15], and is extended here to include dynamic wind force and mathematical description of the motion of each tree component; see Figure 7. In the model, tree components (the trunk, branches, and subbranches) are attached with each other using springs which resulted in a multiple mass-spring system. This tree model is further used in Section 4.2 to model the signal fading due to swaying vegetation. For simplicity, we use a tree model with a trunk and just three branches and three subbranches, as seen in Figure 7. This simple model is sufficient to recreate the rich dynamic behavior of the fading from a real tree, as is demonstrated in the simulations in Section 4.2. Using Newton's second law and the Hooke's law, the equations of motion (displacement) for the tree components in Figure 7 can be formulated using second-order differential equations:

$$\begin{aligned}
m_0\ddot{x}_0(t) &= -\dot{x}_0(t)(c_0 + c_1 + c_3 + c_5) + \dot{x}_1(t)c_1 + \dot{x}_3(t)c_3 \\
&\quad + \dot{x}_5(t)c_5 - x_0(t)(k_0 + k_1 + k_3 + k_5) + x_1(t)k_1 \\
&\quad + x_3(t)k_3 + x_5(t)k_5 + f_0(t), \\
m_1\ddot{x}_1(t) &= -\dot{x}_1(t)(c_1 + c_2) + \dot{x}_2(t)c_2 + \dot{x}_0(t)c_1 \\
&\quad - x_1(t)(k_1 + k_2) + x_2(t)k_2 + x_0(t)k_1 + f_1(t), \\
m_2\ddot{x}_2(t) &= c_2(\dot{x}_1(t) - \dot{x}_2(t)) + k_2(x_1(t) - x_2(t)) + f_2(t), \\
m_3\ddot{x}_3(t) &= -\dot{x}_3(t)(c_3 + c_4) + \dot{x}_4(t)c_4 + \dot{x}_0(t)c_3 \\
&\quad - x_3(t)(k_3 + k_4) + x_4(t)k_4 + x_0(t)k_3 + f_3(t), \\
m_4\ddot{x}_4(t) &= c_4(\dot{x}_3(t) - \dot{x}_4(t)) + k_4(x_3(t) - x_4(t)) + f_4(t), \\
m_5\ddot{x}_5(t) &= -\dot{x}_5(t)(c_5 + c_6) + \dot{x}_6(t)c_6 + \dot{x}_0(t)c_5 \\
&\quad - x_5(t)(k_5 + k_6) + x_6(t)k_6 + x_0(t)k_5 + f_5(t), \\
m_6\ddot{x}_6(t) &= c_6(\dot{x}_5(t) - \dot{x}_6(t)) + k_6(x_5(t) - x_6(t)) + f_6(t),
\end{aligned} \tag{7}$$

where m_i, k_i, and c_i are the mass, spring constant, and damping factor of tree component i, respectively. The spring constant k_i describes the stiffness of the wood material. While the damping factor c_i describes the energy dissipation due to swaying tree component (aerodynamic damping) and dissipation from internal factors such as root/soil movement and internal wood energy dissipation [15]. $\ddot{x}_i(t)$, $\dot{x}_i(t)$, and $x_i(t)$ are the acceleration, velocity, and position (displacement) of tree component i, respectively. $f_i(t)$ is the time varying induced wind force on tree component i, and is given by [16]

$$f_i(t) = \frac{C_d \rho w_i(t)^2 A_i}{2}, \tag{8}$$

where C_d is the drag coefficient, ρ is the air density, A_i is the projected surface area of the tree component, and $w_i(t)$ is the wind speed (can be simulated using the model shown in Figure 5).

The time varying displacement, $x_i(t)$, of each tree component can then be obtained by solving (7) using state-space modeling:

$$\dot{\mathbf{y}} = \mathbf{A}\mathbf{y} + \mathbf{B}\mathbf{u}, \tag{9}$$

$$\mathbf{x} = \mathbf{C}\mathbf{y} + \mathbf{D}\mathbf{u}, \tag{10}$$

where $\mathbf{y} = \left[x_0(t) \ \cdots \ x_6(t) \ \dot{x}_0(t) \ \cdots \ \dot{x}_6(t)\right]^T$ is the state vector, $\mathbf{u} = \left[f_0(t) \ \cdots \ f_6(t)\right]^T$ is the input vector, and $\mathbf{x} = \left[x_0(t) \ \cdots \ x_6(t)\right]^T$ is the output vector. The matrices **A**, **B**, **C**, and **D** are obtained from (7); see Appendix B. Note that (9) and (10) are for continuous time and can be converted to discrete time using, for example, bilinear transformation.

4.2. Signal Fading due to Swaying Tree. Former studies on the measurements used here suggested that the signal envelope can be represented using the extreme value or lognormal distribution [7]. However, our study shows that the Nakagami-Rice distribution can well represent the measured signal envelop through vegetation. The Chi-Square test has been performed to verify the fitness of Nakagami-Rice and measured signal distribution. For all frequencies, the hypothesis was accepted for 5% significance level. Furthermore, the majority of reported measurement results suggest Nakagami-Rice envelop distribution [8, 17–19]. Therefore, Nakagami-Rice envelop distribution is assumed in the developed simulation model, with the K-factor given by

$$K = \frac{P_d}{P_f}, \tag{11}$$

where P_d and P_f are the power in the direct and diffuse components, respectively. From our measurements, we estimated the Ricean K-factors under different wind conditions using the moment-method reported in [20]; see Figure 8. The reduction of the K-factor suggests that the contribution of the diffuse component increases with increasing wind speed. We can also observe that the K-factor decreases with increasing frequency (due to smaller wavelength).

The time series for the received power is obtained as $|h(t)^2|$, where $h(t)$ is the complex impulse response due to the multipath in the vegetation. For a Ricean distributed signal envelope, the impulse response $h(t)$ can be expressed as the sum of the direct and diffuse signal components as shown in

$$h(t) = \underbrace{a_d \exp(j\theta)}_{\text{Direct}} + \underbrace{\sum_{i=1}^{N=7} a_f \exp\left[j\left(\theta_i - \frac{2\pi}{\lambda}\Delta L_i(t)\right)\right]}_{\text{diffuse}}, \tag{12}$$

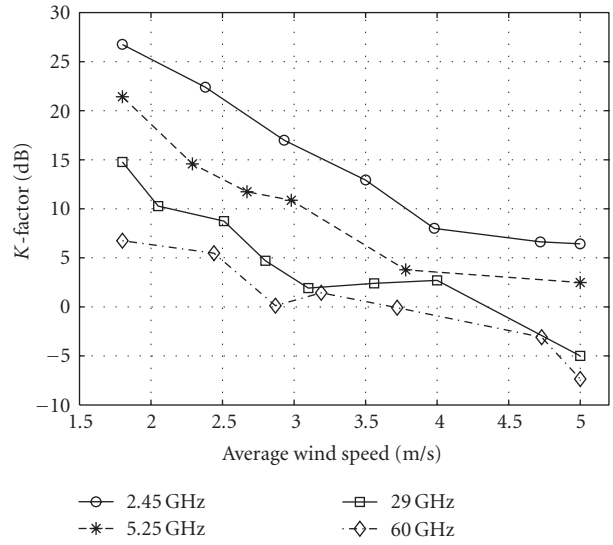

Figure 8: Ricean K-factors as function of average wind speed estimated from measurements at 2.45, 5.25, 29, and 60 GHz after propagating through dry leaved deciduous trees (Site 1).

where the first term in (12) is the contribution of the direct signal component. $a_d = \sqrt{P_d}$ (P_d is as defined in (11)), and θ are the amplitude and phase of the direct signal, respectively. The second term in (12) is the contribution of the diffuse component which is the sum of signals scattered from the tree components. $N = 7$ is the total number of scattering tree components (the trunk, branches, and subbranches; see Figure 7). $a_f = \sqrt{P_f/N}$ is the amplitude of each scattered signal (assumed to be equal for all scattered components), where P_f is as defined in (11), θ_i is the phase uniformly distributed within the range $[0, 2\pi]$, λ is the wavelength, and $\Delta L_i(t)$ is the time varying path length difference due to displacement of the ith tree component shown in Figure 7. Note from (12) that the time varying path length difference, $\Delta L_i(t)$, results in time varying phase changes which in turn gives a fading effect to the received signal. Following the same approach as in (6), $\Delta L_i(t)$ for $i = 1, 2, \ldots, 6$ are given by

$$\begin{aligned}
\Delta L_0(t) &\approx x_0(t)\frac{d_0(L_1+L_2)}{L_1L_2},\\
\Delta L_1(t) &\approx \big(x_0(t)+x_1(t)\big)\frac{d_1(L_1+L_2)}{L_1L_2},\\
\Delta L_2(t) &\approx \big(x_0(t)+x_1(t)+x_2(t)\big)\frac{d_2(L_1+L_2)}{L_1L_2},\\
\Delta L_3(t) &\approx \big(x_0(t)+x_3(t)\big)\frac{d_3(L_1+L_2)}{L_1L_2},\\
\Delta L_4(t) &\approx \big(x_0(t)+x_3(t)+x_4(t)\big)\frac{d_4(L_1+L_2)}{L_1L_2},\\
\Delta L_5(t) &\approx \big(x_0(t)+x_5(t)\big)\frac{d_5(L_1+L_2)}{L_1L_2},\\
\Delta L_6(t) &\approx \big(x_0(t)+x_5(t)+x_6(t)\big)\frac{d_6(L_1+L_2)}{L_1L_2},
\end{aligned} \tag{13}$$

where L_1, L_2, and d_i are as defined in (6), and $x_i(t)$ is obtained from the state-space model in (9) and (10).

Examples of simulated signal fading due to swaying tree using the new model for low- and high-wind speed conditions are shown in Figures 9 and 10, respectively. The simulation parameters are given in Table 3. In general, A_i values in the range 10 to 80 m^2, m_i values in the range 0.01 to 30 kg, k_i values in the range 5×10^2 to 5×10^4 N/m^2, c_i values in the range 0 to 35 can be used in the model. These parameter ranges are obtained by performing simulations using different tree parameters and comparing the simulated first and second-order statistics to these of measurements from Site 1 (since the new model is intended for modeling signal fading due to a single tree). Then, the parameter ranges are defined based on the agreements found between the measured and simulated first- and second-order statistics. Finally, realistic values within the defined parameter ranges are assigned to each tree component; see Table 3 (no curve fitting or numerical optimization is used). For example, as shown above the parameter range found for m_i is between 0.01 to 30 kg, from this a realistic value for m_0 (the trunk) should be close to the upper limit of the parameter rage,that is, somewhere between 15 to 30 kg. In this case, 20 kg is randomly chosen from the realistic value range for m_0; see Table 3. The same selection process based on realistic values within parameter ranges is performed for the other tree parameters. Comparisons of the cumulative distribution functions (CDFs), autocorrelation functions (ACFs), level-crossing rates (LCRs), and average fade durations (AFDs) of the measured and simulated received signals at different frequencies are shown in Figures 11–18. The LCRs and AFDs are normalized to the Root-Mean-Square (RMS) level. The CDF describes the probability distribution of a random variable. While the ACF is a measure of the degree to which two time samples of the same random process are related and is expressed as [21]

$$R_h(t_1, t_2) = E\{h(t_1)h(t_2)\}, \tag{14}$$

where E is the expectation, $h(t_1)$ and $h(t_2)$ are random variables obtained by observing $h(t)$ at time t_1 and t_2, respectively. The LCR measures the rapidity of the signal fading. It determines how often the fading crosses a given threshold in the positive-going direction [22]. The AFD quantifies how long the signal spends below a given threshold, that is, the average time between negative and positive level-crossings [22]. The CDF, ACF, LCR, and AFD determine the first- and second-order statistics of the channel.

The effect of wind speed on the channel statistics can be observed from Figures 11–14 which show comparisons of measured (leaved dry deciduous trees (Site 1) at 29 GHz) and simulated channel statistics during low- and high-wind speed conditions. We can observe from Figure 11 that the probability the received signal is less than a given threshold increases with increasing wind speed. Note also from Figure 12 how fast the ACF decays during high wind speed compared to low wind speed conditions. The increase

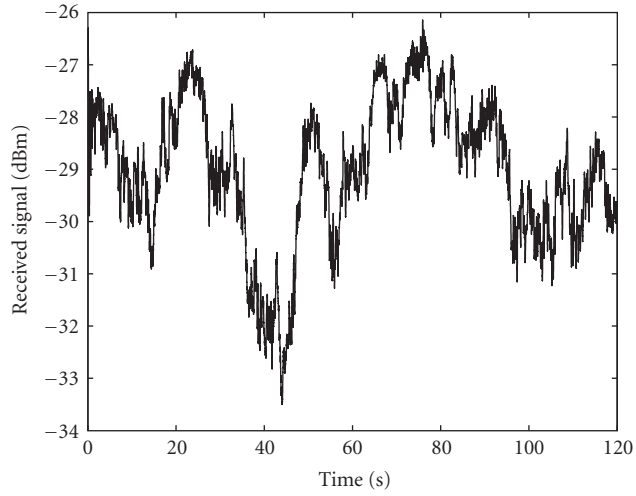

Figure 9: Simulated signal fading using the new model at 29 GHz during low wind speed conditions ($w_m = 2$ m/s). All simulation parameters are given in Table 3.

rate of signal changing activity during windy conditions can be implied from the LCR curves in Figure 13. In addition, the effect of high wind speed which results in deep signal fading with short durations can be observed from the AFD curves shown in Figure 14. The frequency dependency of the channel is evident from Figure 15–18 which show comparisons between measured (leaved dry deciduous trees (Site 1) at 2.45, 5.25, and 60 GHz) and simulated channel statistics during high wind speed conditions ($w_m = 5$ m/s). The probability that the received signal is less than a given threshold increases with increasing frequency; see Figure 15. We can also observe from Figure 16 that the autocorrelation function decays more rapidly for high frequency compared to low-frequency signals. The increasing rate of signal changing activity and the increasing existence of deep signal fading with increasing frequency can be observed from the LCR and AFD curves shown in Figures 17 and 18, respectively. The frequency dependency of the channel statistics is directly related to the signal wavelength. As the frequency increases, the signal wavelength decreases which results in increasing sensitivity to path length differences caused by swaying tree components. In general, the agreements found between the measured and simulated received signals in terms of both first- and second-order statistics are satisfactory; see Figures 11–18. Moreover, the results shown in Figures 11–18 suggest that the swaying of tree components with wind can highly impact the quality and availability of a given link, and should be considered when designing and evaluating systems at different frequencies.

5. Conclusion

In this paper, we use available measurements at 2.45, 5.25, 29, and 60 GHz, and wind speed data to study the dynamic

Table 3: Simulation parameters.

Wind parameters		Other parameters
$w_m = 2$ m/s (low wind)	$C_d = 0.35$ [16]	K-factor for 2.45 GHz = 6 dB (at $w_m = 5$ m/s)
$w_m = 5$ m/s (high wind)	$\rho = 1.226$ kg/m^3 [16]	K-factor for 5.25 GHz = 1 dB (at $w_m = 5$ m/s)
$k_\sigma = 0.434$	$T_s = 0.002$ s	K-factor for 29 GHz = 11 dB (at $w_m = 2$ m/s)
$h = 10$ m		K-factor for 29 GHz = −5 dB (at $w_m = 5$ m/s)
		K-factor for 60 GHz = −6 dB (at $w_m = 5$ m/s)
		$L_1 = 3000$ m and $L_2 = 100$ m

Tree parameters				
$d_0 = 1.0$ m	$A_0 = 66.2$ m^2	$m_0 = 20$ kg	$k_0 = 1.0 \times 10^4$ N/m	$c_0 = 20.0$
$d_1 = 3.0$ m	$A_1 = 21.0$ m^2	$m_1 = 1.0$ kg	$k_1 = 1.0 \times 10^3$ N/m	$c_1 = 15.0$
$d_2 = 3.7$ m	$A_2 = 7.80$ m^2	$m_2 = 0.02$ kg	$k_2 = 7.0 \times 10^3$ N/m	$c_2 = 2.00$
$d_3 = 2.5$ m	$A_3 = 22.9$ m^2	$m_3 = 2.0$ kg	$k_3 = 6.0 \times 10^2$ N/m	$c_3 = 14.0$
$d_4 = 2.7$ m	$A_4 = 9.70$ m^2	$m_4 = 0.03$ kg	$k_4 = 8.0 \times 10^3$ N/m	$c_4 = 1.80$
$d_5 = 2.8$ m	$A_5 = 23.5$ m^2	$m_5 = 2.5$ kg	$k_5 = 1.1 \times 10^3$ N/m	$c_5 = 14.5$
$d_6 = 3.2$ m	$A_6 = 10.4$ m^2	$m_6 = 0.04$ kg	$k_6 = 5.0 \times 10^3$ N/m	$c_6 = 2.00$

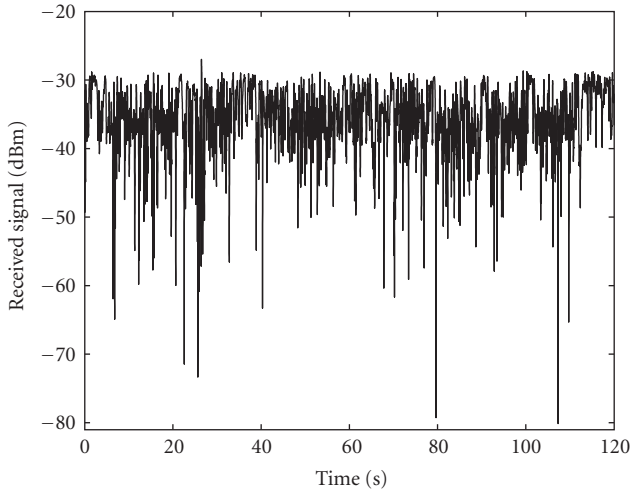

Figure 10: Simulated signal fading using the new model at 29 GHz during high wind speed conditions ($w_m = 5$ m/s). All simulation parameters are given in Table 3.

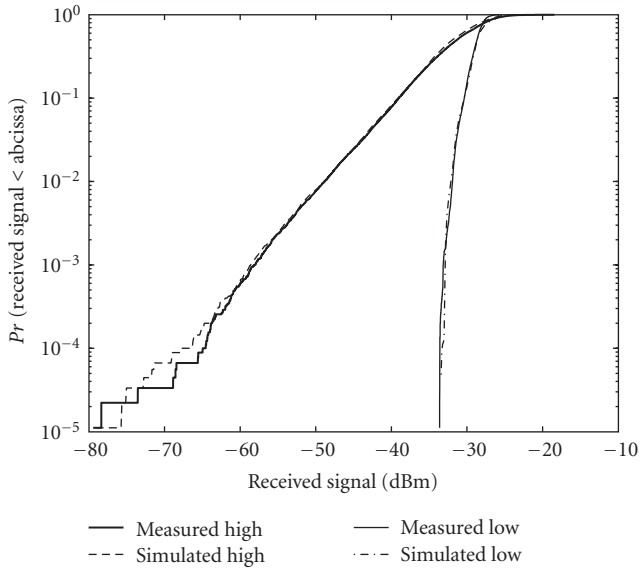

Figure 11: CDFs of measured (dry leaved deciduous trees (Site 1)) and simulated (using the new model) signals at 29 GHz during low ($w_m = 2$ m/s) and high ($w_m = 5$ m/s) wind speed conditions. All simulation parameters are given in Table 3.

effects of vegetation on propagating radiowaves. A new simulation model for generating signal fading due to a swaying tree has been developed by utilizing a multiple mass-spring system to represent a tree and a turbulent wind model. The model is validated in terms of first- and second-order statistics such as CDF, ACF, LCR, and AFD using measurements. The agreements found between the measured and simulated first- and second-order statistics of the received signals through vegetation are satisfactory. Furthermore, Ricean K-factors for different wind speeds are estimated from measurements. In general, the new model has similar dynamical and statistical characteristics as those observed from measurement results and can be used for simulating different capacity enhancing techniques such as adaptive coding and modulation and other fade mitigation techniques.

Appendices

A. Path Length Difference due to Swaying Tree Component

Using a trigonometric analysis of the paths shown in Figure 6, L_3 and L_4 can be expressed as

$$L_3 = \sqrt{L_1^2 + d^2} = L_1\sqrt{1 + \frac{d^2}{L_1^2}},$$
$$L_4 = \sqrt{L_2^2 + d^2} = L_2\sqrt{1 + \frac{d^2}{L_2^2}}. \quad \text{(A.1)}$$

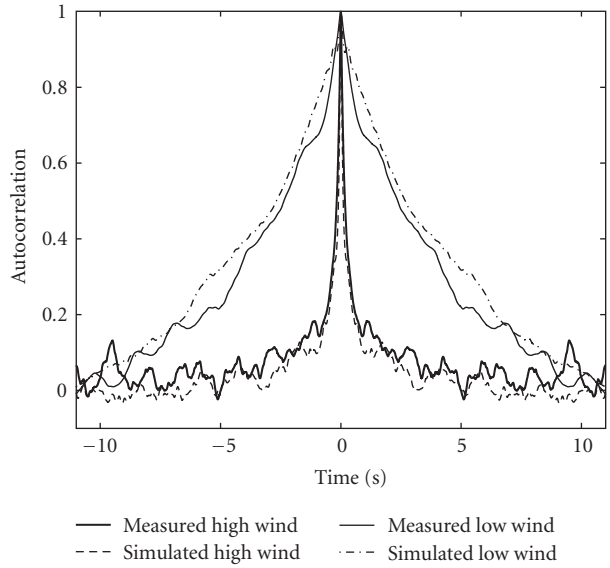

Figure 12: ACFs of measured (dry leaved deciduous trees (Site 1)) and simulated (using the new model) signals at 29 GHz during low ($w_m = 2$ m/s) and high ($w_m = 5$ m/s) wind speed conditions. All simulation parameters are given in Table 3.

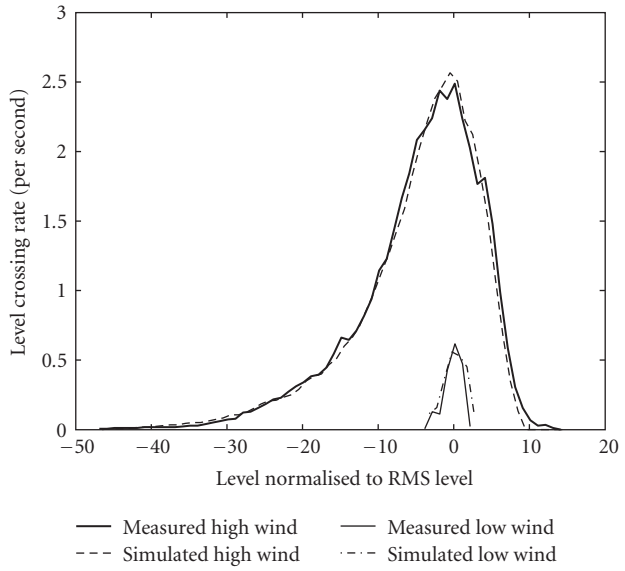

Figure 13: LCRs of measured (dry leaved deciduous trees (Site 1)) and simulated (using the new model) signals at 29 GHz during low ($w_m = 2$ m/s) and high ($w_m = 5$ m/s) wind speed conditions. All simulation parameters are given in Table 3.

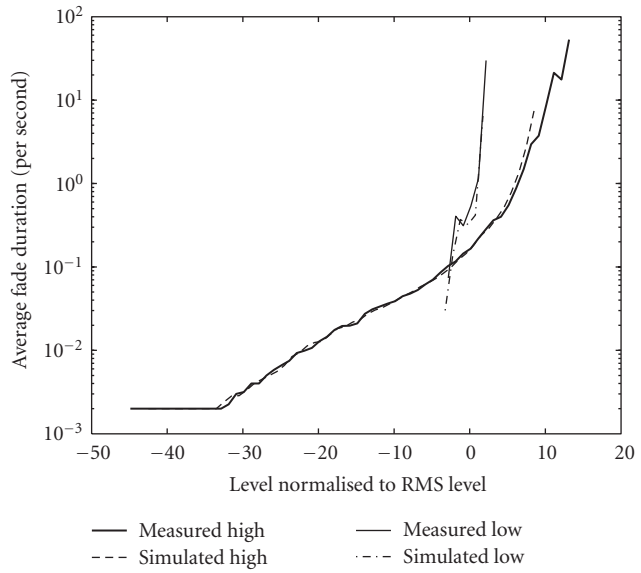

Figure 14: AFDs of measured (dry leaved deciduous trees (Site 1)) and simulated (using the new model) signals at 29 GHz during low ($w_m = 2$ m/s) and high ($w_m = 5$ m/s) wind speed conditions. All simulation parameters are given in Table 3.

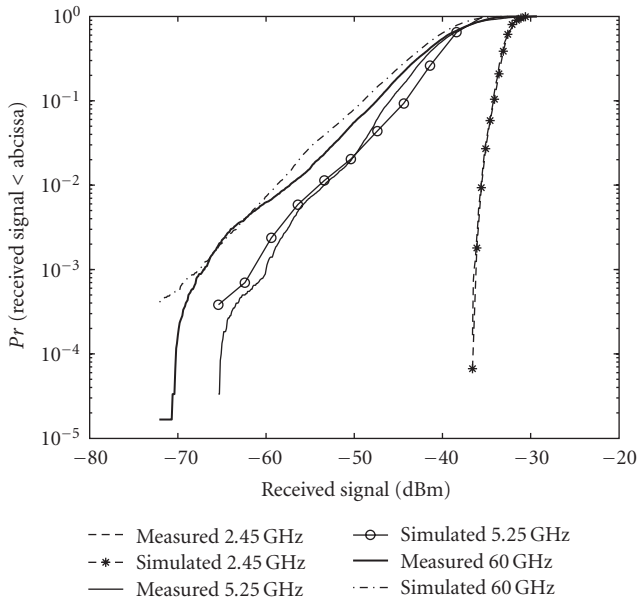

Figure 15: CDFs of measured (dry leaved deciduous trees (Site 1)) and simulated (using the new model) signals at 2.45, 5.25, and 60 GHz during high ($w_m = 5$ m/s) wind speed conditions. All simulation parameters are given in Table 3.

Assuming $L_1 \gg d$ and $L_2 \gg d$, Taylor approximation can be applied to yield

$$L_3 \approx L_1\left(1 + \frac{d^2}{2L_1^2}\right),$$
$$L_4 \approx L_2\left(1 + \frac{d^2}{2L_2^2}\right). \tag{A.2}$$

$L_3 + L_4$ is the path length when a tree component is at rest, and by using (A.2), we get

$$L_3 + L_4 \approx L_1 + L_2 + \frac{d^2}{2}\left(\frac{L_1 + L_2}{L_1 L_2}\right). \tag{A.3}$$

$L_5 + L_6$ is the path length when a tree component is displaced. Again performing a trigonometric analysis of Figure 6 and

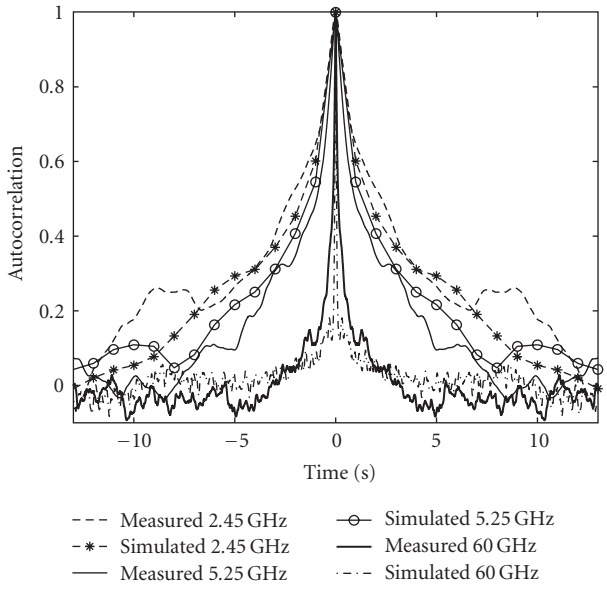

Figure 16: ACFs of measured (dry leaved deciduous trees (Site 1)) and simulated (using the new model) signals at 2.45, 5.25, and 60 GHz during high ($w_m = 5$ m/s) wind speed conditions. All simulation parameters are given in Table 3.

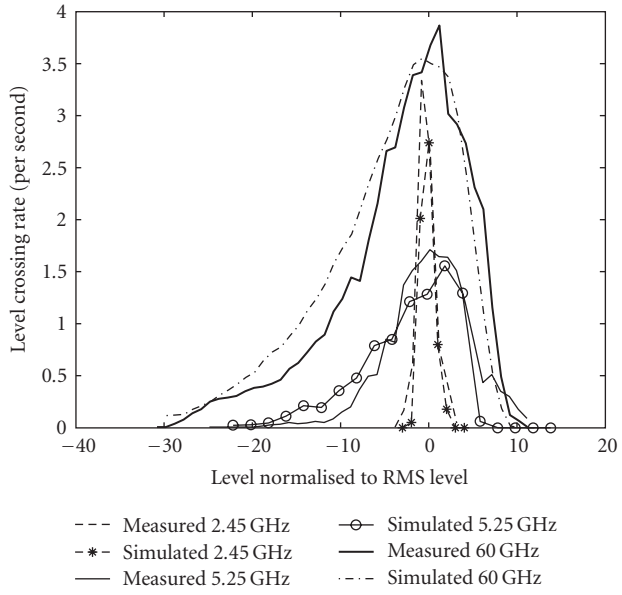

Figure 17: LCRs of measured (dry leaved deciduous trees (Site 1)) and simulated (using the new model) signals at 2.45, 5.25, and 60 GHz during high ($w_m = 5$ m/s) wind speed conditions. All simulation parameters are given in Table 3.

applying a Taylor approximation by assuming $L_1 \gg d + x$ and $L_2 \gg d + x$, $L_5 + L_6$ can be expressed as

$$L_5 + L_6 \approx L_1 + L_2 + \frac{(d+x)^2}{2}\left(\frac{L_1 + L_2}{L_1 L_2}\right). \tag{A.4}$$

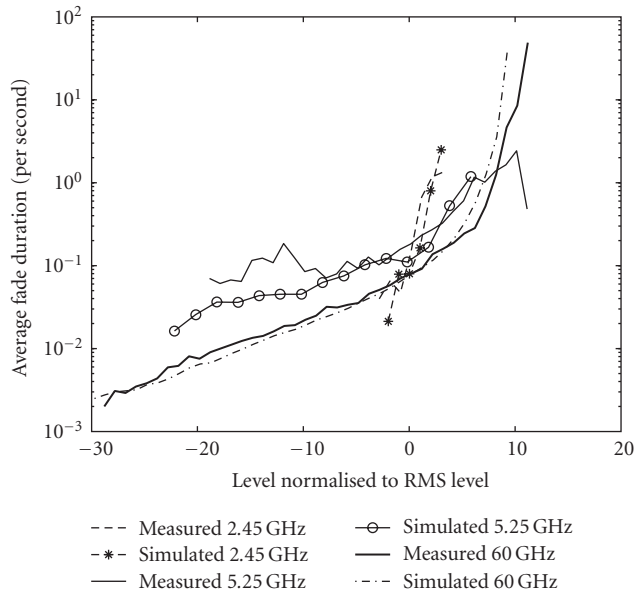

Figure 18: AFDs of measured (dry leaved deciduous trees (Site 1)) and simulated (using the new model) signals at 2.45, 5.25, and 60 GHz during high ($w_m = 5$ m/s) wind speed conditions. All simulation parameters are given in Table 3.

The difference in path length when a tree component is at rest and when it is displaced is then given by

$$\begin{aligned}\Delta L &= (L_5 + L_6) - (L_3 + L_4) \\ &\approx \left(\frac{2dx + x^2}{2}\right)\left(\frac{L_1 + L_2}{L_1 L_2}\right).\end{aligned} \tag{A.5}$$

Assuming further $x \ll d$ (which is valid for trees not located very near the transmitter or the receiver), the path length difference can then be expressed as

$$\Delta L \approx xd\left(\frac{L_1 + L_2}{L_1 L_2}\right). \tag{A.6}$$

B. Matrices for the State-Space Model

The state, $\mathbf{y}$, and input, $\mathbf{u}$, vectors defined in (9) and (10) are given by

$$\mathbf{y} = \left[x_0(t) \;\; \cdots \;\; x_6(t) \;\; \dot{x}_0(t) \;\; \cdots \;\; \dot{x}_6(t)\right]^T, \tag{B.1}$$

$$\mathbf{u} = \left[f_0(t) \;\; \cdots \;\; f_6(t)\right]^T. \tag{B.2}$$

By taking the first derivation of (B.1),

$$\dot{\mathbf{y}} = \left[\dot{x}_0(t) \;\; \cdots \;\; \dot{x}_6(t) \;\; \ddot{x}_0(t) \;\; \cdots \;\; \ddot{x}_6(t)\right]^T, \tag{B.3}$$

where the double derivations $\ddot{x}_0(t) \cdots \ddot{x}_6(t)$ in (B.3) are defined in (7). From (9), $\dot{\mathbf{y}}$ is given by

$$\dot{\mathbf{y}} = \mathbf{A}\mathbf{y} + \mathbf{B}\mathbf{u}, \tag{B.4}$$

where $\mathbf{y}$ and $\mathbf{u}$ are as defined in (B.1) and (B.2). In order (B.4) to be equal to (B.3), the matrices $\mathbf{A}$ and $\mathbf{B}$ have to be equal to

$$\mathbf{A} = \begin{pmatrix} \mathbf{0}_{7\times7} & \mathbf{I}_{7\times7} \\ \mathbf{A_{21}} & \mathbf{A_{22}} \end{pmatrix}, \tag{B.5}$$

where $\mathbf{0}_{7\times7}$ and $\mathbf{I}_{7\times7}$ are 7×7 zero and identity matrices, respectively. $\mathbf{A_{21}}$ and $\mathbf{A_{22}}$ in (B.5) are given by

$$\mathbf{A_{21}} = \begin{pmatrix} -\frac{(k_0+k_1+k_3+k_5)}{m_0} & \frac{k_1}{m_0} & 0 & \frac{k_3}{m_0} & 0 & \frac{k_5}{m_0} & 0 \\ \frac{k_1}{m_1} & -\frac{(k_1+k_2)}{m_1} & \frac{k_2}{m_1} & 0 & 0 & 0 & 0 \\ 0 & \frac{k_2}{m_2} & -\frac{k_2}{m_2} & 0 & 0 & 0 & 0 \\ \frac{k_3}{m_3} & 0 & 0 & -\frac{(k_3+k_4)}{m_3} & \frac{k_4}{m_3} & 0 & 0 \\ 0 & 0 & 0 & \frac{k_4}{m_4} & -\frac{k_4}{m_4} & 0 & 0 \\ \frac{k_5}{m_5} & 0 & 0 & 0 & 0 & -\frac{(k_5+k_6)}{m_5} & \frac{k_6}{m_5} \\ 0 & 0 & 0 & 0 & 0 & \frac{k_6}{m_6} & -\frac{k_6}{m_6} \end{pmatrix}, \tag{B.6}$$

$$\mathbf{A_{22}} = \begin{pmatrix} -\frac{(c_0+c_1+c_3+c_5)}{m_0} & \frac{c_1}{m_0} & 0 & \frac{c_3}{m_0} & 0 & \frac{c_5}{m_0} & 0 \\ \frac{c_1}{m_1} & -\frac{(c_1+c_2)}{m_1} & \frac{c_2}{m_1} & 0 & 0 & 0 & 0 \\ 0 & \frac{c_2}{m_2} & -\frac{c_2}{m_2} & 0 & 0 & 0 & 0 \\ \frac{c_3}{m_3} & 0 & 0 & -\frac{(c_3+c_4)}{m_3} & \frac{c_4}{m_3} & 0 & 0 \\ 0 & 0 & 0 & \frac{c_4}{m_4} & -\frac{c_4}{m_4} & 0 & 0 \\ \frac{c_5}{m_5} & 0 & 0 & 0 & 0 & -\frac{(c_5+c_6)}{m_5} & \frac{c_6}{m_5} \\ 0 & 0 & 0 & 0 & 0 & \frac{c_6}{m_6} & -\frac{c_6}{m_6} \end{pmatrix}, \tag{B.7}$$

$$\mathbf{B} = \begin{pmatrix} \mathbf{0}_{7\times7} \\ \mathbf{B_{21}} \end{pmatrix}, \tag{B.8}$$

where $\mathbf{B_{21}}$ in (B.8) is a diagonal matrix expressed as $\mathbf{B_{21}} = \text{diag}\{1/m_0 \cdots 1/m_6\}$.

The output vector $\mathbf{x}$ in (10) is defined as

$$\mathbf{x} = \begin{bmatrix} x_0(t) & \cdots & x_6(t) \end{bmatrix}^T. \tag{B.9}$$

From (10), $\mathbf{x}$ is given by

$$\mathbf{x} = \mathbf{C}\mathbf{y} + \mathbf{D}\mathbf{u}. \tag{B.10}$$

For (B.10) to be equal to (B.9), the matrices $\mathbf{C}$ and $\mathbf{D}$ have to be equal to

$$\begin{aligned} \mathbf{C} &= (\mathbf{I}_{7\times7} \quad \mathbf{0}_{7\times7}), \\ \mathbf{D} &= (\mathbf{0}_{7\times7}). \end{aligned} \tag{B.11}$$

Acknowledgments

This work is supported by the research council of Norway (NFR). The authors would like to thank the Communications Research Centre Canada (CRC), especially Simon Perras for providing measurement data. The authors would like also to thank Morten Topland of UNIK for fruitful discussions.

References

[1] M. Cheffena, *Modeling and prediction of millimeter wavelength channels*, Ph.D. thesis, Norwegian University of Science and Technology, Trondheim, Norway, October 2008.

[2] M. O. Al-Nuaimi and A. M. Hammoudeh, "Measurements and predictions of attenuation and scatter of microwave signals by trees," *IEE Proceedings: Microwaves, Antennas and Propagation*, vol. 141, no. 2, pp. 70–76, 1994.

[3] I. J. Dilworth and B. L'Ebraly, "Propagation effects due to foliage and building scatter at millimetre wavelengths," in *Proceedings of the 9th International Conference on Antennas and Propagation*, vol. 2, pp. 51–53, Eindhoven, The Netherlands, April 1995.

[4] Recommendation ITU-R P.833-5, "Attenuation in vegetation," Tech. Rep. P.833-2, ITU, Geneva, Switzerland, 2005.

[5] A. M. Randle, *Dynamic radio channel effects from L-band foliage scatter*, Ph.D. thesis, University of York, York, UK, September 1999.

[6] K. H. Craig, Ed., "Propagation planning procedures for LMDS," AC215 CRABS, Deliverable D3P1b, January 1999, http://www.telenor.no/fou/prosjekter/crabs.

[7] S. Perras and L. Bouchard, "Fading characteristics of RF signals due to foliage in frequency bands from 2 to 60 GHz," in *Proceedings of the 5th International Symposium on Wireless Personal Multimedia Communications*, vol. 1, pp. 267–271, Honolulu, Hawaii, USA, October 2002.

[8] M. H. Hashim and S. Stavrou, "Dynamic impact characterization of vegetation movements on radiowave propagation in controlled environment," *IEEE Antennas and Wireless Propagation Letters*, vol. 2, no. 1, pp. 316–318, 2003.

[9] T. Sofos and P. Constantinou, "Propagation model for vegetation effects in terrestrial and satellite mobile systems," *IEEE Transactions on Antennas and Propagation*, vol. 52, no. 7, pp. 1917–1920, 2004.

[10] M. Cheffena and T. Ekman, "Modeling the dynamic effects of vegetation on radiowave propagation," in *Proceedings of the IEEE International Conference on Communications (ICC '08)*, pp. 4466–4471, Beijing, China, May 2008.

[11] W. E. Leithead, S. de la Salle, and D. Reardon, "Role and objectives of control for wind turbines," *IEE Proceedings C*, vol. 138, no. 2, pp. 135–148, 1991.

[12] C. Nichita, D. Luca, B. Dakyo, and E. Ceanga, "Large band simulation of the wind speed for real time wind turbine simulators," *IEEE Transactions on Energy Conversion*, vol. 17, no. 4, pp. 523–529, 2002.

[13] E. B. Muhando, T. Senjyu, N. Urasaki, A. Yona, H. Kinjo, and T. Funabashi, "Gain scheduling control of variable speed WTG under widely varying turbulence loading," *Renewable Energy*, vol. 32, no. 14, pp. 2407–2423, 2007.

[14] "*European Standard for Wind Loads*," Eurocode EN 1991-1-4, WIND ACTION.

[15] K. R. James, N. Haritos, and P. K. Ades, "Mechanical stability of trees under dynamic loads," *American Journal of Botany*, vol. 93, no. 10, pp. 1522–1530, 2006.

[16] H. Peltola, S. Kellomäki, H. Väisänen, and V.-P. Ikonen, "A mechanistic model for assessing the risk of wind and snow damage to single trees and stands of Scots pine, Norway spruce, and birch," *Canadian Journal of Forest Research*, vol. 29, no. 6, pp. 647–661, 1999.

[17] J. C. DalBello, G. L. Siqueira, and H. L. Bertoni, "Effects of vegetation on urban cellular systems," in *Proceedings of IEEE International Conference on Universal Personal Communications (ICUPC '98)*, vol. 1, pp. 113–116, Florence, Italy, October 1998.

[18] A. Kajiwara, "LMDS radio channel obstructed by foliage," in *Proceedings of IEEE International Conference on Communications (ICC '00)*, vol. 3, pp. 1583–1587, New Orleans, La, USA, June 2000.

[19] N. Naz and D. D. Falconer, "Temporal variations characterization for fixed wireless at 29.5 GHz," in *Proceedings of the 51st IEEE Vehicular Technology Conference (VTC '00)*, vol. 3, pp. 2178–2182, Tokyo, Japan, May 2000.

[20] L. J. Greenstein, D. G. Michelson, and V. Erceg, "Moment-method estimation of the Ricean K-factor," *IEEE Communications Letters*, vol. 3, no. 6, pp. 175–176, 1999.

[21] B. Sklar, *Digital Communications*, Prentice-Hall, Englewood Cliffs, NJ, USA, 2001.

[22] S. R. Saunders, *Antennas and Propagation for Wireless Communication Systems*, John Wiley & Sons, New York, NY, USA, 2003.

Hindawi Publishing Corporation
EURASIP Journal on Wireless Communications and Networking
Volume 2009, Article ID 532474, 8 pages
doi:10.1155/2009/532474

Research Article

Towards a Performance Boundary in Calibrating Indoor Ray Tracing Models

Jaouhar Jemai[1] and Thomas Kürner[2]

[1] *Ubisense AG, Development and Services, 80637 Munich, Germany*
[2] *Institut für Nachrichtentechnik, Technische Universität Carolo-Wilhelmina Braunschweig, 38106 Braunschweig, Germany*

Correspondence should be addressed to Jaouhar Jemai, jaouhar_jemai@hotmail.com

Received 27 July 2008; Revised 18 December 2008; Accepted 20 February 2009

Recommended by Jun-ichi Takada

This paper investigates the performance boundaries of a calibrated deterministic indoor channel model. From a propagation modeling point of view, this process allows to assess the weakness of ray tracing and sets the boundary conditions for a such modeling method. The principle of the deterministic model calibration used in this work focuses upon the estimation of optimal material parameters by means of a few pilot measurements and a simulated annealing method. This technique improves the accuracy of the prediction model for all measurement positions including those not considered by the calibration. The performance of the calibrated ray tracing model and the sensitivity of the calibration to the number of pilot measurements have been investigated. For this investigation, a measurement campaign has been conducted within an indoor office building at 2.45 GHz with 100 MHz bandwidth. Furthermore, the model performance has been compared to empirical indoor models.

1. Objective and Introduction

The blind prediction, based on a priori approximate knowledge of material parameters, often shows an obvious mismatch with the measurements. Even if predicted path loss values are accurate enough like, for example, in [1], time dispersion parameters could show a significant mismatch. Ray tracing-based conventional deterministic modeling methods use geometrically accurate data and rely on tabulated values for the electrical parameters of the building materials. For instance, the authors in [2] made direct measurements of the building materials. However, the material parameters remain approximate and impossible to define accurately for each building, especially when the building materials are a heterogeneous mixture of unknown components, for which no electromagnetic measurement values are available. Therefore, a calibration of these material parameters, reducing the mismatch between the model and the measurements, is required. The issue of deterministic modeling calibration has been addressed in very few works. In [3], only the dielectric constant of each wall have been tuned separately and the gradient method is used to estimate the solution. However, using the gradient method in conjunction with this tuning provides generally a local minimum and does not necessarily provide the optimal solution.

As the relation between power taps and material parameters is a nonlinear combinatorial relationship, the simulated annealing approach used in this paper provides the general optimal solution by simultaneously changing the dielectric constant and loss tangent of all material parameters with a changing step at each range of iterations. The method proposed converges to a global solution and avoids to be dropped into a local minimum as the gradient method does. The performance and robustness of this calibration procedure is analyzed in this paper by means of an indoor measurement campaign within an office building.

This paper is organized as follows. Section 2 presents the ray tracing model. Section 3 investigates the calibration process and the calibration algorithm. Subsequently, the conducted measurement campaigns and the calibration results for an indoor office environment are highlighted in Section 4. Finally, Section 5 addresses the sensitivity of the calibration to the measurements and assesses the boundary of the modeling methods.

2. The Wideband Semideterministic Prediction Model

The prediction model has been presented earlier by the authors in [4–6]. It has been derived by means of two core components; a geometric engine and an electromagnetic engine. While the geometric engine derives the propagation paths based on the accurate information of the 3D building database, the electromagnetic engine computes the propagation mechanisms and integrates the antenna radiation patterns.

The model requires an accurate 3D indoor database with detailed information describing the scattering objects (walls, doors, and windows), their thickness and their dielectric properties. The required building parameters introduced in the database are the relative dielectric constant ε_r and the loss tangent $\tan\delta$. According to their electromagnetic material properties, the structures of the building are classified into N different classes with common dielectric material parameters.

Besides free-space propagation, the propagation tool computes the Fresnel equations, considering multiple reflections and transmission through walls. Depending on whether the antennas is horizontally or vertically polarized, the system considers the corresponding reflection/transmission coefficients and also the angle of departure (AoD) and angle of arrival (AoA) corresponding to each path. Interactions up to the 3rd order reflection have been considered. Many simulations have confirmed that this order provides a compromise between the accuracy of channel parameter (path loss and delay dispersion) and the reasonable computation time, which is also in accordance with [7]. The tool supports as much transmissions as the wave encounters in its propagation path. It accounts for the single diffraction using the uniform theory of diffraction (UTD) [8].

Thus, the channel model could be represented as a power delay profile (PDP) expressed by

$$h(\tau) = \sum_{k=1}^{L_p} \alpha_k \delta(\tau - \tau_k), \tag{1}$$

where P is the number of taps, α_k and τ_k are the power and time of arrival (ToA) of the kth tap. The deterministic channel modeling provides channel characteristics with an infinite bandwidth. Hence, an infinite discrete time resolution is achieved, enabling all MPCs to be resolved. However, as the measurement bandwidth is generally limited, the resolution of the measurement equipment could not enable the detection of all multipath components. Each group of closely spaced MPCs has been represented with a particular tap delay L_p, the power of which is the sum of these MPCs power. The PDP could then be written as

$$h(\tau) = \sum_{k=1}^{L_p} \sum_{n=1}^{k_n} \alpha_{k_n} \delta(\tau - \tau_k), \tag{2}$$

whereby k_n is the number of MPCs clustered together to form the kth tap.

Since typically only 2D radiation patterns (horizontal and vertical) are available, the developed model derives the 3D antenna radiation pattern through a bilinear interpolation knowing the measured 2D patterns in E- and H-planes [9]. Moreover, for a better accuracy, the system model integrates also 3D measured antenna patterns within an anechoic chamber.

3. Model Calibration

The calibration consists in extracting relevant multipath components (MPCs), for instance once reflected paths, simultaneously from the model and measurement. Afterwards, the simulated annealing is performed to optimize the material parameters.

3.1. Extraction of Parameters for Calibration. The measured and predicted PDPs h_{meas} and h_{mod} are given by

$$\begin{aligned} h_{\text{meas}}(\tau) &= \sum_{k=1}^{Lp_{\text{meas}}} (\alpha_k)_{\text{meas}} \delta(\tau - \tau_k), \\ h_{\text{mod}}(\tau) &= \sum_{k=1}^{Lp_{\text{mod}}} (\alpha_k)_{\text{mod}} \delta(\tau - \tau_k). \end{aligned} \tag{3}$$

After identifying the direct path, according to the arrival time corresponding to the distance separating Tx and Rx, particular P power taps (e.g., once reflected paths) with a power above the noise threshold have been extracted from the measurement and the model simultaneously. The noise threshold is computed from each measurement based on a dynamic noise clipping. Hence, two vectors of power taps have been formed which are $[[(\alpha_k)_{\text{meas}}]_{n=1}^{P}]^T$ and $[[(\alpha_k)_{\text{mod}}]_{n=1}^{P}]^T$. The calibration uses the electromagnetic engine, the power tap matrices and the involved building structures to optimize the material parameters incorporated by the deterministic model.

3.2. Simulated Annealing Algorithm: Practical Implementation for Material Parameters Estimation. The "Simulated Annealing" is analogous to the phenomenon of heating a material and letting it cool gradually until reaching a steady state. By the cooling process, the material reaches a global optimum, for which a global minimum energy crystalline structure is dissipated. Starting with an initial solution s (set of material parameters for the N classes) at a relatively high chosen temperature T_0, a neighbor solution s' is afterwards generated as a next solution for which the evolution in cost, $\Delta E(s, s') = E(s') - E(s)$, is evaluated. If the cots decreases, the generated neighbor solution becomes the current one, otherwise the algorithm decides with a certain probability whether s remains or s' becomes the current solution. The probability of accepting a transition, causing a decrease $\Delta E(s, s')$ in the cost, is called the acceptance function and is set to $e^{-\Delta E/T}$. T is the parameter that corresponds to temperature in the analogy with the physical annealing process. The algorithm runs L steps with the same

Table 1: Simulated annealing algorithm parameters.

Notation	Meaning
s	A random solution as a set of material parameters
$E(s)$	Objective function
T_0	Initial temperature of the stepped geometric decrease
A	Geometric decrease coefficient
L	Number of steps running with constant temperature
ST	Maximum steps the algorithm runs without many changes

temperature. Afterwards, the changing step of the parameters is decreased geometrically with the factor A towards zero. The process is stopped after ST steps if the objective function remains unchanged. The final solution is considered as the absolute optimum. The four configuration parameters (T_0, A, L, and ST) considered by the algorithm are described in Table 1.

The initial material properties are defined using tabulated values available in literature and knowledge of the construction material category. The electromagnetic properties of some different conventional building materials, for example, at the WLAN frequencies can be found in literature [2, 10, 11]. However, some materials are a mixture of unknown components, for which no electromagnetic measurement values are available. Therefore, the optimization process starts from a common value for all these materials, corresponding, for example, to the concrete ($\varepsilon_r = 4.95$, $\tan\delta = 0.01$) at ambient temperature as measured in [11]. The optimized objective (cost) function is defined as the root mean square error between the measured and the predicted tap powers for all M measurements with P_m propagation paths each. A total of 990 indoor planes (walls) of the building have been grouped into 20 different classes of structures. Starting from an initial set of material parameters as initial solution for structure classes, the initial objective function is computed at each new iteration i as

$$C_i = \frac{1}{M}\sum_{m=1}^{M}\frac{1}{P_m}\sqrt{\sum_{n=1}^{P_m}\left((\alpha_{mn})_{\text{mod}} - (\alpha_{mn})_{\text{meas}}\right)_i^2}, \quad (4)$$

where M is the number of conducted measurements, P_m is the number of paths within the measurement m, and α_{mn} are the power taps from (1). The parameters $(\alpha_{mn})_{\text{mod}}$ and $(\alpha_{mn})_{\text{meas}}$ denote the predicted and measured powers of the MPCs, respectively.

4. Measurement Campaign and Calibration Results

4.1. Measurement Campaign. The measurements have been conducted within an indoor office building environment, for which the antenna placements are depicted in Figure 2. In the frequency domain, a vector network analyzer is connected through a GPIB connection to a notebook. It sweeps the channel with a bandwidth of 100 MHz around the central frequency 2.45 GHz. The channel impulse response

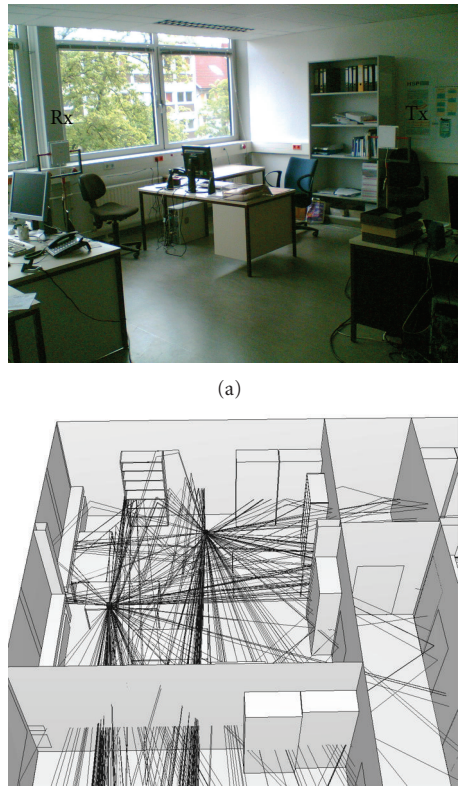

(a)

(b)

Figure 1: (a) A measurement configuration within an office room with (b) a 3D ray tracing.

in the time domain is obtained by the inverse fast Fourier transform (ifft) of the measured complex channel transfer function. In order to overcome the leakage problem of side lobes, while preserving a reasonable pulse width within the channel impulse response, a Hamming window is applied. Two identical WLAN directional antennas, with 14 dBi gain and a half-power beam width of 30°, have been connected to the ports of the VNA via two cables of 10 m length each. The corresponding radiation patterns have been measured in 3D in an anechoic chamber at the frequency of 2.45 GHz and have been introduced into the model. Both antennas can be directed in azimuth and elevation in the range 0–350° with steps of 10° and are positioned at a height level of 1.25 m. Using directional antennas is favorable for focusing the reception on a specific direction targeting a better identification of reflections impinging from the surrounding environment. The performance has been investigated in terms of RMS delay spread (σ_τ [ns]), maximum excess delay ($\tau_{\max}$ [ns]) and path loss (L [dB]), which is computed considering the sum over all MPCs powers above the noise threshold. The channel parameters have been computed considering a noise clipping. A total number of 38 measurements corresponding to 4 transmitter locations, associated with 20 receiver positions on the second floor have been conducted, whereby different antenna tilts (with steps of 90°) have been considered at some positions. These locations are shown in Figure 2. The building database

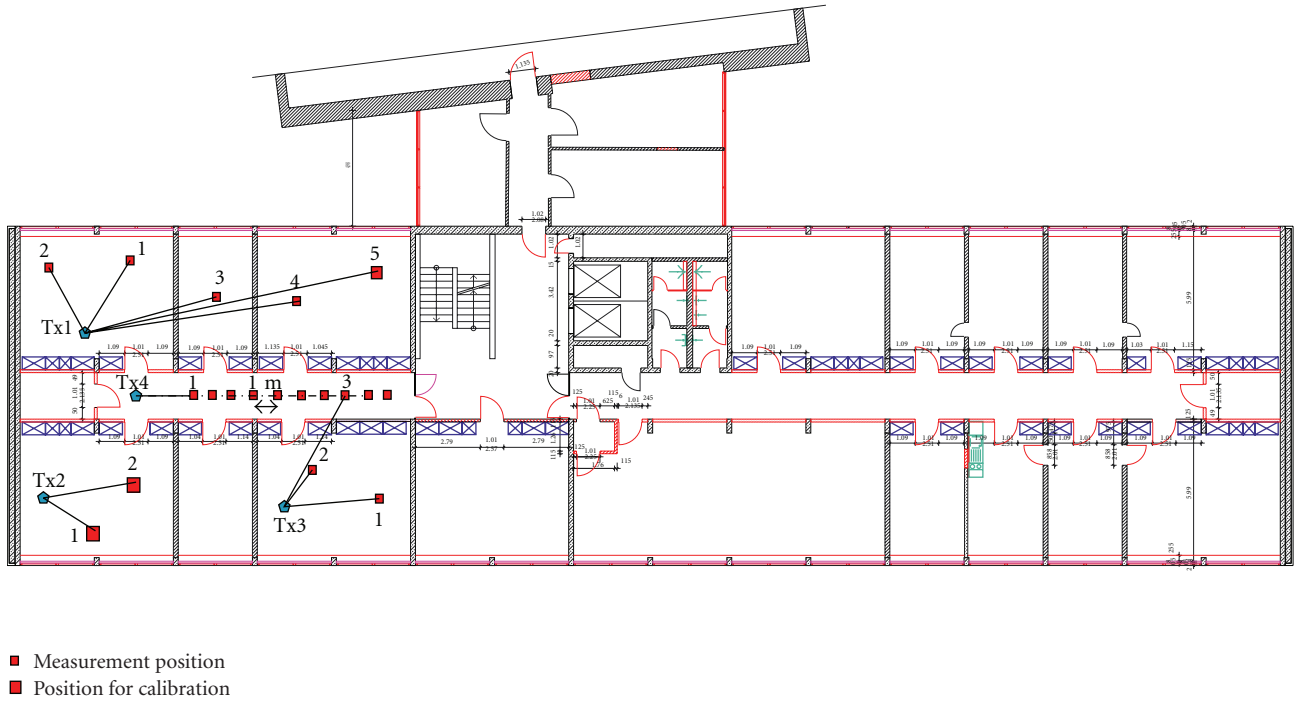

Figure 2: Indoor transmitter and receiver locations.

gathers 900 elementary planes constituting the structures (walls, doors, windiws, cupboards, bookshelves, and tables), as shown in Figure 1.

The offices where the measurements have been conducted are representative of the entire institute building and gather most of the building structures. Moreover, 9 aligned measurements starting at 3 m from the transmitter have been conducted on the floor (as depicted in Figure 2) due to its characteristics enabling LOS conditions and wave-guiding effects.

4.2. Calibration Performance. The calibration has been performed using a set of three measurements for LOS (Tx2-Rx1, Tx2-Rx2) and for NLOS (Tx1-Rx5) as presented in bold squares in Figure 2. Figure 3 displays the PDP (before and after calibration).

The positions Tx2-Rx1 is included in the calibration, Tx1-Rx2 in the neighbor room, and Tx4-Rx1 situated on the corridor are both not used as calibration data. The initial cost function prior to calibration amounts to 5.2 dB, whereas the one after calibration is 1.3 dB. The PDPs have been normalized referring to the direct path power. The good match of the model is resumed in Table 2 regarding channel parameters.

Though initially not included in the calibration, the measurements Tx1-Rx2 and Tx4-Rx1 show a good match with the calibrated model. As expected, the measurement Tx2-Rx1 shows a better match than the other measurements not included in the calibration. However, the advantage of the model resides in providing globally more accurate parameters at any location within the environment without need of huge measurement campaigns to cover the whole building. This is an advantage over the statistical modeling as presented, for example, in [6].

Table 2: Summary of results for the three positions.

Position	Parameter	Measurement	Uncalibrated	Calibrated
Tx2-Rx1	σ_τ [ns]	10.3	2.8	8.1
	$\tau_{\max}$ [ns]	170	60	160
	L [dB]	42.9	44.5	42.2
Tx1-Rx2	σ_τ [ns]	16	5.5	13.8
	$\tau_{\max}$ [ns]	170	70	120
	L [dB]	41.2	43.8	40.4
Tx4-Rx1	σ_τ [ns]	11.8	1.3	7.9
	$\tau_{\max}$ [ns]	160	40	170
	L [dB]	28.8	28.3	28.7

4.2.1. Overall Analysis. An overall improvement of the calibrated model compared to the uncalibrated one is obviously noticeable in most cases. The delay dispersion parameters are considerably improved as the power taps are calibrated. This is demonstrated in Table 3 showing the overall improvement by the new calibrated model in terms of prediction error over all measurements, where the mean, the standard deviation, the minimum, and the maximum error are denoted by $\overline{\Delta}$, Δ_σ, $\Delta_{\min}$, and $\Delta_{\max}$. Hence, the calibrated model delivers globally a significant improvement in characterizing the channel. A mean prediction error of 1.5 dB and a standard deviation of 4 dB are provided by the calibrated model. At a few positions, channel parameters did not improve due to the presence

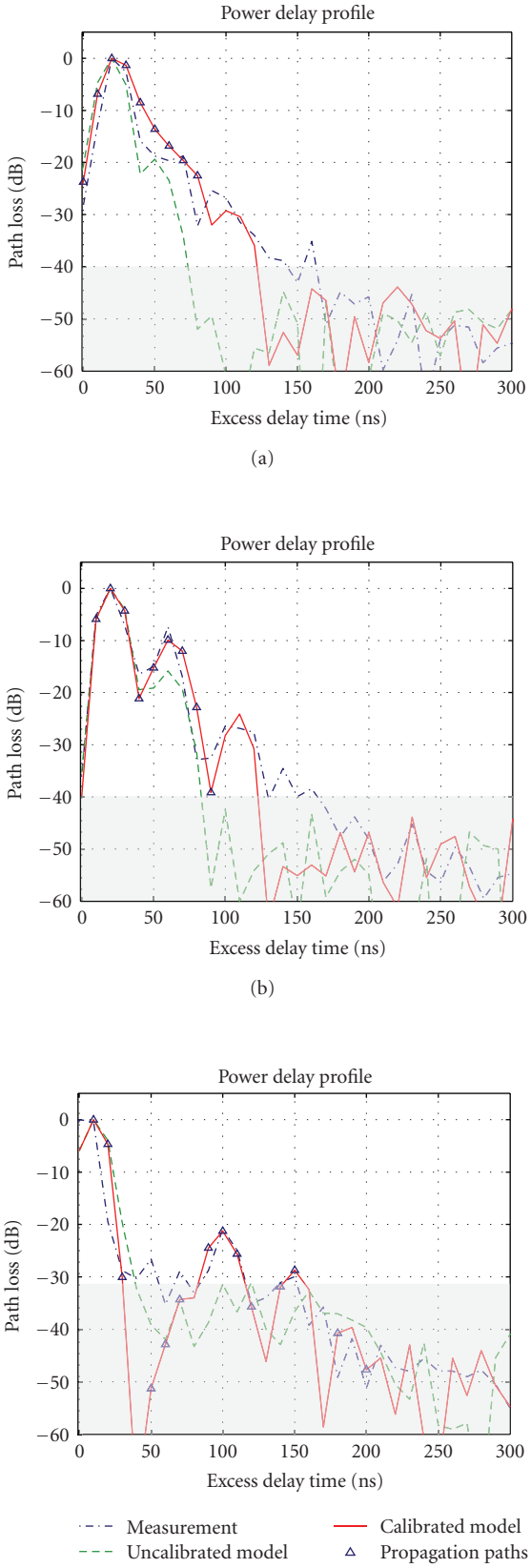

Figure 3: PDP for the measurements (a) Tx2-Rx1 (used as calibration data), (b) Tx1-Rx2 (not used as calibration data), and (c) Tx4-Rx1 (not used as calibration data).

Table 3: Overall prediction error of the model before and after calibration.

Parameter	Statistics	Uncalibrated	Calibrated
σ_τ [ns]	$\overline{\Delta}$	8	4
	Δ_σ	5.1	4.7
	$\Delta_{\min}$	1.5	−5.6
	$\Delta_{\max}$	22.8	18.1
$\tau_{\max}$ [ns]	$\overline{\Delta}$	46	11.9
	Δ_σ	48.1	30.1
	$\Delta_{\min}$	−40	−30
	$\Delta_{\max}$	140	80
L [dB]	$\overline{\Delta}$	1.6	1.3
	Δ_σ	9.1	4
	$\Delta_{\min}$	−23.5	−10.5
	$\Delta_{\max}$	21.1	7.3

Table 4: Path loss prediction error statistics of COST 231 models and calibrated ray tracing.

Model	OSM	MWM	Ray tracing
$\overline{\Delta}$	−5.3	−4.1	1.3
Δ_σ	10.5	9.2	4
$\Delta_{\max}$	26.8	17.8	7.3
$\Delta_{\min}$	−14.8	−17.4	−10.5

of other objects with different materials or due to other propagation mechanisms not considered by the model.

4.2.2. Performance Over COST 231 Models. COST 231 models (one slope model and multiwall model) [12] are narrowband indoor prediction models. These models have been fitted using the same measurements used for the ray tracing. These models are given by the following equations

$$L_{\text{OSM}} = 50.7 + 17.3\,\log(d)\ [\text{dB}], \tag{5}$$

whereas the MWM model is given by

$$L_{\text{MWM}} = 40 + 20\log(d) + c + \sum_w L_w k_w\ [\text{dB}], \tag{6}$$

where the constant loss $c = -6.7$ dB and the wall loss $L_w = 15.7$ dB have been determined by calibration. A comparison of the results of the calibrated model performance over the conventional COST 231 models for all 38 measurements are summarized in Table 4. It is obvious that the calibrated model outperforms the two empirical models. An average error of 1.3 dB is achieved by the ray tracing model, whereas the ones of OSM and MWM remain between −6 and −4 dB. Compared to the COST 231 models, which have a standard deviation between 11 and 9 dB, the calibrated ray tracing model achieves a smaller standard deviation of 4 dB.

Originally, empirical models provide less accuracy compared to ray tracing models, as they only consider the direct path between the transmitter and the receiver. This is the main cause of their weakness especially within a rich multipath indoor environment.

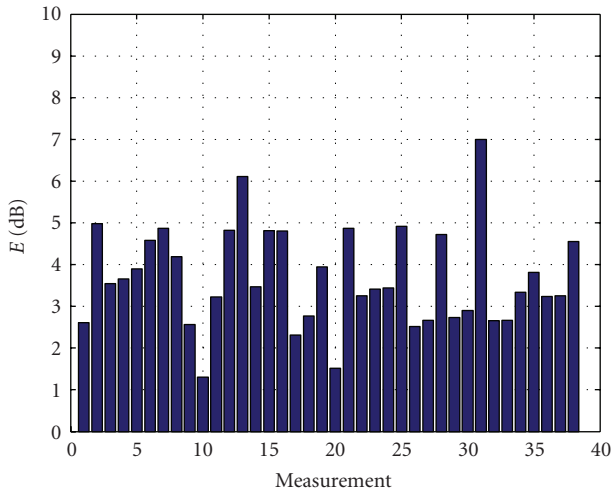

Figure 4: Cost function using one measurement.

5. Sensitivity of the Calibration to the Measurements

Analyzing the performance of the calibration reveals some investigations to be dealt with comprehensively. In this section, the degree of the model performance improvement added by the calibration is assessed as a function of the calibration set size. First, the effect of one measurement is investigated. Subsequently, the impact of increasing the calibration set size has been analyzed.

5.1. Single Measurement-Based Calibration. The optimization on a single measurement is useful to provide an insight into the degree of improvement to be expected with an adequate choice of material parameters. Each of the 38 measurements has been used for calibration of the model and the cost function for this measurement as well as the modeling error are computed for all measurements. Obviously, by virtue of their representative locations in the building, some measurements perform better than others when used for calibration. For instance, measurements 10 and 20 provide the best match with a cost of 1.2 to 1.5 dB (see Figure 4), whereas other measurements (2, 13, and 31) deliver the worst match with an error between 5 and 7 dB.

Each measurement of the 38 has been used singularly for calibration. The overall results of the improvement using one measurement are shown in Figure 5, where $\bar{\varepsilon}$ denotes the absolute average prediction error between the model and the measurements for the complete set of 38 measurements, expressed by

$$\bar{\varepsilon} = \frac{1}{38}\sum_{i=1}^{38} |\Delta_i|, \tag{7}$$

where Δ_i is the prediction error for the ith measurement.

The uncalibrated plot (dashed line) is constant as it is the difference between the measurement and prediction for all the set of data before calibration. It is noticeable that the average error reaches an optimum of 3 dB. However, at some other, less representative locations of the entire building, the calibration results are rather degraded.

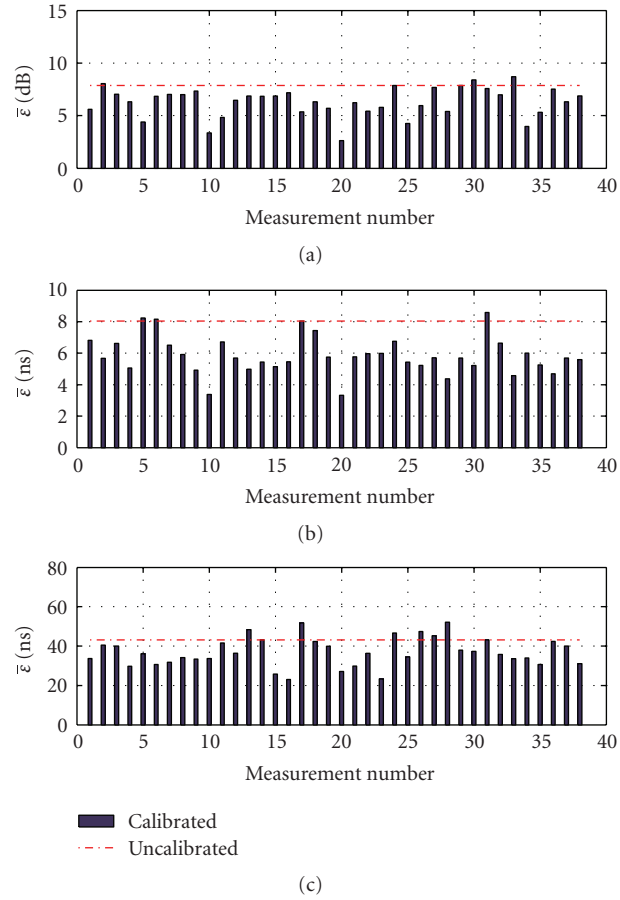

Figure 5: Average error for all measurements with a calibration set of one measurement for (a) path loss, (b) RMS delay spread, and (c) maximum excess delay.

5.2. Measurement Set Size Influence. In order to keep the computation time reasonable with the increasing number of possible combinations, all possible combinations from the first 15 measurements have been considered ($n = 1, \ldots, 15$). The remaining 15 measurements have been added to the set (one each new calibration process) without combination. At each calibration computation, the resulting cost function is recorded and plotted versus the calibration set size (number of measurements) in Figure 6. The cost function undergoes an exponential decay with the variation trend given by the equation in the figure.

Figure 7 shows the average of the errors between the measurements and the calibrated model for all combinations of the 30 measurements, when the number of measurements used to optimize the floor plan is increased. $\bar{\varepsilon}$ denotes the absolute average prediction error for all measurements together. At each calibration process, the calibration set size is incremented by one measurement and the calibration error for all positions is computed. All combinations of measurements have been considered to derive the average

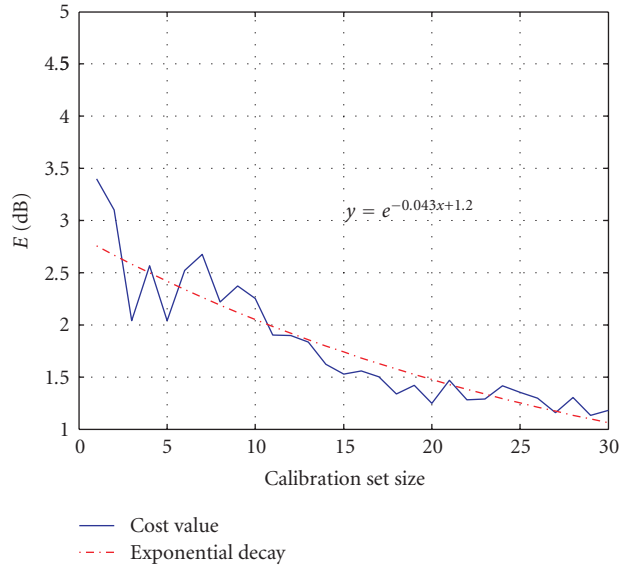

Figure 6: Cost function with increasing size of the calibrating measurement set.

error. The overall degree of improvement in terms of time dispersion and path loss parameters is illustrated in Figure 7.

Henceforth, the remarkable fact which flows from these results is that the error diminishes as the calibration set size increases. This error reaches a fluctuation status around the number of 10, where the modeling error starts to fluctuate around a constant value. This reveals effectively the performance boundary of this deterministic model. It is noteworthy that the prediction error of path loss and time dispersion parameters exhibits a general decay trend with increasing calibration set size. However, a judicious calibration requires a compromise between a best performance and a lower computation time and complexity.

6. Conclusions

This paper addresses the subject of a new deterministic model calibration technique based on simulated annealing, which improves the model performance by means of a few pilot measurements.

The basic facts that emerge from this paper are mainly the model performance improvement and the performance limit reached with more measurements. Indeed, the calibrated model outperforms the standard uncalibrated one with a mean error of 1.3 dB and a standard deviation of 4 dB. With an increasing size of the calibration set, the calibration reaches a steady state for a number of measurements of 10 and starts to deviate around a constant value which shows the performance limit of the ray tracing modeling method. The calibration positions should be chosen in a way to cover the different kinds of rooms in the building in order to enable the coverage of major structures within the environment.

Besides its advantage of compensating for the tedious task of manually tuning the building dielectric parameters plan, the calibration produces an optimized building plan

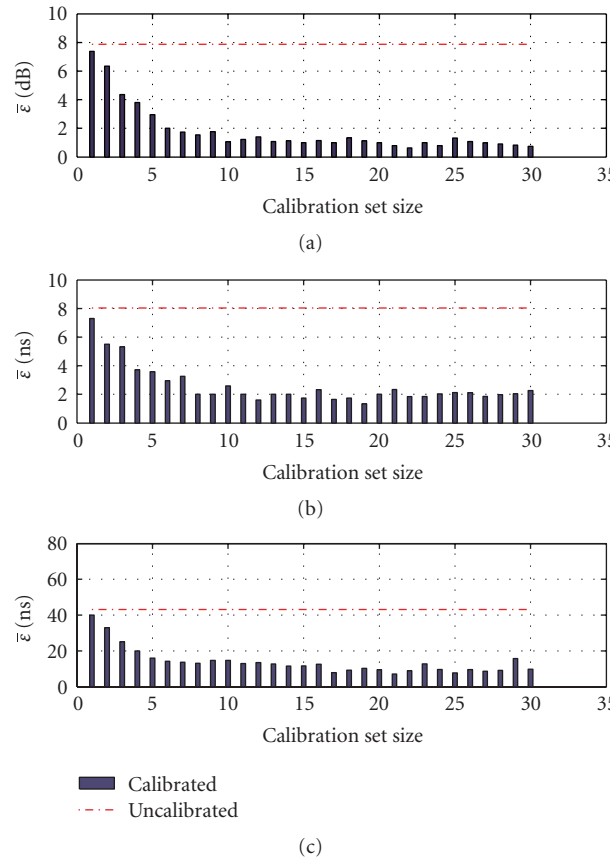

Figure 7: Average error for all measurements in terms of (a) path loss, (b) RMS delay spread, and (c) maximum excess delay with increasing size of the calibrating measurement set.

that works for any conventional ray tracing model. It has been shown that, though the model accuracy improves with an increasing number of measurements used for the optimization, it is indeed bounded and tends to a steady state. The calibration modeling error starts to fluctuate around its extremum after a certain number of measurements, which obviously shows the limits of the deterministic modeling by means of ray tracing.

Directional antennas (as used in this paper) enhance the signal strength and the impinging waves from a certain direction. Omnidirectional antennas can also be used as in [6].

The more the structures a floor plan has the bigger the calibration set size should be in order to optimize all material parameters. Furthermore, the calibrating measurements should involve main propagation paths reflected on the structures to be calibrated.

References

[1] G. Wölfle, *Adaptive Modelle zur Funknetzplanung und zur Berechnung der Empfangsqualität in Gebäuden*, Ph.D. thesis, Institut für Hochfrequenztechnik der Universität Stuttgart, Stuttgart, Germany, 1999.

[2] S. Y. Seidel and T. S. Rappaport, "Site-specific propagation prediction for wireless in-building personal communication

system design," *IEEE Transactions on Vehicular Technology*, vol. 43, no. 4, pp. 879–891, 1994.

[3] J. Beneat and N. Bailey, "Optimization of building material properties for accurate indoor ray tracing models," in *Proceedings of the IEEE Military Communications Conference (MILCOM '04)*, vol. 2, pp. 1010–1014, Monterey, Calif, USA, October-November 2004.

[4] J. Jemai and T. Kürner, "Calibration of indoor channel models," in *Proceedings of the ITG/VDE Mobile Radio Conference, Technologies and Applications*, pp. 31–36, Osnabrück, Germany, May 2007.

[5] J. Jemai and T. Kürner, "Broadband WLAN channel sounder for IEEE 802.11b," *IEEE Transactions on Vehicular Technology*, vol. 57, no. 6, pp. 3381–3392, 2008.

[6] J. Jemai, I. Schmidt, and T. Kürner, "UWB channel: from statistical aspects to calibration-based deterministic modeling," in *Proceedings of the German Microwave Conference (GeMIC '08)*, Hamburg, Germany, March 2008, *European Microwave Journal*. In press.

[7] R. A. Valenzuela, S. Fortune, and J. Ling, "Indoor propagation prediction accuracy and speed versus number of reflections in image-based 3-D ray-tracing," in *Proceedings of the 48th IEEE Vehicular Technology Conference (VTC '98)*, vol. 1, pp. 539–543, Ottawa, Canada, May 1998.

[8] D. A. McNamara, C. W. I. Pistorius, and J. A. G. Malherbe, *Introduction to the Uniform Geometrical Theory of Diffraction*, Artech House, Boston, Mass, USA, 1990.

[9] F. Gil, A. R. Claro, J. M. Ferreira, C. Pardelinha, and L. M. Correia, "A 3D interpolation method for base-station-antenna radiation patterns," *IEEE Antennas and Propagation Magazine*, vol. 43, no. 2, pp. 132–137, 2001.

[10] R. M. Buehrer, A. Safaai-Jazi, W. Davis, and D. Sweeney, "Ultra-wideband propagation measurements and modeling," Final Report, DARPA NETEX Program, Virginia Technology, Blacksburg, Va, USA, January 2004.

[11] H. C. Rhim and O. Büyüköztürk, "Electromagnetic properties of concrete at microwave frequency range," *ACI Materials Journal*, vol. 95, no. 3, pp. 262–271, 1998.

[12] E. Damosso, Ed., "Digital mobile radio towards future generation systems," Cost 231 Final Report, European Commission, Bruxelles, Belgium, 1999, http://www.lx.it.pt/cost231/.

Hindawi Publishing Corporation
EURASIP Journal on Wireless Communications and Networking
Volume 2009, Article ID 308606, 13 pages
doi:10.1155/2009/308606

Research Article

Applying FDTD to the Coverage Prediction of WiMAX Femtocells

Alvaro Valcarce, Guillaume De La Roche, Álpar Jüttner, David López-Pérez, and Jie Zhang

Centre for Wireless Network Design (CWIND), University of Bedfordshire, D109 Park Square, Luton, Bedfordshire LU1 3JU, UK

Correspondence should be addressed to Alvaro Valcarce, alvaro.valcarce@beds.ac.uk

Received 28 July 2008; Revised 4 December 2008; Accepted 13 February 2009

Recommended by Michael A. Jensen

Femtocells, or home base stations, are a potential future solution for operators to increase indoor coverage and reduce network cost. In a real WiMAX femtocell deployment in residential areas covered by WiMAX macrocells, interference is very likely to occur both in the streets and certain indoor regions. Propagation models that take into account both the outdoor and indoor channel characteristics are thus necessary for the purpose of WiMAX network planning in the presence of femtocells. In this paper, the finite-difference time-domain (FDTD) method is adapted for the computation of radiowave propagation predictions at WiMAX frequencies. This model is particularly suitable for the study of hybrid indoor/outdoor scenarios and thus well adapted for the case of WiMAX femtocells in residential environments. Two optimization methods are proposed for the reduction of the FDTD simulation time: the reduction of the simulation frequency for problem simplification and a parallel graphics processing units (GPUs) implementation. The calibration of the model is then thoroughly described. First, the calibration of the absorbing boundary condition, necessary for proper coverage predictions, is presented. Then a calibration of the material parameters that minimizes the error function between simulation and real measurements is proposed. Finally, some mobile WiMAX system-level simulations that make use of the presented propagation model are presented to illustrate the applicability of the model for the study of femto- to macrointerference.

1. Introduction

The *finite-difference time-domain* (FDTD) [1] method for electromagnetic simulation is today one of the most efficient computational approximations to the Maxwell equations. Its accuracy has motivated several attempts to apply it to the prediction of radio coverage [2, 3], though one of the main limitations is still the fact that FDTD needs the implementation of a highly time-consuming algorithm. Furthermore, the deployment of metropolitan wireless networks in the last years has recently triggered the need for radio network planning tools that aid operators to design and optimize their wireless infrastructure. These tools rely on accurate descriptions of the underlying physical channel in order to perform trustworthy link- and system-level simulations with which to study the network performance. To increase the reliability of these tools, accurate radiowave propagation models are thus necessary.

Propagation models like ray tracing [4, 5] have been around already for some time. They have shown to be very accurate, as well as efficient from the computational point of view, except in environments like indoor where too many reflections need to be computed. In [6], a discrete model called Parflow has been proposed in the frequency domain, reducing a lot the complexity of the problem but bypassing the time-related information such as the delays of the different rays.

The FDTD model, which solves the Maxwell equations on a discrete spatial and temporal grid, can be also considered as a feasible alternative for this purpose. This method is attractive because all the propagation phenomena (reflections, diffractions, refractions, and transmission through different materials) are implicitly taken into account throughout its formulation. In [7], a hybridization of FDTD with a geometric model is proposed. In this approach, FDTD is applied only in small complex areas and combined with ray tracing for the more open space regions. Yet, the running time of such an approach is still too large to consider it for practical wireless networks planning and optimization. The evaluation of the FDTD equations at the frequencies of the

current and future wireless networks (UMTS, WiMAX, etc.) requires the use of extremely small spatial steps compared to the size of the obstacles within the scenario. In femtocell environments such as residential areas, this would lead to the use of matrices that require extremely large memory spaces, making infeasible its computation on standard off-the-shelf computers. In order to solve this issue, a reformulation of the problem at a lower frequency [8] is possible and necessary.

The main contribution of this paper is thus the introduction of a heuristics-based calibration approach that solves the lower-frequency approximation by directly matching the FDTD prediction to real WiMAX femtocell measurements. The outcome of this calibration procedure will be the properties of the materials that best resemble the recorded propagation conditions. These can be later reused for further simulations in similar scenarios and at the same frequency. Nevertheless, propagation models always perform better if a measurements-based calibration is carried out in situ [9]. Hence, the approach presented here can also be implemented in a coverage prediction tool and be subject to calibration with new measurements for increased accuracy of the FDTD model in a given scenario.

Over the last few years, the traditional central processing units (CPUs) have started to face the physical limits of their achievable processing speed. This has lead to the design of new processor architectures such as multicore and the specialization of the different parts of computers. On the other hand, programmable graphics hardware has shown an increase on its parallel computing capability of several orders of magnitude, leading to novel solutions to compute electromagnetics [10]. Graphics chipsets are becoming cheaper and more powerful, being their architecture well suited for the implementation of parallel algorithms. In [11], for instance, a ray-tracing GPU implementation has been proposed. FDTD is an iterative and parallel algorithm, being all the pixels updated simultaneously at each time iteration. This fact makes FDTD an extremely suitable method to be implemented on a parallel architecture [12]. By following the recently released *compute unified device architecture* (CUDA) [13], this paper presents an efficient GPU implementation of an FDTD model able to reduce further the computing time.

One final problem to address when dealing with FDTD is the proper configuration of the *absorbing boundary condition* (ABC). For efficiency reasons, the *convolutional perfectly matched layer* (CPML) is to be used. In order to provide the highest absorption coefficient for the problem of interest, adequate parameters must be chosen so a method for the calibration of the CPML parameters is presented.

2. WiMAX Femtocells

Due to the flexibility of its MAC and PHY layers and to the capability of supporting high data rates and *quality of service* (QoS) [14], *wireless interoperability for microwave access* (WiMAX) is considered one of the most suitable technologies for the future deployment of cellular networks.

On the other hand, *femtocell access points* (FAPs) are pointed out as the emerging solution, not only to solve indoor coverage problems, but also to reduce network cost and improve network capacity [15].

Femtocells are low-power base stations designed for indoor usage that have the objective of allowing cellular network service providers to extend indoor coverage where it is limited or unavailable. Femtocells provide radio coverage of a certain cellular network standard (GSM, UMTS, WiMAX, LTE, etc.) and they are connected to the service provider via a broadband connection, for example, digital subscriber line (DSL). These devices can also offer other advantages such as new applications or high indoor data rates, and thus reduced indoor call costs and savings of phone battery.

According to recent surveys [16], around 90% of the data services and 60% of the mobile phone calls take place in indoor environments. Scenarios such as homes or offices are the favorite locations of the users, and these areas will support most of the traffic in the following years. WiMAX femtocells appear thus as a good solution to improve indoor coverage and support higher data rates and QoS. Furthermore, there are already several companies involved in the manufacture [17] and deployment [18] of these OFDMA-based devices.

Since a massive deployment of femtocells is expected to occur as soon as of 2010, the impact of adding a new femtocell layer to the existing macrocell layer stills needs to be investigated. The number and position of the femtocells will be unknown, and hence a controlled deployment of macrocells throughout traditional network planning can no longer be a solution used by the operator to enhance the network performance. Therefore, a detailed analysis of the interference between both layers, femto and macro, and the development of self-configuring and self-healing algorithms and techniques for femtocells are needed. Due to this, accurate network link-level and system-level simulations will play an important role to study these scenarios before femtocells are widely deployed.

Since femto-macrocell deployments will take place in hybrid indoor/outdoor scenarios, propagation models able to perform well in both environments are required. On the one hand, empirical methods [19] such as Xia-Bertoni or COST231 Walfish-Ikegami are not suitable for this task because they are based on macrocell measurements and are specifically designed for outdoor environments. Ray tracing has shown excellent performance in outdoor scenarios but its computational requirements become too large [20] when they come to compute diffraction- and reflections-intense scenarios. For instance, in indoor environments this results in long computation times [21], forcing ray-based approaches to restrict the amount of reflections that are computed. The same happens in cases where the simulation of street canyons requires a large number of reflections. On the other hand, finite-difference methods such as FDTD are able of accounting for all of the field interactions as long as the simulation is run until the steady state and the grid resolution describes accurately the environment. Therefore, these methods appear as an appealing and accurate alternative [22] for the modeling of hybrid indoor/outdoor scenarios.

3. Optimal FDTD Implementation

Since femtocells are designed to be located indoors and have an effect only in the equipment premises and a small surrounding area, in the case of low-buildings residential areas, properly tuned bidimensional propagation models should be able to precisely predict the channel behavior. The problem under consideration (femtocells coverage prediction) can be thus restricted to the two-dimensional case. Considering typical femtocells antennas with a vertical polarization and following the terminology given in [23], the FDTD equations can be written in the TM_Z mode as follows:

$$\begin{aligned}
H_x|_{i,j+1/2}^{n+1} &= H_x|_{i,j+1/2}^{n} - D_b|_{i,j+1/2} \\
&\quad \cdot \left[\frac{E_z|_{i,j+1}^{n+1/2} - E_z|_{i,j}^{n+1/2}}{\Delta\kappa_{y_{j+1/2}}} + \Psi_{H_{x,y}}|_{i,j+1/2}^{n+1/2} \right], \\
H_y|_{i+1/2,j}^{n+1} &= H_y|_{i+1/2,j}^{n} + D_b|_{i+1/2,j} \\
&\quad \cdot \left[\frac{E_z|_{i+1,j}^{n+1/2} - E_z|_{i,j}^{n+1/2}}{\Delta\kappa_{x_{i+1/2}}} + \Psi_{H_{y,x}}|_{i+1/2,j}^{n+1/2} \right], \\
E_z|_{i,j}^{n+1/2} &= C_a|_{i,j} \cdot E_z|_{i,j}^{n-1/2} + C_b|_{i,j} \\
&\quad \cdot \left[\Psi_{E_{z,x}}|_{i,j}^{n} - \Psi_{E_{z,y}}|_{i,j}^{n} + \frac{H_y|_{i+1/2,j}^{n} - H_y|_{i-1/2,j}^{n}}{\Delta\kappa_{x_i}} \right. \\
&\quad \left. - \frac{H_x|_{i,j+1/2}^{n} - H_x|_{i,j-1/2}^{n}}{\Delta\kappa_{y_j}} \right],
\end{aligned} \tag{1}$$

where H is the magnetic field and E is the electrical field in a discrete grid sampled with a spatial step of Δ. D_b, C_a, and C_b are the update coefficients that depend on the properties of the different materials inside the environment. $\Psi_{H_{x,y}}$, $\Psi_{H_{y,x}}$, $\Psi_{E_{z,x}}$, and $\Psi_{E_{z,y}}$ are discrete variables with nonzero values only in some CPML regions and are necessary to implement the absorbing boundary.

However, the propagation of TM_Z cylindrical waves in 2D FDTD simulations is by nature different from the 3D case. In order to minimize the error caused by this approximation, the current model is calibrated using femtocell measurements recorded in a real environment (see Section 5). This guarantees that the final simulation result resembles the real propagation conditions as faithfully as possible. It is also to be noticed that femtocell antennas are omnidirectional in the horizontal plane, emitting thus much less energy in the vertical direction. Moreover, in residential environments containing houses with a maximum of two floors, the main propagation phenomena occur in the horizontal plane. That is why restricting the prediction to the 2D case is only acceptable for this or similar cases, and not appropriate for constructions with bigger open spaces such as airports, train stations, or shopping centers.

From the computational point of view, restricting the problem to the 2D case is still not enough to achieve timely results for the study of femtocells deployments and their influence into the macrocell network. FDTD is very computationally demanding and therefore a specific implementation must be developed. The main purpose of this section is thus to present two techniques that aid to solve the scenario within reasonable execution times. The first technique reduces the complexity of the problem by increasing the spatial step used to sample the scenario, that is, it chooses a simulation frequency lower than that of the real system. The second technique presents a programming model that optimizes memory access for implementations in standard graphics cards.

3.1. Lower-Frequency Approximation and Model Calibration. The running time of the FDTD method depends, among other things, on the number of time iterations required to reach the steady state, that is, the stable state of the coverage simulation. To summarize, this number of iterations depends on the following.

(i) The number of obstacles inside the environment under consideration: the more the walls are, the more reflective and diffractive effects that will occur.

(ii) The size of the environment in FDTD cells: a larger environment will need more iterations for the signal to reach all the cells of the scenario.

In order to accurately describe the environment, the number of obstacles should not be reduced. It is thus interesting to try to reduce the size of the problem, which can be achieved by using a larger spatial step Δ. To describe the simulation scenario, Δ must also be small compared to the size of the obstacles. Furthermore, to avoid dispersion of the numerical waves within the Yee lattice, the spatial step also needs to be several times smaller than the smallest wavelength to be simulated [24]. For example, an $f_{\mathrm{real}} = 3.5\,\mathrm{GHz}$ WiMAX simulation would require a spatial step smaller than $\lambda = 8.5\,\mathrm{cm}$ according to

$$\Delta = \frac{\lambda}{N_\lambda}. \tag{2}$$

Numerical dispersion in 2D FDTD simulations causes anisotropy of the propagation in the spatial grid. However, these effects can be reduced if a fine enough spatial grid is used. It is shown in [25] that with $N_\lambda = 10$, the velocity-anisotropy error is $\Delta v_{\mathrm{aniso}} \approx 0.9\%$, introducing thus a distortion of about 9 cells for every 1000 propagated cells. However, these errors become meaningless after the calibration procedure introduced in Section 5.3, which corrects the power distribution so that it resembles the real propagation case according to the recorded measurements.

A scenario for the study of femto-to-macro interference has a typical size of around 100×100 meters so sampling the scenario with $\Delta = 0.85\,\mathrm{cm}$ is not feasible in terms of computer implementation. A frequency reduction is thus necessary [26] to cope with memory and computational restrictions. This frequency reduction comes obviously at a cost because the reflections, refractions, transmissions, and diffractions behave differently depending on the frequency. Since the physical properties of the different materials are frequency dependent, reflections, refractions and transmissions through materials will vary. To overcome this problem,

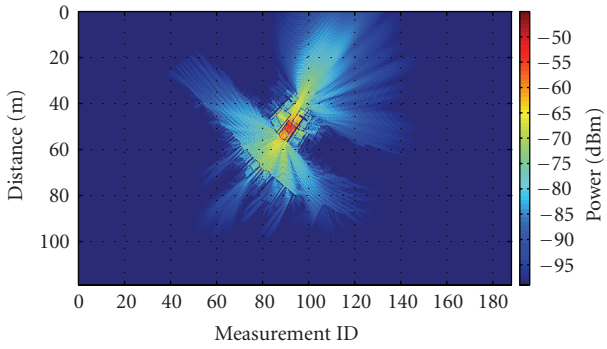

Figure 1: Example of a calibrated femtocell coverage prediction subject to diffraction errors due to lower-frequency FDTD simulation.

the approach presented here consists on performing a calibration of such parameters. This calibration, based on real measurements, will find values for the materials parameters in order to model, at a lower frequency, their behavior at the real frequency. This search is performed by minimizing the *root mean square error* (RMSE) between simulation and measurements, and the details of such a method are described in Section 5.3.

The effects of simulating with a lower frequency for WiMAX at 3.5 GHz have been already studied in [8], where it was shown that even after calibration, the predictions are still subject to an error due to diffractive effects. Nevertheless, it is well known that reflections dominate over diffractions in indoor environments, and the main power leakage of the femtocell from indoor to outdoor occurs by means of transmissions through wooden doors and glass windows (see Figure 1). Furthermore, in streets like the one shown in the current scenario, canyon effects caused by reflections are the main propagation phenomenon so it is clear that diffraction is not a significant propagation means in femtocell environments.

Additionally, it was shown in [8] that the absolute value of the error due to diffraction is limited and that the overall error of the simulation will depend only on the number of diffractive obstacles. In Section 5.4 a postprocessing filter is proposed as a means to reduce the fading errors due to this phenomenon. For comparative purposes, an unfiltered lower-frequency prediction is shown in Figure 1. The more accurate postprocessed prediction is explained later and displayed in Figure 9.

3.2. Parallel Implementation on GPU. If the previously described simplification reduces the size of the environment to simulate, the focus of this section is to present an implementation of the algorithm that reduces further the simulation time. In wireless networks planning and optimization, the aim is to run several system-level simulations to test hundreds of combinations of parameters for each base station. This implies that several base stations (emitting sources) must be simulated. It is thus necessary to reach simulation times on the order of seconds for each source. In order to reach this objective and since each cell of an FDTD environment performs similar computation (update of the cell own field values taking into account the neighboring cells), an approach is the use of parallel multithreaded computing.

The implementation of finite-difference algorithms on parallel architectures such as *field-programmable gate-arrays* (FPGAs) [27] and graphics processing units [28] has been recently highly regarded by the FDTD community. For instance, speeds of up to 75 Mcps(mega cells per second) have been claimed [29] for a 2D implementation in an FPGA. However, FPGAs are costly devices whose use is not as common as that of GPUs, which are present today in almost every personal computer. Therefore, the interest on programmable graphics hardware has increased and some solutions are already being proposed [10] as a feasible means of achieving shorter computation times for this type of algorithms.

By programming an *NVIDIA* GPU device with the new CUDA architecture [13], a 2D-FDTD algorithm has been implemented. With this technology, it is not necessary to be familiarized with the graphics pipeline and only some parallel programming and C language knowledge are necessary to exploit the properties of the GPU. This reduces the learning curve for scientists interested in quickly testing their parallel algorithms, while eliminating the redundancy of *general purpose computing on GPU* (GPGPU) code based on graphics libraries such as OpenGL.

The number of *single instruction, multiple thread* (SIMT) multiprocessors in each GPU varies between different cards, and each multiprocessor is able to execute a block of parallel threads by dividing them into groups named *warps*. Depending on the features (memory and processing capability) of a given multiprocessor, a certain number of threads will be executed parallely. It is thus important to balance the amount of memory that a thread will use, otherwise the memory could be fully occupied by less threads than the maximum allowed by the multiprocessor. It is in the programmer best interest to maximize the number of threads to be executed simultaneously [30]. Therefore and to maximize the multiprocessor occupancy, five different types of kernels (GPU programs) have been designed to compute different parts of the scenario as shown in Figure 2. The central area is the computational domain containing the scenario that needs to be simulated. Meanwhile, the other four areas represent the four absorbing boundary regions at the limits of the environment.

To compare the performance of such an implementation with traditional nonparallel approaches, the simulation of a 1200×1700 pixels scenario has been tested under three different platforms. 3000 iterations were required to reach the steady state in this environment. MATLAB, which makes use of the AMD core math library (ACML) and is thus very optimized for matrices computation, is used as the nonparallel reference. Then a standard laptop graphics card (GeForce 8600M GT) and a high-performance computing card (TESLA C870) are tested. The main differences between these two cards are the number of multiprocessors (4 and 32) and the card memory (256 MB and 1.5 GB). The different performance results can be checked in Table 1.

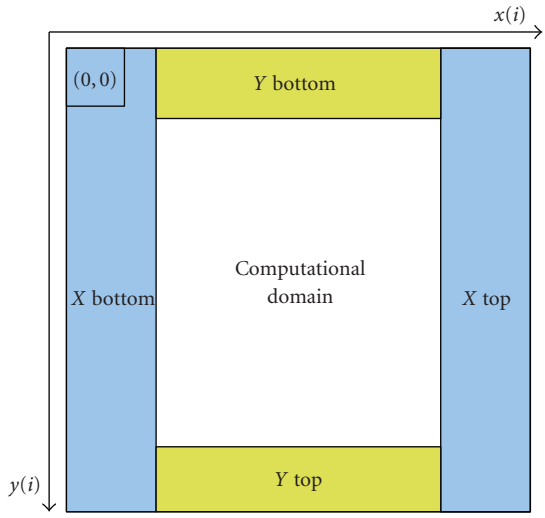

Figure 2: Fragmentation of the simulation scenario for independent kernels execution.

Table 1: Performance of the algorithm running on different platforms when computing three thousand iterations of a scenario of size 1200×1700.

	MATLAB	GF 8600M GT	TESLA C870
Running time:	72 min	43 s	8 s
Usable speed:	1.42 Mcps	142.24 Mcps	764.55 Mcps
Gross speed:	1.48 Mcps	148.79 Mcps	799.72 Mcps

The achieved running time (8 seconds) for a complete radio coverage can be considered as a reasonably quick propagation prediction, fulfilling thus the requirements in terms of speed for wireless network planning in the presence of randomly distributed femtocells. This way, a high number of network configurations can be tested within acceptable times by the operator.

4. Calibration of the Absorbing Boundary Condition

FDTD is a precise method for performing field predictions in small environments and it has been widely applied in several areas of the industry, such as the simulation of microwave circuits or antennas design. But during many years, the computation of precise solutions in unbounded scenarios remained a great challenge.

In 1994 Berenger introduced the *perfectly matched layer* (PML) [31], an efficient numerical absorbing material matched to waves of whatever angle of incidence. The next improvement of this method occurred in 2000, when Roden and Gedney presented a more efficient implementation called *convolutional perfectly matched layer* (CPML) [32], which has since been one of the better regarded choices for this purpose.

However, the CPML must be carefully configured in order to properly exploit its full potential. The absorptive properties of the CPML depend mainly on the wave k-vector, which is a function of the type of source being used, and it will therefore present different reflection coefficients for simulations performed at different frequencies. A proper selection of parameters is thus necessary.

An error function based on the reflection error of the CPML is presented next, as well as a continuous optimization approach to find its minimum in the solutions space formed by the CPML parameters.

4.1. The CPML Error Function

4.1.1. The Optimization Parameters. The CPML method maps the Maxwell equations into a complex stretched-coordinate space by making use of the *complex frequency-shifted* (CFS) tensor

$$s_w = \kappa_w + \frac{\sigma_w}{a_w + j\omega\varepsilon_0}, \quad w = x, y, z, \tag{3}$$

where, following the notation of [24], w indicates the direction of the tensor coefficient.

In order to avoid reflections between the *computational domain* (CD) and the CPML boundary due to the discontinuity of s_w, the losses of the CPML must be zero at the CD interface. These losses are then gradually increased [31] in an orthogonal direction from the CD interface to the outer *perfect electric conductor* (PEC) boundary. A polynomial grading of a_w, κ_w, and σ_w has shown [24] to be quite efficient for this task:

$$\begin{aligned} a_w(w) &= a_{w,\max}\left(\frac{d-w}{d}\right)^{m_a}, \\ \kappa_w(w) &= 1 + (\kappa_{w,\max} - 1)\left(\frac{w}{d}\right)^{m}, \\ \sigma_w(w) &= \left(\frac{w}{d}\right)^{m}\sigma_{w,\max}, \end{aligned} \tag{4}$$

where d is the depth of the CPML, m and m_a are the grading orders. An approximate optimal $\sigma_{w,\max}$ can also be estimated to outcome a given reflection error $R(0)$ with

$$\sigma_{w,\text{opt}} = -\frac{(m+1)\ln[R(0)]}{2\eta d}, \tag{5}$$

where η is the impedance of the background material [24].

However, which precise values of $a_{\max}$, $\kappa_{\max}$, and $\sigma_{\max}$ to choose for a specific FDTD simulation remains an open question. The solution to this problem is thus the combination of parameters that configures the most absorbing CPML for a given source and number of FDTD time steps. Since the optimal value of $\sigma_{\max}$ is close to (5), the factor $F_\sigma = \sigma_{\max}/\sigma_{w,\text{opt}}$ can be defined for notation simplicity and be subject to the optimization process. The intervals to search for the optimal solution when using a continuous soft source are presented in Table 2 and can be defined as

$$\begin{aligned} a_{\max} &\in [a^1_{\max}, a^2_{\max}], \\ \kappa_{\max} &\in [\kappa^1_{\max}, \kappa^2_{\max}], \\ F_\sigma &\in [F^1_\sigma, F^2_\sigma]. \end{aligned} \tag{6}$$

Table 2: Typical properties of the search parameters.

	Range	Precision	n
$a_{\max}$	$[0, 0.5]$	0.0001	20
$\kappa_{\max}$	$[1, 50]$	0.1	15
F_σ	$[0.5, 1.5]$	0.01	12

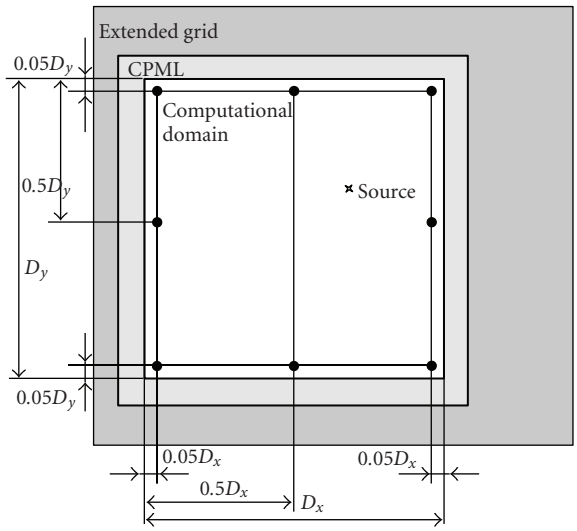

Figure 3: Sounding points in a 2D grid of size (D_x, D_y). The depth of the extended grid in each direction varies depending on the position of the source.

4.1.2. The Error Function. This section presents CPML calibration results for 2D TM_Z simulations where the electrical field E_z is the output magnitude from each FDTD simulation. In order to evaluate a given solution we compare it to a reference simulation that is free of reflections at the border. This reference simulation must be computed [24] using a grid large enough to avoid that reflections bounce back into the computational domain. As long as the FDTD simulation is implemented with first-order derivatives, a wavefront can only advance one cell per time step. In order to construct the extended grid in this case, the number of cells that must be added to the original grid in each direction can be thus calculated by simply considering the number of FDTD steps and the position of the source (see Figure 3).

To assess the optimal CPML configuration, it is necessary to analyze the time evolution of the simulated grid. For the sake of efficiency and to provide a reasonable estimation of the behavior of the CPML, the grid will be *sounded* only at certain key points. The highest reflection error occurs typically near the borders and corners of the CD so a homogeneous selection of sounding points is that shown in Figure 3.

The output of the reference simulation will therefore be the value of the electrical field $E_{z_{\text{ref}}}|^n_{i_p,j_p}$ at each sounding point p with coordinates (i_p, j_p) and at time step n. Defining similarly the output of each optimization simulation as $E_z|^n_{i_p,j_p}$, the relative error for the same sounding point and at the same time step is

$$\varepsilon_{\text{rel}}|^n_{i_p,j_p} = \left| \frac{E_z|^n_{i_p,j_p} - E_{z_{\text{ref}}}|^n_{i_p,j_p}}{\max_n \{E_{z_{\text{ref}}}|^n_{i_p,j_p}\}} \right|. \tag{7}$$

Each optimization simulation performs N FDTD time steps. Therefore to obtain an indicator of the relative error value over the time, the RMS relative error is computed for each sounding point:

$$\varepsilon_{\text{rel}_{\text{RMS}}}|_{i_p,j_p} = \sqrt{\frac{1}{N}\sum_{n=0}^{N-1} \left(\varepsilon_{\text{rel}}|^n_{i_p,j_p}\right)^2}. \tag{8}$$

Finally, and in order to obtain a general indicator of the error for the whole scenario, the average value of (8) for all the sounding points is to be computed. The error function for a given combination of parameters can be thus defined as

$$\text{error}(a_{\max}, \kappa_{\max}, F_\sigma) = \frac{1}{N_p}\sum_{p=0}^{N_p-1} \varepsilon_{\text{rel}_{\text{RMS}}}|_{i_p,j_p}. \tag{9}$$

Numerical experiments have shown that (9) does not vary much by adding more sounding points. $N_p = 8$ represents therefore a good compromise between sounding efficiency and reliability of the error function.

4.2. The Calibration Process

4.2.1. The Optimization Algorithm. The objective of this section is to present a method to compute the combination of $(a_{\max}, \kappa_{\max}, F_{\sigma_{\max}})$ that minimizes (9). Several tests indicate that (9) is unimodal along the $a_{\max}$, $\kappa_{\max}$, and F_σ dimensions, that is, (9) has only one minimum in the region given by (6). In order to find the optimum without evaluating the error function at a large number of candidate solutions, a smarter approach can be applied by minimizing (9) along each dimension sequentially and independently. Algorithm 1 presents this approach, being the stop condition the location of a satisfactory minimum lower than ϵ or the evaluation of a maximum number $n_{\max}$ of iterations.

In order to find the minimum of the error function for each dimension of the space of solutions, it is necessary to evaluate (9) at several positions within the search intervals (6). Each of these evaluations needs to perform an FDTD simulation, which is the most time-consuming part of the algorithm. To minimize these, a Fibonacci search algorithm [33] is to be used. This algorithm narrows down the search interval by sequentially evaluating the error function at two positions within the interval and reusing one of these evaluations in the next step. Therefore only one function evaluation is necessary at each step. Table 2 contains the precision achieved for the example intervals and the required length n of the Fibonacci sequence for each parameter.

4.3. ABC Calibration Results. Figure 4 presents a contour plot of the error function described by (9). The function

$\kappa_{\max,\text{opt}} \Leftarrow U(\kappa^1_{\max}, \kappa^2_{\max})$
$F_{\sigma,\text{opt}} \Leftarrow U(F^1_\sigma, F^2_\sigma)$
$n \Leftarrow 1$
$\text{error}_n \Leftarrow \epsilon$
while $\text{error}_n \geq \epsilon$ and $n \leq n_{\max}$ **do**
  $a_{\max,\text{opt}} \Leftarrow \arg\min_{a_{\max}} \{\text{error}(a_{\max}, \kappa_{\max,\text{opt}}, F_{\sigma,\text{opt}})\}$
  $\kappa_{\max,\text{opt}} \Leftarrow \arg\min_{\kappa_{\max}} \{\text{error}(a_{\max,\text{opt}}, \kappa_{\max}, F_{\sigma,\text{opt}})\}$
  $F_{\sigma,\text{opt}} \Leftarrow \arg\min_{F_\sigma} \{\text{error}(a_{\max,\text{opt}}, \kappa_{\max,\text{opt}}, F_\sigma)\}$
  $\text{error}_n = \text{error}(a_{\max,\text{opt}}, \kappa_{\max,\text{opt}}, F_{\sigma,\text{opt}})$
  $n++$
end while

Algorithm 1: Minimization of the error function by means of coordinatewise minimization subroutines.

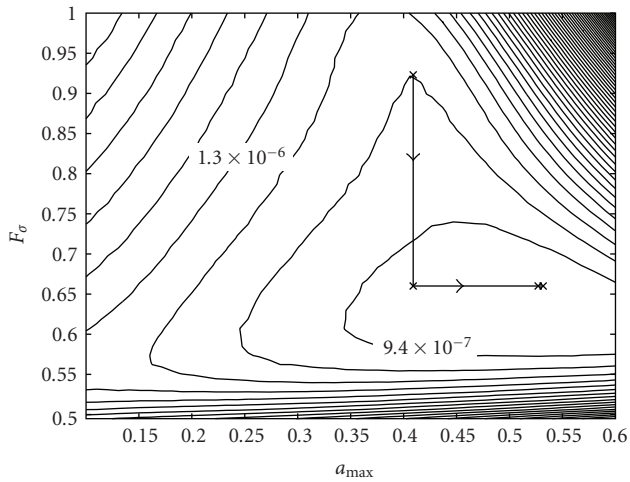

Figure 4: Contour plot of the error function with $\kappa_{\max,\text{opt}} \approx 1.06$ for a modulated Gaussian pulse of width 0.4 nanosecond and an oscillating frequency of 3.5 GHz. The graph also shows the solutions found by Algorithm 1 and the evolution until the optimum.

values were obtained by computing the error at 2500 different locations of the 2D space of solutions given by $(a_{\max}, F_\sigma)$ for the optimal value of $\kappa_{\max}$. The size of the FDTD scenario for this example is of 256×256 cells with the source located at the coordinates $(i_s, j_s) = (128, 128)$ and being the spatial and time steps 8.6 mm and 10.5 picoseconds, respectively. The CPML has a depth of 16 cells and a total of $N = 800$ FDTD time steps were performed to compute each value of the error function. The applied source was a Gaussian pulse with a temporal width of 400 picoseconds and modulated with a sinusoidal frequency of 3.5 GHz, which is the frequency of WiMAX in Europe.

Figure 4 also displays the error points found at each iteration of Algorithm 1 after minimizing in the $a_{\max}$ and F_σ dimensions. In this example, F_σ is initialized with a random value within its range and the optimal solution is reached in just 3 iterations. Without fixing $\kappa_{\max}$ and optimizing in all three dimensions, the minimum is reached in only 4

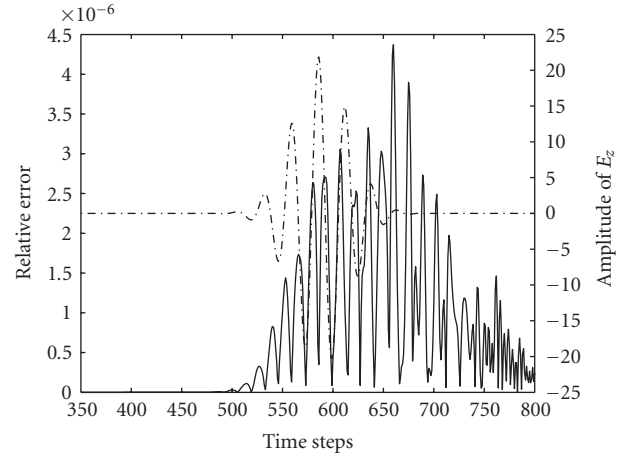

Figure 5: Time evolution of the relative error (solid line) at the upper left point (see Figure 3). The dash-dotted line is the value of the electrical field at the same sounding point.

iterations. But clearly the number N_{FDTD} of required FDTD simulations is much greater and can be calculated by

$$N_{\text{FDTD}} = 4 \cdot \left[(n_{a_{\max}} - 2) + (n_{\kappa_{\max}} - 2) + (n_{F_\sigma} - 2) \right]. \quad (10)$$

To obtain, for instance, the precision shown in Table 2, N_{FDTD} accounts for a total of 164 simulations. Using the previously mentioned parallel computing architecture, these can be computed in less than 2 minutes on a laptop graphics card.

Once the algorithm has converged, the quality of the solution can be tested by computing an FDTD simulation using the obtained CPML calibration parameters. Figure 5 presents the change over time of the relative error at a corner point in the scenario described by Figure 3. It is clear in this example that the relative error never exceeds $5 \cdot 10^{-6}$, yielding thus an excellent absorption coefficient.

5. Calibration of the Propagation Model

In FDTD, the parameters that define each material and therefore play an active role in the final simulation result are three:

(i) relative electrical permittivity ε_r;

(ii) relative magnetic permeability μ_r;

(iii) electrical conductivity σ.

Due to the 2D and lower-frequency simplifications applied to this model, it should not be expected that the values of the materials parameters at the real frequency perform the same as at the simulation frequency. The correct values of these parameters must be therefore chosen carefully in order for the simulation result to resemble faithfully the reality. As advanced in Section 3.1, this can be achieved by using real coverage measurements to find the proper combination of parameters that better match the prediction to the measurements.

Table 3: Main parameters of experimental femtocell.

EIRP	12 dBm
Center frequency	3.5 GHz
Transmitter height	77 cm
Vertical Beamwidth	9°
Tilt	0°

5.1. Coverage Measurements. In order to measure the accuracy of the presented model, a measurements campaign has been performed. The chosen scenario was a residential area with two-floor houses in a medium-size British town. The femtocell excitation is an oscillatory source implemented on a vector signal generator and configured as shown in Table 3. The emitting antennae are omnidirectional in the azimuth plane with a gain of 11 dBi in the direction of maximum radiation.

Since one of the main objectives of this work is to introduce a propagation model for the study of interference scenarios in femtocells deployments, the measurements have been performed mainly outdoors. This way, the indoor-to-outdoor propagation case, proper of femto-to-macro interference scenarios, is characterized. Figure 6 shows the collected power data laid over a map of the scenario under study.

5.1.1. Measurements Postprocessing. Raw power measurements are not yet useful for the calibration of a finite-difference propagation model. The data must first undergo a postprocessing phase during which outliers will be removed. Such postprocessing is detailed next.

Removal of Location Outliers. The location of the outdoor measurement points has been obtained using GPS coordinates but these coordinates are sometimes subject to errors. At this stage every measurement matching the next properties must be removed: out of range GPS coordinates, coordinates inside of a building, no GPS coverage or coordinates outside of the scenario.

Removal of Noise Bins. In areas of low coverage, it is possible that the measured signal becomes indistinguishable from the background noise. Those measurements are thus also classified as outliers. In order to clearly distinguish signal from noise, a large recording of the noise in the examined frequency band and location area has been performed. This way, the noise has been found to follow an approximate normal distribution with mean of $\overline{N} = -132$ dBm and a standard deviation of $\sigma_N = 3.2$ dB. Any measurement value that falls within a $2\sigma_N$ range of $\overline{N}$ is thus considered to be an outlier.

Spatial Filtering. The used source is a narrowband frequency pulse. Therefore, the collected measurements are also subject to narrowband fading effects which are usually modelled using random processes. In order for these measurements to be useful for the calibration of deterministic models, the randomness due to fading needs to be removed. Hence, a spatial filtering of the measurements has been applied by following the 40-Lambda averaging criterion [34]. The final state of the measurements is shown in Figure 7.

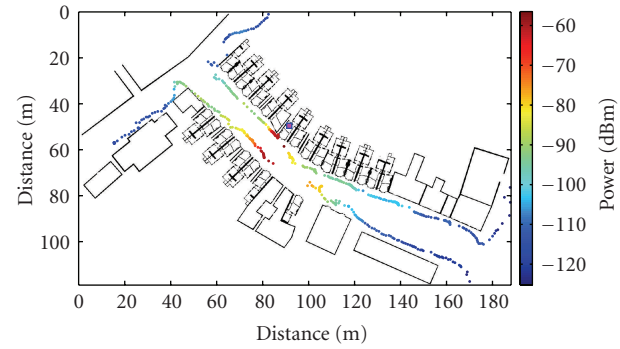

Figure 6: Power measurements and simulation scenario. The location of the transmitter is marked with a magenta square.

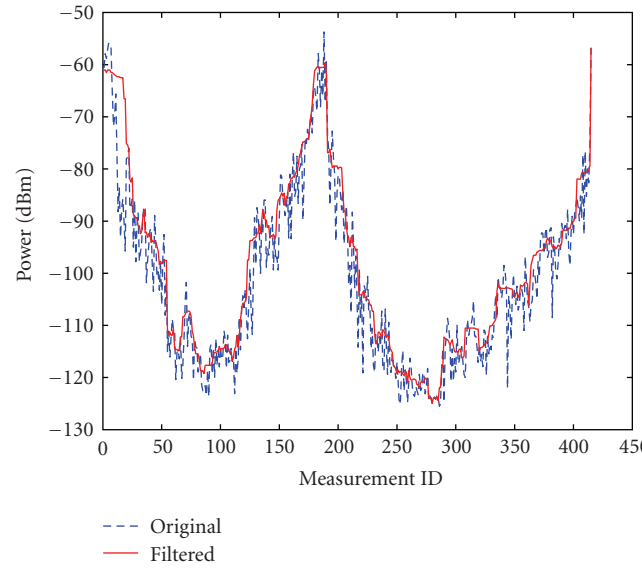

Figure 7: Power measurements after postprocessing.

5.2. The Materials Error Function. The objective of the model tuning is to configure the materials involved in the FDTD simulation so that they show in the computational domain a similar behavior to the reality. If $(\varepsilon_{r_m}, \mu_{r_m}, \sigma_m)$ represents the properties of material m, a solution s to a problem involving N_m materials is thus $\Omega^s_{N_m}$:

$$\Omega^s_{N_m} = \bigcup_{m=1}^{N_m} (\varepsilon_{r_m}, \mu_{r_m}, \sigma_m). \tag{11}$$

Each measurement point p (with $p \in [0, N_p - 1]$ and N_p the number of points) is assigned a measured power value P_{mes_p}. Similarly and for an FDTD prediction calibrated with $\Omega^s_{N_m}$ the same point can be assigned a predicted power value

$P^s_{\text{pred}_p}$. The error of the prediction at point p can be then expressed as

$$E^s_p = P_{\text{mes}_p} - P^s_{\text{pred}_p}, \tag{12}$$

being $\text{ME}^s = \overline{E^s_p}$ the mean error of all N_p points, which can also be interpreted as the offset between the measurements and the predictions. Once the model is calibrated, the tuned mean error ME^t is computed. Then the ME of any other prediction can be greatly reduced by simply adding ME^t to the predictions.

The root mean square error is often used as a good estimate of the accuracy of a propagation model. The RMSE will hence be the error function subject to minimization. For an FDTD configuration $\Omega^s_{N_m}$, the RMSE can be thus computed as

$$\text{RMSE}(\Omega^s_{N_m}) = \sqrt{\frac{1}{N_p}\sum_{p=0}^{N_p-1}|E^s_p|^2}. \tag{13}$$

5.3. Metaheuristics-Based Calibration. Once the error function has been defined, a brute-force approach to find an optimal solution to the problem could be, for instance, to test all possible $\Omega^s_{N_m}$ until a solution that minimizes (13) is found. Since the properties of the materials are all real, the space of solutions for $\Omega^s_{N_m}$ is infinite and a smarter approach is needed. In this work, a meta-heuristics optimization algorithm is proposed as a feasible way of searching the space of solutions. The algorithm applied here is *simulated annealing*, though the same concept also applies to other heuristic algorithms, as long as they are properly configured.

Simulated Annealing (SA) [35] is an optimization algorithm based on the physical technique of *annealing*, widely used in metallurgy. From the point of view of the minimization of an error function, SA works by setting the state of the system to a solution $\Omega^s_{N_m}$, and evaluating neighbor solutions $\Omega^{s'}_{N_m}$ to try to find a better one ($\text{RMSE}(\Omega^{s'}_{N_m}) < \text{RMSE}(\Omega^s_{N_m})$). If a better solution is found, then the current state of the system is updated to the new solution $\Omega^{s'}_{N_m}$. If, however, a worst solution is found, the state of the system is set to this new neighbor solution with probability P. P is called the *acceptance probability function* (APF) and it is a function of $\text{RMSE}(\Omega^s_{N_m})$, $\text{RMSE}(\Omega^{s'}_{N_m})$, and a variable T called the temperature that is progressively decreased as the calibration progresses. The acceptance probability function must meet certain requirements in order to accept better solutions than the current state and worst solutions when the temperature is high, that is, at the beginning of the calibration process. A simple APF that follows these criteria is

$$P(\Omega^s_{N_m}, \Omega^{s'}_{N_m}, T) = e^{(\text{RMSE}(\Omega^s_{N_m}) - \text{RMSE}(\Omega^{s'}_{N_m}))/T}, \tag{14}$$

but the user of SA is free to choose any APF to its convenience.

The way the temperature T is decreased is also subject to many implementations. In this paper, the value of the temperature at each stage k is obtained as follows:

$$T_k = f * T_{k-1}, \tag{15}$$

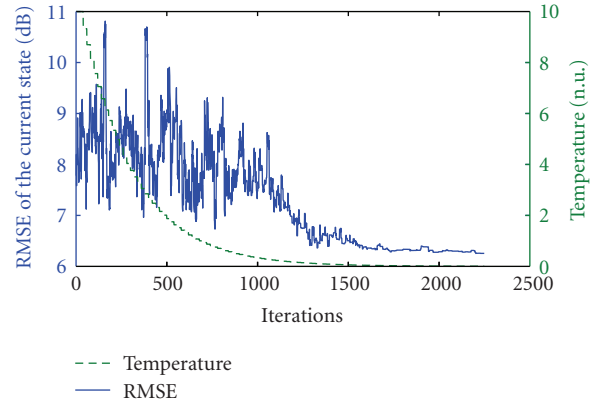

Figure 8: Evolution of the RMSE of the FDTD prediction when choosing the materials parameters using simulated annealing. The temperature is expressed in natural units, $T_1 = 10$ and $f = 0.9326$.

with $k \in [2, L_T]$ and L_T is the number of different temperature levels. f is called the annealing factor and it is related to the rate with which the temperature decreases from one stage to the next one.

The evolution of the state of the system by means of SA is displayed in Figure 8, as well as the evolution of the temperature. For this calibration, $L_T = 100$ different levels of temperature have been defined and the system is let free to test $N_T = 20$ different neighbors at each temperature level. This way, the physical process of annealing is resembled much more faithfully than if the temperature was decreased at each SA iteration. The idea behind this is to allow the system to perform a deeper search at each temperature level before decreasing its chances of escaping local minima.

The way neighbor solutions are chosen can also be decided freely by the user. Since the purpose here is to find the optimal values of different materials, only one material is modified at each stage. Furthermore, only one parameter of this material is modified. This way, a local search in the very neighborhood of the current state is guaranteed.

The calibration displayed in Figure 8 is performed using the measurements and scenario shown in Figure 6. For this scenario and according to the most commonly used construction materials in the United Kingdom, five different materials have been assumed: air as the background material, plaster for the inner walls, wood for the doors and furniture, glass for the windows, and brick for the houses outer walls. The final values of the parameters for these materials after the calibration are shown in Table 4. The electrical conductivity σ is expressed in $S \cdot m^{-1}$ and the refraction index n, computed as $n = \sqrt{\varepsilon_r \cdot \mu_r}$, is provided as reference.

5.4. Fading Removal Filter. The spatial step for this calibration is $\Delta = 12\,\text{cm}$ with $N_\lambda = 10$ for good isotropic propagation, yielding thus a wavelength of $\lambda = 1.2\,\text{m}$. This means that the simulation frequency is approximately $f_{\text{sim}} = 250\,\text{MHz}$, while the real frequency of the WiMAX

Table 4: Calibrated parameters of the materials at 3.5 GHz.

	ε_r	μ_r	σ	n
Air	1.8824	0.7280	$7.2273 \cdot 10^{-4}$	1.1706
Plaster	1.1182	1.2779	0.0196	1.1954
Wood	1.7522	0.2802	0.0440	0.7007
Glass	5.1358	1.2516	0.0045	2.5353
Brick	3.5789	7.661	0.0014	5.2390

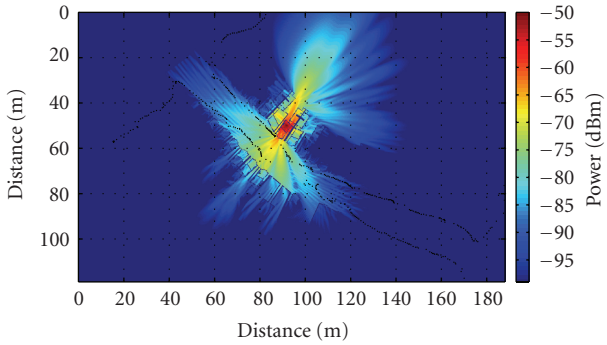

Figure 9: Filtered coverage prediction of a WiMAX femtocell with a 3.5 GHz measurements-based calibrated FDTD model.

measurements is $f_{\text{real}} = 3.5$ GHz. Following the terminology presented in [8], the frequency reduction factor is defined as

$$\text{FRF} = \frac{f_{\text{sim}}}{f_{\text{real}}}, \tag{16}$$

which has in this case a value of FRF $\approx$ 0.071. Due to the reasons expressed in Section 3.1, a prediction performed with the final calibration results of Table 4 is still subject to errors at diffracting obstacles. Such an error is limited and can be easily evaluated for each obstacle with

$$\nu_{\text{sim}} = \sqrt{\text{FRF}}\nu_{\text{real}},$$
$$E = 20 \log\left(\frac{\sqrt{(\nu_{\text{real}} - 0.1)^2 + 1} + \nu_{\text{real}} - 0.1}{\sqrt{(\nu_{\text{sim}} - 0.1)^2 + 1} + \nu_{\text{sim}} - 0.1}\right), \tag{17}$$

where ν is a geometrical parameter that depends on the specific disposition of the scenario (see [36] for details).

Since diffraction introduces wrong fading effects, a spatial (2D) average moving filter has been applied as a postprocessing method to reduce the impact of the frequency reduction. A decrease of up to 0.33 dB has been observed in the value of the RMSE, and up to 3 dB in macrocell-calibrated models. A coverage prediction performed by the calibrated FDTD model and postprocessing filter is shown in Figure 9 along with the measurements used for the calibration.

After the postprocessing filter, the final obtained RMSE is of 6 dB and a comparison between the FDTD predictions and the measurements is displayed in Figure 10.

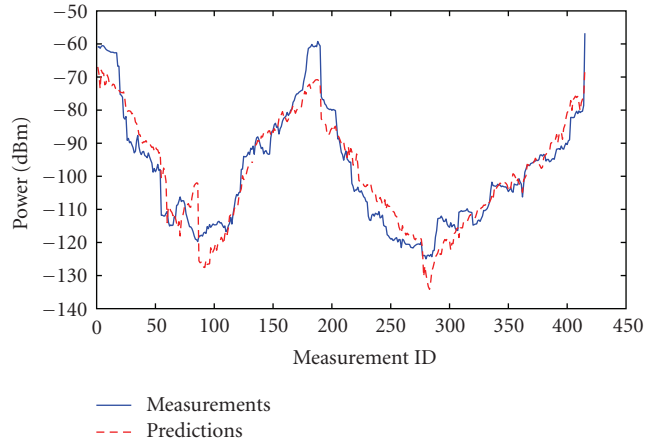

Figure 10: Comparison between the FDTD predictions and the measurements at 3.5 GHz. RMSE = 6 dB.

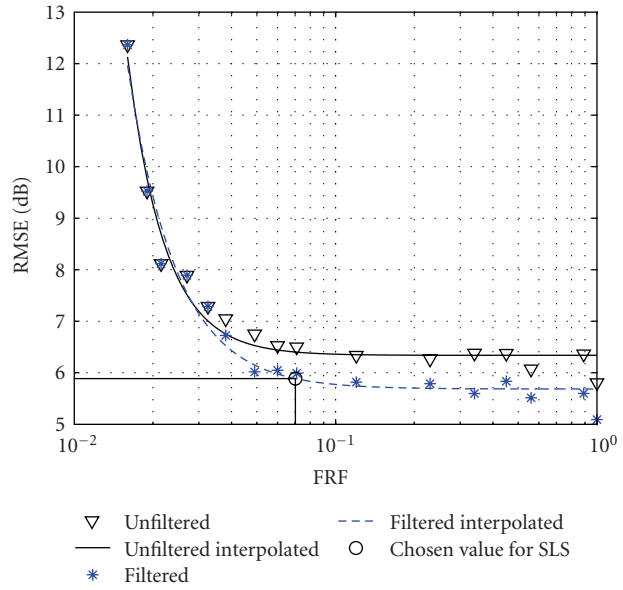

Figure 11: Evolution of the RMSE after calibration, with respect to the frequency reduction factor (FRF).

5.5. Accuracy Validation. Finally, in order to assess the accuracy of the FDTD propagation model, calibrations have been performed at the real and several lower frequencies. The analyzed range of simulated frequencies comprises values of $\text{FRF}|_{f_{\text{real}}=3.5\,\text{GHz}}$ between 10^{-2} and 1, being displayed in Figure 11 the errors of the simulations after calibration. From this figure it is also clear how the filtering introduced in the previous section contributes to the reduction of the RMSE.

Furthermore, the data also shows that proper lower-frequency calibrations of the model are able to reach performances close to that of the true frequency. However, the simulation frequency should not be reduced indefinitely. This is because of the increase in the size of the spatial

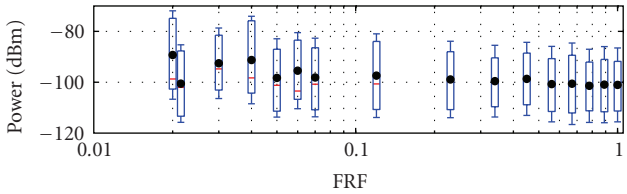

Figure 12: Dependence of the power distribution with respect to the frequency reduction factor (FRF).

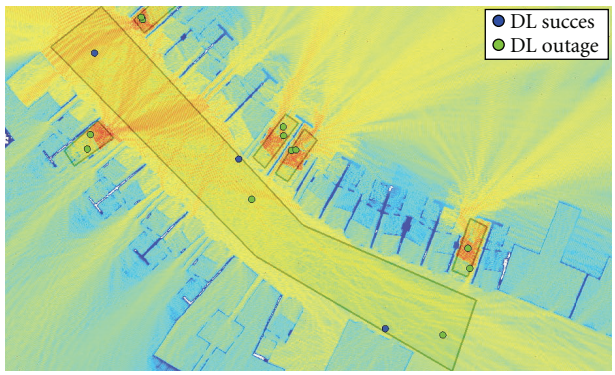

Figure 13: WiMAX system-level simulation in a hybrid femtocell/macrocell scenario.

step as f_{sim} decreases. If Δ becomes too large, the spatial resolution might not be enough to accurately describe the simulation scenario and the diffraction phenomena, bypassing some features of the environment. As a consequence of this, the error grows quickly and reaches values that could be achieved with simpler propagation models. Therefore, a compromise between the computational complexity and the model accuracy must be achieved. For the scenario under consideration, Figure 11 shows that a value of FRF $\approx$ 0.071 has been chosen. This value, located in the elbow of the RMSE curve guarantees a low error without compromising the execution time and is used in Section 6 to perform system-level simulations of WiMAX femtocells.

In order to examine the achievable accuracy in the overall scenario, a different measurements route has also been used to test the coverage prediction. For this purpose, the transmitter was placed in a different room within the femtocell premises and new measurements were recorded along the street. When compared to the FDTD prediction performed with FRF $\approx$ 0.071 the total error was RMSE $\approx$ 7.2 dB which differs 1.2 dB from the originally calibrated error. This indicates that the accuracy of the model calibration can be improved by taking more points into consideration. Nevertheless it also indicates that the results presented in Table 4 can still be used in similar scenarios while keeping reasonable RMSE levels.

The reduction of the simulation frequency also has an effect on the interference patterns that arise in the simulation as a result of phase differences in the propagated waves. In order to analyze the phase behavior of the simulation, the received power distribution is illustrated in Figure 12 as a box plot. The lower and upper limits of the boxes represent the first and third quartiles, while the red horizontal line is the median of the data. The mean received power is indicated by a dark dot and the extremes of the whiskers are located one standard deviation below and above the mean. Due to the calibration of the received power, it is clear from this figure that the overall power distribution remains approximately invariant for those values of FRF, where a low-prediction error can be achieved.

6. System-Level Simulations (SLSS)

The applicability of the presented propagation predictions to the study of a macro-femtocell hybrid scenario is presented here by means of mobile WiMAX (IEEE 802.16e-2005) system-level simulations with private access femtocells. The target of this experimental evaluation is to show how a measurements-based calibrated FDTD model can help the operator to predict common interference problems between users of the macrocell and the femtocell.

The scenario used for this experimental evaluation was the same residential street presented in Figure 6. A nonuniformly deployed WiMAX hybrid network formed by one macrocell and five femtocells was used for this case of study. The femtocells were located in five different households along the street, while the macrocell is positioned in an area located further away from the street under consideration. This is realistic, since femtocells are mainly aimed at users with poor indoor macrocell coverage. To perform the system-level simulation, different traffic maps were used for both the indoor and outdoor environments. There is one indoor traffic map per femtocell and house, which contains two randomly positioned users, and there is one outdoor traffic map in the street, containing five users.

The static system-level simulator functions by recording hundreds of snapshots with random positions of the macrocell and femtocell users. As the power distribution remains constant with the reduction of the FRF (see Figure 12) and the location of the users varies between different snapshots, particular phase errors at given sites in the coverage prediction do not affect the final SLS statistics. Furthermore, it has been experimentally confirmed that the probability of outage, as well as the average throughput of the different cells in the system-level simulations, is not altered by the reduction of the simulation frequency.

This case of study makes use of private access femtocells, which means that indoor users are allowed to connect, depending on the signal quality, to their own femtocell or to the macrocell. On the other hand, outdoor users are only allowed to connect to the macrocell.

For illustration purposes of the applicability of the presented propagation model, only downlink is considered.

It is illustrated in Figure 13 that an outdoor user connected to a distant macrocell is jammed due to the interference coming from nearby femtocells. In this case, the green users are successful, while the blue users suffer outage in downlink. A user will be successful or in outage depending on whether they are able or not of obtaining their requested throughputs and QoS from the network in order to use their services (video). In the example shown here, it occurs that there are three users on the street connected to the macrocell, who are using the same WiMAX subchannel as another femtocell user during the same time interval (symbol). In this case and as predicted by the FDTD model, the signal level of the carrier is smaller than the signal power of the interference, resulting thus in a poor signal quality. Due to this, the macrocell user is jammed and the communication cannot be supported by the network.

7. Conclusion

In this paper, the coverage prediction of WiMAX femtocells by means of a calibrated FDTD model is studied. The reduction of the simulation frequency is proposed as a simplification of the problem which is required for computational reasons. The use of a parallel architecture such as the computation on a graphics card is also proposed as a feasible mean of reducing the computation time.

An optimal method to obtain an acceptable combination of parameters, which maximizes the absorbing properties of the CPML boundary condition for FDTD electromagnetic simulations, is also proposed. Furthermore, an error function that measures the relative error of the electrical field prediction near the CPML has been modelled. In addition to this, a Fibonacci search-based method is presented as a fast way to explore the solutions space and reach the minimum point without falling in the need to compute the error function at thousands of different solutions.

A method for the calibration of the materials involved in the FDTD simulation has also been presented. This model tuning approach, based on simulated annealing, is introduced as a way to match the propagation predictions to the reality. Then, a spatial averaging filter has been used as a mean to solve prediction errors at diffractive obstacles due to the lower-frequency simplification. The accuracy of the method has been validated by performing calibrations at a wide range of simulation frequencies, analyzing the power distribution and evaluating the predictions with a different measurements route.

Finally, system-level mobile WiMAX simulations that use this FDTD propagation model have been presented. This exemplifies the interference caused by indoors-located WiMAX femtocells to outdoor users of the macrocell. This way, the need for hybrid indoor/outdoor propagation models is evinced.

Acknowledgments

This work is supported by the EPSRC-funded research Project EP/F067364/1 with title "The feasibility study of WiMAX based femtocell for indoor coverage." It is also partially supported by two EU FP6 projects on 3G/4G Wireless Network Design: "RANPLAN-HEC" with Grant no. MEST-CT-2005-020958 and EU FP6 "GAWIND" with Grant no. MTKD-CT-2006-042783.

References

[1] K. Yee, "Numerical solution of inital boundary value problems involving Maxwell's equations in isotropic media," *IEEE Transactions on Antennas and Propagation*, vol. 14, no. 3, pp. 302–307, 1966.

[2] C. D. Sarris, K. Tomko, P. Czarnul, et al., "Multiresolution time domain modeling for large scale wireless communication problems," in *Proceedings of IEEE Antennas and Propagation Society International Symposium (APS '01)*, vol. 3, pp. 557–560, Boston, Mass, USA, July 2001.

[3] G. Rodriguez, Y. Miyazaki, and N. Goto, "Matrix-based FDTD parallel algorithm for big areas and its applications to high-speed wireless communications," *IEEE Transactions on Antennas and Propagation*, vol. 54, no. 3, pp. 785–796, 2006.

[4] S. Fortune, "Algorithms for prediction of indoor radio propagation," Tech. Rep., AT&T Bell Laboratories, Murray Hill, NJ, USA, January 1998.

[5] F. Aguado, F. P. Fontan, and A. Formella, "Indoor and outdoor channel simulator based on ray tracing," in *Proceedings of the 47th IEEE Vehicular Technology Conference (VTC '97)*, vol. 3, pp. 2065–2069, Phoenix, Ariz, USA, May 1997.

[6] J.-M. Gorce, K. Jaffrès-Runser, and G. de la Roche, "Deterministic approach for fast simulations of indoor radio wave propagation," *IEEE Transactions on Antennas and Propagation*, vol. 55, no. 3, part 2, pp. 938–948, 2007.

[7] Y. Wang, S. Safavi-Naeini, and S. K. Chaudhuri, "A hybrid technique based on combining ray tracing and FDTD methods for site-specific modeling of indoor radio wave propagation," *IEEE Transactions on Antennas and Propagation*, vol. 48, no. 5, pp. 743–754, 2000.

[8] Á. V. Rial, G. de la Roche, and J. Zhang, "On the use of a lower frequency in finite-difference simulations for urban radio coverage," in *Proceedings of the 67th IEEE Vehicular Technology Conference (VTC '08)*, pp. 270–274, Singapore, May 2008.

[9] X. Liming and Y. Dacheng, "A recursive algorithm for radio propagation model calibration based on CDMA forward pilot channel," in *Proceedings of the 14th IEEE Personal, Indoor and Mobile Radio Communications (PIMRC '03)*, vol. 1, pp. 970–972, Beijing, China, September 2003.

[10] P. P. M. So, "Time-domain computational electromagnetics algorithms for GPU based computers," in *Proceedings of the International Conference on Computer as a Tool (EUROCON '07)*, pp. 1–4, Warsaw, Poland, September 2007.

[11] T. Rick and R. Mathar, "Fast edge-diffraction-based radio wave propagation model for graphics hardware," in *Proceedings of the 2nd International ITG Conference on Antennas (INICA '07)*, pp. 15–19, Munich, Germany, March 2007.

[12] W. Yu, R. Mittra, T. Su, Y. Liu, and X. Yang, *Parallel Finite-Difference Time-Domain Method*, Artech House, Boston, Mass, USA, 2006.

[13] *NVIDIA CUDA Compute Unified Device Architecture Programming Guide*, NVIDIA, Santa Clara, Calif, USA, 1st edition, November 2007.

[14] J. G. Andrews, A. Ghosh, and R. Muhamed, *Fundamentals of WiMAX Understanding Broadband Wireless Networking*, Prentice-Hall, Boston, Mass, USA, 2007.

[15] "Femtoforum," http://www.femtoforum.org/.

[16] G. Mansfield, "Femtocells in the US market—business drivers and consumer propositions," in *Proceedings of the FemtoCells Europe Conference*, London, UK, June 2008.

[17] "PC6530 OFDMA(IEEE802.16e-2005) Femtocell Technology Platform," Tech. Rep., picoChip, Bath, UK, 2008.

[18] D. Williams, "WiMAX Femtocells—a technology on demand for cable MSOs," in *Proceedings of the FemtoCells Europe Conference*, London, UK, June 2008.

[19] Á. V. Rial, H. Krauss, J. Hauck, M. Buchholz, and F. A. Agelet, "Empirical propagation model for WiMAX at 3.5 GHz in an urban environment," *Microwave and Optical Technology Letters*, vol. 50, no. 2, pp. 483–487, 2008.

[20] G. Wolfle, R. Wahl, P. Wildbolz, and P. Wertz, "Dominant path prediction model for indoor and urban scenarios," in *Proceedings of the 11th COST 273*, Duisburg, Germany, September 2004.

[21] Y. Corre and Y. Lostanlen, "3D urban propagation model for large ray-tracing computation," in *Proceedings of the International Conference on Electromagnetics in Advanced Applications (ICEAA '07)*, pp. 399–402, Torino, Italy, September 2007.

[22] A. Lauer, I. Wolff, A. Bahr, J. Pamp, and J. Kunisch, "Multimode FDTD simulations of indoor propagation including antenna properties," in *Proceedings of the 45th IEEE Vehicular Technology Conference (VTC '95)*, vol. 1, pp. 454–458, Chicago, Ill, USA, July 1995.

[23] A. Taflove, "Application of the finite-difference time-domain method to sinusoidal steady-state electromagnetic-penetration problems," *IEEE Transactions on Electromagnetic Compatibility*, vol. 22, no. 3, pp. 191–202, 1980.

[24] A. Taflove and S. C. Hagness, *Computational Electrodynamics: The Finite-Difference Time-Domain Method*, Artech House, Boston, Mass, USA, 3rd edition, 2005.

[25] A. Taflove and S. C. Hagness, in *Computational Electrodynamics: The Finite-Difference Time-Domain Method*, chapter 4, pp. 111–116, Artech House, Boston, Mass, USA, 3rd edition, 2005.

[26] J. Li, J.-F. Wagen, and E. Lachat, "Effects of large grid size discretization on coverage prediction using the ParFlow method," in *Proceedings of the 9th IEEE Personal, Indoor and Mobile Radio Communications (PIMRC '98)*, vol. 2, pp. 879–883, Boston, Mass, USA, September 1998.

[27] "EMPhotonics," 2001, http://www.emphotonics.com/.

[28] D. K. Price, J. R. Humphrey, and E. J. Kelmelis, "GPU-based accelerated 2D and 3D FDTD solvers," in *Physics and Simulation of Optoelectronic Devices XV*, M. Osinski, F. Henneberger, and Y. Arakawa, Eds., vol. 6468 of *Proceedings of SPIE*, San Jose, Calif, USA, January 2007.

[29] R. N. Schneider, M. M. Okoniewski, and L. E. Turner, "A software-coupled 2D FDTD hardware accelerator [electromagnetic simulation]," in *Proceedings of IEEE Antennas and Propagation Society International Symposium (APS '04)*, vol. 2, pp. 1692–1695, Monterey, Calif, USA, June 2004.

[30] A. Valcarce, G. de la Roche, and J. Zhang, "A GPU approach to FDTD for radio coverage prediction," in *Proceedings of the 11th IEEE Singapore International Conference on Communication Systems (ICCS '08)*, pp. 1585–1590, GuangZhou, China, November 2008.

[31] J.-P. Berenger, "A perfectly matched layer for the absorption of electromagnetic waves," *Journal of Computational Physics*, vol. 114, no. 2, pp. 185–200, 1994.

[32] J. A. Roden and S. D. Gedney, "Convolution PML (CPML): an efficient FDTD implementation of the CFS-PML for arbitrary media," *Microwave and Optical Technology Letters*, vol. 27, no. 5, pp. 334–339, 2000.

[33] M. Avriel and D. J. Wilde, "Optimality proof for the symmetric Fibonacci search technique," *Fibonacci Quarterly*, vol. 4, pp. 265–269, 1966.

[34] W. Lee and Y. Yeh, "On the estimation of the second-order statistics of log normal fading in mobile radio environment," *IEEE Transactions on Communications*, vol. 22, no. 6, pp. 869–873, 1974.

[35] S. Kirkpatrick, C. D. Gelatt Jr., and M. P. Vecchi, "Optimization by simulated annealing," *Science*, vol. 220, no. 4598, pp. 671–680, 1983.

[36] "Recommendation P.526-10 on Propagation by Diffraction," ITU-R, 2007.

Hindawi Publishing Corporation
EURASIP Journal on Wireless Communications and Networking
Volume 2009, Article ID 687238, 16 pages
doi:10.1155/2009/687238

Research Article

A Time-Variant MIMO Channel Model Directly Parametrised from Measurements

Nicolai Czink,[1,2] Thomas Zemen,[1] Jukka-Pekka Nuutinen,[3] Juha Ylitalo,[3] and Ernst Bonek[4]

[1] *Telecommunications Research Center Vienna (FTW), 1220 Vienna, Austria*
[2] *Smart Antennas Research Group, Stanford University, Stanford, CA 94305, USA*
[3] *Elektrobit Ltd., 90570 Oulu, Finland*
[4] *Institute of Communications and Radio Frequency Engineering, Vienna University of Technology, 1040 Vienna, Austria*

Correspondence should be addressed to Nicolai Czink, czink@ftw.at

Received 2 July 2008; Revised 27 November 2008; Accepted 12 March 2009

Recommended by Mansoor Shafi

This paper presents the Random-Cluster Model (RCM), a stochastic time-variant, frequency-selective, propagation-based MIMO channel model that is directly parametrised from measurements. Using a fully automated algorithm, multipath clusters are identified from measurement data without user intervention. The cluster parameters are then used to define the propagation environment in the RCM. In this way, the RCM provides a direct link between MIMO channel measurements and MIMO channel modelling. For validation, we take state-of-the-art MIMO measurements, and parametrise the RCM exemplarly. Using three different validation metrics, namely, mutual information, channel diversity, and the novel Environment Characterisation Metric, we find that the RCM is able to reflect the measured environment remarkably well.

1. Introduction

Multiple-input multiple-output technology (MIMO) [1] made its way in the recent years from an information-theoretic shooting star [2] to actual products on the mass market [3, 4]. Currently the 3GPP [5] is standardising MIMO for the next generation's mobile communications, what is called Long Term Evolution (LTE) as well as IEEE is standardising MIMO for WiMAX [6]. Already information theory told that the promise of increased spectral efficiency of MIMO systems is *only* available when the radio channel permits, but this seems to have faded out of people's memory.

Despite this fact, numerous algorithms were developed, mostly considering ideal uncorrelated i.i.d. Rayleigh fading channels between the transmit and receive antennas, which is only true in rich-scattering environments with sufficiently large antenna spacings at both transmitter and receiver. Otherwise, the performance of the algorithms deteriorates. To reach the goal of gigabit transmissions over the wireless link, one needs to include the knowledge of the actual channel into the algorithms. Thus, an accurate model of the propagation channel is paramount.

One can distinguish between three different types of MIMO channel models: (i) channel models for developing signal-processing algorithms, for example, [7, 8]. These models describe the radio channel by the *correlations between the different links*, established between individual antenna elements. This makes the model mathematically tractable, yet inaccurate when it comes to reflecting real-world propagation conditions, because current correlation-based models always base on the Rayleigh-fading (or, to some extent, Ricean fading) assumption. While the so-called "Kronecker" model [7] is favoured by many people because it can be treated by random-matrix theory [9], the Weichselberger Model [8] shows a much better fit to measurement data [10, 11]. (ii) channel models for MIMO deployment in a given environment, for example, ray-tracing [12, 13]. These models try to predict MIMO conditions given a map (or floor plan) for optimal positioning of MIMO-enabled base stations, which comes with high demands on computational power and accuracy of environment data bases; (iii) channel models for testing of algorithms and systems, for example, [14–16, Chapter 6.8]. These models typically represent a certain kind of propagation scenario (like indoor offices,

or outdoor picocells), without considering a specific propagation environment. This is achieved by modelling the *propagation environment* in a *stochastic* way. Such models usually have a medium complexity and represent realistic channels very well, however a closed-form expression of the channel model, as in the first case, does not exist. The major difference between these models is their ability to describe time variation.

A time-variant channel is an essential feature of *mobile* communications. The 3GPP Spatial Channel Model (SCM) [14] is well suited for simulating random-access communications. It models the channel in blocks (so-called "drops"), during which the channel only undergoes Doppler fading, but after a drop, the channel changes completely. This assumption makes it impossible to test signal processing algorithms that track the channel parameters between different snapshots. Additionally, the abrupt changes between the drops are challenging for hardware testing using channel simulators, since the device under test and the channel model need to be synchronized. A major improvement is the WINNER II geometry-based stochastic channel model [15], which includes a smooth transition between drops. This smooth transition is only provided by the full implementation of the WINNER II model. The popular downscaled version "clustered-delay line" does not provide the basis to track the channel! The COST 273 MIMO channel model [16, Chapter 6.8] does not use the concept of drops, but intrinsically models the channel in a smooth way. While the user is moving through a randomly-generated map, he is illuminated via groups of different propagation paths depending on his location on this map. When the receiver moves out of a certain region "visibility region", a particular group of paths fades out, and vice versa. Unfortunately, the COST 273 model is not yet completely parametrised, nor fully implemented.

1.1. Contribution. In this paper, we present the novel Random-Cluster Model (RCM), a geometry-based stochastic MIMO channel model for time-variant frequency-selective channels. The application of the RCM focuses on algorithm and system testing, yet it is parametrised directly from measurements.

The Random-Cluster Model uses multipath clusters to model the radio channel. Generally, multipath clusters can be seen as groups of propagation paths having similar parameters. We concisely define a cluster by its mathematical description provided in Section 2.2. Clusters allow to characterise the propagation environment in a compact way using much less parameters than characterisation by individual multipath components (MPCs). This data reduction is the primary purpose for using clusters in radio channel models. Clusters were first only observed in delay domain by Saleh and Valenzuela [17]. Their concept was extended to the joint angle-of-arrival/delay domain in [18]. Recently [19] developed a test to prove the existence or non-existence of clusters in propagation path estimates from channel measurements, showing that clusters indeed exist independent of the authors' view. We were able to match clusters to real-world scattering objects [20].

Several innovations were necessary to construct the RCM, some of which have been introduced in conference papers. First, to accurately parametrise the RCM, *automatic clustering techniques* are necessary. The first semiautomatic approach for clustering MIMO channel data was introduced in [21]. We gradually extended these ideas by a meaningful *joint* clustering approach [22], a power-weighted clustering algorithm [23], a criterion to decide on the number of clusters, a reasonable initial guess, and the ability to track clusters over multiple time-variant snapshots [24]. The mere fact that clusters *can* be tracked demonstrates that clustering makes sense showing that they obviously stem from scattering objects. The automatic parametrisation by identifying clusters *without user intervention* turned out to be essential to process a large amount of multiantenna measurement data.

Regarding the ability to describe time-variant channels, the RCM is capable to model random-access channels, and, in addition, to cover continuous transmission in a time-variant environment as well by creating smoothly time-variant channel realisations. A major innovation of the RCM is the concept of *linearly moving clusters*. In this article, we will use the RCM to model smoothly time-variant channels. (A first description of the RCM, modelling random-access channels only was provided in [25], and [26] briefly outlines the ideas of using clusters for time-variant channel modelling.)

The RCM is a *stochastic* MIMO channel model, yet it is parametrised directly from measurements. By double-directional MIMO channel measurements in a specific environment, a single multivariate pdf of the cluster parameters is created, which is representative for the electromagnetic wave propagation in this environment. The parameters of a single realisation are drawn from this distribution. In this way, the RCM is a stochastic channel model, deriving its parameters directly from measurements.

The complexity of the RCM should be divided into (i) the parametrisation complexity and (ii) the execution complexity. Regarding the parametrisation complexity, the RCM is parametrised automatically from measurements, even if the number of parameters appears to be high. The execution complexity of the RCM is governed by the calculation of the channel matrix, as in all other prominent physical channel models [27]. It adds up to $22 \cdot LN_{\mathrm{Tx}}N_{\mathrm{Rx}}B$ real operations, where L denotes the number of MPCs, N_{Tx} and N_{Rx} denote the number of transmit and receive antennas, respectively, and B denotes the number of frequency samples, for which the channel matrix is calculated.

The ultimate challenge for any channel model is its comparison to measurements. We will describe the extensive validation of the RCM against measurements using three different validation metrics: (i) mutual information [2], (ii) channel diversity [28], and (iii) the novel Environment Characterisation Metric [29]. We find that the RCM is able to reflect the measured time-variant environment noticeably well. Additionally, we will demonstrate why the popular mutual information "capacity" is a poor validation metric for *time variant* MIMO channel models.

1.2. Organisation. This article is organised as follows. Section 2 provides a first overview of the features of the Random Cluster Model. Section 2.1 outlines the structure of the RCM, Section 2.2 details the description of the environment by multipath clusters. The initialisation of the model is provided in Section 2.3, and details on the implementation of the time variance are given in Section 2.4. Section 3 describes the model validation by first outlining the validation framework. We then introduce the validation metrics used in Section 3.2, followed by the validation results in Section 3.3. Finally, Section 4 concludes the article. In Appendix A, we provide an overview of the measurements used for parametrisation and validation.

2. The Random-Cluster Model

The RCM is based on the concept of multipath clusters. The most significant feature of the RCM is that it is parametrised directly from *channel measurements* by an *automatic* procedure. In this way, the RCM is *specific to the environment*; it closes the gap between channel measurements and channel modelling. Nonetheless it is a stochastic model as we will clarify shortly.

The novel approach of the RCM is to describe the time-variant geometry of the channel *completely* by *statistical cluster parameters*. Clusters provide a compact way of describing the underlying propagation environment. To accurately parametrise the clusters, we extract their parameters from measurements. An important feature of the MIMO channel also reflected by the model is the coupling between propagation paths in space and time, also known as the double-directional MIMO channel model [30]. To enable time-variance, *clusters* may move, relative to the Tx or Rx. By this, the RCM creates correlated snapshots in time of the propagation environment.

Summarising, the model has the following properties. It is

(i) cluster-based,

(ii) propagation-based, but stochastic,

(iii) double-directional,

(iv) time-variant.

What the RCM Provides. The main focus of the RCM is link-level simulation, for both algorithm testing and device testing. It is well suited to reflect time-variant scenarios that are similar, but not equal to the ones measured before. A major feature is that the parametrisation of the RCM, directly derived from measurements, is achieved automatically. In this way it perfectly fills the gap between channel *sounding* and channel *simulation*. Typical applications include testing in specifically challenging channel situations, or in specific application scenarios.

In contrast to "playback simulations" [31] where previously recorded impulse response data from a channel sounder are used to directly model the environment, the RCM is neither fixed in bandwidth, antenna array parameters, or simulation duration.

What the RCM Does Not Provide. By the way it is parametrised, the RCM is very specific in reflecting a certain type of environment. Being rooted in the COST 273 model [16, Chapter 6.8], one might think that the RCM is an all-purpose model. The model user will be warned that it does not perform like this. Many aspects that make a model very general have been intentionally omitted in the RCM in order to reduce complexity, for example, a dedicated path loss calculation, or a description of general environments.

For scenarios close to the measured ones, the RCM will still perform better than other (even standardised) models available, but proper parametrisation is always necessary.

The RCM is definitely not intended for supporting MIMO *deployment*. Since the model does not include any geometry, it is not suited for predicting the properties of the electromagnetic field in specific locations on a map, particularly not in environments that were not measured before.

2.1. General Model Structure. In the following we describe the RCM by its flow diagram shown in Figure 1. The RCM consists of two major parts: the *initialisation*, and the implementation of *smooth time variation*:

(1) During initialisation, a first snapshot of the scenario is generated from the environment parameter function.

(2) The implementation of the smooth time variation is split in two parts: (i) moving the clusters introduces small-scale changes to the environment and generates the Doppler-induced fading; (ii) the birth/death-process accounts for shadowing and large-scale changes.

Both of these parts rely on an accurate parametrisation of the environment. In the next paragraphs we will first detail how the environment is described. Subsequently we will explain the model flow step by step.

2.2. Environment Description—Multipath Clusters. Multipath clusters are the basis for the RCM. Each cluster is described by a number of parameters (Table 1), which are stacked into the cluster parameter vector $\boldsymbol{\Theta}_c$. We distinguish between the *cluster location parameters* (mean delay, azimuth and elevation positions), *cluster spread parameters* (delay spread, angular spreads), *cluster power parameters* (power of the cluster and power of the snapshot in which the cluster exists), *cluster number parameters* (number of paths within the cluster, average number of coexisting clusters in the same snapshot), and *cluster movement parameters* (change rates of the cluster location and power parameters, and cluster lifetime).

A time-variant environment may contain transitions between different *propagation conditions*, for example, from LOS to NLOS and back. Clusters in these propagation conditions have quite different properties. Different propagation conditions are mainly reflected by two simple parameters: the snapshot power and the number of clusters. These two parameters are included in the set of cluster parameters,

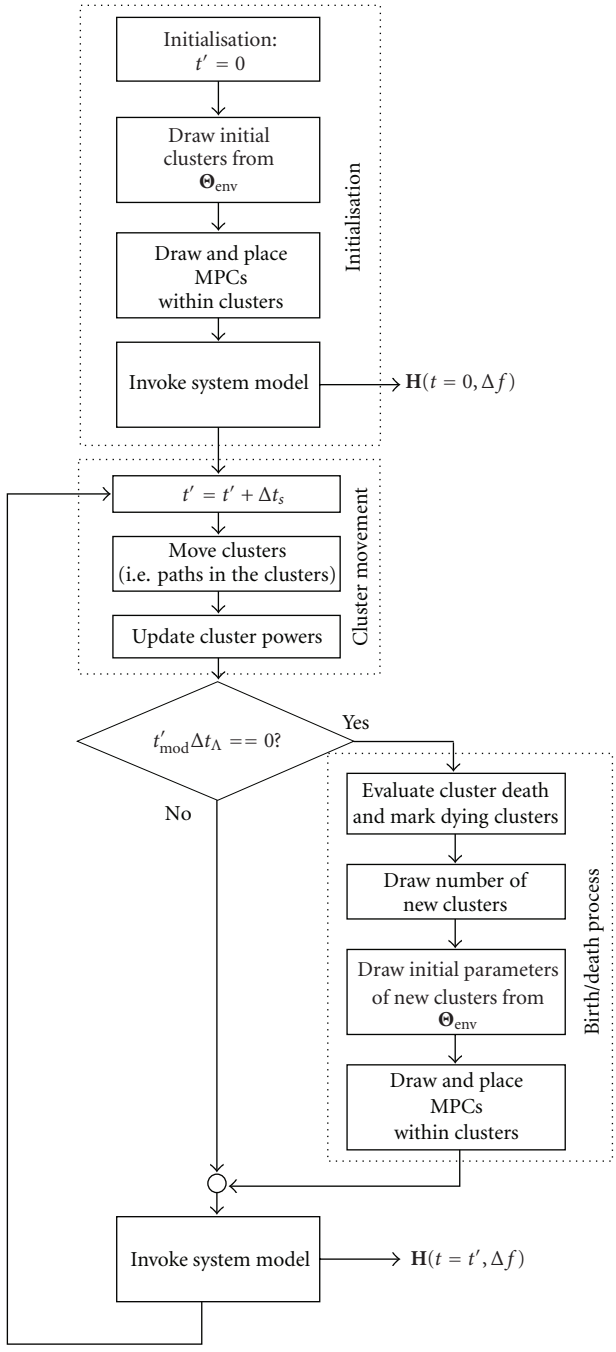

Figure 1: Flow diagram of the Random-cluster model.

being *cluster selection parameters*. They label clusters for specific propagation conditions in a statistical way.

2.2.1. Geometrical Interpretation. A straight-forward extension of a MIMO channel description by single, discrete MPCs, is the usage of multipath clusters.

Clusters are able to describe a double-directional wave-propagation environment in the same way as multipath components do. Figure 2 illustrates this concept. A cluster represents a unique link between the transmitter and the receiver having a certain power, a certain direction of departure, direction of arrival, and delay. Extending the concept of a single MPC, a cluster shows a certain spread in its parameters, describing the size of the cluster in space.

This leads to a significant reduction in the number of parameters. One cluster describing a manifold of multipath components showing similar propagation parameters is described by only 21 parameters (see Table 1), while a single MPC already needs 12 parameters (such seemingly large numbers of parameters are necessary for a *time-variant* description of clusters and propagation paths).

When we look at a cluster that stems from multiple bounces of an electromagnetic wave on its way from Tx to Rx, Figure 2 shows how a cluster appears when perceived from Tx and Rx separately. The cluster splits up in two parts. For single-bounce scattering, these two parts of a cluster overlap physically. For a direct path (line-of-sight), the cluster contains only a strong, single path. From the cluster parameters, one cannot deduct whether the cluster stems from single or from multiple-bounces scattering. From a modelling perspective concentrating on clusters, however, this knowledge is redundant (the same applies to MIMO modelling by multipath components). Note that we are using

Table 1: Cluster parameters of a single cluster, contained in $\mathbf{\Theta}_{\mathbf{c}}$.

Symbol	Cluster parameter
$\overline{\tau}$	Cluster mean delay
$\overline{\varphi}_{\text{Tx}}$	Azimuth cluster position at Tx
$\overline{\varphi}_{\text{Rx}}$	Azimuth cluster position at Rx
$\overline{\theta}_{\text{Tx}}$	Elevation cluster position at Tx
$\overline{\theta}_{\text{Rx}}$	Elevation cluster position at Rx
σ_τ	Cluster delay spread
$\sigma_{\varphi_{\text{Tx}}}$	Cluster azimuth spreads seen from Tx
$\sigma_{\varphi_{\text{Rx}}}$	Cluster azimuth spreads seen from Rx
$\sigma_{\theta_{\text{Tx}}}$	Cluster elevation spreads seen from Tx
$\sigma_{\theta_{\text{Rx}}}$	Cluster elevation spreads seen from Rx
σ_γ^2	Cluster mean power
ρ	Total snapshot power, in which the cluster occurs
N_c	Number of clusters coexisting in the snapshot
N_p	Number of paths within a cluster
$\Delta\sigma_\gamma^2$	Change rate of cluster power per travelled wavelength in dB
$\Delta\overline{\tau}$	Change rate of cluster mean delay per travelled wavelength
$\Delta\overline{\varphi}_{\text{Rx}}$	Change rate of cluster mean AOA per travelled wavelength
$\Delta\overline{\varphi}_{\text{Tx}}$	Change rate of cluster mean AOD per travelled wavelength
$\Delta\overline{\theta}_{\text{Rx}}$	Change rate of cluster mean EOA per travelled wavelength
$\Delta\overline{\theta}_{\text{Tx}}$	Change rate of cluster mean EOD per travelled wavelength
Λ	Cluster lifetime

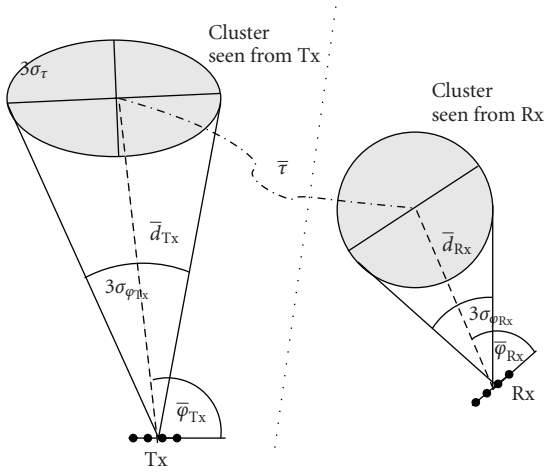

Figure 2: Geometrical interpretation of the RCM, demonstrated for a single cluster.

multiple clusters to describe the multipath structure of the radio channel, but Figure 2 shows just one cluster.

2.2.2. Environment pdf. In a measured environment, different kinds of clusters occur. We regard the parameters of these clusters as an ensemble of a multivariate distribution, which we call the *environment pdf*, (we use the established statistical notation, where $\boldsymbol{\theta}_c$ is the argument of the pdf of the random vector $\boldsymbol{\Theta}_c$),

$$\boldsymbol{\Theta}_{\mathrm{env}} \doteq f_{\boldsymbol{\Theta}_c}(\boldsymbol{\theta}_c). \tag{1}$$

The environment pdf characterises the multipath structure in a *specific measured environment*. In this way, the environment is completely parametrised by a description that is purely statistical. In some cases, this multivariate distribution may be multimodal and does not necessarily follow a simple closed-form distribution.

2.2.3. Parametrisation. The parameters of the RCM are characterized by the environment pdf, which can conveniently be estimated from MIMO channel measurements in a straightforward way.

(1) *MIMO channel measurements* provide multiple impulse responses of the scenario. While the channel sounder continuously records frequency-selective MIMO channel matrices at each time instant "*snapshots*", the transmitter is moved to capture the time-variant properties of the scenario.

(2) *Propagation paths are estimated* from each snapshot of the channel measurements using a high-resolution parameter estimation. For this purpose we used the Initialization-and-Search-Improved SAGE (ISIS) estimator [32] to estimate 100 paths from every measured snapshot.

(3) We *identify and track clusters* in these propagation paths using the fully automatic framework presented in [24]. This framework has the following key features.

(a) The initial guess algorithm identifies the cluster locations by separating clusters as far as possible in the parameter space while taking already existing clusters from previous snapshots into account. The number of clusters is estimated by a power-threshold criterion.

(b) The clustering is optimized using the KPowerMeans algorithm [23], which makes clusters as compact as possible. This is achieved by including the concept of path power into the classic KMeans algorithm and by enabling joint clustering by appropriate scaling of the input data.

(c) Clusters are tracked using a Kalman filter between snapshots, where a probabilistic cluster fitting criterion decides whether a cluster has actually moved or has to be regarded as new.

As a result we obtain the parameters of all clusters in the measured environment, as described in Table 1. The change-rate parameters and cluster lifetimes are determined by the tracking of the clusters. Typical examples of the change-rate parameters and more discussion about their physical interpretation are provided in [33].

(1) We *estimate the environment pdf* from all identified clusters using a kernel density estimator (KDE) [34].

The KDE approximates the underlying distribution by a sum of kernels. In this way, even multimodal distributions can be described easily. As result, the environment pdf can be written as

$$\boldsymbol{\Theta}_{\mathrm{env}} = f_{\boldsymbol{\Theta}_c}(\boldsymbol{\theta}_c) = \frac{1}{N_K}\sum_{i=1}^{N_K} K\left(\boldsymbol{\theta}_c, \boldsymbol{\mu}_{\boldsymbol{\Theta}_i}, \mathbf{C}_{\boldsymbol{\Theta}_i}\right), \tag{2}$$

where $\boldsymbol{\mu}_{\boldsymbol{\Theta}_i}$ and $\mathbf{C}_{\boldsymbol{\Theta}_i}$ denote the mean and covariance of the ith kernel, and N_K denotes the number of kernels used.

To parametrise the environment pdf for the RCM, we use Gaussian kernels, hence a Gaussian mixture pdf, such that

$$K\left(\boldsymbol{\theta}_c, \boldsymbol{\mu}_{\boldsymbol{\Theta}_i}, \mathbf{C}_{\boldsymbol{\Theta}_i}\right) = \frac{1}{(2\pi)^{D/2}\left|\mathbf{C}_{\boldsymbol{\Theta}_i}\right|^{1/2}} \times exp\left(-\frac{1}{2}\left(\boldsymbol{\theta}_c - \boldsymbol{\mu}_{\boldsymbol{\Theta}_i}\right)^{\mathrm{T}} \mathbf{C}_{\boldsymbol{\Theta}_i}^{-1}\left(\boldsymbol{\theta}_c - \boldsymbol{\mu}_{\boldsymbol{\Theta}_i}\right)\right), \tag{3}$$

where $D = 21$ denotes the dimension of the cluster parameter vector. We used Gaussian kernels for their low complexity and analytical tractability. Furthermore, Gaussian kernels manage to describe all kinds of (continuous) pdfs with low error [35].

The kernel parameters $\boldsymbol{\mu}_{\boldsymbol{\Theta}_i}$ and $\mathbf{C}_{\boldsymbol{\Theta}_i}$ need to be estimated. The input data for this estimation are the identified clusters from a measurement route.

A straight-forward way to find the kernel parameters is to choose the N_K equal to the total number of identified clusters. Each individual identified cluster is used as (mean) parameter for an individual kernel. The variances of the

kernel can then be estimated using the minimum average mean integrated squared error (AMISE) criterion [35]. This parametrisation approach is the most accurate one, although the number of kernels may become quite large.

Of course, the obtained environment pdf is very specific to the measured environment since it is directly parametrised from measurements.

Figure 3 shows four different two-dimensional cuts of the same environment pdf, which was evaluated from a measurement run at 2.55 GHz in the office environment, described in the appendix. These two-dimensional pdfs are colour coded from black (low probability) to white (high probability).

It becomes obvious that the environment pdf is indeed a multimodal distribution, strongly depending on which parameters are observed. For example, Figure 3(a) demonstrates that clusters with large mean delay usually have weaker power, which was to be expected. Additionally, Figure 3(b) details from which Rx directions clusters with stronger power appear. Some of the cluster parameters are even intrinsically correlated. For instance, Figures 3(c)-3(d) show that there is a correlation between the cluster azimuth spreads. Additional values of the environment pdf can be found in [33, 36, Chapter 7.4].

2.3. RCM Initialisation. The initialisation procedure generates the first snapshot of the model.

2.3.1. Drawing Initial Cluster Parameters. The environment pdf $\boldsymbol{\Theta}_{\text{env}}$ provides a description for all kinds of clusters that were identified in the environment. To actually generate a snapshot, the momentary propagation condition of the environment must be selected. This is done by determining the intended snapshot power and the number of clusters (which are the cluster selection parameters). Their joint distribution function is contained in the environment pdf.

Thus, we draw cluster parameters in a stepwise procedure.

(i) First, we obtain the pdf of the number of clusters, $f(N_c)$, by marginalizing the environment pdf to the number of clusters, which is done by integrating the environment pdf over the other dimensions. Then the actual number of clusters for the first snapshot, $\widetilde{N}_c$, is determined by drawing a random sample from this pdf. Since the number of clusters must be an integer number, the ceiling of the drawn value is assigned to $\widetilde{N}_c$.

(ii) Then, we obtain the pdf of the snapshot power (given the number of clusters) by conditioning the environment pdf on the chosen number of clusters $\widetilde{N}_c$, and marginalising it to the snapshot power. From this marginal distribution $f(\rho \mid \widetilde{N}_c)$, the *intended* snapshot power, $\widetilde{\rho}$, is determined by drawing a random sample from this pdf. This intended snapshot is only used as a selection criterion for the clusters to be drawn in the next steps. In general, the sum power of the clusters will not exactly match the intended snapshot power.

(iii) Finally, to select a specific type of clusters, the environment pdf is conditioned on both the number of clusters and on the intended snapshot power, $f(\boldsymbol{\Theta}_c \mid \widetilde{N}_c, \widetilde{\rho})$. From this final distribution, we draw $\widetilde{N}_c$ cluster parameter sets $\widetilde{\boldsymbol{\Theta}}_c$.

These parameters are drawn from a multivariate sum-of-Gaussian distribution, which sometimes leads to invalid parameters because of the Gaussian tails. For this reason, the drawn spread parameters and the mean delay are lower-bounded by zero, the number of paths within a cluster is rounded to the next larger integer and lower bounded by one, and the drawn cluster lifetime is rounded to the closest integer value larger or equal to one. In this way, we can retain the low-complexity kernel density estimation but still create valid cluster parameters for the model.

These (post-processed) cluster parameters specify the multipath structure of the initial snapshot.

2.3.2. Placing Multipath Components within the Clusters.

(1) In every cluster c, the corresponding number of paths (which is an initial cluster parameter drawn before), $\widetilde{N}_{p,c}$, is placed as follows. Every path is described by the *path* parameters: complex amplitude (γ), total delay (τ), and the azimuth and elevation of arrival and departure, respectively, $(\varphi_{\text{Tx/Rx}}, \theta_{\text{Tx/Rx}})$.

The delay is drawn from a Gaussian distribution with its mean and variance given in the cluster parameters. Similarly, the angular parameters are drawn from a *wrapped* Gaussian distribution [37] (in the wrapped Gaussian distribution, all realisations are mapped to their principal value in $[-\pi, \pi)$), where the mean and variance are again determined in the cluster parameters (Table 1). All paths within a cluster show the same amplitude, $|\gamma_{p,c}| = \sqrt{\rho_c / \widetilde{N}_{p,c}}$, determined by the total cluster power and the number of paths within a cluster, and have a random phase, which is drawn from a uniform distribution $\mathcal{U}(-\pi, \pi)$.

After having placed paths in all clusters, the propagation environment of the initial snapshot is completely specified by its *multipath structure*.

2.3.3. Generating the MIMO Channel Matrix "System Model". To calculate the MIMO channel matrix, we use the common approach of a bandwidth filter and antenna filters [38].

The time-dependent MIMO channel transfer matrix is calculated from the multipath structure as

$$\begin{aligned}\mathbf{H}(t, \Delta f) = \sum_{c=1}^{\widetilde{N}_c} \sum_{p=1}^{\widetilde{N}_{p,c}} & \gamma_{p,c}(t) \\ & \cdot \mathbf{a}_{\text{Rx}}\left(\varphi_{\text{Rx},p,c}(t), \theta_{\text{Rx},p,c}(t)\right) \\ & \cdot \mathbf{a}_{\text{Tx}}^{\text{T}}\left(\varphi_{\text{Tx},p,c}(t), \theta_{\text{Tx},p,c}(t)\right) \\ & \cdot \mathrm{e}^{-j2\pi\Delta f \tau_{p,c}(t)},\end{aligned} \tag{4}$$

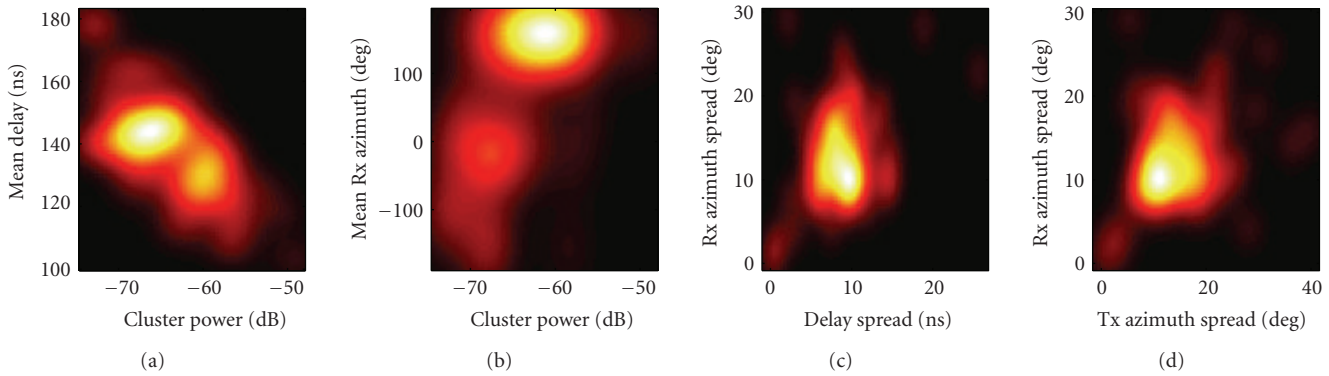

Figure 3: Exemplary marginal distributions of the environment pdf.

at a certain frequency bin Δf equidistantly spaced on a limited bandwidth between $[f_0 - B/2, f_0 + B/2]$, where f_0 denotes the carrier frequency and B the simulated bandwidth. The antenna array patterns are described in $\mathbf{a}_{\mathrm{Tx/Rx}}(\varphi_{\mathrm{Tx/Rx}}, \theta_{\mathrm{Tx/Rx}})$, and the subset p, c denotes the pth path in cluster c. This calculation dominates the computational complexity of the model (a low-complexity implementation of this equation is also available in [39]).

For the exemplary implementation of the RCM that we validated (see Section 3), we imply an 8×8 MIMO configuration with uniform linear arrays at both link ends, a bandwidth of 20 MHz, and 32 frequency bins. The centre frequency was set to either 2.55 GHz or to 5.25 GHz matching the measurement. An 8×8 configuration provides a much tougher test whether a model renders the spatial environment properties correctly than the 4×4 or 2×2 configurations envisaged for LTE. By including the actual antenna array pattern, the RCM can easily be extended to arbitrary array configurations other than ULAs.

2.4. Implementation of the Time Variation. After the generation of the initial snapshot, the RCM generates channels correlated in time. The implementation of the time variation, based on the novel idea of *linearly moving clusters*, is an integral part of the model. In this way, both stationary and nonstationary time-variant channels can be modelled.

2.4.1. Time Bases. We distinguish between small-scale and large-scale time variations. Small-scale variations, which introduce fading, take place every sampling instant. Large-scale variations, reflecting changes in the propagation structure, occur in less frequent intervals.

For this reason, the RCM distinguishes between two time bases: the *sampling time interval*, Δt_s, and the *cluster-lifetime interval*, Δt_Λ, where $\Delta t_\Lambda = N_\Lambda \cdot \Delta t_s$. Cluster lifetimes, Λ_c, are multiples of Δt_Λ (see Table 1).

2.4.2. Large-Scale Variation—Cluster Birth/Death Process. In time-variant scenarios, where at least one of the transceivers is moving, the propagation conditions can change significantly. To introduce these large-scale changes into the model, we included a cluster birth/death process.

This birth/death process is motivated from observations in measurements, where clusters smoothly show up, exist over a period of time, and eventually fade away. We reflect this behaviour in our model by three parameters: (i) the cluster lifetime, responsible for the cluster death, (ii) a cluster birth pdf, and (iii) a fade-in/fade-out coefficient.

The lifetime of each cluster is already intrinsically defined in the cluster parameters (see Table 1), which was drawn from the environment pdf when the cluster was created. Cluster death is implemented by decreasing the lifetime of each cluster in every cluster lifetime interval, Δt_Λ. Dying clusters are fading out during the next cluster lifetime interval.

An additional probability mass function (pmf), describing the *number of cluster births per cluster lifetime interval*, is also extracted from the measurements. The extraction method and examples of extracted parameters are provided in [33]. According to this pmf, a number of new clusters are drawn every cluster lifetime interval. After drawing the number of new clusters, the actual parameters of these new clusters are drawn in the same way as described in the initialisation procedure in Section 2.3.1. New-born clusters fade in during the next cluster lifetime interval.

The appearance or disappearance of clusters is done exponentially in the small-scale updates, controlled by the cluster fade-in/fade-out coefficient $|\sigma_{\mathrm{in/out}}|_{\mathrm{dB}}$. Empirical evaluations showed that a maximum cluster attenuation of 10 dB provides best results, hence $|\sigma_{\mathrm{in/out}}|_{\mathrm{dB}} = 10/N_\Lambda$.

Note that our approach is different from using "visibility regions" [40], which cannot be used since we do not consider the actual geometry of the environment.

2.4.3. Small-Scale Variation—Cluster Movement. The RCM models small-scale changes by the movement of the clusters in parameter space. In every sampling time interval, the parameters of the paths within a cluster are linearly incremented. These increments are provided in the cluster parameters $\boldsymbol{\Theta}_c$ of the respective cluster (see Table 1).

The update equations of the pth path in the cth cluster for a moving station with speed v (in wavelengths per second) are given as

$$\begin{aligned}
\tau_{p,c}(t+\Delta t_s) &= \tau_{p,c}(t) + \Delta\overline{\tau}_c \cdot v\Delta t_s,\\
\varphi_{\mathrm{Tx},p,c}(t+\Delta t_s) &= \varphi_{\mathrm{Tx},p,c}(t) + \Delta\overline{\varphi}_{\mathrm{Tx},c} \cdot v\Delta t_s,\\
\varphi_{\mathrm{Rx},p,c}(t+\Delta t_s) &= \varphi_{\mathrm{Rx},p,c}(t) + \Delta\overline{\varphi}_{\mathrm{Rx},c} \cdot v\Delta t_s,\\
\theta_{\mathrm{Tx},p,c}(t+\Delta t_s) &= \theta_{\mathrm{Tx},p,c}(t) + \Delta\overline{\theta}_{\mathrm{Tx},c} \cdot v\Delta t_s,\\
\theta_{\mathrm{Rx},p,c}(t+\Delta t_s) &= \theta_{\mathrm{Rx},p,c}(t) + \Delta\overline{\theta}_{\mathrm{Rx},c} \cdot v\Delta t_s,\\
\left|\gamma_{p,c}(t+\Delta t_s)\right|_{\mathrm{dB}} &= \left|\gamma_{p,c}(t)\right|_{\mathrm{dB}} + \Delta\sigma^2_{\gamma,c} \cdot v\Delta t_s.
\end{aligned} \tag{5}$$

In this way, clusters are moving in delay (causing Doppler shifts) and in angles, and they smoothly change their power. The speed v is a scalar defining how fast clusters move. The "direction" of movement is defined by the cluster movement parameters.

These small-scale changes intrinsically introduce correlated fading. This repeated update inherently creates a Doppler spectrum, where each individual path contributes with its Doppler shift $\nu_{p,c} = -f_0 \cdot v \cdot \Delta\overline{\tau}_c$ (equal for all paths within a cluster). Of course, linear movement is just a first-order approximation of the true movement of clusters, a more complex method can be found in [41]. However, the model validation will show that modelling movements linearly is sufficient to accurately reflecting the time-variant propagation environment.

Whenever a cluster is fading in or fading out due to the birth/death process, the path weights, $\gamma_{p,c}$, are additionally updated over the course of one cluster-lifetime interval by

$$\left|\gamma_{p,c}(t+\Delta t_s)\right|_{\mathrm{dB}} = \left|\gamma_{p,c}(t+\Delta t_s)\right|_{\mathrm{dB}} \pm |\sigma_{\mathrm{in/out}}|_{\mathrm{dB}}. \tag{6}$$

3. Model Validation

Validation is paramount, it scrutinises whether a model reflects important properties of the propagation channel. Particularly for MIMO channels, models need to reflect the *spatial structure* of the channel correctly.

We validated the RCM against MIMO channel measurements carried out with an Elektrobit Propsound CS wideband channel sounder at two centre frequencies of 2.55 GHz and 5.25 GHz. Details about the measurements and the validated scenarios are presented in Appendix A. For validation we will use three different validation metrics reflecting the spatial structure of the channels.

3.1. Validation Framework. We use the following procedure to validate the RCM (Figure 4).

(1) Perform radio channel measurements in representative scenarios and estimate propagation paths [32] from the measurements for every snapshot of the channel.

(2) Parametrise the RCM (see Section 2.2.3).

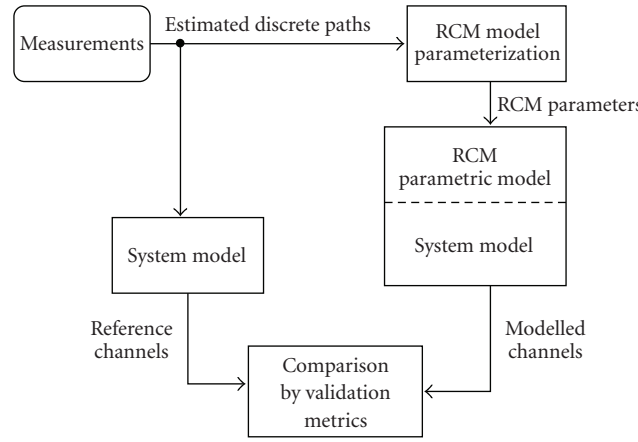

Figure 4: Validation framework.

(3) Generate *reference channels* by applying the system model (see Section 2.3.3) to the estimated paths parameters.

(4) Generate *smoothly time-variant modelled channels* by invoking the RCM.

(5) Compare the modelled channels with the reference channels according to the cdf of different validation metrics.

3.2. Validation Metrics. Before detailing the validation results, we present the different validation metrics. We concentrate on the validation of the *spatial properties* of the modelled channels.

3.2.1. Mutual Information. For the purpose of comparison with literature we take mutual information (MI) for model validation [42, 43]. (Quite frequently the term "capacity" is misused for mutual information.) However, we will show later in this section that MI has an intrinsic disadvantage, which disqualifies it as a good metric *for validating the double-directional multipath structure* of a time-varying channel.

We use the *narrowband MI* at frequency Δf and time t, which is defined as

$$I(t,\Delta f) = \log_2 \det\left[\mathbf{I} + \frac{\mathrm{SNR}}{N_t}\mathbf{H}_n(t,\Delta f)\mathbf{H}_n^{\mathrm{H}}(t,\Delta f)\right], \tag{7}$$

where $\mathbf{H}_n(t,\Delta f)$ denotes the *normalised* channel matrix, hence $\mathbf{H}_n = \mathrm{const} \cdot \mathbf{H}$. We use the normalisation to keep the receive SNR constant, which corresponds to perfect power control at the Tx. In this case, the channel transfer matrix at every time instant is normalized separately as

$$\mathbf{H}_n(t,\Delta f) = \frac{1}{(1/\mathrm{M})\sum_{\Delta f}\left\|\mathbf{H}(t,\Delta f)\right\|_{\mathrm{F}}^2}\mathbf{H}(t,\Delta f), \tag{8}$$

where M denotes the number of frequencies. Then, the validation metric reflects the spatial structure of the channel best. We chose an SNR of 10 dB for the following validation

evaluations. For creating a cdf, we use all time realisations and frequencies as our ensemble of samples.

The deficiencies of MI as a validation metric will now be demonstrated by a meaningful example. This example will also highlight the difference between *average MI* and *ergodic capacity*.

In Figure 5(a) we consider a *single snapshot* measured in the cafeteria environment (see Appendix A.2). This snapshot is described by a number of propagation paths with their parameters power, AoA, AoD, and delay. We now calculate the channel matrix of this scenario using the system model (4). Then, we create further channel realisations by just *changing the phases of the paths randomly*, but do not alter any other parameter. This method was introduced in [44] to generate multiple MIMO fading realisations from *a single measurement*. Note that this does not change the spatial structure of the channel at all. Finally, we calculate the MI for all these realisations according to (8).

Figure 5(b) shows the cdf of the so-computed MI. The *MI varies considerably*, even though the *spatial structure of the channel remains the same*. The reason for this effect is the fading created by randomly changing the phases of the paths. One can see that *mutual information fails to reflect the spatial structure* of a *single realisation* of an environment. A validation metric reflecting the *spatial structure* should provide one unique result, and not a widespread distribution. For this reason, MI is not suited to assess whether a channel model provides a correct spatial representation of the scenario or not.

As the spatial structure determines which gains the channel offers, the RCM strives to reflect the spatial structure as accurately as possible. Thus, also the validation metric should be specific to the spatial structure. Nevertheless, as MI is frequently used for validating MIMO channel models, we will also use MI in this paper, for reasons of comparison, but point out its deficiencies in the results.

3.2.2. Environment Characterisation Metric. The Environment Characterisation Metric (ECM) [29] is directly applied to the *path parameters* rather than to the channel matrix. This section shortly describes the significance of the ECM. For better readability, we will (i) enumerate all paths in each time instant from $l(t') = 1, \ldots, L(t')$, disregarding cluster structures for the time being, and (ii) skip the time index t' in the following derivations whenever it is redundant.

The metric copes with path parameters in different units (angles and delay). For every path l, the *angular data* is transformed into its coordinates on the unit sphere for both Rx and Tx. For angles of arrival the transformation is given as

$$\begin{bmatrix} x_{\mathrm{Rx},l} & y_{\mathrm{Rx},l} & z_{\mathrm{Rx},l} \end{bmatrix} = \frac{1}{2}\begin{bmatrix} \sin(\varphi_{\mathrm{Rx},l})\cdot\sin(\theta_{\mathrm{Rx},l}) & \sin(\varphi_{\mathrm{Rx},l})\cdot\cos(\theta_{\mathrm{Rx},l}) & \cos(\theta_{\mathrm{Rx},l}) \end{bmatrix}, \tag{9}$$

for angles at the Tx it reads similarly. The *delays* are scaled by the maximum expected delay that occurs in the considered snapshots [45], hence $\tilde{\tau}_l = \tau_l/(\tau_l^{(\max)})$. So, every path is now described by seven *dimensionless* parameters collected in

$$\boldsymbol{\pi}_l = \begin{bmatrix} x_{\mathrm{Rx},l} & y_{\mathrm{Rx},l} & z_{\mathrm{Rx},l} & x_{\mathrm{Tx},l} & y_{\mathrm{Tx},l} & z_{\mathrm{Tx},l} & \tilde{\tau}_l \end{bmatrix}^{\mathrm{T}}, \tag{10}$$

and by its power $|\gamma_l|^2$. When considering only azimuthal propagation, the z-direction must be excluded. (Since the elevation estimation from our data was not trustworthy, we excluded elevation in the validation.)

The *environment characterization metric* (ECM) is defined as the empirical covariance matrix of the path parameter vector $\boldsymbol{\pi}$,

$$\mathbf{C}_{\boldsymbol{\pi}} = \frac{\sum_{l=1}^{L} |\gamma_l|^2 (\boldsymbol{\pi}_l - \overline{\boldsymbol{\pi}})(\boldsymbol{\pi}_l - \overline{\boldsymbol{\pi}})^T}{\sum_{l=1}^{L} |\gamma_l|^2}, \tag{11}$$

with the mean parameter vector given as $\overline{\boldsymbol{\pi}} = (\sum_{l=1}^{L} |\gamma_l|^2 \boldsymbol{\pi}_l)/(\sum_{l=1}^{L} |\gamma_l|^2)$.

The ECM has the following properties [29].

(i) The metric is *system independent* as it is calculated from the propagation paths directly. Additionally, the metric is independent of the phases of the propagation paths.

(ii) The main diagonal contains the directional spreads (comparable to the azimuth and elevation spreads) at Rx and Tx, and the (normalized) rms delay spread. In this way, the ECM jointly represents the *spatial structure, and wideband properties* of the channel.

(iii) The trace $\mathrm{tr}\{\mathbf{C}_{\boldsymbol{\pi}}\}$ is the sum of the directional spreads [46] at Rx and Tx plus the (normalized) delay spread.

(iv) The determinant $\det\{\mathbf{C}_{\boldsymbol{\pi}}\}$ describes the volume spanned in the parameter space.

We use the ECM for the following two purposes.

(1) Validating the spatio-temporal multipath structure: the *singular values of the ECM* (SV-ECM) can be interpreted as the *fingerprint* of the scenario, by which one can judge the compactness of the paths in the channel. Assuming that the parameters of all paths span a multidimensional ellipsoid, the SVs describe the lengths of the main axes of this ellipsoid. In this way, it transforms the traditional view of individual parameter spread values into a joint-spread approach. These properties make the SV-ECM genuinely suited for comparing channels. Calculating the SV-ECM for the example shown in Figure 5(a), the snapshot would result in the *same values* of the SV-ECM, no matter which phases the paths have. This demonstrates that the SV-ECM is a consistent metric, reflecting the multipath structure of the channel.

(2) Validating the time-variance: the rate of change of the ECM shows how strongly the parametric channel changes between two neighbouring time instants. To quantify the rate of change between two ECM

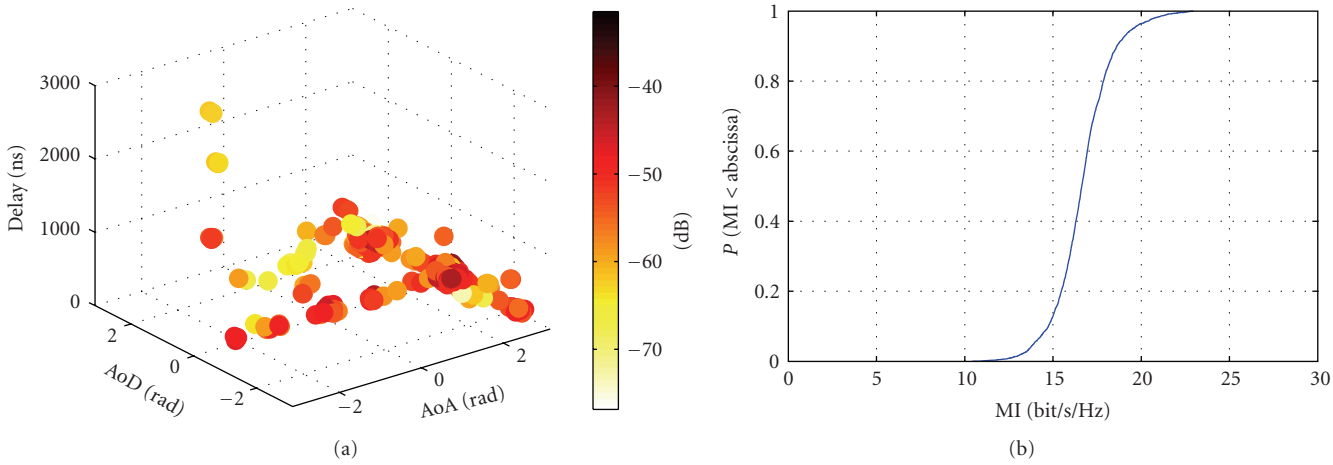

FIGURE 5: Why mutual information (MI) is no good validation metric: (a) multipath structure of an environment; each MPC is represented by a color-coded dot. (b) MI cdf computed from environment (a) by adding random phases to the paths, but not changing them otherwise.

matrices of adjacent snapshots, we use the Frobenius inner matrix product [47] as

$$\xi(\mathbf{C}_{\pi}(t'), \mathbf{C}_{\pi}(t' + \Delta t_s)) = \frac{\mathrm{tr}\left\{\mathbf{C}_{\pi}(t')^{T}\mathbf{C}_{\pi}(t' + \Delta t_s)\right\}}{\|\mathbf{C}_{\pi}(t')\|_{\mathrm{F}}\|\mathbf{C}_{\pi}(t' + \Delta t_s)\|_{\mathrm{F}}}, \quad (12)$$

where $\mathrm{tr}\{\cdot\}$ denotes the matrix trace operator, and $\|\cdot\|_{\mathrm{F}}$ denotes the Frobenius matrix norm. The Frobenius inner product quantifies how similar the eigenvectors of the two matrix arguments are. For collinear matrices, we have $\xi = 1$, while for orthogonal matrices, $\xi = 0$.

3.2.3. Diversity Measure. Spatial diversity describes the number of independent fading links between the Tx and Rx antenna arrays. In a full-diversity system, where all links between the Tx and Rx arrays are independent, one observes a spatial diversity of $N_{\mathrm{Tx}}N_{\mathrm{Rx}}$ [48]. This diversity is directly linked with the uncoded bit-error ratio (BER) performance of MIMO systems [1].

Channel correlation reduces this diversity significantly. Ivrlac and Nossek provided the *Diversity Measure* [28], a way to quantify the available diversity directly from the MIMO channels without taking the detour via BER simulations. We will use this measure to quantify the diversity in both the measured and the modelled channels, and subsequently compare the results.

The Diversity Measure $D(\mathbf{R})$ of a MIMO system described by a channel matrix $\mathbf{H}$ with channel correlation matrix $\mathbf{R} = \mathrm{E}\{\mathrm{vec}(\mathbf{H})\mathrm{vec}(\mathbf{H})^{\mathrm{H}}\}$ is given by

$$D(\mathbf{R}) = \left(\frac{\mathrm{tr}(\mathbf{R})}{\|\mathbf{R}\|_{\mathrm{F}}}\right)^{2}. \quad (13)$$

Invoking the channel *correlation* matrix implicitly assumes the channel to be stationary over the time period of a sliding window. We want to bring to attention that the *channel correlation matrix* used here is entirely different from the *path covariance matrix* used as ECM in (11). To estimate samples of the channel correlation matrix, we chose a sliding window over $W = 8$ snapshots and all frequencies, that is,

$$\mathbf{R}(t) = \frac{1}{MW}\sum_{\Delta f}\sum_{t=t'}^{t'+W\Delta t_s}\mathrm{vec}\{\mathbf{H}(t, \Delta f)\}\mathrm{vec}\{\mathbf{H}(t, \Delta f)\}^{\mathrm{H}}, \quad (14)$$

with $\mathbf{H}(t, \Delta f)$ defined in (4). These estimated correlation matrices for all time instants are taken as ensemble to obtain the cdf of (13).

3.3. Validation Results. This paper presents validation results for two particularly interesting scenarios, (i) a measurement route in an office scenario, *without* line of sight between transmitter and receiver, and (ii) a route within a cafeteria (large room) mostly with LOS between transmitter and receiver (see Figure 11 in Appendix A.2). The Tx was moved through the rooms while the Rx was placed at a fixed position. The cafeteria scenario is a particularly challenging one, difficult to represent by any MIMO channel model, as it is a combination of two totally different propagation environments, depending on whether the LOS between Rx and Tx is blocked or not. For validation we generated *smoothly-time varying channels* using the RCM and used the three validation metrics described in the previous paragraphs. The validation of more scenarios can be found in [36, Chapter 4].

First, we use the ECM to *validate the spatiotemporal multipath structure*. Figure 6 compares the SV-ECM of the modelled paths with those identified directly from measurements "reference channels", both at 2.55 GHz and at 5.25 GHz, neglecting elevation. The ECM offers five SVs, shown as dashed lines (RCM) and solid lines (measurements). We observe that, judging from the ECM, the multipath structure is quite similar at the two carrier frequencies in both scenarios. The NLOS office scenario is much better matched at 2.55 GHz than at 5.25 GHz. At 5.25 GHz, the third and

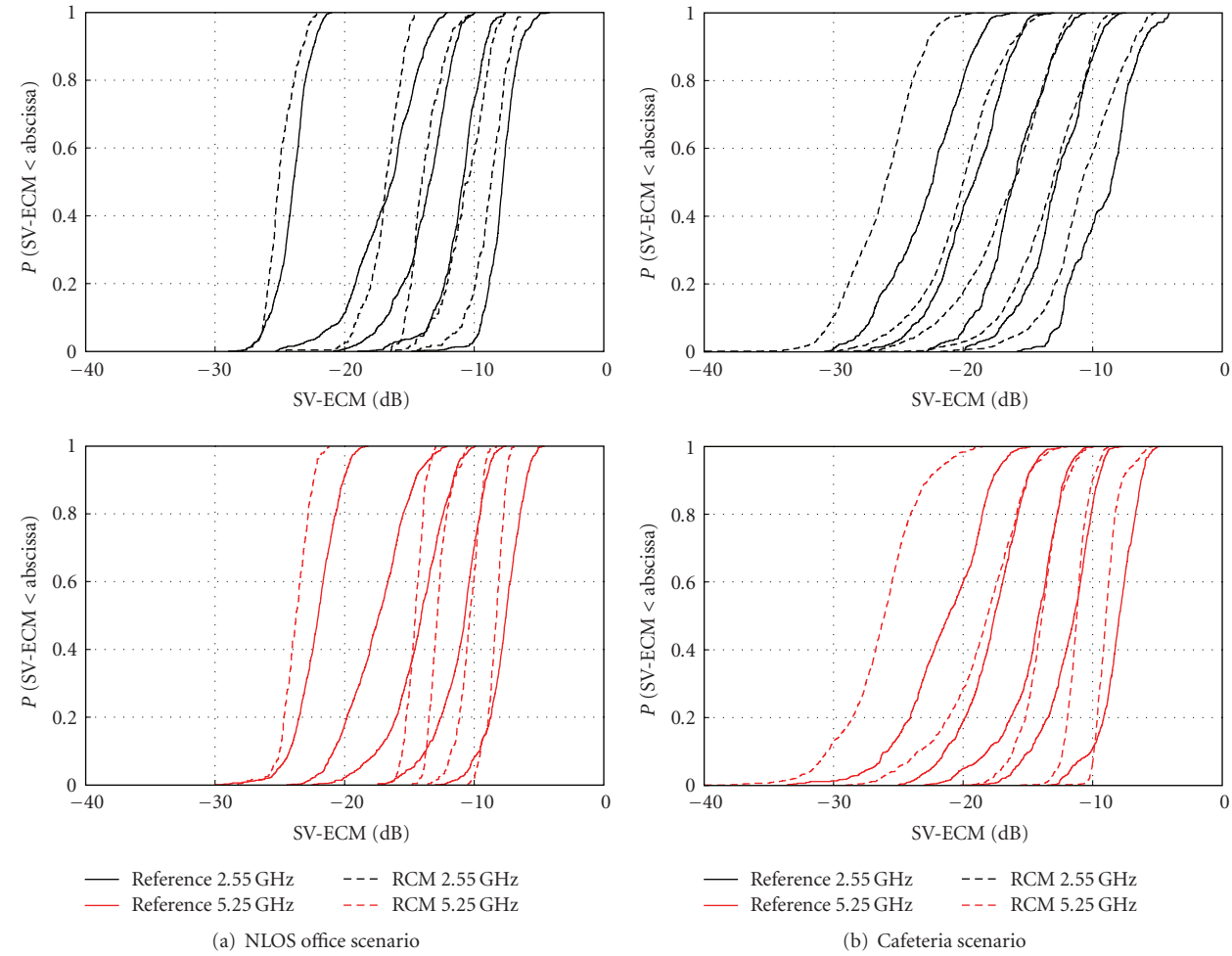

(a) NLOS office scenario (b) Cafeteria scenario

Figure 6: Model validation using the Environment Characterisation Metric. Shown are the distributions of the five singular values of the ECM.

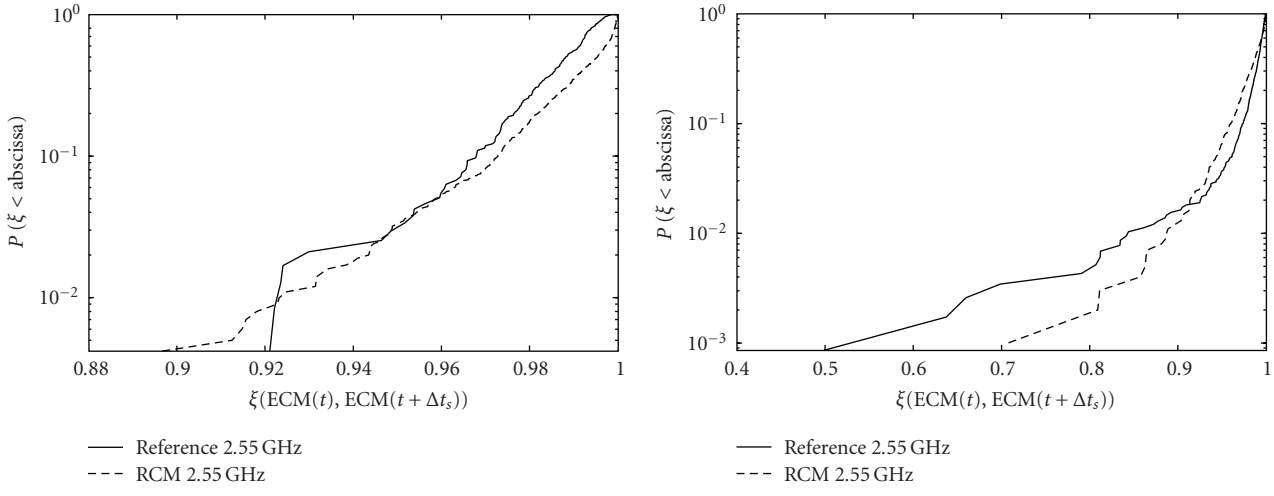

(a) NLOS office scenario (b) Cafeteria scenario

Figure 7: Time-variant validation using the Environment Characterisation Metric: CDF of collinearity between snapshots adjacent in time ($\Delta t = 0.22$ seconds).

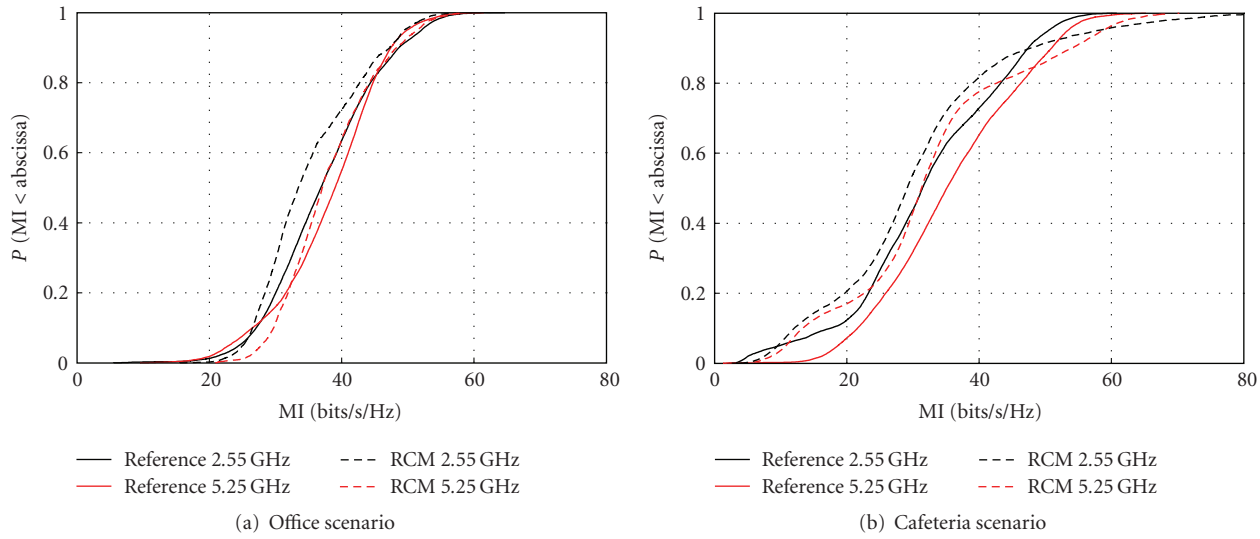

(a) Office scenario (b) Cafeteria scenario

Figure 8: Model validation using mutual information.

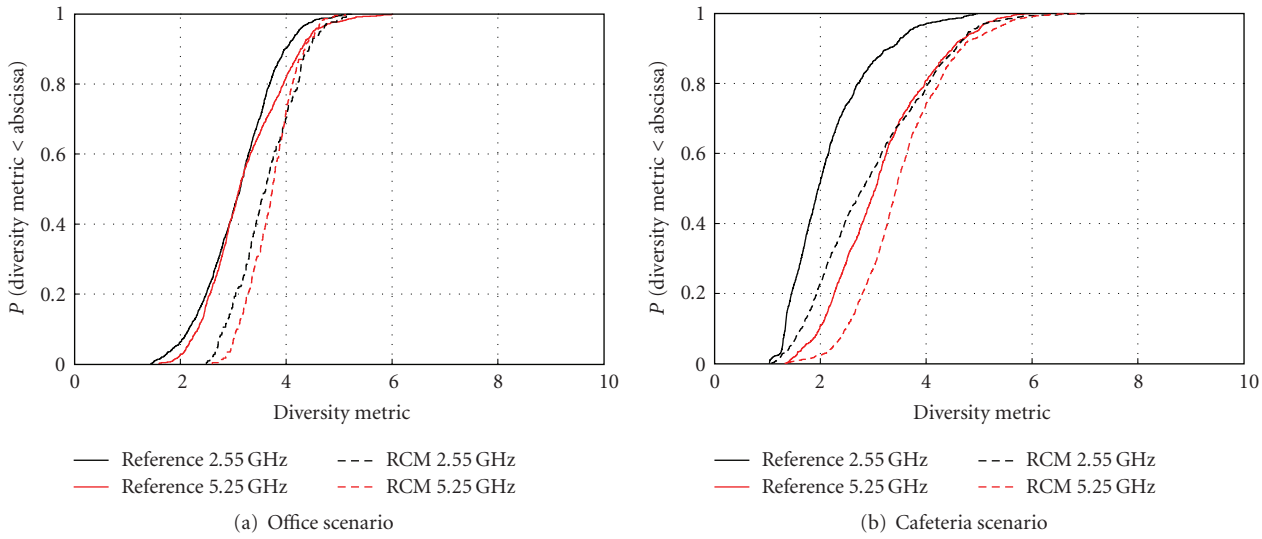

(a) Office scenario (b) Cafeteria scenario

Figure 9: Model validation using the diversity measure.

fourth SV-ECM of the modelled channels obviously have a positive bias. The reason for this poor match is an environment pdf that has little variation, particularly in the cluster receive azimuth position domain. This leads to reduced randomness when drawing the parameters of the scenarios, resulting in steeper SV-ECM cdfs. Considering the cafeteria scenario, there is much stronger variability, but still the environment is represented quite well. In both scenarios, the smallest SV-ECM of the modelled channels has a significant negative bias. We found the reason for this to be outlier paths that were estimated from the measurement, but these are not modelled by the RCM.

In a second step, we use the collinearity between two ECM matrices to *validate the time variance*. Figure 7 quantifies how strongly the channels change from snapshot to snapshot. In detail, the figure shows the cdfs of the ECM distances evaluated between all two adjacent time instants for both the modelled channels and the reference channels. A value of $\xi = 1$ indicates that the channels did not change, while smaller numbers indicate changes in the multipath structure.

In the NLOS office scenario, where the SNR of the measurement was only average, we observe that the model has a slightly lower number of small changes than the reference channels (rightmost part of Figure 7(a)). This is due to the path parameter estimation algorithm, which always estimates a number of outlier paths that appear at random in any single time snapshot. In the cafeteria scenario, we observe much stronger changes than in the office scenario due to the changes in the LOS part of the environment. The measurement SNR was high, so random outliers were no problem, as the rightmost part of the curves show. Between

the outage probabilities of 10^{-2} and 1, the model fits the measurement very well, which is the statistically relevant part. The few much larger changes that are observed in the measurements occur during the abrupt transition from LOS to NLOS.

Next, we present the validation using *mutual information*. Figure 8 shows the cdf of the evaluated mutual information for both modelled and reference channels at both carrier frequencies. We observe that the MI of the modelled channels have a negative bias in both scenarios. This could be already expected from the ECM validation, where the spreading of the paths (strongest SV-ECM) was also slightly too low. We discourage the use of MI for validating the spatial structure of the radio channel, since *MI is influenced by both spatial structure and fading*.

Finally, Figure 9 compares the Diversity Measure values of the modelled channels with the reference channels. In both scenarios, diversity is slightly overmodelled. While this is also a common effect of analytical channel models, there is no connection here. It may also happen that the RCM undermodels diversity. This result could also have been expected from the MI cdfs, where the cdf of the modelled channels showed a sligtly steeper slope than the cdf of the reference channels.

4. Conclusions

The presented Random-Cluster Model is well able to reflect the spatial properties of measured time-variant MIMO channels, even if the properties of the environment are varying between LOS and NLOS. By its direct parametrisation from measurement data, the RCM is specific to the measured environment. Since the RCM is propagation-based, the RCM is also scalable in carrier frequency, in bandwidth, and in its antenna array configuration. Still, it is a stochastic model. The propagation environment is described using a multivariate pdf of the cluster parameters. Depending on the accuracy of the estimation of this pdf from measurements, the parametrisation complexity is scalable. Time variance is implemented by linear cluster movement. Using the recommended clustering algorithm in combination with a Kernel Density Estimator, the RCM is parametrised automatically without user interaction.

Validation showed a close fit between the channels modelled by the RCM, and reference channels obtained from the measurements. Even though the RCM was only successfully validated against indoor measurements, the model structure is also well suited to represent outdoor radio channels, when adapting the parameters, respectively. This renders the RCM to be ideally suited to model particularly interesting propagation conditions that were measured before.

Appendix

A. Channel Measurements

This appendix describes the channel measurement equipment and the investigated scenarios.

Table 2: Parameter settings for the PropSound Channel Sounder[CS].

Parameter	2.55 GHz	5.25 GHz
Transmit power [dBm]	26	26
Bandwidth [MHz]	200	200
Chip frequency [MHz]	100	100
Number of TX antennas	56	50
Number of RX antennas	8	32
Code length [μs]	2.55	2.55
Channel sampling rate [Hz]	92.6	59.4
Cycle duration [μs]	1542.24	8415.00
TX antenna height [m]	1.53	1.53
RX antenna height [m]	1.05	0.82

A.1. Equipment

We employed a wideband radio channel sounder, EB Propsound CS [49], which utilizes periodic pseudorandom binary signals. The sounder is described in more detail in [50]. In sounding, M-sequences with adjustable code lengths are transmitted and multiplexed by switching the transmit and receive antennas. The spread spectrum signal has 100 Mchip/s chip rate and switches through all the antennas with the cycle rates presented in Table 2. Thus, sequential radio channel measurement between all possible TX and RX antenna pairs is achieved. The number of antenna elements used is inversely proportional to the cycle rate. The sounder was operated in burst-mode, that is, after four measuring cycles there was a break to allow real-time data transfer to the hard disk unit. During the measurements, a real-time display of the received impulse responses (IRs) could be monitored from the control laptop computer. In addition to basic data handling features, the post-processing tools include the ISIS (Initialization and Search Improved SAGE) software to identify individual MPCs by a super-resolution SAGE algorithm employing maximum likelihood techniques for parameter estimation [51].

The selected antenna arrays (Figure 10) are able to capture largely the spatial characteristics of the radio channel at *both* link-ends. The 2.55 GHz array (Figure 10(a)) used at the TX consists of 28 dual-polarized patch elements. The elements are positioned in a way that allows channel probing in the *full* azimuth domain. The upper ring of antenna elements in the ODA was not operative on one link end, so elevation information was not extracted from the measurements. Figure 10(b) shows the uniform circular array with 7 + 1 monopoles used at the RX end at 2.55 GHz. It supports full azimuth direction probing but not the elevation. At 5.25 GHz both TX and RX had 25 element patch arrays shown in Figure 10(c). Their properties are similar to the 2.55 GHz patch array. Table 3 shows the azimuth and elevation coverage of the antennas.

All antennas had been calibrated in an anechoic chamber. The signal model on which SAGE is based is using the measured array pattern data for calculating the angles of impinging or outgoing waves. In the calibration process, the antenna pattern of each single element was measured in

(a) 3 × 8 ODA, 2.55 GHz

(b) 7 + 1 UCA, 2.55 GHz

(c) 2 × 9 ODA, 5.25 GHz

Figure 10: Antenna arrays. (a) 2.55 GHz omni-directional patch array (ODA), (b) 2.55 GHz circular monopole array (UCA), (c) 5.25 GHz ODA.

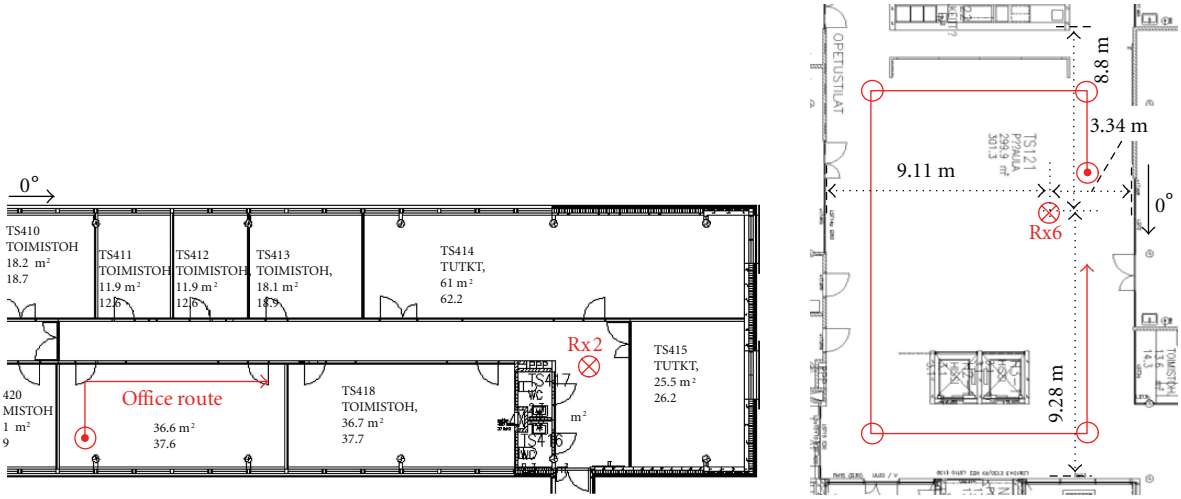

(a) Office environment

(b) Cafeteria

Figure 11: Measured scenarios.

Table 3: Antenna parameters.

Antenna	Azimuth coverage	Elevation coverage
3 × 8 ODA 2.55 GHz	−180° · · · 180°	−55° · · · 90°
7 + 1 UCA 2.55 GHz	−180° · · · 180°	0° · · · 60°
2 × 9 ODA 5.25 GHz	−180° · · · 180°	−55° · · · 90°

amplitude and phase over azimuth and elevation, resulting in an azimuth/elevation matrix. This measurement was done for both horizontal and vertical polarisation. To minimize the interference of WLAN and Bluetooth, one center frequency for the measurements was chosen to be 2.55 GHz. Still, there seems to have been (spurious) radiation from these devices above 2.45 GHz, so we had to expect an enhanced noise floor in the IRs. The ensuing smaller dynamic range resulted in a smaller number of paths that ISIS could extract from the measurement. At the other center frequency of 5.25 GHz we did not observe any interference.

A.2. Scenarios

We took measurements on 28 different routes [36], of which we analyse two particularly interesting ones in this paper. The outer walls of the building were reinforced concrete or brick-stone walls, while inside walls were mostly of plasterboard with internal metal mounts.

The first measurement, NLOS throughout, was done in an office environment, where the receiver was fixed in the corridor and the transmitter was moved along a route in an office (Figure 11(a)).

The second measurement, predominantly LOS, was recorded in a cafeteria with metal tables and chairs. The receiver was fixed on a table, and the transmitter was moved along a route in the room. The Tx-Rx distance variation was large, and the LOS between transmitter and receiver was sometimes shadowed by an elevator (Figure 11(b)). People were moving randomly in the environment.

Acknowledgments

This work was partly carried out in the frameworks of the European Projects NEWCOM, COST 273, and COST 2100. The authors thank Elektrobit for partly funding the Ph.D. work of N. Czink and for providing the measurement equipment. The authors gratefully acknowledge the help of Veli-Matti Holappa and Mikko Alatossava during the

measurement campaign. The Telecommunications Research Center Vienna (ftw.) is supported by the Austrian Government and the City of Vienna within the competence centre programme COMET.

References

[1] A. J. Paulraj, D. A. Gore, R. U. Nabar, and H. Bölcskei, "An overview of MIMO communications—a key to gigabit wireless," *Proceedings of the IEEE*, vol. 92, no. 2, pp. 198–218, 2004.

[2] I. E. Telatar, "Capacity of multi-antenna Gaussian channels," Tech. Rep. BL0112170-950615-07TM, AT&T Bell Laboratories, Murray Hill, NJ, USA, 1995.

[3] http://www.beceem.com.

[4] http://www.linksys.com.

[5] "3GPP—The 3rd Generation Partnership Project," 2008, http://www.3gpp.org.

[6] "IEEE 802.16 working group on broadband wireless access standards," 2008, http://wirelessman.org.

[7] D.-S. Shiu, G. J. Foschini, M. J. Gans, and J. M. Kahn, "Fading correlation and its effect on the capacity of multielement antenna systems," *IEEE Transactions on Communications*, vol. 48, no. 3, pp. 502–513, 2000.

[8] W. Weichselberger, M. Herdin, H. Özcelik, and E. Bonek, "A stochastic MIMO channel model with joint correlation of both link ends," *IEEE Transactions on Wireless Communications*, vol. 5, no. 1, pp. 90–100, 2006.

[9] A. Edelman and N. R. Rao, "Random matrix theory," *Acta Numerica*, vol. 14, pp. 233–297, 2005.

[10] L. C. Wood and W. S. Hodgkiss, "MIMO channel models and performance metrics," in *Proceedings of IEEE Global Telecommunications Conference (GLOBECOM '07)*, pp. 3740–3744, Washington, DC, USA, November 2007.

[11] S. Wyne, A. F. Molisch, P. Almers, G. Eriksson, J. Karedal, and F. Tufvesson, "Outdoor-to-indoor office MIMO measurements and analysis at 5.2 GHz," *IEEE Transactions on Vehicular Technology*, vol. 57, no. 3, pp. 1374–1386, 2008.

[12] T. Fügen, J. Maurer, C. Kuhnert, and W. Wiesbeck, "A modelling approach for multiuser MIMO systems including spatially-colored interference," in *Proceedings of IEEE Global Telecommunications Conference (GLOBECOM '04)*, vol. 2, pp. 938–942, Dallas, Tex, USA, November-December 2004.

[13] V. Degli-Esposti, D. Guiducci, A. de'Marsi, P. Azzi, and F. Fuschini, "An advanced field prediction model including diffuse scattering," *IEEE Transactions on Antennas and Propagation*, vol. 52, no. 7, pp. 1717–1728, 2004.

[14] "Spatial channel model for Multiple Input Multiple Output (MIMO) simulations," Tech. Rep. TR 25.996 V6.1.0, 3GPP, Valbonne, France, September 2003.

[15] P. Kyösti, J. Meinilä, L. Hentilä, et al., "WINNER II channel models (d1.1.2v1.1)," November 2007, http://www.ist-winner.org.

[16] L. Correia, Ed., *Mobile Broadband Multimedia Networks*, Academic Press, San Diego, Calif, USA, 2006.

[17] A. Saleh and R. Valenzuela, "A statistical model for indoor multipath propagation," *IEEE Journal on Selected Areas in Communications*, vol. 5, no. 2, pp. 128–137, 1987.

[18] Q. H. Spencer, B. D. Jeffs, M. A. Jensen, and A. L. Swindlehurst, "Modeling the statistical time and angle of arrival characteristics of an indoor multipath channel," *IEEE Journal on Selected Areas in Communications*, vol. 18, no. 3, pp. 347–360, 2000.

[19] H. Xiao, A. G. Burr, L. Hentilä, and P. Kyösti, "Statistical technique to identify clusters from multi-dimensional measurement data," in *Proceedings of the 2nd European Conference on Antennas and Propagation (EuCAP '07)*, pp. 1–7, Edinburgh, UK, November 2007.

[20] G. D. Galdo, N. Czink, and M. Haardt, "Cluster spatial localization from high-resolution parameter estimation," in *Proceedings of IEEE/ITG Workshop on Smart Antennas (WSA '06)*, pp. 1–7, Ulm, Germany, March 2006.

[21] J. Salo, J. Salmi, N. Czink, and P. Vainikainen, "Automatic clustering of nonstationary MIMO channel parameter estimates," in *Proceedings of the 2nd International Conference on Telecommunications (ICT '05)*, Cape Town, South Africa, May 2005.

[22] N. Czink, P. Cera, J. Salo, E. Bonek, J-.P. Nuutinen, and J. Ylitalo, "Improving clustering performance using multipath component distance," *Electronics Letters*, vol. 42, no. 1, pp. 33–35, 2006.

[23] N. Czink, P. Cera, J. Salo, E. Bonek, J.-P. Nuutinen, and J. Ylitalo, "A framework for automatic clustering of parametric MIMO channel data including path powers," in *Proceedings of IEEE Vehicular Technology Conference (VTC '06)*, pp. 114–118, Montreal, Canada, September 2006.

[24] N. Czink, R. Tian, S. Wyne, et al., "Tracking time-variant cluster parameters in MIMO channel measurements," in *Proceedings of the 2nd International Conference on Communications and Networking in China (ChinaCom '07)*, pp. 1147–1151, Shanghai, China, August 2007.

[25] N. Czink, E. Bonek, L. Hentilä, J.-P. Nuutinen, and J. Ylitalo, "A measurement-based random-cluster MIMO channel model," in *Proceedings of IEEE Antennas and Propagation International Symposium*, pp. 5363–5366, Honolulu, Hawaii, USA, June 2007.

[26] N. Czink, E. Bonek, J. Ylitalo, and T. Zemen, "Measurement-based time-variant MIMO channel modelling using clusters," in *Proceedings of the 29th General Assembly of the International Union of Radio Science (URSI '08)*, Chicago, Ill, USA, August 2008.

[27] P. Kyösti and T. Jämsä, "Complexity comparison of MIMO channel modelling methods," in *Proceedings of the 4th IEEE Internatilonal Symposium on Wireless Communication Systems (ISWCS '07)*, pp. 219–223, Trondheim, Norway, October 2007.

[28] M. T. Ivrlac and J. A. Nossek, "Quantifying diversity and correlation in Rayleigh fading MIMO communication systems," in *Proceedings of the 3rd IEEE International Symposium on Signal Processing and Information Technology (ISSPIT '03)*, pp. 158–161, Darmstadt, Germany, December 2003.

[29] N. Czink, G. D. Galdo, X. Yin, E. Bonek, and J. Ylitalo, "A novel environment characterizationmetric for clustered MIMO channels: used to validate a SAGE parameter estimator," *Wireless Personal Communications*, vol. 46, no. 1, pp. 83–98, 2008.

[30] M. Steinbauer, A. F. Molisch, and E. Bonek, "The double-directional radio channel," *IEEE Antennas and Propagation Magazine*, vol. 43, no. 4, pp. 51–63, 2001.

[31] J. Kolu, J.-P. Nuutinen, T. Jämsä, J. Ylitalo, and P. KyÖsti, "Playback simulations of measured MIMO radio channels," COST 273, TD(04)110, COST, Gothenburg, Sweden, June 2004.

[32] B. H. Fleury, M. Tschudin, R. Heddergott, D. Dahlhaus, and K. I. Pedersen, "Channel parameter estimation in mobile radio environments using the SAGE algorithm," *IEEE Journal on Selected Areas in Communications*, vol. 17, no. 3, pp. 434–450, 1999.

[33] N. Czink, R. Tian, S. Wyne, et al., "Cluster parameters for time-variant MIMO channel models," in *Proceedings of the 2nd European Conference on Antennas and Propagation (EuCAP '07)*, pp. 1–8, Edinburgh, UK, November 2007.
[34] A. Ihler, "Kernel Density Estimation Toolbox for MATLAB (R13)," July 2007, http://ttic.uchicago.edu/~ihler/code.
[35] D. W. Scott, *Multivariate Density Estimation*, John Wiley & Sons, New York, NY, USA, 1992.
[36] N. Czink, *The random-cluster model—a stochastic MIMO channel model for broadband wireless communication systems of the 3rd generation and beyond*, Ph.D. dissertation, Technische Universität Wien, Vienna, Austria, FTW Dissertation Series, December 2007.
[37] K. V. Mardia and P. E. Jupp, *Directional Statistics*, John Wiley & Sons, New York, NY, USA, 2000.
[38] P. Almers, E. Bonek, A. Burr, et al., "Survey of channel and radio propagation models for wireless MIMO systems," *EURASIP Journal on Wireless Communications and Networking*, vol. 2007, Article ID 19070, 19 pages, 2007.
[39] F. Kaltenberger, T. Zemen, and C. W. Üeberhuber, "Low-complexity geometry-based MIMO channel simulation," *EURASIP Journal on Advances in Signal Processing*, vol. 2007, Article ID 95281, 17 pages, 2007.
[40] H. Asplund, A. A. Glazunov, A. F. Molisch, K. I. Pedersen, and M. Steinbauer, "The COST 259 directional channel model—part II: macrocells," *IEEE Transactions on Wireless Communications*, vol. 5, no. 12, pp. 3434–3450, 2006.
[41] J. W. Wallace and M. A. Jensen, "Time-varying MIMO channels: measurement, analysis, and modeling," *IEEE Transactions on Antennas and Propagation*, vol. 54, no. 11, pp. 3265–3273, 2006.
[42] V. Erceg, L. Schumacher, P. Kyritsi, et al., "TGn channel models," Tech. Rep., IEEE P802.11, Geneva, Switzerland, 2004, http://grouper.ieee.org/groups/802/11/.
[43] P. Kyösti, D. Laselva, L. Hentilä, and T. Jämsä, "Validating IST-WINNER indoor MIMO radio channel model," in *IST Mobile and Wireless Summit*, Mykonos, Greece, June 2006.
[44] A. F. Molisch, M. Steinbauer, M. Toeltsch, E. Bonek, and R. S. Thomä, "Capacity of MIMO systems based on measured wireless channels," *IEEE Journal on Selected Areas in Communications*, vol. 20, no. 3, pp. 561–569, 2002.
[45] M. Steinbauer, H. Özcelik, H. Hofstetter, C. F. Mecklenbräuker, and E. Bonek, "How to quantify multipath separation," *IEICE Transactions on Electronics*, vol. E85-C, no. 3, pp. 552–557, 2002.
[46] B. H. Fleury, "First- and second-order characterization of direction dispersion and space selectivity in the radio channel," *IEEE Transactions on Information Theory*, vol. 46, no. 6, pp. 2027–2044, 2000.
[47] G. Golub and C. van Loan, *Matrix Computations*, The Johns Hopkins University Press, London, UK, 3rd edition, 1996.
[48] C. Oestges and B. Clerckx, *MIMO Wireless Communications*, Academic Press, London, UK, 2007.
[49] Elektrobit EB Propsim, 2008, http://www.propsim.com.
[50] L. Hentilä, P. Kyösti, J. Ylitalo, X. Zhao, J. Meinilä, and J.-P. Nuutinen, "Experimental characterization of multi-dimensional parameters at 2.45 and 5.25 GHz indoor channels," in *Proceedings of the Wireless Personal Multimedia Communications (WPMC '05)*, pp. 254–258, Aalborg, Denmark, September 2005.
[51] B. H. Fleury, P. Jourdan, and A. Stucki, "High-resolution channel parameter estimation for MIMO applicationsusing the SAGE algorithm," in *Proceedings of the International Zurich Seminar on Broadband Communications*, pp. 1–9, Zurich, Switzerland, February 2002.

Hindawi Publishing Corporation
EURASIP Journal on Wireless Communications and Networking
Volume 2009, Article ID 804021, 16 pages
doi:10.1155/2009/804021

Research Article

Mobile Station Spatio-Temporal Multipath Clustering of an Estimated Wideband MIMO Double-Directional Channel of a Small Urban 4.5 GHz Macrocell

Lawrence Materum,[1] Jun-ichi Takada,[1] Ichirou Ida,[2] and Yasuyuki Oishi[2]

[1] *Takada Laboratory, Department of International Development Engineering, Graduate School of Science and Engineering, Tokyo Institute of Technology, 2-12-1-S6-4, O-okayama, Meguro-ku, Tokyo 152-8550, Japan*
[2] *Fujitsu Limited, 5-5 Hikari-no-oka, Yokosuka, Kanagawa 239-0847, Japan*

Correspondence should be addressed to Lawrence Materum, lawrence@ap.ide.titech.ac.jp

Received 2 August 2008; Revised 11 December 2008; Accepted 5 February 2009

Recommended by Michael A. Jensen

Multipath clusters in a wireless channel could act as additional channels for spatial multiplexing MIMO systems. However, identifying them in order to come up with better cluster channel models has been a hurdle due to how they are defined. This paper considers the identification of these clusters at the mobile station through a middle ground approach—combining a globally optimized automatic clustering approach and manual clustering of the physical scatterers. By including the scattering verification in the cluster identification, better insight into their behavior in wireless channels would be known, especially the physical realism and eventually a more satisfactorily accurate cluster channel model could be proposed. The results show that overlapping clusters make up the majority of the observed channel, which stems from automatic clustering, whereas only a few clusters have clear delineation of their dispersion. In addition, it is difficult to judge the physical realism of overlapping clusters. This further points to a need for the physical interpretation and verification of clustering results, which is an initial step taken in this paper. From the identification results, scattering mechanisms of the clusters are presented and also their selected first and second order statistics.

1. Introduction

The clustering of multipaths has started to be considered as an aspect of multiple-input multiple-output (MIMO) propagation channel models [1–3]. Given that they exist and depending on the target MIMO application, accurate knowledge of them in the channel is one of the ways to take advantage of the benefits of MIMO systems, especially that of spatial multiplexing systems, wherein these clusters could act as additional channels. Characterizing multipath clusters should therefore be satisfactorily accurate and this hinges on the reality of these clusters. This starts by identifying them appropriately. Many previous studies (e.g., [1, 4–7]) identified multipath clusters manually/visually after some preprocessing. Manual clustering approaches are the majority of the methods used in identifying multipath clusters. Distinct from these manual clustering approaches are automatic clustering approaches [8–11], which on the other hand are the minority. These automatic clustering approaches were made in response to the cumbersomeness of identifying clusters manually from large estimated channel data derived from channel sounding. Table 1 shows a comparison of these two approaches. Each approach has its own strengths and weaknesses. One big deficiency of current automatic clustering approaches is their lack of physical realism, that is, the multipath clustering results may not correspond to physical objects in the environment, thus they may just be numerical and inaccurate. In contrast, manual approaches could check the physical validity of the clustering results.

In this paper, a middle ground approach developed inductively from employing each approach is presented. It tries to draw the advantages of automatic and manual clustering. The automatic clustering approach is applied to estimated channel data, and then verified by manual clustering. The general goal is basically to understand the behavior

Table 1: Comparison of two multipath cluster identification approaches.

Automatic clustering	Manual clustering
– real-world clusters are complicated	– unwieldy and subjective
– mathematically trackable	– physically trackable
– number-based	– object-based
– "better" number processor	– "better" object processor

Table 2: Medav-RUSK-Fujitsu wideband MIMO channel sounder.

Carrier frequency	4.5 GHz
Bandwidth	120 MHz
BS antenna	Uniform rectangular array $2 \times 4 \times 2$ elements (row × col. × pol.) V & H polarized patch antennas
MS antenna	Stacked uniform circular array $2 \times 24 \times 2$ elements (row × col. × pol.) V & H polarized patch antennas
Transmit signal	Wideband multitone
Maximum delay setting	3.2 μs
Number of MIMO channels	1536

Table 3: Small urban macrocell scenario.

BS height	~ 85 m
MS height	~ 1.80 m
BS-MS distance	~ 230–400 m
Structure type	residential & industrial

of multipath clusters. However, the specific focus of this paper is to identify clusters more effectively. The outcomes consisted of overlapping clusters, which was attributed to automatic clustering, and clusters with clear delineation, attributed to the manual clustering approach. The result demonstrates the need for the physical interpretation and validation of automatic clustering results, which is an initial step done in this paper. This paper is structured then as follows. In Section 2, the source of the estimated MIMO channel data is described. This is followed by an overview of the approach in Section 3. The details of the approach are discussed in Sections 3.1 and 3.2, which refer to automatic and manual multipath clustering, respectively. Sections 2–3.2 comprise the highlighted part of the framework behind this paper as portrayed in Figure 1. After these sections, the results and subsequent discussions are laid out in Section 4. Finally, conclusions are summarized and drawn.

2. Estimated MIMO Channel

After a macrocell site survey and planning for a measurement campaign in Kawasaki City, Kanagawa, Japan, channel sounding was performed using the Medav-RUSK-Fujitsu MIMO channel sounder [12]. Pertinent details of this wideband channel sounder and the measurement site are in described in Tables 2 and 3, respectively. The array antennas

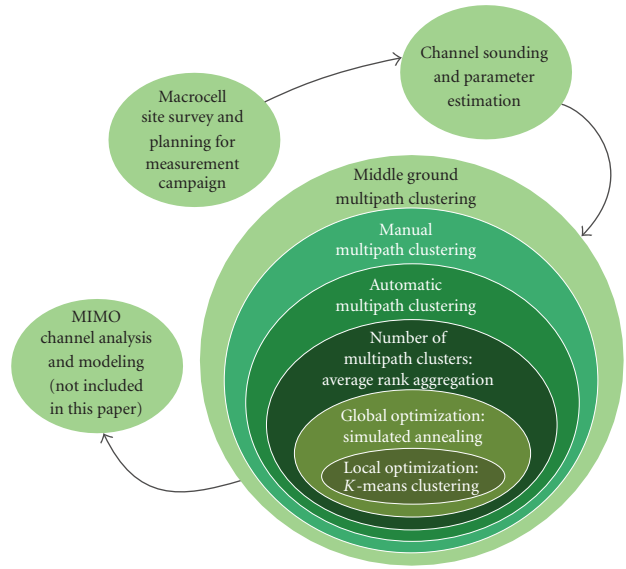

Figure 1: Overall framework. The prominent group presented in this paper shows the progression of the middle ground multipath clustering approach from the automatic clustering optimization to manual multipath clustering.

that were used were carefully calibrated in an anechoic chamber, which is important for path parameter estimation [13, 14]. A map of the small urban macrocell showing the base station (BS) and mobile station (MS) positions is shown in Figure 2. Photographs of selected positions are shown in Figure 3. With this measurement setup, time snapshots of the channel were taken after midnight under a clear spring weather while the MS was moved at a slowly walking pace along the street. In between MS positions, the MS movement covers a 20 m length route, starting and ending with static measurements.

A maximum likelihood multidimensional parameter estimation algorithm was used to extract the delay (τ), azimuth (ϕ), and co-elevation (θ) angle of departure (AoD), ϕ and θ angle of arrival (AoA), and the four complex polarimetric weights ($\gamma_{VV}, \gamma_{VH}, \gamma_{HV}, \gamma_{HH}$) including the diffuse components [15, 16], where V and H denote the vertical polarization and horizontal polarization, respectively. Briefly, the co-elevation angle is referred to here as the elevation angle. The estimation algorithm is based on the double-directional channel concept, which makes the results independent of the antennas used [17]. The measurement site and the estimated channel are precursors to the multipath clustering progression described in Figure 1.

3. Bicombinational Multipath Clustering

There has been basically two views in identifying multipath clusters in order to achieve a supposed satisfactorily accurate cluster channel model. One view is manual clustering, which is usually done through visual or manual means while the other is automatic clustering, which is performed algorithmically (see Table 1). Manual clustering could be

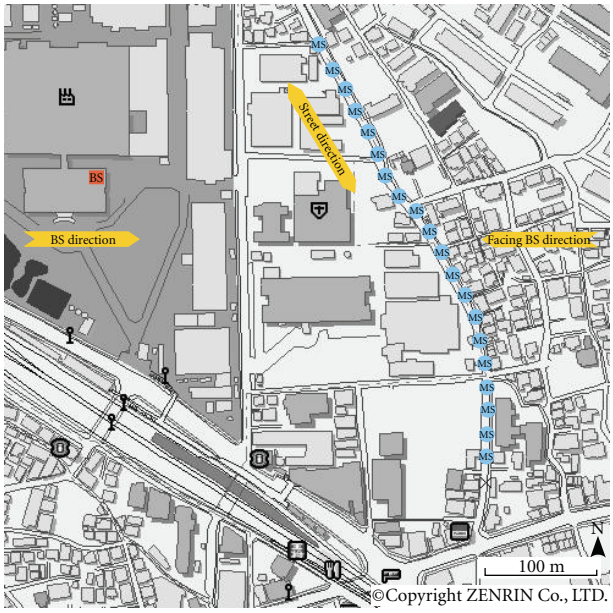

Figure 2: BS and MS positions in the measurement site. The BS antenna was placed on top of a building which was the highest one in that location (Figure 3(c)), whereas the MS positions were along the street. The average height of the buildings around the BS was less than half its height.

(a) A view from the BS

(b) A view from an MS position near the southeast side of Figure 2

(c) A view of the BS from an MS position

Figure 3: Views of the measurement site.

seen to operate like "group of patterns are seen, therefore they are clusters," whereas for automatic clustering "group of patterns are numerically optimized, so they are clusters." Thus, one approach depends on what is seen, but the other on numbers. Visual reliance per se or numerical reliance per se tend to focus only on their respective results. The approach of this paper tries to combine the strengths of each view.

Given the backdrop notion that modeling clusters starts by their correct identification, three factors were considered in the middle ground clustering approach. These factors are listed in Table 4.

In this paper, the multidimensional Euclidean distance was used primarily as the similarity/dissimilarity measure (see Section 3.1), whereas for the significance measure, clusters were considered primarily by their power (specifically, power proportion; see Section 4.1), and for the validation measure, they were verified: (i) numerically by the average rank aggregation (Section 3.1.3) of their clustering validity indices, and (ii) manually by their corresponding or associated scatterers and propagation mechanisms. It is noted that this is an important step in validating clusters produced by automatic clustering as it connects with the physical environment. It has been observed that this validation is lacking in many existing publications on multipath clusters.

A middle ground approach developed inductively from employing each view [18, 19], and then both views are presented here. In the automatic clustering side, a locally optimal clustering algorithm was used together with a stochastically global optimization strategy. The results of the optimization are evaluated using the average rank aggregation of several optimal clustering validity indices in order to find the best number of clusters. In the manual clustering side, the goal is to verify the automatic clustering results in relation to the physical environment (see Section 3.2). The progression of this bicombinational multipath clustering approach is presented in Figure 1. After preprocessing the estimated channel, the multipath clustering problem is optimally solved both on the global and local scales through simulated annealing and K-means clustering. As shown in Figure 1, the number of multipath clusters are then evaluated after these optimization stages. These optimization and evaluation stages make up the automatic multipath clustering section. Afterwards, the results are used in the manual clustering section. Combining these two sections together gives the middle ground clustering approach. Since the focus is to identify multipath clusters in a better way, the modeling aspect in Figure 1 is not included in the paper, but should be done in the future.

Table 4: Factors considered in the middle ground clustering approach.

Factor	Possible quantification	Gives an answer to
Similarity/dissimilarity measure	Multidimensional distance, probability density function, ...	How near/far are multipaths from each other?
Significance measure	Shape, size, power, mutual information, target application performance, ...	Which multipaths are considered?
Validation measure	Clustering validity index, physics, scatterers, ...	How are the identified clusters validated?

Before presenting the details of the multipath clustering approach in Sections 3.1, 3.2, other related aspects of processing the estimated channel are described as follows.

Preprocessing. The clustering was done jointly in all the spatial and temporal dimensions of the channel parameters. The lth path channel data for clustering is denoted here as

$$\mathbf{X}_l = [\tau_l \quad \phi_l^{\text{AoD}} \quad \theta_l^{\text{AoD}} \quad \phi_l^{\text{AoA}} \quad \theta_l^{\text{AoA}}], \tag{1}$$

which represent the delay and direction dimensions. Before automatic clustering was performed, the angular data in $\mathbf{X}$ were first transformed to their direction cosines in order to transform them into a linear scale. Thus $\dim\{\mathbf{X}\} = 7$ as a result of mapping the two-unit spherical dimensions (azimuth and elevation) to three-unit Cartesian dimensions ($\mathbb{S}^2 \rightarrow \mathbb{R}^3$). Included with this preprocessing is the normalization or scaling of each dimension in $\mathbf{X}$ to have zero mean and unit variance. Further, the strongest paths that represent the line of sight (LoS) were removed using the single path estimate. This was based on the goal of only modeling clusters that are due to multipath mechanisms. It also follows the identification framework proposed in [20], where the LoS component is subtracted. In addition, six snapshots of every MS position shown in Figure 2 were combined for automatic clustering. This six-snapshot frame corresponds to a physical distance of about 2.5 m, which is the resolution of the channel sounder. This snapshot framing was done for all the snapshots in an MS position. Dynamic parameters are not considered in this paper, so only a static six-snapshot frame of every MS position were used. Furthermore, because of the limitations of the channel sounder for dynamic outdoor measurements, the Doppler dimension was not included. Specifically, the storage system of the channel sounder could not write as fast as the system measures the next Doppler block due to the time length in processing the buffered data before storage. Furthermore, it was not feasible to reduce the number of antenna elements at the BS and MS, and also the number of frequency bins in order to match the rate of the storage system.

Pruning. After determining the number of multipath clusters, cluster pruning was performed as suggested in [9]. The pruning was done simultaneously in six dimensions. These dimensions are the cluster power, the root-mean-square (rms) delay spread, and the rms spreads of the ϕ and θ AoDs and AoAs. In the multipath cluster pruning implementation, all paths run into a loop. In that loop, a path is pruned if *all* the remaining cluster power and clusters spreads without it are $\geq$99% of the unpruned cluster power and rms spreads.

Propagation Mechanism Classes. As was done in [1, 4, 21], different propagation mechanism classes were considered, which are also adopted here. These propagation mechanism classes basically depend on the layout of the measurement. Thus they belong to the property of the scatterers in the environment. The considered propagation mechanism classes are (i) *BS direction*, (ii) *facing BS direction*, and (iii) *street direction* classes. Each one is divided further into two: (a) *roof direction* and (b) *ground direction* classes. Knowing these propagation mechanisms classes could show how multipath clusters are related to the measurement site. These classes are based on the direction where a cluster comes from as seen at the MS. Figure 2 roughly shows these directions. Since the viewpoint was at the MS, the street direction was used as a reference in determining the BS direction and facing BS direction. So the BS direction refers to those multipaths whose azimuth AoAs come from the left side of the street, while those that are from the right side are the facing BS directions. The limiting 86-degree field-of-view of the MS patch antennas was used to determine the extent of the street direction region. From the estimated MIMO channel data, the azimuth AoA reference was placed at 0°. This reference was parallel to the street direction for all the MS positions. For the elevation propagation mechanism classes, the roof direction classes are those multipaths whose co-elevation AoAs are above the MS ($\theta < 90°$), and otherwise for the ground directions.

3.1. Automatic Multipath Clustering. The local and global optimizations done in solving the multipath clustering problem, and the evaluation of the number of multipath clusters are described in what follows.

3.1.1. Locally Optimal Clustering. Without consistent reproducibility, manual cluster identification methods can become unwieldy and subjective when applied to large estimated channel data derived from channel sounding. So the use of clustering algorithms has been an alternative. Here, the K-means algorithm [22] for clustering the estimated channel data was used. It has been used previously in

[9, 10]. The K-means clustering algorithm gives a locally optimal solution to a nondeterministic polynomial-time-hard (NP-hard) problem [23–26]:

$$\begin{aligned} \text{minimize} \quad & \sum_{k=1}^{K}\sum_{l=1}^{L} V_{kl}\, d(\mathbf{X}_l, \boldsymbol{\mu}_k) \\ \text{subject to} \quad & \sum_{k=1}^{K} V_{kl} = 1, \quad V_{kl} \in \{0,1\}, \end{aligned} \tag{2}$$

where K is the number of clusters, V_{kl} is the assignment indicator of $\mathbf{X}_l$ to the kth cluster ($V_{kl} \in \mathbf{V}^{K\times L}$), $\boldsymbol{\mu}_k$ is the kth cluster centroid, and $d(\mathbf{X}_l, \boldsymbol{\mu}_k)$ is the distance measure between $\mathbf{X}_l$ and $\boldsymbol{\mu}_k$. As was mentioned, the multidimensional Euclidean distance was used for d. The power was not used in weighing the distance measure in the K-means clustering implementation as was done in [9], because clustering result trials done by the authors converged to almost the same results. Moreover, it also lessens the computation time because of the use of simulated annealing (Section 3.1.2). Using the distance measure on the dimensions of $\mathbf{X}$, a cluster is then seen as a group of multipaths having similar delay and direction which are spread around a certain centroid.

K-means clustering with the multidimensional Euclidean distance was used instead of kernel-based K-means and/or spectral clustering methods [27]. Though admittedly these methods could group nonconvex-shaped clusters, as opposed to multidimensional Euclidean K-means, the determination of the tuning parameters that these approaches use is not straightforward. In the end, nonconvex multipath clusters could be more complicated to model, given that they have been verified to physically exist and are significant. In this paper, K-means clustering, which is a partitional way of clustering, was used because it is dynamic in moving $\mathbf{X}_l$'s from one cluster to another [28]. This is in contrast to hierarchical clustering methods (e.g., single-linkage [11]), which are static in the sense that $\mathbf{X}_l$'s assigned to a cluster cannot be moved to other clusters in later iterations to minimize the objective function [28]. Using K-means to solve (2) is an expectation-maximization (EM) variation in the hard sense [29].

3.1.2. Globally Optimal Clustering. Equation (2) is an optimization problem and its objective function could have many local minima. It is a combinatorial minimization problem where K-means is only able to guarantee locally optimal solutions, that is, in general its result is one among the local minima and may not be the global minima. Using simulated annealing, this local minima feature of K-means could be circumvented at the price of expensive computation. Simulated annealing is a globally stochastic optimization strategy that is conceptually a Monte Carlo method modeled according to physical annealing from statistical mechanics [30], which is a form of the Metropolis-Hastings algorithm [31, 32]. It has been used in various combinatorial optimization problems and has been also successful in circuit and antenna array design problems [30, 33]. A pseudocode using simulated annealing with clustering is shown in Table 5.

The statistical polynomial-time cooling schedule [34] was used for the initial value and reduction of the control parameter T, and also for the stopping condition. Using this cooling schedule, the initial value of T was iteratively calculated through several Markov chains using (3) until the initial acceptance ratio χ_0 is achieved. Here χ_0 was set to 0.9:

$$T_{\text{ini}} = \langle \Delta_{d^+} \rangle \left[\ln\left(\frac{m_2}{m_2\chi_0 - m_1(1-\chi_0)} \right) \right]^{-1}. \tag{3}$$

In (3), m_1, initially zero in the first Markov chain, is the number of Markov transitions from i to j, where $d_i \geqslant d_j$; m_2, also initially zero, is the number of Markov transitions from i to j, where $d_i < d_j$; and $\langle \Delta_{d^+} \rangle$ is the average Δ_d for m_2 transitions (i.e., $\Delta_d > 0$, $\Delta_d = d_j - d_i$). For the reduction of T at the ith iteration, it was obtained as

$$T_i = T_{i-1}\left[1 + \frac{T_{i-1}\ln(1+\delta)}{3\sigma_{d_{T_{i-1}}}} \right]^{-1}, \tag{4}$$

where δ is the decrement parameter, which was set to 0.1, and $\sigma_{d_{T_{i-1}}}$ is the standard deviation of d in the Markov chain at T_{i-1}. Finally, convergence is reached when the stop criterion

$$\left| \frac{T}{\langle d(T_{\text{ini}}) \rangle} \frac{\partial \langle d_{\text{s}}(T) \rangle}{\partial T} \right| < \epsilon \tag{5}$$

is satisfied, where $\langle d_{\text{s}}(T) \rangle$ is the smoothed $\langle d(T) \rangle$ over the length of the Markov chains, whereas ϵ is the stop parameter, which was set to 1×10^{-3}. The statistical polynomial-time cooling schedule is a thorough approach and theoretically based way of running simulated annealing as compared to empirical cooling schedules. For the theoretical basis of the control parameter cooling schedule, readers are referred to [34].

In Table 5, $\boldsymbol{\mu}_{\text{ini}}$ is randomly chosen from $\mathbf{X}$; however, it is further refined by the long Markov chains and the nearest neighborhood-based centroid selection. At most, 30 nearest neighborhood paths of $\boldsymbol{\mu}_{\text{c}}$ in $\mathbf{X}$ were the candidates for the random selection of $\boldsymbol{\mu}_{\text{n}}$. The closeness was measured using the multidimensional Euclidean distance. In the same table, the constant N_0 was set to 3, which was a compromise between efficiency of the available computing resource and effectiveness of the simulated annealing implementation. It is noted that a deterministic cluster centroid initialization could also be used as was done in [35]. However, by virtue of the large search space of multipath centroids in running the K-means clustering algorithm inside simulated annealing, closer solutions to (2) are achieved because simulated annealing could jump away from being trapped in a local minima.

In condensed matter physics, annealing is a thermal process for achieving low energy states of a solid. It starts by heating the solid until it melts, and continuous by cooling it carefully until its lowest-energy state is reached. Low temperature, however, does not guarantee that the lowest-energy state [30] will be attained. The heating temperature must be high enough, and then cooling down must be sufficiently slow in order to generate a sequence of states of

Table 5: Clustering with simulated annealing pseudocode.

T	Control parameter
$\boldsymbol{\mu}_{\text{ini}} \in \mathbb{R}^{\dim\{\mathbf{X}\}\times K}$	Initial $\boldsymbol{\mu}$
$\boldsymbol{\mu}_{\text{n}} \in \mathbb{R}^{\dim\{\mathbf{X}\}\times K}$	Nearest neighborhood-based $\boldsymbol{\mu}$
$\{d_{\text{c}}, \boldsymbol{\mu}_{\text{c}}, \mathbf{V}_{\text{c}}\}$	Current values
$\{d_{\text{b}}, \boldsymbol{\mu}_{\text{b}}, \mathbf{V}_{\text{b}}\}$	Best values
$\{d_{\text{f}}, \boldsymbol{\mu}_{\text{f}}, \mathbf{V}_{\text{f}}\}$	Feasible values
$R \in [0, 1)$	Uniformly distributed random number
$N_{\max} = N_0 \cdot \dim\{\mathbf{X}\}$	Length of the Markov chains [34]

(1) **for** $K = 2$ to $K_{\max}$ **do**
(2) get the initial value of T based on $\mathbf{X}$
(3) $\{d_{\text{c}}, \boldsymbol{\mu}_{\text{c}}, \mathbf{V}_{\text{c}}\} \Leftarrow$ K-means $\Leftarrow \{\mathbf{X}, \boldsymbol{\mu}_{\text{ini}}, K\}$
(4) $\{d_{\text{b}}, \boldsymbol{\mu}_{\text{b}}, \mathbf{V}_{\text{b}}\} \Leftarrow \{d_{\text{c}}, \boldsymbol{\mu}_{\text{c}}, \mathbf{V}_{\text{c}}\}$
(5) **while** true **do**
(6) **for** $N = 1$ **to** $N_{\max}$ **do**
(7) select $\boldsymbol{\mu}_{\text{n}}$ among the nearest neighborhood of $\boldsymbol{\mu}_{\text{c}}$ in $\mathbf{X}$
(8) $\{d_{\text{f}}, \boldsymbol{\mu}_{\text{f}}, \mathbf{V}_{\text{f}}\} \Leftarrow$ K-means $\Leftarrow \{\mathbf{X}, \boldsymbol{\mu}_{\text{n}}, K\}$
(9) $\Delta = d_{\text{f}} - d_{\text{c}}$
(10) **if** $\Delta \leq 0$ **or** $\exp(-\Delta/T) > R$ **then**
(11) $\{d_{\text{c}}, \boldsymbol{\mu}_{\text{c}}, \mathbf{V}_{\text{c}}\} \Leftarrow \{d_{\text{f}}, \boldsymbol{\mu}_{\text{f}}, \mathbf{V}_{\text{f}}\}$
(12) **if** $d_{\text{c}} < d_{\text{b}}$ **then**
(13) $\{d_{\text{b}}, \boldsymbol{\mu}_{\text{b}}, \mathbf{V}_{\text{b}}\} \Leftarrow \{d_{\text{c}}, \boldsymbol{\mu}_{\text{c}}, \mathbf{V}_{\text{c}}\}$
(14) **end if**
(15) $\boldsymbol{\mu}_{\text{c}} \Leftarrow \boldsymbol{\mu}_{\text{n}}$
(16) **end if**
(17) **end for**
(18) reduce T
(19) break if stopping condition is met
(20) **end while**
(21) return $\{\boldsymbol{\mu}_{\text{b}}, \mathbf{V}_{\text{b}}\}$
(22) **end for**

Algorithm 1

the solid, and not to miss the lowest-energy state, otherwise the solid will become metastable. When the cooling is done this way, the solid could reach thermal equilibrium at each temperature. A large number of gradations is thus presented by the slow-cooling temperature schedule. This annealing process was simulated by [31] where the energy difference at each state of the solid is accepted when they reach thermal equilibrium, which could be described by the Boltzmann distribution. The temperature of the annealing process corresponds then to the control parameter T. So Table 5 could then be concisely described by allowing K-means clustering to be run through long Markov chains, with sufficiently high initial T, which is then carefully decreased, the accepted solution to (2) approaches the global minima in the stochastic sense. In contrast to other clustering algorithms [8–11, 36], their results may only be locally optimal.

3.1.3. Number of Clusters (K). Determining the best K is difficult because it requires a priori knowledge of the formation of multipath clusters in the environment, which is not practically available. Nonetheless, it could be found by evaluating the clustering results using criteria set forth by clustering validity indices. These criteria are mainly based on cohesion (compactness) and separation measures of the clusters. So a clustering validity index tells the quality of clustering results that could give the best grouping. The indices that were used are described in what follows. These indices are optimizing in nature, that is, the maximum or minimum values of their arguments indicate the appropriate clustering.

(a) *Silhouette Index.* The Silhouette index s_{lk} could measure how similar a multipath l is to all multipaths in its own cluster $\mathcal{C}_k$ compared to all multipaths of the cluster nearest to it [37]. It is expressed as

$$s_{lk} = \frac{(b_{lk} - a_{lk})}{\arg\max\{b_{lk}, a_{lk}\}}, \tag{6}$$

where

$$a_{lk} = \frac{1}{|\mathcal{C}_k|} \sum_{\mathbf{X}\in\mathcal{C}_k} d(\mathbf{X}_l, \mathbf{X}_{l'})_{l'\neq l} \tag{7}$$

is the average distance of $\mathbf{X}_l$ to $\mathbf{X}_{l'}$ in $\mathcal{C}_k$; whereas

$$b_{lk} = \arg\min_{k'\neq k}\left\{\frac{1}{|\mathcal{C}_{k'}|} \sum_{\mathbf{X}_{l'}\in\mathcal{C}_{k'}} d(\mathbf{X}_{lk}, \mathbf{X}_{l'k'})\right\} \tag{8}$$

is the average distance of $\mathbf{X}_l$ of $\mathcal{C}_k$ to all $\mathbf{X}_{l'}$ of the nearest $\mathcal{C}_{k'}$. A $s_{lk} = +1$ means well-separated clusters whereas -1 signifies the opposite. Following [8], the best K could be found as

$$K_{\text{SI}} = \arg\max_K\left\{\frac{1}{K}\sum_k\left(\frac{1}{|\mathcal{C}_k|}\sum_{l\in\mathcal{C}_k} s_{lk}\right)\right\}. \tag{9}$$

(b) *Davies-Bouldin Index.* This index is a function of the ratio of the intracluster separation sum (S_i) to the intercluster separation [38]. The best K is found as

$$K_{\text{DB}} = \arg\min_K\left\{\frac{1}{K}\sum_k\left(\arg\max_{k'\neq k}\left\{\frac{S_k + S_{k'}}{d(\boldsymbol{\mu}_k, \boldsymbol{\mu}_{k'})}\right\}\right)\right\}, \tag{10}$$

where

$$S_i = \frac{1}{|\mathcal{C}_i|}\sum_{l\in\mathcal{C}_i} d(\mathbf{X}_l, \boldsymbol{\mu}_i). \tag{11}$$

(c) *Caliński-Harabasz Index.* This index is a ratio of the trace of the between-cluster scatter matrix to the trace of the within-cluster scatter matrix [39]. The best K using this index is

$$K_{\text{CH}} = \arg\max_K\left\{\frac{\text{Trace}(\mathbf{B})/(K-1)}{\text{Trace}(\mathbf{W})/(L-K)}\right\}, \tag{12}$$

where $\mathbf{B}$ and $\mathbf{W}$ are, respectively, given as

$$\begin{aligned}\mathbf{B} &= \sum_k |\mathcal{C}_k|\, d(\boldsymbol{\mu}_k, \boldsymbol{\mu}) d^{\text{T}}(\boldsymbol{\mu}_k, \boldsymbol{\mu}),\\ \mathbf{W} &= \sum_k \sum_{l\in\mathcal{C}_k} d(\mathbf{X}_l, \boldsymbol{\mu}_k) d^{\text{T}}(\mathbf{X}_l, \boldsymbol{\mu}_k),\end{aligned} \tag{13}$$

where $\boldsymbol{\mu}$ is the global centroid of the estimated channel in an MS position.

The Davies-Bouldin index and Caliński-Harabasz index were also used in [9]. Clustering algorithms that have basically the same objective function as that in (2) could result in being over-clustered or under-clustered as K is varied [40]. When the clustering results in either case, clustering validity indices that use intracluster and intercluster separation measures have a tendency to decrease or increase monotonically. This effect makes it difficult to determine the number of clusters. Moreover, the K's determined by (9), (10), and (12) are based on the clustering results of only a single value of K considered in its argument. Instead of considering only a single K, the Kim-Parks index [40], and the dynamic index [41] considered here give a validity that considers all the K's used. Considering all the K's used in a clustering validity index could avoid the monotone effect [40, 41]. A disadvantage of using these two clustering validity indices is the increase in computation time.

(d) *Kim-Parks Index.* This index is a function of the sum of (i) the total intracluster separation, as a measure of under-partition, and (ii) an over-partition function of the minimum distance between cluster centroids. Using it, the best K is taken as

$$K_{\mathrm{KP}} = \arg\min_{K}\left\{\left(\frac{1}{K}\sum_{k} S_k\right) + \frac{K}{\arg\min_{k'\neq k}\{d(\boldsymbol{\mu}_k,\boldsymbol{\mu}_{k'})\}}\right\}, \tag{14}$$

where each summand of the argument is normalized as $x_{\mathrm{arg}} = (x - x_{\min})/(x_{\max} - x_{\min})$.

(e) *Dynamic Index.* This index tries to include the geometrical aspect of $\mathbf{X}$ while taking into account the affinity of each cluster [41]. It determines the best K as

$$K_{\mathrm{DI}} = \arg\min_{K}\left\{\frac{\arg\max\{d(\boldsymbol{\mu}_k,\boldsymbol{\mu}_{k'})\}}{\arg\min_{k'\neq k}\{d(\boldsymbol{\mu}_k,\boldsymbol{\mu}_{k'})\}} + \frac{\zeta}{K}\frac{\sum_l\sum_k \mathrm{var}(\mathbf{X}_l \in \mathcal{C}_k)}{\sum_l \mathrm{var}(\mathbf{X}_l)}\right\}, \tag{15}$$

where

$$\zeta = \frac{\arg\max\{d(\mathbf{X}_l,\mathbf{X}_{l'})\}}{\arg\min_{l\neq l'}\{d(\mathbf{X}_l,\mathbf{X}_{l'})\}} \cdot \frac{\sum_l \mathrm{var}(\mathbf{X}_l)}{\sum_l\sum_{k=1}^{2}\mathrm{var}(\mathbf{X}_l \in \mathcal{C}_k)}, \tag{16}$$

whereas $\mathrm{var}(\cdot)$ denotes the variance.

Average Rank Aggregation. For different K's, each argument in K_{SI}, K_{DB}, K_{CH}, K_{KP}, and K_{DI}—denoted here by $\varkappa(K)$—has a different scale from one another, an example of which is shown in Table 6. Since these $\varkappa(K)$'s differ in evaluating the qualities of the clustering results, it is also not straightforward to normalize them to one scale. To address these issues and to not only depend on one clustering validity index result, the weighted voting aggregation of [42] was adopted but with a proposed modification: instead of scoring $\varkappa(K)$'s by weighted votes, they are scored by their statistical rank—$\mathrm{sr}(\varkappa)$. This removes the bias in the determination of the best K as it does not depend on the weights. The rank aggregation strategy is shown in Table 7 using the $\varkappa(K)$ example in Table 6. The result suggests that the best K is 3 based on the highest $\mathrm{sr}(\cdot)$ of the $\mathrm{sr}(\varkappa)$ average of all clustering validity indices. The next highest $\mathrm{sr}(\cdot)$'s could be checked as well if the clustering result of the highest one does not meet the criteria. As a comparison, when weights are used and are determined optimally or heuristically, the use of the average rank aggregation strategy offers a significant reduction in the overall computation time.

Table 6: Example $\varkappa(K)$ for $K = 2$ to $K = 6$.

K	$\varkappa(K)$				
	$\varkappa_{\mathrm{SI}}$	$\varkappa_{\mathrm{DB}}$	$\varkappa_{\mathrm{CH}}$	$\varkappa_{\mathrm{KP}}$	$\varkappa_{\mathrm{DI}}$
2	0.547	0.703	12.806	0.554	43.286
3	0.074	0.358	33.817	0.074	22.074
4	0.044	0.542	34.866	1.019	26.626
5	0.03	0.671	33.326	1.619	31.477
6	−0.047	0.463	27.885	1.501	26.531

Table 7: Average rank aggregation applied to the data in Table 6.

K	$\mathrm{sr}(\varkappa)$					
	$\mathrm{sr}_{\mathrm{SI}}$	$\mathrm{sr}_{\mathrm{DB}}$	$\mathrm{sr}_{\mathrm{CH}}$	$\mathrm{sr}_{\mathrm{KP}}$	$\mathrm{sr}_{\mathrm{DI}}$	$\mathrm{sr}(\langle\forall\mathrm{sr}\rangle)$
2	5	1	1	4	1	2
3	4	5	4	5	5	5
4	3	3	5	3	3	4
5	2	2	3	1	2	1
6	1	4	2	2	4	3

3.2. Manual Multipath Clustering. Real-world clusters could have irregular shapes like nonspherical or nonellipsoidal multipaths groupings, which could be readily recognized by the human eye, but not automatically by mathematical algorithms [8]. Several aspects that contribute to this irregular shaping are the dimensionality of $\mathbf{X}$ and manifold cluster characteristics due to the physical environment. Accommodating functionalities, for example, contracting projections and separators [43], which address these shapes adaptively in the mathematical clustering algorithm would result in an inefficient algorithm. Thus, the authors consider that the human aspect should not be ignored in the cluster validation analysis, especially in the verification of the physical realism of the clustering of multipath estimates as was also similarly done in [1, 4, 6], and not just fully depend on mathematical clustering results. This validation then incorporates the so-called *domain knowledge* (from data-mining terminology) in validating clusters.

Drawing selected principles from a procedure outlined in [18], and with the aid of careful mapping of the directional orientation on fisheye photographs of measured positions at

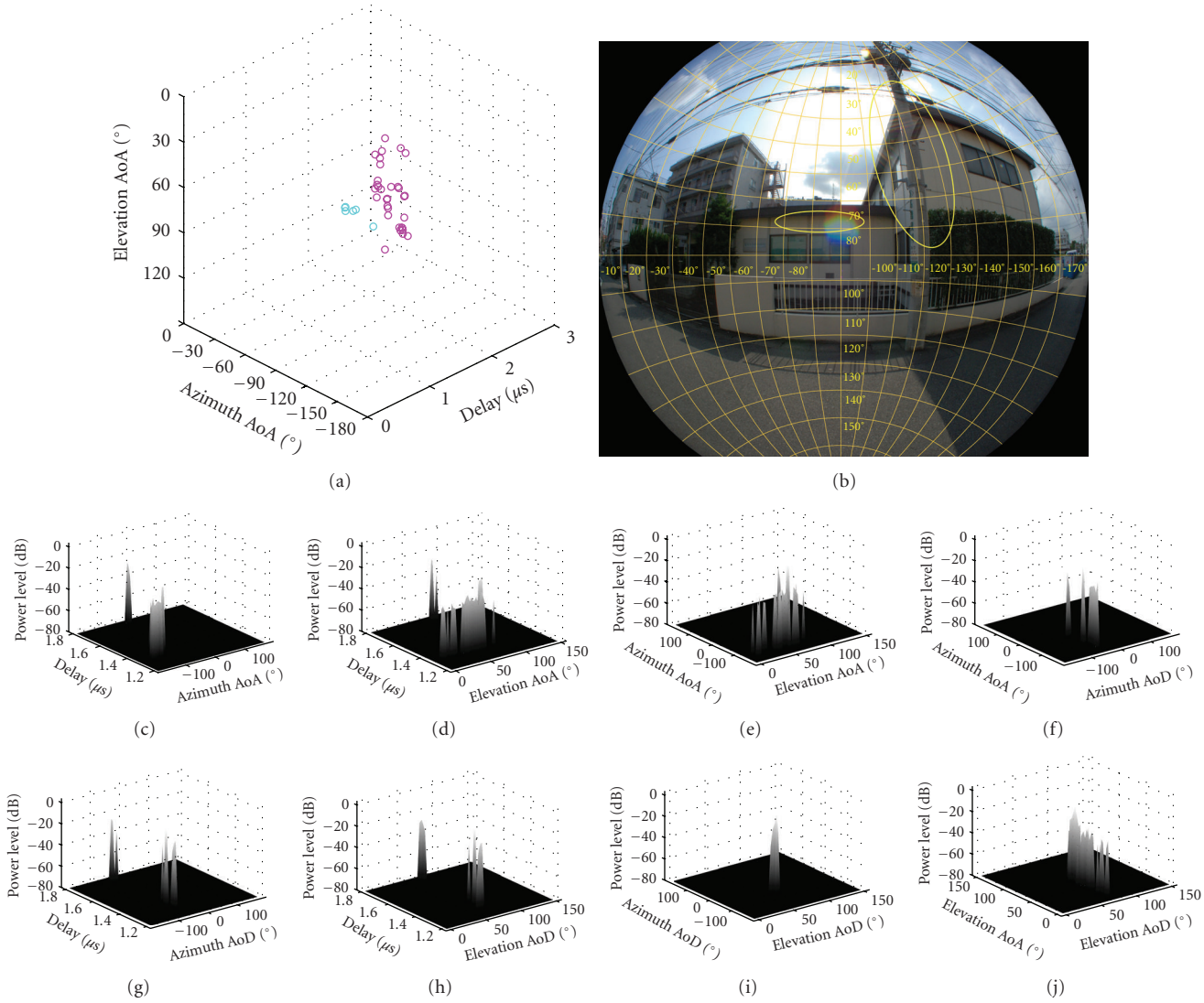

Figure 4: Outcome of the clustering approach at one position of an MS measurement location.

the MS, corresponding scatterers of each cluster were visually identified. This was done by viewing the automatic clustering results in several dimensions in conjunction with fisheye photographs of the MS position where automatic clustering was performed. A fisheye image is basically a projection of a hemispherical image to a plane. The following criteria were used in verifying the results of automatic clustering:

(i) within-processing limitations,

(ii) non-overlapping in delay,

(iii) scatterer existence.

The channel sounder resolution is included in (i). For the case of using the multidimensional Euclidean K-means algorithm, its processing limitation results in verifying only observable convex-shaped clusters. The non-overlapping criterion was used in order to delineate clusters from paths that may not be part of it, thus keeping the verity of cluster dispersion. Delay overlap of the clusters was allowed only in one dimension. As was done in [10], singleton clusters were not included as clusters since the results show that they have relatively weak power. However, it is also recognized that a singleton cluster could be considered as a cluster of rays if they have significant power [44]. When clusters have been verified, statistics are gathered such as their most likely scatterer type, the number of clusters, and the propagation mechanism class. This manual clustering is seen as an important step in validating clusters produced by automatic clustering as it connects with the physical environment, which is lacking in many existing publications on multipath clustering.

4. Results and Discussion

Applying the clustering approach presented in Section 3 to the estimated channel described in Section 2, Figure 4 shows one of the results. The automatic clustering result in Figure 4(a) was verified by the manually identified clusters

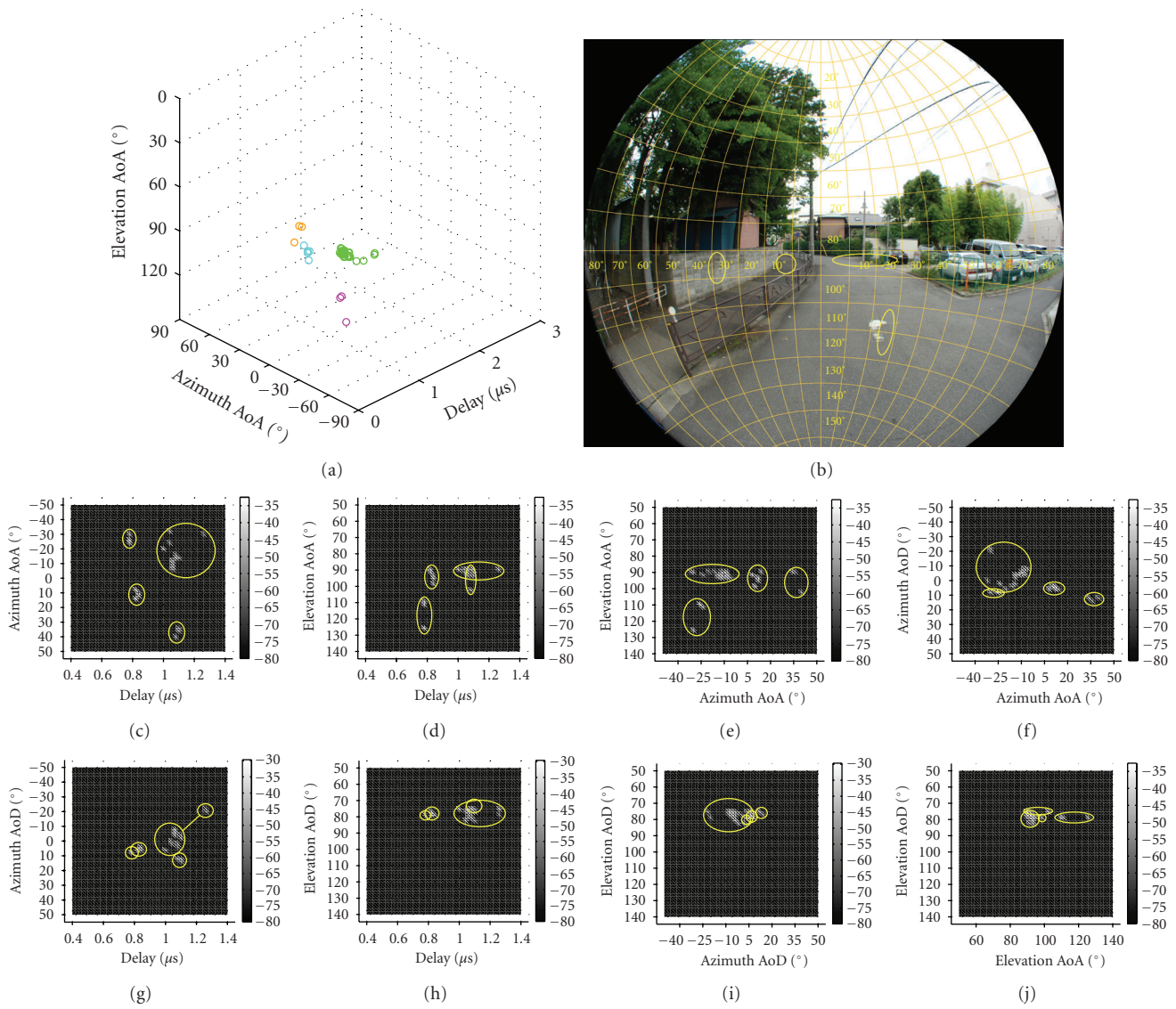

Figure 5: Another example showing four multipath clusters.

in Figure 4(b). The cluster-scattering objects were attributed to the single-storey and two-storey concrete buildings. To further verify these two clusters, their power profiles were examined, which are shown in Figures 4(c)–4(j). Comparing the plots in this figure, the two clusters are clearly seen in the azimuth-delay profiles than in the azimuth-elevation profiles due to the intersection of cluster elevation AoAs. These two clusters were not only observable at the MS and BS side through their azimuth-delay profiles but could also be confirmed through their AoA-AoD profiles (except slightly for the AoD profiles due to the closeness of the cluster elevation directions). Similarly, Figure 5 shows a result with four multipath clusters. Two of the cluster-scattering objects were attributed to the asphalt road, whereas the other two were attributed to the concrete wall and concrete sidewalk. These results confirmed that the clustering approach was able to capture clusters that fall within its capability andlinebreak criteria.

Using the manual clustering criteria set forth in Section 3.2 also resulted in clusters that were classified as *mathematical clusters*, which are hereafter called α-clusters. Many of the clusters that fall into this category are those that overlap with other clusters in their scenarios, whereas others are singleton clusters. Among the criteria, the overlapping—in delay and/or direction—of these clusters was the main reason why they were classified as α-clusters. Figure 6 shows an example of these clusters, where the overlapping of three clusters could be seen. Possible grounds for these α-clusters are (i) *other components* (far clusters, clusters at the locality of the BS, nonclusters, dynamic paths, etc.), or (ii) *errors* (plane wave model failure, estimation errors, spectral line splitting, etc.). Because of the channel sounding setup at the measurement site, the authors determined to identify clusters at the MS side. As Figures 2 and 3 show, the BS was located on the highest building in the macrocell setup. Thus, the plausibility of having clusters at the BS was low.

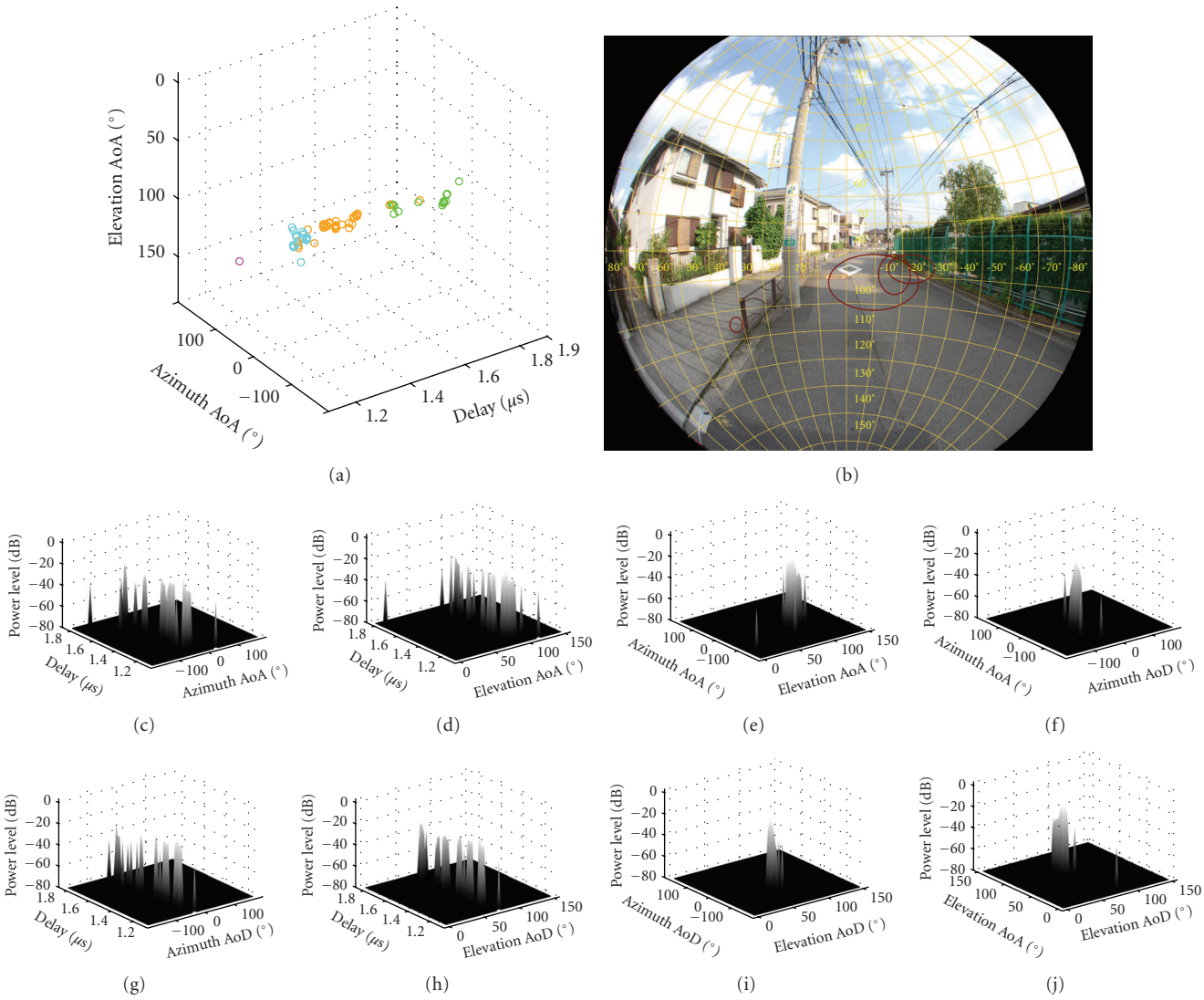

Figure 6: A mathematical clustering result—overlapping clusters.

Table 8: Percentage of cluster propagation mechanism classes.

Classes	Ground [%][a]	Roof [%][a]	Overall [%][a]
Street direction	10.63/16.93	12.2/13.39	22.83/30.32
BS direction	5.12/7.09	6.3/5.12	11.42/12.21
Facing BS direction	4.72/7.48	6.69/4.33	11.41/11.81

[a]α-clusters/β-clusters.

This could also be examined in the AoA-AoD profiles in both the azimuth and elevation dimensions in Figures 4(f), 4(j), 5(f), 5(j), 6(f), and 6(j). The narrowness of the AoD range spanned by the clusters in these power profiles indicates the absence of clustering at the BS side.

4.1. Power Proportion. Collecting the clustering results of the approach applied to the estimated MIMO channel data, the significance measure (see Section 3) of the clusters are examined here in terms of their power proportion. The use of power proportion as a measure of cluster significance has been also used in [6]. For a certain MS measurement location, this power proportion is defined here as the ratio of the cluster path power to the total path power. For a cluster $\mathcal{C}_k$, it is expressed as

$$P_{\mathrm{p}}^{\mathcal{C}_k} = \frac{\sum_{l\in\mathcal{C}_k}(1/2)\left(|\gamma_{\mathrm{VV},l}|^2+|\gamma_{\mathrm{VH},l}|^2+|\gamma_{\mathrm{HV},l}|^2+|\gamma_{\mathrm{HH},l}|^2\right)}{\sum_{l}(1/2)\left(|\gamma_{\mathrm{VV},l}|^2+|\gamma_{\mathrm{VH},l}|^2+|\gamma_{\mathrm{HV},l}|^2+|\gamma_{\mathrm{HH},l}|^2\right)}. \tag{17}$$

α-clusters were found to represent the majority of clustering outcomes in terms of their power proportion. On the other hand, the minority were categorized as *small clusters*, which are hereafter called β-clusters. The cumulative distribution of the power proportion of these clusters is shown in Figure 7. The plot shows that β-clusters have a relatively smaller power proportion than α-clusters. Their low values were due to the removal of the strongest component as described in Section 3

Table 9: Material-type percentage of the β-cluster scatterers.

Material type	Street direction		BS direction		Facing BS direction		Overall [%]
	Ground [%]	Roof [%]	Ground [%]	Roof [%]	Ground [%]	Roof [%]	
Metal	5.9	12.3	7.8	3.4	2	3.9	35.3
Concrete	8.8	6.9	3.9	2.9	6.9	1	30.4
Asphalt	15.2	–	0.5	–	1	–	16.7
Brick	0.5	5.8	–	–	1	2	9.3
Mixed (metal, concrete, foliage, window)	–	5.4	–	–	–	2.9	8.3

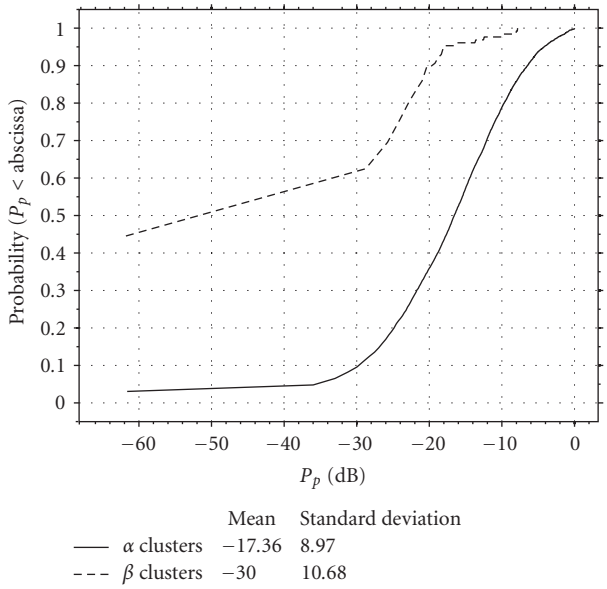

Figure 7: Distribution of the power proportion.

(*Preprocessing*). Thus, in using the approach, α-clusters and β-clusters resulted, where the distinctions between the two are as follows: (i) α-clusters were mainly a result of the mathematical/automatic clustering approach, whereas β-clusters were that of the manual clustering approach; (ii) many α-clusters had overlapping clusters whereas β-clusters had clear-cut delineation of their associated/corresponding scatterers, thus they have physical meaning; (iii) α-clusters had more energy than β-clusters. The results show that these overlapping clusters could basically be considered as outcomes of automatic clustering since they comprised the majority of the observed channel in terms of their power proportion. Furthermore, only a few clusters had a clear delineation of their dispersion. There is a difficulty then in judging the physical realism of overlapping clusters. This overlapping defeats the concept of spatial multiplexing, where cluster channel models that are used in simulations must be satisfactorily accurate. Moreover, this further points to a need for the physical interpretation and validation of clustering results, which is an initial step done in this paper, and further refinement or improvement is called for. This may somehow address the arbitrariness in identifying clusters. From these results, one may infer partial clustering of the channel at the MS. However, there is indeed a great deal of arbitrariness in defining and determining clusters [7]. For example, the general consensus is that a cluster is a group of paths that have "similar" characteristics but is "distinct" from other path groups, but its quantification may differ from one automatic clustering to another (like the power-weighted multipath component distance [9]; cosine angle for directions and absolute delay difference [11]). Furthermore, from the systems-engineering view, cluster scatterers may not be important, which may be contrary to the radio-propagation-engineering view. Hence, the characteristics of these clusters are shown in what follows.

4.2. Cluster Scatterer Mechanism Classes. As discussed in Section 3, propagation mechanism classes were taken from the results. Table 8 shows the cluster propagation mechanism classes whereas Table 9 gives the type of scatterers corresponding to the clusters. Since β-clusters had a clearer delineation than α-clusters, only β-clusters are included in Table 9.

As a comparison, in a similar area [45], the BS direction and facing BS direction were noted to have strong multipath contributions. For street directions, it has been observed that later-arriving multipaths propagate through street canyons [46], and in [47] it was observed that a significant number of multipaths comes from such directions. These observations are consistent with the values in Table 8, where the street direction dominated. In the same table, the BS direction and facing BS direction classes have almost the same contribution. Furthermore, the cluster scatterers were mostly metallic-type materials followed by concrete, asphalt, and brick, as shown in Table 9.

4.3. Cluster Characteristics. The condensed parameters of the cluster characteristics considered are the following:

(i) cluster average power (P_{ave})
(ii) number of clusters
(iii) cluster fading factor (κ)
(iv) cluster delay
(v) cluster spreads (σ_τ, σ_ϕ, σ_θ)
(vi) cluster polarization ratios.

The cluster fading factor is defined here as the ratio of the power of the strongest cluster to that of all the other clusters. It is pointed out that σ_ϕ was computed according to the circular angular spread calculation in [48] to avoid the

Table 10: Summary of cluster statistical parameters in urban/suburban macrocellular environments.

Cluster parameters	Kawasaki, Japan [this paper] Street residential-industrial (230–400 m)[a]		Helsinki, Finland [6] Street[c] (~ 500 m)[a]		Square[c] (~ 300 m)[a]		Louvain-la-Neuve, Belgium [7] Residential (300–400 m)[a]		Campus (50–400 m)[a]		Science park (260–450 m)[a]	
	Mean[b]	Stdev[b]	Mean	Stdev	Mean	Stdev	Mean	Stdev	Mean	Stdev	Mean	Stdev
P_{ave} [dB]	−15.35/ − 28.17	13.83/11.24	–	–	–	–	−10.24[d]	5.18[d]	−9.02[d]	5.6[d]	−8.16[d]	5.72[d]
K	6.83/7.11	0.99/4.76	14	–	10	–	1.01	0.61	1.11	0.59	1.6	0.73
κ [dB]	4.26/1.43	5.24/5.33	3.65	2.29	2.26	1.99	−0.14	6.39	2.5	6.53	−1.4	6.54
τ [μs]	1.11/1.1	0.271/0.255	2.83	1.04	1.38	0.46	0.22[d]	0.21[d]	0.19[d]	0.21[d]	0.13[d]	0.13[d]
$\sigma_{\phi^{AoD}}$ [°]	4.67/1.34	5.55/1.25	–	–	–	–	–	–	–	–	–	–
$\sigma_{\phi^{AoA}}$ [°]	29.43/8.42	15.18/20.8	4.2	1.94	4.57	2.07	11.09	2.04	9.18	2.13	11.74	1.89
$\sigma_{\theta^{AoD}}$ [°]	2.83/1.17	3.86/1.25	–	–	–	–	–	–	–	–	–	–
$\sigma_{\theta^{AoA}}$ [°]	6.8/3.83	4.63/2.84	–	–	–	–	–	–	–	–	–	–
σ_τ [ns]	29.35/16.5	37.32/23.9	27.22	40.68	28.5	42.57	10.46	1.78	8.28	1.88	9.1	1.78
XPR [dB][e]	–	–	10.39	4.69	10.72	2.37	–	–	–	–	–	–
XPR_V^{BS} [dB]	8.63/8.73	5.2/5.37	–	–	–	–	–	–	–	–	–	–
XPR_H^{BS} [dB]	9.77/9.88	4.59/4.95	–	–	–	–	–	–	–	–	–	–
XPR_V^{MS} [dB]	9.24/8.61	4.46/5.95	–	–	–	–	–	–	–	–	–	–
XPR_H^{MS} [dB]	9.15/10.01	4.95/5.87	–	–	–	–	–	–	–	–	–	–
CPR [dB]	−0.52/ − 1.28	3.74/4.8	–	–	–	–	–	–	–	–	–	–

[a]BS-MS distance.
[b]α-clusters/β-clusters.
[c]single realization.
[d]50th percentile data.
[e]single-input multiple-output (SIMO).

ambiguous 2π periodicity. The four cross-polarization ratios and co-polarization ratio of the clusters were computed, respectively, as follows:

$$XPR_V^{BS} = 10\log_{10}\left(\frac{\sum_{l\in\mathcal{C}_k}|\gamma_{VV,l}|^2}{\sum_{l\in\mathcal{C}_k}|\gamma_{VH,l}|^2}\right), \quad (18)$$

$$XPR_H^{BS} = 10\log_{10}\left(\frac{\sum_{l\in\mathcal{C}_k}|\gamma_{HH,l}|^2}{\sum_{l\in\mathcal{C}_k}|\gamma_{HV,l}|^2}\right), \quad (19)$$

$$XPR_V^{MS} = 10\log_{10}\left(\frac{\sum_{l\in\mathcal{C}_k}|\gamma_{VV,l}|^2}{\sum_{l\in\mathcal{C}_k}|\gamma_{HV,l}|^2}\right), \quad (20)$$

$$XPR_H^{MS} = 10\log_{10}\left(\frac{\sum_{l\in\mathcal{C}_k}|\gamma_{HH,l}|^2}{\sum_{l\in\mathcal{C}_k}|\gamma_{VH,l}|^2}\right), \quad (21)$$

$$CPR = 10\log_{10}\left(\frac{\sum_{l\in\mathcal{C}_k}|\gamma_{VV,l}|^2}{\sum_{l\in\mathcal{C}_k}|\gamma_{HH,l}|^2}\right). \quad (22)$$

The cross-polarization ratio (XPR) indicates the degree of polarization of the paths in a cluster incur from being vertically polarized to being horizontally polarized, or vice versa, whereas the copolarization ratio (CPR) shows the degree of vertical polarization with respect to the horizontal polarization. In the notation in (18)–(21), XPR_V^{MS}, for example, is the XPR at the MS for paths that originated with V polarization, with the channel assumed to be reciprocal.

The mean and standard deviation of the cluster characteristics are placed together in Table 10. In the table, stdev refers to the standard deviation. The mean and standard deviation of the data in [6, 7] were also calculated and then tabulated. Observing this table, the angular spreads at the MS were larger than at the BS, indicating further that the degree of cluster scattering was concentrated at the MS. The $\sigma_{\phi^{AoA}}$ of the α-clusters was remarkable due to their overlapping characteristics. Compared to the COST 273 MIMO channel model [3], its corresponding $\sigma_{\phi^{AoA}}$ is 35°. Overall, the results are relatively comparable given the difference of the measured routes and setup. In addition, the results were influenced mostly by the different clustering criteria used by each author. These criteria basically give the cluster definition. It is also noted that the high delay resolution of the channel sounder that was used could include or exclude clusters that were subsequently identified by the methodology discussed in Section 3. Future target applications may have different capabilities (e.g., transmission scheme) and/or may not have such resolution in place in user terminals right away.

4.4. Parameter Correlation. To examine any linear dependencies among the cluster parameters, their correlation coefficients were taken. The computed correlation coefficient matrices of the α- and β-cluster parameters are portrayed in Figures 8(a) and 8(b), respectively. From these matrices,

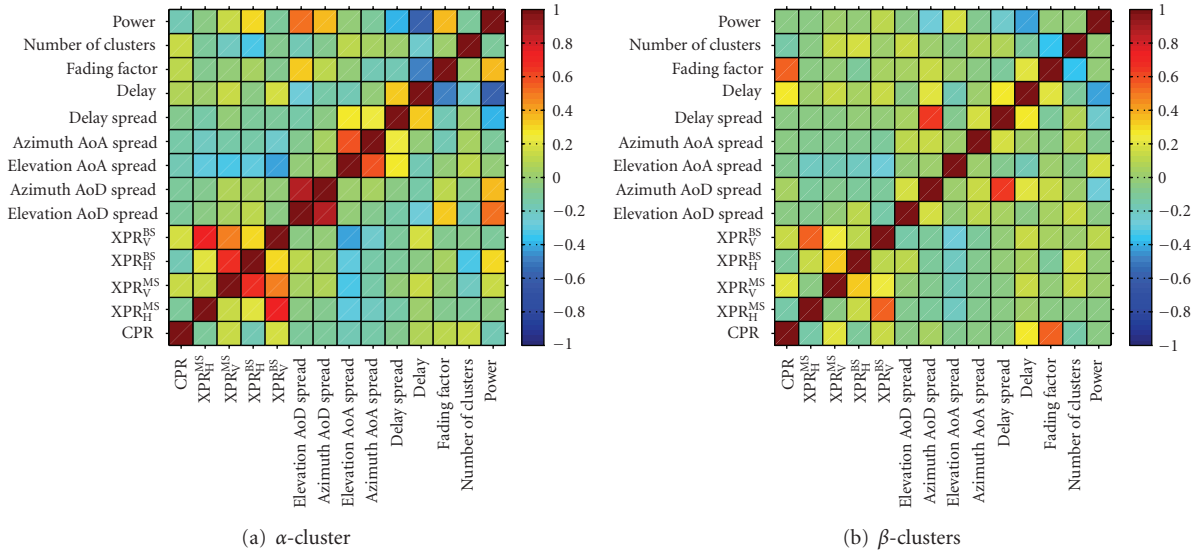

(a) α-cluster (b) β-clusters

Figure 8: Correlation coefficient matrix of the cluster parameters.

Table 11: Medium-to-large correlation among the α-cluster parameters.

Parameter 1	Parameter 2	Correlation coefficient
Azimuth AoD spread	Elevation AoD spread	0.86
Power	Delay	−0.58
Azimuth AoA spread	Elevation AoA spread	0.56
Power	Elevation AoD spread	0.52
Fading factor	Elevation AoD spread	0.52
Fading factor	Delay	−0.47
Elevation AoA spread	XPR_V^{BS}	−0.41

Table 12: Medium-to-large correlation among the β-cluster parameters.

Parameter 1	Parameter 2	Correlation coefficient
Delay spread	Azimuth AoD spread	0.65
Fading factor	CPR	0.53
Power	Delay	−0.41
K	Fading factor	−0.35

medium-to-large correlation coefficients are tabulated in Tables 11 and 12. Not included in the table are those polarization parameters that correlated due to the reciprocity of the channel.

Considering the common results of both clusters, the correlation between cluster power and delay and also that of fading factor and delay are apparent, given that clusters with long delays have smaller power than those with short delays.

For α-clusters in the considered macrocell, the azimuth and elevation AoD spread correlation could indicate that the spreading at the BS was concentrated toward the MS given that their spreads are also small as seen in Table 10. For the azimuth and elevation AoA spread correlation, it could attest that the spreading becomes proportional to the scattering object. These two results may seem to be connected with the correlation between the elevation AoD spread and (i) the power, and also (ii) the fading factor, thus signifying the concentration of these α-clusters. In the case of the elevation AoA spread and the XPR_V^{BS} correlation, it may roughly follow that polarization rotation still occurs even when the cluster elevation dispersion is narrow.

For the β-clusters, the correlation between the delay spread and azimuth AoD spread corresponds to the majority of the propagation mechanism class. In the considered macrocell, the street direction is somehow concentric from the BS, which is lateral to where the MS is located (see Figure 2). Thus a large cluster azimuth AoD spread corresponds to those multipaths that would incur more delays in going through those street canyons. This delay spread and angular spread correlation has also been observed in [49]. For the correlation between the fading factor and CPR, it could show that the dominant clusters were vertically polarized. Lastly, the negative correlation between the number of clusters and the fading factor could indicate that when there are more clusters in the scenario, the tendency of having dominant clusters is somehow dampened. These correlation results are consistent with the observed results previously discussed in this paper.

5. Conclusions

In this paper, a methodology has been presented with the goal of identifying multipath clusters in a better way. Part of it is a globally optimized automatic clustering approach, which was used to identify multipath clusters at the mobile station from estimated MIMO channel parameters derived from a small urban macrocell measurement at 4.5 GHz. The other part of the approach is the successive manual clustering verification, in which the automatic clustering

results were validated by identifying their corresponding or associated scatterers in the physical environment. Using this approach resulted in having (i) mathematical clusters, which are mostly characterized by overlapping clusters and are basically an outcome of automatic clustering, and (ii) small clusters, which have small power but clearly delineated clusters as produced by the manual clustering approach.

The overlapping of clusters makes it difficult to judge their physical realism, which further leads to the need for the physical interpretation of automatic clustering results, which is an initial step done in this paper and needs further improvement. This may somehow address the arbitrariness in identifying clusters. Due to the standoff present in defining clusters and their physical analysis, the authors proceeded to show the characteristics of both the mathematical clusters and small clusters. It was found that the street propagation mechanism class dominated. As a result of manual clustering, the physical realism of multipath clusters was also identified in terms of the type of the scatterer material. Metallic materials, followed by concrete, and then asphalt were the major types of cluster scatterers. It was found that the considered cluster characteristics agree with existing results, however, the difference largely depends on the criteria set forth by the clustering approach.

It is expected that the statistical property of the wireless channel will be different in other environments, for other frequency bands (e.g., 0.7, 30, and 60 GHz), and for other channel sounder resolutions. Secondary reasons for the differences are the modeling and various approaches used in the channel estimation and the subsequent channel analysis, synthesis, verification, errors, and application goals. With the use of the high-resolution channel sounder at 4.5 GHz in the urban macrocell considered here, it is noted that the target application and its available processing could define if the cluster characteristics in the evaluation would aid in its overall design. The disadvantages of the methodology are the expensive computation of simulated annealing in automatic clustering and the considerable user interaction required in the manual clustering approach. On the other hand, the automatic clustering results are better since they are not confined to local minima limitations, and the manual clustering approach could give an aspect of the physical scattering realism of the clusters, which is lacking in many automatic clustering results in the available literature. Furthermore, this bicombinational clustering approach underscores the importance of incorporating validation in cluster identification. It is noted that further research work on improving the multipath clustering approach, as well as doing the channel analysis/modeling further is vital in order to understand the characteristics of multipath clusters.

Acknowledgment

The National Institute of Information and Communications Technology of Japan (NICT) is acknowledged for funding and supporting this research.

References

[1] M. Toeltsch, J. Laurila, K. Kalliola, A. F. Molisch, P. Vainikainen, and E. Bonek, "Statistical characterization of urban spatial radio channels," *IEEE Journal on Selected Areas in Communications*, vol. 20, no. 3, pp. 539–549, 2002.

[2] H. Asplund, A. A. Glazunov, A. F. Molisch, K. I. Pedersen, and M. Steinbauer, "The COST 259 directional channel model-part II: macrocells," *IEEE Transactions on Wireless Communications*, vol. 5, no. 12, pp. 3434–3450, 2006.

[3] L. Correia, *Mobile Broadband Multimedia Networks: Techniques, Models and Tools for 4G*, Academic Press, Oxford, UK, 2006.

[4] J. Laurila, K. Kalliola, M. Toeltsch, K. Hugl, P. Vainikainen, and E. Bonek, "Wideband 3D characterization of mobile radio channels in urban environment," *IEEE Transactions on Antennas and Propagation*, vol. 50, no. 2, pp. 233–243, 2002.

[5] K. Yu, Q. Li, and M. Ho, "Measurement investigation of tap and cluster angular spreads at 5.2 GHz," *IEEE Transactions on Antennas and Propagation*, vol. 53, no. 7, pp. 2156–2160, 2005.

[6] L. Vuokko, P. Vainikainen, and J. Takada, "Clusters extracted from measured propagation channels in macrocellular environments," *IEEE Transactions on Antennas and Propagation*, vol. 53, no. 12, pp. 4089–4098, 2005.

[7] C. Oestges and B. Clerckx, "Modeling outdoor macrocellular clusters based on 1.9-GHz experimental data," *IEEE Transactions on Vehicular Technology*, vol. 56, no. 5, pp. 2821–2830, 2007.

[8] J. Salo, J. Salmi, N. Czink, and P. Vainikainen, "Automatic clustering of nonstationary MIMO channel parameter estimates," in *Proceedings of the 12th International Conference on Telecommunications (ICT '05)*, Cape Town, South Africa, May 2005.

[9] N. Czink, P. Cera, J. Salo, E. Bonek, J.-P. Nuutinen, and J. Ylitalo, "A framework for automatic clustering of parametric MIMO channel data including path powers," in *Proceedings of the 64th IEEE Vehicular Technology Conference (VTC '06)*, pp. 114–118, Montreal, Canada, September 2006.

[10] W. Dong, J. Zhang, X. Gao, P. Zhang, and Y. Wu, "Cluster identification and properties of outdoor wideband MIMO channel," in *Proceedings of the 66th IEEE Vehicular Technology Conference (VTC '07)*, pp. 829–833, Baltimore, Md, USA, September-October 2007.

[11] M. Kwakkernaat and M. Herben, "Analysis of scattering in mobile radio channels based on clustered multipath estimates," *International Journal of Wireless Information Networks*, vol. 15, no. 3-4, pp. 107–116, 2008.

[12] http://www.channelsounder.de.

[13] M. Landmann, A. Richter, and R. Thoma, "Performance evaluation of antenna arrays for high-resolution DOA estimation in channel sounding," in *Proceedings of the International Symposium on Antennas and Propagation (ISAP '04)*, Sendai, Japan, August 2004.

[14] M. Landmann, W. Kotterman, and R. Thoma, "On the influence of incomplete data models on estimated angular distributions in channel characterisation," in *Proceedings of the 2nd European Conference on Antennas and Propagation (EuCAP '07)*, pp. 1–8, Edinburgh, UK, November 2007.

[15] R. Thoma, M. Landmann, and A. Richter, "RIMAX—a maximum likelihood framework for parameter estimation in multidimensional channel sounding," in *Proceedings of*

the International Symposium on Antennas and Propagation (ISAP '04), pp. 53–56, Sendai, Japan, August 2004.

[16] A. Richter, *Estimation of radio channel parameters: models and algorithms*, Ph.D. dissertation, Ilmenau University of Technology, Ilmenau, Germany, 2005.

[17] M. Steinbauer, A. F. Molisch, and E. Bonek, "The double-directional radio channel," *IEEE Antennas and Propagation Magazine*, vol. 43, no. 4, pp. 51–63, 2001.

[18] L. Materum, K. Sivasondhivat, J. Takada, I. Ida, and Y. Oishi, "Identification of relatively strong clusters in an NLOS scenario at a small urban macrocell mobile station," in *Proceedings of the International Symposium on Antennas and Propagation (ISAP '07)*, pp. 157–160, Niigata, Japan, August 2007.

[19] L. Materum, J. Takada, I. Ida, and Y. Oishi, "Improved multipath clustering of a small urban macrocellular MIMO environment at 4.5 GHz," in *Proceedings of the International Symposium on Antennas and Propagation (ISAP '08)*, pp. 854–857, Taipei, Taiwan, October 2008.

[20] N. Czink and C. Oestges, "The COST 273 MIMO channel model: three kinds of clusters," in *Proceedings of the 10th IEEE International Symposium on Spread Spectrum Techniques and Applications (ISSSTA '08)*, pp. 282–286, Bologna, Italy, August 2008.

[21] K. Sivasondhivat, J. Takada, I. Ida, and Y. Oishi, "Experimental analysis and site-specific modeling of channel parameters at mobile station in an urban macrocellular environment," *IEICE Transactions on Communications*, vol. E91-B, no. 4, pp. 1132–1144, 2008.

[22] J. MacQueen, "Some methods for classification and analysis of multivariate observation," in *Proceedings of the 5th Berkeley Symposium on Mathematical Statistics and Probability*, pp. 281–297, Berkeley, Calif, USA, December-January 1967.

[23] W. H. E. Day, "Complexity theory: an introduction for practitioners of classification," in *Clustering and Classification*, P. Arabie, L. J. Hubert, and G. De Soete, Eds., pp. 199–233, World Scientific, London, UK, 1996.

[24] W. J. Welch, "Algorithmic complexity: three NP-hard problems in computational statistics," *Journal of Statistical Computation and Simulation*, vol. 15, no. 1, pp. 17–25, 1982.

[25] M. R. Garey and D. S. Johnson, *Computers and Intractability: A Guide to the Theory of NP-Completeness*, W. H. Freeman, New York, NY, USA, 1979.

[26] P. Brucker, "On the complexity of clustering problems," in *Optimization and Operations Research*, R. Henn, B. Korte, and W. Oettli, Eds., vol. 157 of *Lecture Notes in Economics and Mathematical Systems*, pp. 45–54, Springer, Berlin, Germany, 1978.

[27] I. S. Dhillon, Y. Guan, and B. Kulis, "Weighted graph cuts without eigenvectors a multilevel approach," *IEEE Transactions on Pattern Analysis and Machine Intelligence*, vol. 29, no. 11, pp. 1944–1957, 2007.

[28] H. Frigui and R. Krishnapuram, "A robust competitive clustering algorithm with applications in computer vision," *IEEE Transactions on Pattern Analysis and Machine Intelligence*, vol. 21, no. 5, pp. 450–465, 1999.

[29] D. J. C. MacKay, *Information Theory, Inference and Learning Algorithms*, Cambridge University Press, New York, NY, USA, 2003.

[30] S. Kirkpatrick, C. D. Gelatt Jr., and M. P. Vecchi, "Optimization by simulated annealing," *Science*, vol. 220, no. 4598, pp. 671–680, 1983.

[31] N. Metropolis, A. W. Rosenbluth, M. N. Rosenbluth, A. H. Teller, and E. Teller, "Equation of state calculations by fast computing machines," *The Journal of Chemical Physics*, vol. 21, no. 6, pp. 1087–1092, 1953.

[32] W. K. Hastings, "Monte Carlo sampling methods using Markov chains and their applications," *Biometrika*, vol. 57, no. 1, pp. 97–109, 1970.

[33] V. Murino, A. Trucco, and C. S. Regazzoni, "Synthesis of unequally spaced arrays by simulated annealing," *IEEE Transactions on Signal Processing*, vol. 44, no. 1, pp. 119–122, 1996.

[34] E. Aarts and J. Korst, *Simulated Annealing and Boltzmann Machines*, John Wiley & Sons, New York, NY, USA, 1989.

[35] N. Czink, R. Tian, S. Wyne, et al., "Tracking time-variant cluster parameters in MIMO channel measurements," in *Proceedings of the 2nd International Conference on Communications and Networking in China (CHINACOM '07)*, pp. 1147–1151, Shanghai, China, August 2007.

[36] N. Czink, E. Bonek, L. Hentilä, J.-P. Nuutinen, and J. Ylitalo, "Cluster-based MIMO channel model parameters extracted from indoor time-variant measurements," in *Proceedings of IEEE Global Telecommunications Conference (GLOBECOM '06)*, pp. 1–5, San Francisco, Calif, USA, November-December 2006.

[37] P. J. Rousseeuw, "Silhouettes: a graphical aid to the interpretation and validation of cluster analysis," *Journal of Computational and Applied Mathematics*, vol. 20, no. 1, pp. 53–65, 1987.

[38] D. L. Davies and D. W. Bouldin, "A cluster separation measure," *IEEE Transactions on Pattern Analysis and Machine Intelligence*, vol. 1, no. 2, pp. 224–227, 1979.

[39] T. Caliński and J. Harabasz, "A dendrite method for cluster analysis," *Communications in Statistics: Theory and Methods*, vol. 3, no. 1, pp. 1–27, 1974.

[40] D.-J. Kim, Y.-W. Park, and D.-J. Park, "A novel validity index for determination of the optimal number of clusters," *IEICE Transactions on Information and Systems*, vol. E84-D, no. 2, pp. 281–285, 2001.

[41] A.-O. Boudraa, "Dynamic estimation of number of clusters in data sets," *Electronics Letters*, vol. 35, no. 19, pp. 1606–1608, 1999.

[42] N. Bolshakova and F. Azuaje, "Improving expression data mining through cluster validation," in *Proceedings of the 4th International IEEE EMBS Special Topic Conference on Information Technology Applications in Biomedicine (ITAB '03)*, pp. 19–22, Birmingham, UK, April 2003.

[43] A. Hinneburg, *Density-based clustering in large databases using projections and visualizations*, Ph.D. dissertation, Martin Luther University of Halle-Wittenberg, Halle, Germany, 2002.

[44] N. Czink, *The random-cluster model—a stochastic MIMO channel model for broadband wireless communication systems of the 3rd generation and beyond*, Ph.D. dissertation, Vienna University of Technology, Vienna, Austria, 2007.

[45] N. Kita, W. Yamada, A. Ando, D. Mori, T. Takao, and H. Watanabe, "Characteristics of direction of arrival in residential area in 5-GHz band," in *Proceedings of the IEICE Society Conference*, vol. B-1–14, Hokkaido, Japan, September 2005.

[46] A. Molisch, *Wireless Communications*, Wiley-IEEE Press, Chichester, UK, 2005.

[47] T. Hayashi, A. Yamamoto, K. Ogawa, and G. F. Pedersen, "An analysis of radio propagation characteristics using ray-tracing techniques on an outdoor propagation experiment," Tech. Rep. AP2008-2, IEICE, Osaka, Japan, April 2008.

[48] European Telecommunications Standards Institute, "Universal mobile telecommunications system (UMTS); spacial channel model for multiple input multiple output (MIMO) simulations," *ETSI TR-125-996-V7.0.0*, 2007.

[49] N. Czink, E. Bonek, L. Hentilä, P. Kyösti, J.-P. Nuutinen, and J. Ylitalo, "The interdependence of cluster parameters in MIMO channel modeling," in *Proceedings of the 1st European Conference on Antennas and Propagation (EuCAP '06)*, pp. 1–6, Nice, France, November 2006.

Hindawi Publishing Corporation
EURASIP Journal on Wireless Communications and Networking
Volume 2009, Article ID 195480, 13 pages
doi:10.1155/2009/195480

Research Article

Reduced Complexity Channel Models for IMT-Advanced Evaluation

Yu Zhang,[1] Jianhua Zhang,[1] Peter J. Smith,[2] Mansoor Shafi,[3] and Ping Zhang[4]

[1] *Wireless Technology Innovation Institute, Beijing University of Posts and Telecommunications, P.O. Box 92, Beijing 100876, China*
[2] *Department of Electrical and Computer Engineering, University of Canterbury, Private Bag 4800, 8140 Christchurch, New Zealand*
[3] *Telecom New Zealand, P.O. Box 293, 6001 Wellington, New Zealand*
[4] *Key Laboratory of Universal Wireless Communications, Beijing University of Posts and Telecommunications, P.O. Box 92, Beijing 100876, China*

Correspondence should be addressed to Yu Zhang, yu_zhang@ieee.org

Received 31 July 2008; Revised 6 November 2008; Accepted 26 February 2009

Recommended by Claude Oestges

Accuracy and complexity are two crucial aspects of the applicability of a channel model for wideband multiple input multiple output (MIMO) systems. For small number of antenna element pairs, correlation-based models have lower computational complexity while the geometry-based stochastic models (GBSMs) can provide more accurate modeling of real radio propagation. This paper investigates several potential simplifications of the GBSM to reduce the complexity with minimal impact on accuracy. In addition, we develop a set of broadband metrics which enable a thorough investigation of the differences between the GBSMs and the simplified models. The impact of various random variables which are employed by the original GBSM on the system level simulation are also studied. Both simulation results and a measurement campaign show that complexity can be reduced significantly with a negligible loss of accuracy in the proposed metrics. As an example, in the presented scenarios, the computational time can be reduced by up to 57% while keeping the relative deviation of 5% outage capacity within 5%.

1. Introduction

The pioneering work by Winters [1], Telatar [2], Foschini and Gans [3] ignited enormous interest in multiple input multiple output (MIMO) systems as they have the potential to provide remarkable spectral efficiencies when the channel exhibits rich scattering. Wideband wireless systems with multiple antennas have been recognized as one of the most promising candidates for next generation mobile systems which are also known as IMT-Advanced systems. It is well known that the propagation conditions have a crucial impact on the design, simulation, and deployment of new communication systems. Therefore, it is of great interest to characterize and model the wideband MIMO channel to enable accurate simulations of system performance. Propagation characteristics have been investigated thoroughly based on measured data from channel sounding in various different scenarios [4–8]. An overview of the state-of-the-art channel models is provided in [9]. These channel models can be divided into two major categories: (a) the correlation based models, for example, the Kronecker model [10] and the Weichselberger model [11]; and (b) the parametric or geometry-based stochastic models (GBSMs), for example, the COST 259 directional channel model (DCM) [12], the COST 273 channel model [13], the 3rd Generation Partnership Project (3GPP) spatial channel model (SCM) [14], and the WINNER channel model [15, 16], and so forth. Because of their simplicity, the correlation-based models are widely used for analyzing and designing space-time transmission technologies. The GBSM is more complex and less easy to use. One feature of a GBSM is that the simulation is divided into a number of drops which can be thought as channel segments with infinite time. Within each drop, different random geometries are generated. This

modeling methodology is adopted by the International Telecommunication Union (ITU) for the evaluation of IMT-Advanced systems [17].

In comparison with the broadly adopted traditional tapped delay line (TDL) models in the GSM and IMT-2000 systems, there are two main challenges for the IMT-Advanced channel model. Firstly, the TDL models in [18, 19] have an invariant channel profile. (The "channel profile" stands for the channel characteristics over a fading distance of tens of wavelengths, in spatial, temporal, and frequency domains, including the power delay profile (PDP), power angular spectrum (PAS), Doppler spectrum, and so forth.) However, even for a single link, geometry-based MIMO channel models need multiple channel profiles to accurately characterize the extra degrees of freedom induced by employing multiple antennas. As a result, far more random variables (RVs) have to be embedded into the channel model than are required by the TDL models. Secondly, because of the higher data rates targeted with a system bandwidth of up to 100 MHz, many more multipath components (MPCs) can be resolved, which leads to an increase in the number of taps for wideband MIMO channel models. Since the system level evaluation of radio interface technologies (RITs) usually requires the generation of multiple users dropped into a 19 hexagonal cell network, these two challenges faced by GBSMs make the evaluation a time consuming exercise. Hence, there is an urgent need to simplify the geometry-based MIMO channel models. As the correlation-based models have greatly reduced computational complexity, several papers have tried to bridge the gap between the correlated models and GBSMs. The separability of spatial-temporal correlation in the 3GPP SCM model is investigated in [20], which proposed a correlation-based model to replace the geometry-based model. A numerically efficient approximation of spatial correlation models is proposed in [21], which shows a good fit to the existing parametric models with a uniform linear array (ULA) or uniform circular array (UCA) for an angular spread (AS) smaller than 10°. A simplified approach to apply the 3GPP SCM model was suggested in [22], which was also proposed for the evaluation of the 3GPP long-term evolution (LTE) systems. Correlation-based replacements of the GBSM can substantially reduce the computational complexity. However, in such simplified models the antenna geometries and radiation patterns cannot be altered easily by the user of the model. On the other hand, this feature is automatically enabled by the geometry-based modeling for the propagation parameters and antennas.

In this paper, we investigate five possible simplifications to the GBSM model. These simplifications are much more straightforward than those obtained by converting a GBSM to its correlation-based counterpart. A series of metrics are proposed to evaluate the impact of the simplification on the channel model behavior. These metrics cover various different perspectives of the assessment of RITs with MIMO applications, including spatial multiplexing, spatial diversity, symbol error probability, and temporal behavior. The proposed simplifications and metrics are validated with a baseline model which is extracted from MIMO channel measurements in both indoor and outdoor environments. A computational complexity analysis is also presented. Since the simplifications are made under the original structure of the GBSM, the ability to select values for physically-based geometric parameters is maintained. Hence, the users of the simplified models can control the antenna configurations and link geometries as they do with the GBSM, while experiencing lower computational effort.

The main contributions of this paper are as follows:

(i) a range of broadband metrics are proposed and used for evaluating the full system behavior of wideband MIMO channel models;

(ii) a series of potential simplifications to the IMT-Advanced channel model are developed. The simplified models have fixed and fewer parameters that result in a negligible loss of performance as verified by a range of metrics;

(iii) measurements of an indoor channel with both line-of-sight (LOS) and scattered components were taken in China. The data was used to fit a WINNER style model [17] as the baseline GBSM. The metrics were then used to compare the simplified models with the GBSM and with the measured data;

(iv) the metrics were also evaluated with an outdoor non line-of-sight (NLOS) channel in the WINNER model [16] to demonstrate the validity of proposed simplifications.

The rest of the paper is organized as follows. A GBSM baseline model is briefly described in Section 2. A series of metrics for evaluating the performance of simplified wideband channel models are presented in Section 3. The proposed simplifications are described in Section 4. A comparative analysis of the simulation results and conclusions are given in Sections 5 and 6, respectively.

2. Baseline Channel Model

Currently, the primary channel model [17] for IMT-Advanced system evaluation is based on the WINNER channel model. Hence, in this paper we take the WINNER model as a baseline. Consider a single downlink of a wideband MIMO system with an S-element BS array and a U-element MS array. The channel impulse response (CIR) at time t, delay τ is modeled as

$$\mathbf{H}(\tau,t)=\sqrt{\frac{K}{K+1}}\mathbf{H}_0(t)\delta(\tau)+\sqrt{\frac{1}{K+1}}\sum_{n=1}^{N}\mathbf{H}_n(t)\delta(\tau-\tau_n), \tag{1}$$

where K is the Rician K-factor on a linear scale, $\mathbf{H}_0(t)$ is the channel coefficient matrix corresponding to the LOS ray, N is the number of clusters, $\mathbf{H}_n(t)$, $n=1,2,\ldots,N$, is the nth NLOS channel coefficient component, and $\delta(\cdot)$ is the Dirac delta function. Here, we assume that the clusters are the zero-delay-spread-clusters (ZDSCs) defined in [15], that is, a cluster is constituted by a number of rays, or propagation paths, diffused in angle domains. The rays within the same

cluster have the same propagation delay, and the power dispersion of a cluster in angle domains is characterized by cluster angular spread of departure (ASD) and cluster angular spread of arrival (ASA). The elements of the $U \times S$ matrix $\mathbf{H}_n(t) = (h_{usn}(t))$ are given by

$$h_{us0}(t) = \mathbf{c}_{\mathrm{BS},s}^{\mathrm{T}}(\phi_{\mathrm{LOS}}) \cdot \mathbf{X}(\mathbf{\Phi}_{\mathrm{LOS}}) \cdot \mathbf{c}_{\mathrm{MS},u}(\varphi_{\mathrm{LOS}}) \cdot \exp\left[jk\|\mathbf{v}\| \cos\left(\varphi_{\mathrm{LOS}} - \phi_v\right)t\right] \tag{2}$$

for $n = 0$,

$$h_{usn}(t) = \sqrt{\frac{P_n}{M}} \sum_{m=1}^{M} \mathbf{c}_{\mathrm{BS},s}^{\mathrm{T}}(\phi_{nm}) \cdot \mathbf{X}(\mathbf{\Phi}_{nm}, \kappa_{nm}) \cdot \mathbf{c}_{\mathrm{MS},u}(\varphi_{nm}) \cdot \exp\left[jk\|\mathbf{v}\| \cos\left(\varphi_{nm} - \phi_v\right)t\right] \tag{3}$$

for $n = 1, 2, \ldots, N$. In (2) and (3), $(\cdot)^{\mathrm{T}}$ stands for matrix transposition, P_n is the power resulting from the nth cluster, M is the number of rays in each cluster. The angles in (2) and (3) are illustrated in Figure 1, where ϕ_{LOS} is the angle of departure (AoD) for the LOS ray with respect to the BS broadside, φ_{LOS} is the angle of arrival (AoA) for the LOS ray with respect to the MS broadside, ϕ_{nm} is the AoD for the mth ray of the nth cluster with respect to the BS broadside, while φ_{nm} is the AoA with respect to the MS broadside, the mean AoD and mean AoA of the nth cluster is defined as $\phi_n = (1/M)\sum_{m=1}^{M} \phi_{nm}$ and $\varphi_n = (1/M)\sum_{m=1}^{M} \varphi_{nm}$, respectively. ϕ_v is the angle of the MS velocity vector $\mathbf{v}$ with respect to the MS broadside. $\mathbf{c}_{\mathrm{BS},s}(\phi_{nm}) = [c_{\mathrm{BS},s}^{\mathrm{V}}(\phi_{nm}), c_{\mathrm{BS},s}^{\mathrm{H}}(\phi_{nm})]^{\mathrm{T}}$ is the complex antenna response of the sth element of the BS array in the direction of ϕ_{nm} with respect to the reference phase center of the array, with $c_{\mathrm{BS},s}^{\mathrm{V}}(\cdot)$ and $c_{\mathrm{BS},s}^{\mathrm{H}}(\cdot)$ referring to the vertical and horizontal polarization directions, respectively. The vector $\mathbf{c}_{\mathrm{MS},u}(\varphi_{nm})$ is defined similarly. $\mathbf{\Phi}_{nm} = [\Phi_{nm}^{\mathrm{VV}}, \Phi_{nm}^{\mathrm{VH}}, \Phi_{nm}^{\mathrm{HV}}, \Phi_{nm}^{\mathrm{HH}}]^{\mathrm{T}}$ is the initial random phase vector of the mth ray of the nth cluster. The superscripts used in $\Phi_{nm}^{p_1 p_2}$ denote that the ray originates in the p_1 direction and arrives in the p_2 direction. $\mathbf{\Phi}_{\mathrm{LOS}} = [\Phi_{\mathrm{LOS}}^{\mathrm{VV}}, \Phi_{\mathrm{LOS}}^{\mathrm{HH}}]^{\mathrm{T}}$ is the initial random phase vector for the LOS ray. The polarization matrices $\mathbf{X}(\mathbf{\Phi}_{\mathrm{LOS}})$ and $\mathbf{X}(\mathbf{\Phi}_{nm}, \kappa_{nm})$ are given by

$$\mathbf{X}(\mathbf{\Phi}_{\mathrm{LOS}}) = \begin{pmatrix} \exp\left(j\Phi_{\mathrm{LOS}}^{\mathrm{VV}}\right) & 0 \\ 0 & \exp\left(j\Phi_{\mathrm{LOS}}^{\mathrm{HH}}\right) \end{pmatrix},$$

$$\mathbf{X}(\mathbf{\Phi}_{nm}, \kappa_{nm}) = \begin{pmatrix} \exp\left(j\Phi_{nm}^{\mathrm{VV}}\right) & \sqrt{\kappa_{nm}} \exp\left(j\Phi_{nm}^{\mathrm{VH}}\right) \\ \sqrt{\kappa_{nm}} \exp\left(j\Phi_{nm}^{\mathrm{HV}}\right) & \exp\left(j\Phi_{nm}^{\mathrm{VV}}\right) \end{pmatrix}, \tag{4}$$

where κ_{nm} is the inverse of the XPR for the nth cluster and mth ray. The XPR in decibels, is independent for each cluster and ray, and follows the Gaussian distribution $\mathcal{N}(\mu_{\mathrm{XPR}}, \sigma_{\mathrm{XPR}}^2)$. The constant k is the wave number $2\pi/\lambda$ with λ denoting the carrier wavelength in meters.

For each drop, the parameters required by (2) and (3) can be broken down into three sets: the LOS parameters $\{K, \phi_{\mathrm{LOS}}, \varphi_{\mathrm{LOS}}, \mathbf{\Phi}_{\mathrm{LOS}}\}$, the cluster parameters $\{(P_n, \tau_n, \phi_n, \varphi_n) : n = 1, 2, \ldots, N\}$, and the ray parameters $\{(\phi_{nm}, \varphi_{nm}, \mathbf{\Phi}_{nm}, \kappa_{nm}) : n = 1, 2, \ldots, N; m = 1, 2, \ldots, M\}$. According to the modeling methodology behind the WINNER channel model, for a specific scenario, the root-mean-square (RMS) delay spread (DS) τ_{RMS}, azimuth ASD ϕ_{RMS}, azimuth ASA φ_{RMS}, standard deviation of shadow fading (SF) $\sigma_{\xi,\mathrm{dB}}$, and the Rician K-factor K_{dB} for the LOS case are correlated log-normal RVs. Hence, the 5-dimensional random vector $\mathbf{L} = [\log_{10}(\tau_{\mathrm{RMS}}), \log_{10}(\phi_{\mathrm{RMS}}), \log_{10}(\varphi_{\mathrm{RMS}}), \sigma_{\xi,\mathrm{dB}}, K_{\mathrm{dB}}] \sim \mathcal{N}(\boldsymbol{\mu}_{\mathbf{L}}, \mathbf{\Sigma}_{\mathbf{L}})$, where $\boldsymbol{\mu}_{\mathbf{L}} = [\mu_{\mathrm{DS}}, \mu_{\mathrm{ASD}}, \mu_{\mathrm{ASA}}, 0, \mu_{K,\mathrm{dB}}]$ is the mean vector and $\mathbf{\Sigma}_{\mathbf{L}}$ is the covariance matrix. The standard deviations of the normal RVs in $\mathbf{L}$ are denoted by σ_X, and the cross-correlation coefficients between the normal RVs in $\mathbf{L}$ are denoted by ρ_{XY}, where X and Y are placeholders for DS, ASD, ASA, SF, and K. The detailed definitions of μ_X, σ_X, and ρ_{XY} are summarized in Table 1, where $\mathrm{E}(\cdot)$ is the expectation operator, $\mathrm{Var}(X)$ stands for the variance of RV X, and $\mathrm{Corr}(X, Y)$ denotes the cross-correlation coefficient of two RVs X and Y. The five parameters in $\mathbf{L}$ are called large-scale parameters (LSPs) [16] since they are invariant in a channel segment, or drop, which covers a fading distance of the order of tens of wavelengths.

The realization of the Rician-K factor together with realizations of the other LSPs, that is, the realization of the Gaussian random vector $\mathbf{L}$, are drawn to follow the distribution $\mathcal{N}(\boldsymbol{\mu}_{\mathbf{L}}, \mathbf{\Sigma}_{\mathbf{L}})$. The LOS ray angles, ϕ_{LOS} and φ_{LOS}, are geometrically determined by the relative positions of BS and MS, and by the broadside orientations of both BS and MS array. The cluster parameters, $\{\tau_n\}$, $\{P_n\}$, and $\{(\phi_n, \varphi_n)\}$ are sequentially generated according to the exponential delay distributions, exponential/uniform power delay profile (PDP), and wrapped Gaussian power angular spectrum (PAS), respectively. The shape of delay distributions, PDP and PAS, can be determined by realizations of the LSPs, that is, τ_{RMS}, ϕ_{RMS}, and φ_{RMS}, which are generated together with K as mentioned above. The ray parameters $\{(\phi_{nm}, \varphi_{nm}) : n = 1, 2, \ldots, N; m = 1, 2, \ldots, M\}$ are obtained by adding predefined offset angles to ϕ_n or φ_n to follow Laplacian PASs with given per cluster angular spread. The elements in the initial phases $\mathbf{\Phi}_{\mathrm{LOS}}$ and $\mathbf{\Phi}_{nm}$ are independent and identically distributed uniform in $(-\pi, \pi)$. A detailed procedure of the generation of these parameters can be found in [16]. Within a drop, all these parameters are invariant. Thus, a single drop cannot reflect the propagation characteristics for a given scenario and multiple-drop simulation is needed even for link-level performance evaluation.

3. Evaluation Metrics for Wideband MIMO Channels

To evaluate the impact of various potential simplifications to the channel model, proper metrics for wideband MIMO channels are needed. Usually, spatial-temporal correlations are used as two simple but fundamental metrics for MIMO channel models. However, this paper aims to go further and develops a thorough approach to studying the full system behavior, through a more complex set of metrics. This set includes mutual information, diversity gain, error

Table 1: Definitions of first- and second-order statistics of LSPs.

$\mu_{\mathrm{DS}} = \mathrm{E}[\log_{10}(\tau_{\mathrm{RMS}})]$	$\rho_{\mathrm{ASD,DS}} = \mathrm{Corr}[\log_{10}(\phi_{\mathrm{RMS}}), \log_{10}(\tau_{\mathrm{RMS}})]$
$\mu_{\mathrm{ASD}} = \mathrm{E}[\log_{10}(\phi_{\mathrm{RMS}})]$	$\rho_{\mathrm{ASA,DS}} = \mathrm{Corr}[\log_{10}(\varphi_{\mathrm{RMS}}), \log_{10}(\tau_{\mathrm{RMS}})]$
$\mu_{\mathrm{ASA}} = \mathrm{E}[\log_{10}(\varphi_{\mathrm{RMS}})]$	$\rho_{\mathrm{ASD,SF}} = \mathrm{Corr}[\log_{10}(\phi_{\mathrm{RMS}}), \sigma_{\xi,\mathrm{dB}}]$
$\mu_{K,\mathrm{dB}} = \mathrm{E}[K_{\mathrm{dB}}]$	$\rho_{\mathrm{ASA,SF}} = \mathrm{Corr}[\log_{10}(\varphi_{\mathrm{RMS}}), \sigma_{\xi,\mathrm{dB}}]$
	$\rho_{\mathrm{ASD,ASA}} = \mathrm{Corr}[\log_{10}(\phi_{\mathrm{RMS}}), \log_{10}(\varphi_{\mathrm{RMS}})]$
$\sigma^2_{\mathrm{DS}} = \mathrm{Var}[\log_{10}(\tau_{\mathrm{RMS}})]$	$\rho_{\mathrm{DS,SF}} = \mathrm{Corr}[\log_{10}(\tau_{\mathrm{RMS}}), \sigma_{\xi,\mathrm{dB}}]$
$\sigma^2_{\mathrm{ASD}} = \mathrm{Var}[\log_{10}(\phi_{\mathrm{RMS}})]$	$\rho_{\mathrm{ASD,K}} = \mathrm{Corr}[\log_{10}(\phi_{\mathrm{RMS}}), K_{\mathrm{dB}}]$
$\sigma^2_{\mathrm{ASA}} = \mathrm{Var}[\log_{10}(\varphi_{\mathrm{RMS}})]$	$\rho_{\mathrm{ASA,K}} = \mathrm{Corr}[\log_{10}(\varphi_{\mathrm{RMS}}), K_{\mathrm{dB}}]$
$\sigma^2_{K,\mathrm{dB}} = \mathrm{Var}[K_{\mathrm{dB}}]$	$\rho_{\mathrm{DS,K}} = \mathrm{Corr}[\log_{10}(\tau_{\mathrm{RMS}}), K_{\mathrm{dB}}]$
$\sigma^2_{\mathrm{SF}} = \mathrm{Var}[\sigma_{\xi,\mathrm{dB}}]$	$\rho_{\mathrm{SF,K}} = \mathrm{Corr}[\sigma_{\xi,\mathrm{dB}}, K_{\mathrm{dB}}]$

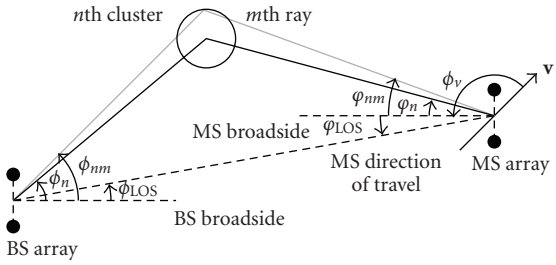

Figure 1: Definition of angles in WINNER channel model.

rate, and temporal behavior. Recall that, in the baseline model, a scenario is characterized by multiple drops with different realizations of LSPs. For either link- or system-level simulation, the overall performance of all drops is concerned. Based on this fact, these metrics are designed for evaluating the average behavior over multiple drops. With such metrics, we can try to examine whether the proposed simplified model has equivalent behavior in the scenario level. The proposed metrics are described in what follows.

3.1. Spatial Multiplexing Metric. Outage capacity is a widely adopted metric to evaluate the spatial multiplexing ability of an MIMO channel, because it is the main benefit provided by this MIMO mode. The outage capacity, or the cumulative distribution function (CDF) of the channel capacity, when the channel is unknown to the transmitter is preferred to the ergodic capacity which can be derived from the CDF. This is because the ergodic capacity is often insensitive to the exact channel characteristics, whereas the capacity distribution is more easily affected. Hence, the outage capacity provides a more rigorous test. The capacity of a time-invariant frequency-selective fading MIMO channel is given by [23]

$$C = \frac{1}{B}\int_B \log_2 \det\left[\mathbf{I}_U + \frac{\rho}{S}\mathbf{H}(f)\mathbf{H}(f)^{\dagger}\right]\mathrm{d}f, \tag{5}$$

where $(\cdot)^{\dagger}$ stands for conjugate transpose, B is the bandwidth, ρ denotes the signal-to-noise ratio (SNR) and $\mathbf{H}(f)$ is the normalized frequency domain channel matrix with unitary average channel power gain, that is,

$$\mathrm{E}\left(\|\mathbf{H}(f)\|_{\mathrm{F}}^2\right) = US. \tag{6}$$

Note that $\mathbf{H}(f)$ is the transform of the composite impulse response with the delays, so the capacity obtained from (5) is the broadband capacity. In (5), we have assumed equal power allocation and no water filling is done both in the frequency and space domains. Given an SNR ρ, the $100q\%$ outage capacity C_q is defined as the spatial multiplexing metric, that is, $\Pr[C < C_q] = q$.

3.2. Spatial Diversity Metric. When the channel is known to the transmitter, spatial diversity is related to the dominant eigenmodes of the channel matrix. Hence, we choose the marginal CDF of each ordered eigenvalue of the channel correlation matrix as the spatial diversity metric. Let $\lambda_{(n)}(f)$, $n = 1, 2, \ldots, U$, be the eigenvalues of $\mathbf{H}(f)\mathbf{H}(f)^{\dagger}$ in descending order, that is,

$$\lambda_{(1)}(f) \geqslant \lambda_{(2)}(f) \geqslant \cdots \geqslant \lambda_{(U)}(f). \tag{7}$$

Note that, (7) implies that $\lambda_{(n)}(f) = 0$ for $r < n \leqslant U$, where $r = \mathrm{rank}[\mathbf{H}(f)\mathbf{H}(f)^{\dagger}]$. For $n = 1, 2, \ldots, r$, the r empirical distribution functions obtained from $\{\lambda_{(n)}(f) : f \in [-B/2, B/2]\}$ are used as the spatial diversity metric. Note that this approach is quite unusual. The eigenvalues are being considered as random variables over frequency rather than over different channel realizations for the same frequency. For example, considering the maximum eigenvalue, a range of values is obtained from measurements or simulations over frequency and not over different channel realizations. This reflects the focus of the paper on broadband metrics.

3.3. Symbol Error Probability. The exact symbol error probability (SER) of singular value decomposition (SVD)-based MIMO receivers using uncoded transmission is derived in [24] for flat-fading channels. We generalize the result to the frequency selectivity case. If only the first m principal eigen modes are activated for the SVD-based transmission and the uncoded BPSK scheme is adopted, the symbol error probability for a given SNR level ρ is given by

$$\mathrm{SER}(\rho) = 1 - \frac{1}{2^m B}\int_{-B/2}^{B/2} \mathrm{E}\left\{\prod_{i=1}^{m} \mathrm{erfc}\left(-\sqrt{\frac{\rho\lambda_{(i)}(f)}{2S}}\right)\right\}\mathrm{d}f, \tag{8}$$

where $\mathrm{erfc}(x)$ is the complementary error function. For a fixed SER value, let the required SNR be ρ_0 for the baseline

model and ρ_1 for the simplified model. The SNR shift, $\Delta\rho = |\rho_1 - \rho_0|$, is defined as the SER metric.

3.4. Temporal Behavior of MIMO Capacity. The capacity of the time-variant MIMO channel is a stochastic process. The temporal behavior of the MIMO channel model can be partially reflected by the level crossing rate (LCR) across a capacity level C_T (denoted as $\mathsf{LCR}(C_T)$) and the average fading duration (ADF) of the capacity process below C_T [25]. Let μ_C be the mean capacity, and σ_C^2 be the capacity variance. Defining the standardized capacity values as $\widetilde{C} = (C - \mu_C)/\sigma_C$, we focus on the $\mathsf{LCR}(\widetilde{C}_T)$ which is the LCR of the normalized capacity, $\widetilde{C}$, across $\widetilde{C}_T$. Results are shown for $\mathsf{LCR}(\widetilde{C}_T)$ normalized by the maximum Doppler frequency f_D, versus the outage probability given by $P_{out}(\widetilde{C}_T) = \Pr[\widetilde{C} < \widetilde{C}_T]$ [25].

4. Potential Simplifications

4.1. Clipping Clusters with Lower Power. In [26], the computational complexity of channel model simulation was divided into three different categories: (a) complexity of channel coefficient generation, (b) number of required parameters, and (c) the complexity of simulation. Both (a) and (c) are proportional to the number of delay taps. Hence, the computational complexity can be reduced if the number of delay taps can be reduced. However, the impact of reducing the number of delay taps needs to be investigated. The clipping is based on the fact that the average power of some clusters is relatively low with respect to the maximum cluster power. Consider a scenario with N clusters, where the average cluster power of the nth cluster is P_n in decibels. Denote the cluster indexing set as $\mathcal{I} = \{1, 2, \ldots, N\}$. For a given cluster power threshold, P_{th} in decibels, the cluster is clipped if its power is below this threshold when the power of the dominant cluster is chosen as a reference. The reduced number of clusters is an RV

$$N_{clipped} = \sum_{n=1}^{N} I\left(P_n < \max_{k\in\mathcal{I}} P_k - P_{th}\right), \tag{9}$$

where $I(A)$ is the indicator function of event A, namely,

$$I(A) = \begin{cases} 1, & \text{event } A \text{ is true,} \\ 0, & \text{otherwise.} \end{cases} \tag{10}$$

As mentioned in [26], the computational time for simulation is dominated by the convolution operation, and the time required by such an operation is proportional to the number of delay taps (or the number of clusters). Consequently, if we normalize the computational time after clipping by the time required before clipping, the *normalized computational time* (NCT) can be defined as the ratio of the average number of remaining clusters to the number of original clusters, that is,

$$\mathsf{NCT}(P_{th}) = 1 - \frac{1}{N}\mathrm{E}(N_{clipped}). \tag{11}$$

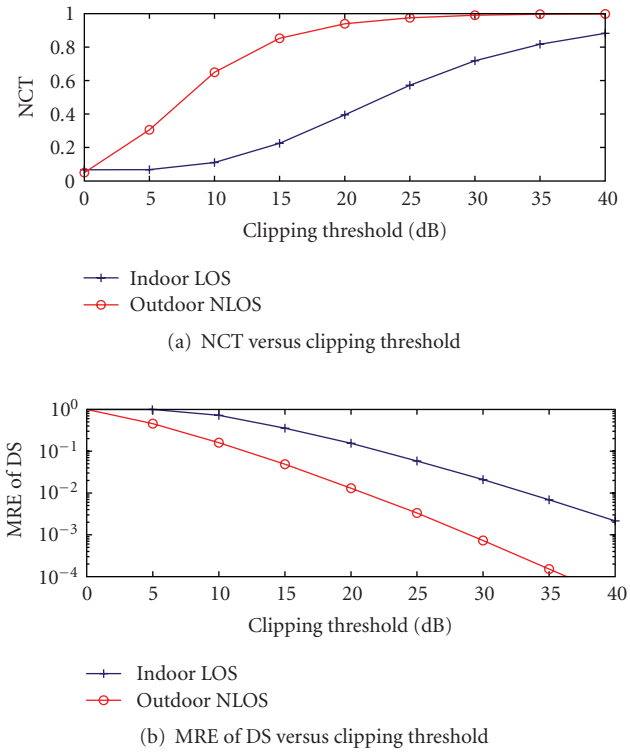

(a) NCT versus clipping threshold

(b) MRE of DS versus clipping threshold

FIGURE 2: The impact of clipping threshold on the efficiency and the accuracy (averaged over 10^4-drop runs).

When the clipping threshold $P_{th} = 0$ dB, only the cluster with maximum power remains. Thus the minimum NCT is obtained, that is, $\mathsf{NCT}(0) = 1/N$. When $P_{th} \to \infty$, no cluster will be clipped and NCT converges to one. The NCT indicates the benefit gained by clipping the low-power clusters. Figure 2(a) shows the relationship of NCT versus the clipping threshold for the model parameterized in Table 3. The NCT is averaged over 10^4 simulation runs. It shows that the average computational complexity can be reduced by more than 40% when a 25 dB clipping threshold is adopted for the "Indoor LOS" case, while a 15% improvement can be expected for the "Outdoor NLOS" case if $P_{th} = 15$ dB. The NLOS case requires a higher clipping threshold with respect to the LOS case to archive the same NCT reduction. As for the LOS case, the power of LOS ray is stronger than the NLOS rays such that most clusters were clipped out for a low threshold. For the NLOS case, the power difference among clusters is not so large as for the LOS case. So, even with a lower threshold, clusters are more likely to be clipped.

To keep the total power of the remaining clusters unitary, the loss of the power of the clipped clusters needs to be compensated. For a given threshold, P_{th}, the indexing set $\mathcal{I}$ can be separated into two disjoint sets, $\mathcal{I}_0 = \{n : P_n < \max_{k\in\mathcal{I}} P_k - P_{th}\}$ and its complement $\mathcal{I}_1 = \mathcal{I} \setminus \mathcal{I}_0$. If cluster n is clipped subject to a certain threshold, its power, P_n, can be combined with the power of the closest neighboring cluster m which is given by

$$m = \arg\min_{k\in\mathcal{I}_1} |\tau_k - \tau_n|, \quad \forall n \in \mathcal{I}_0. \tag{12}$$

A direct consequence of clipping clusters is the bias in the RMS delay spread which is inversely proportional to the coherent bandwidth, a critical parameter. For a given drop, denotes the RMS delay spread before and after clipping with a threshold P_{th} as τ_{RMS} and $\widetilde{\tau}_{\text{RMS}}$, respectively. The mean relative error (MRE) of the RMS delay spread versus the clipping threshold is defined by

$$\epsilon_{\text{DS}}(P_{\text{th}}) = \text{E}\left(\frac{\left|\widetilde{\tau}_{\text{RMS}} - \tau_{\text{RMS}}\right|}{\tau_{\text{RMS}}}\right), \tag{13}$$

which is plotted in Figure 2(b). It shows, as expected, that as the threshold becomes larger, the relative error ϵ_{DS} becomes smaller. The MRE of DS is more sensitive to the clipping threshold in the NLOS case. Particularly, ϵ_{DS} is around 5% when the clipping threshold $P_{\text{th}} = 15\,\text{dB}$ for the outdoor NLOS case or $P_{\text{th}} = 25\,\text{dB}$ for the indoor LOS case.

4.2. Fixed RMS Delay Spread. In order to estimate a given performance metric via Monte Carlo simulation, the number of random samples required to achieve a given level of confidence depends on the number of RVs involved in the simulation. As mentioned above, random realizations of five LSPs need to be drawn from their own distributions. The angular spread at both ends of the link, that is, ASD and ASA, will have a crucial impact on the spatial correlation properties of the MIMO channel. Hence, we propose fixing the RMS DS at its mean value to reduce the number of RVs. Although this will change the per drop behavior of the channel model, mainly in the delay domain, the average behavior will only be slightly affected as shown in Section 5.

4.3. Fixed XPR. In addition to fixing the RMS DS as a constant, we can also fix the XPR. The behavior of MIMO systems with cross-polarized antennas was investigated in [27] with the 3GPP/3GPP2 SCM model. These results showed that the change in mean capacity as the XPR varies is negligible for a $\pm 45^{\circ}$ cross-polarized 2×2 system. Hence, we propose fixing the XPR at its mean value and investigate the impact of this simplification on the metrics given in Section 3.

4.4. Uncorrelated LSPs. The LSPs, DS, ASD, ASA, SF, and Rician-K factor, are correlated in the baseline channel model. However, as shown in Table 3, the parameters extracted from field measurements show that some LSPs are weakly correlated or even uncorrelated, for example, Rician-K factor versus ASA or ASD, ASD versus ASA, DS versus ASA, and so forth. Some similar weak correlation properties are also reported in the literature [16, 17]. We remove the correlations between the LSPs and investigate the impact of this simplification.

5. Results and Discussions

5.1. Channel Measurements and Parameter Extraction

5.1.1. Measurement System. To extract the parameters required by the baseline model, wideband channel data were collected using the Elektrobit Propsound CS [28] MIMO channel sounder, which uses pseudorandom binary signals (PRBS) and time-division multiplexed (TDM) switching. The transmitted power was 26 dBm and the length of the PRBS was 511 symbols. The transmitter (TX) was equipped with a dual-polarized omnidirectional array (ODA) with a maximum of 50 elements. The receiver (RX) employed a vertically polarized 8-element uniform circular array (UCA). Figures 3(a) and 3(b) show, respectively, the configurations of the TX and RX antenna arrays. Schematic plots of both antenna arrays are given in Figure 4. The spacing between the neighboring elements in both the ODA and the UCA is half a wavelength. All 8×50 subchannels are sounded by activating each TX-RX element pair consecutively within a time period which is referred to as a measurement cycle. A temporal snapshot refers to the impulse response measured within a measurement cycle. The temporal snapshot rate is also the cycle rate. The measurement settings are summarized in Table 2.

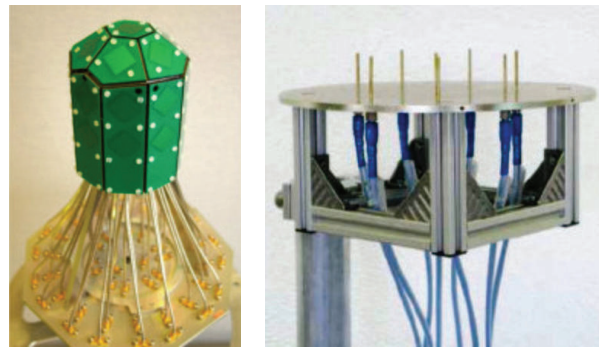

(a) TX array (b) RX array

Figure 3: Configurations of the antenna arrays used in the measurements.

Table 2: General sounder parameters.

Item	Setting
Center frequency	5.25 GHz
Chip rate	100 MHz
Sampling rate	200 MHz
TX power at antenna input	26 dBm
PN code length	511
Temporal snapshot rate	21.7 Hz
Number of elements of TX array	50
Number of elements of RX array	8

5.1.2. Measurement Environment. Stationary measurements were conducted in the corridor of a teaching building on the campus of Beijing University of Posts and Telecommunications (BUPT), China as the indoor scenario [29]. The dimension of a single floor is $120 \times 45 \times 6\,\text{m}^3$. The TX array and RX array were located about 1.5 m and 2.5 m above the floor level, respectively. All 8×50 elements on both TX and RX arrays are enabled during the measurements.

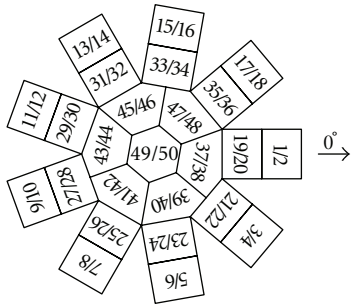

(a) TX array

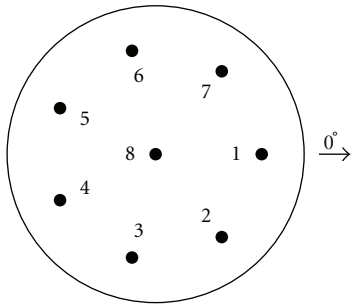

(b) RX array

Figure 4: Schematic plots of the antenna arrays used in the measurements.

Figure 5 illustrates the layout of indoor measurements in the corridor. The RX was fixed as the base station and is marked with the arrow denoting the reference direction. The TX was measured at the 32 locations marked as "TX Position." At each spot, 100 temporal snapshots of raw data were recorded. In this environment, the walls along the corridor and between the rooms are made of bricks with plastic poster boards on the surface. The floor has a marble surface and the doors of the rooms are wooden. The entrance doors are made of glass with aluminum frames.

5.1.3. Method of Noise Cut. Receiver noise was superimposed on the measured CIRs. Hence, before either estimating channel parameters or determining capacity in (5), we need to choose an appropriate dynamic range of the measured CIRs to perform the noise cut. Following [30], the *per subchannel dynamic noise cut* method is applied in this paper. Given a temporal snapshot, the noise floor P_{floor} was calculated for each subchannel. As a rule of thumb, a 6 dB noise margin Δ_{noise} added to the estimated noise floor can guarantee the noise is better cut. The per subchannel dynamic range of a measured CIR is defined as

$$\mathrm{DR} = \min\left\{P_{\text{peak}} - \left(P_{\text{floor}} + \Delta_{\text{noise}}\right), \mathrm{DR}_{\max}\right\}, \tag{14}$$

where P_{peak} is the peak value of PDP for the given subchannel and $\mathrm{DR}_{\max} = 25$ dB is the predefined maximum dynamic range.

5.1.4. Parameters for the Baseline Model. For each temporal snapshot, the multipath channel is described by the superposition of L rays. The rays are characterized by the parameter

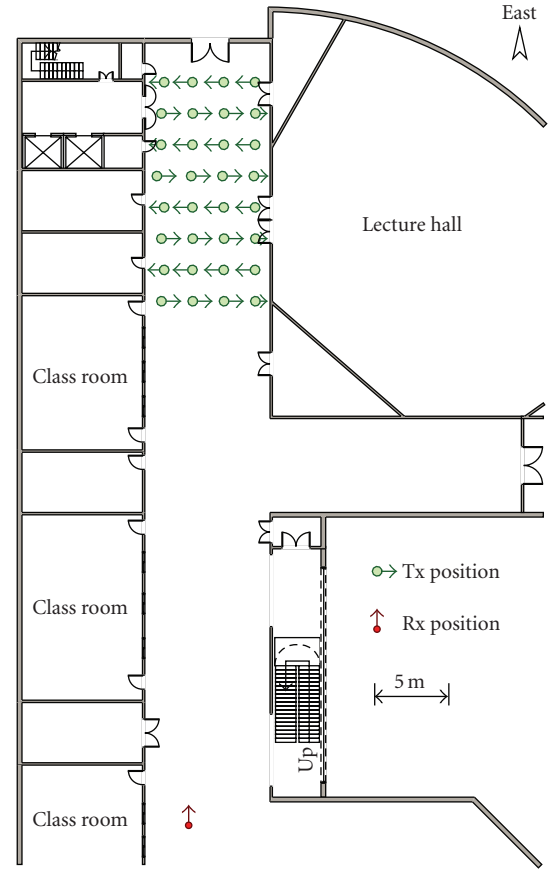

Figure 5: Layout of the indoor measurements in the corridor.

set $\mathcal{P} = \{(\tau_\ell, \phi_\ell, \theta_\ell, \varphi_\ell, \vartheta_\ell, \nu_\ell, \mathbf{X}_\ell) : \ell = 1, 2, \ldots, L\}$. Here, τ_ℓ, ϕ_ℓ, θ_ℓ, φ_ℓ, ϑ_ℓ, and ν_ℓ denote the excess delay, the azimuth of departure, the elevation of departure, the azimuth of arrival, the elevation of arrival, and the Doppler shift of the ℓth ray. The polarization matrix reads $\mathbf{X}_\ell = (\alpha_{\ell,p_2,p_1})_{2\times 2}$. The complex entry α_{ℓ,p_2,p_1} represents the weight for the ℓth ray that originates in the p_1 direction and arrives in the p_2 direction. Under the assumption of far-field and planar wave propagation, the Space-Alternating Generalized Expectation maximization (SAGE) algorithm [31, 32] is utilized to estimate the parameter set $\mathcal{P}$ from each temporal snapshot of the measured CIRs. The first- and second-order statistics of these parameters in $\mathcal{P}$ correspond to the LSPs described in Section 2, and are summarized in Table 3. The estimated maximum Doppler shift f_{D} is 1 Hz for the indoor measurements.

For reasons of space a full description of the parameter extraction methodology cannot be given here. However, the references [16, 31, 32] contain the necessary details. The basic approach can be summarized as below. The measured data is taken and the SAGE algorithm [31, 32] is used to obtain samples of the 7 parameters in $\mathcal{P}$ from each temporal snapshot. Following the WINNER methodology [16], these samples are then used to find the parameters in the columns entitled "Indoor" in Table 3. Finally, these tabulated parameters are sufficient to define the terms in

Table 3: Parameters for the baseline channel model.

Parameter	Unit	Indoor[a]	Outdoor[b]	Parameter	Unit	Indoor[a]	Outdoor[b]
μ_{DS}	$\log_{10}[s]$	−7.70	−7.12	$\rho_{ASD,DS}$		0.17	0.20
σ_{DS}		0.18	0.12	$\rho_{ASA,DS}$		0.01	0.40
μ_{ASD}	$\log_{10}[^\circ]$	1.60	1.19	$\rho_{ASA,SF}$		−0.02	−0.40
σ_{ASD}		0.18	0.21	$\rho_{ASD,SF}$		−0.18	0.00
μ_{ASA}		1.62	1.55	$\rho_{DS,SF}$		−0.18	−0.70
σ_{ASA}		0.22	0.20	$\rho_{ASD,ASA}$		0.07	0.10
σ_{SF}	dB	3.0	4.0	$\rho_{ASD,K}$	—	−0.09	N/A
μ_K		4.7	N/A	$\rho_{ASA,K}$		−0.07	N/A
σ_K		0.9	N/A	$\rho_{DS,K}$		−0.32	N/A
r_τ	—	3.6	1.0	$\rho_{SF,K}$		0.57	N/A
μ_{XPR}	dB	3.7	8.0	Cluster ASD	°	5	10
σ_{XPR}		9.6	3.0	Cluster ASA		11	22
N	—	15	16	M	—	20	20

[a]Parameters for the indoor case are obtained from the measurements described in Section 5.1.
[b]The NLOS case of the "Urban macrocell (C2)" scenario in the WINNER channel model [16].

the channel coefficients given in (2) and (3) by the steps described in [16].

Besides the indoor LOS case, an outdoor NLOS case is also selected as shown in Table 3. The parameters in the columns entitled "Outdoor" are the same as those for the NLOS case of the "Urban macrocell (C2)" scenario in the WINNER channel model [16]. The definition of each parameter can be found in Section 2.

5.2. Simulation Assumptions. To investigate the impact of the proposed simplifications on channel behavior, we constrain the antenna configuration and bandwidth to match the measurement campaign. We select 9 elements from the 50-element MS array and 7 elements from the 8-element BS array to form a 9×7 downlink MIMO channel. This approach is both manageable from a complexity point of view and is in agreement with the measurement configuration described previously. The selected BS array is a 7-element vertical polarized uniform circular array, that is, the 7+1 UCA without the central element. The MS antenna array is a 9-element dual-polarized uniform circular array which can be thought as the center ring of the 2×9 ODA (with odd elements from no. 19 to no. 35 in Figure 4(a)). For both antenna arrays, the element spacing is half a wavelength. The field patterns of real antennas are embedded into the baseline and simplified models to regenerate equivalent sets of MIMO channel matrix realizations. The embedding of field patterns is archived by substitution of the array patterns obtained in an anechoic chamber as $\mathbf{c}_{BS,s}$ and $\mathbf{c}_{MS,u}$ into (2) and (3). The channel coefficients are generated following [33] and by replacing the scenario specific parameters in [33] with those in Table 3. For the indoor case, all other parameters of the model are set to match those obtained in the measurement campaign. This includes reference directions for both antenna arrays. The assumptions are summarized in Table 4. The channel is sampled at a frequency four times the maximum Doppler frequency. The results are obtained by averaging over 1000 simulation runs(or drops) [14]. (The number of drops is chosen to be manageable from a complexity point of view and also to ensure satisfactory convergence of the metric.) The fading distance of 50 wavelengths is assumed for each drop.

For brevity, we designate the simplified models as "SM-" suffixed with a letter. SM-A refers to the full model where the clusters are clipped out with a 25 dB threshold for the indoor LOS case or a 15 dB threshold for the outdoor NLOS case. SM-B takes the full model and fixes RMS DS as a constant. SM-C fixes XPR at its mean value and SM-D removes the cross-correlations between LSPs. SM-E applies all the simplifications in SM-A, B, C, and D simultaneously. The designators are listed in Table 5. In the following simulation results, the measured results are given as a reference for Indoor scenario only.

5.3. Simulation Results and Discussion

5.3.1. Ordered Eigenvalue Distributions. The marginal CDFs of the first five principal eigenvalues for the baseline and simplified models are as shown in Figure 6. It can be seen that the proposed simplifications have a very minor impact on the distribution of the first principal eigenvalue. Removing the cross-correlations between LSPs has made little change to the distribution of ordered eigenvalues. Similarly, fixing the RMS DS leads to a negligible effect on the eigenvalues. As predicted, the impact on the spatial correlations is not significant and hence there is little impact on the eigenvalues. Figure 6(a) also tells us that the distortion of different ordered eigenvalues differs when SM-C or SM-E is applied. For example, with SM-C, $\lambda_{(2)}$ is underestimated while $\lambda_{(4)}$ and $\lambda_{(5)}$ are overestimated with respect to the baseline model. Figure 6(b) shows that for outdoor NLOS case, the ordered eigenvalue distribution is less sensitive to all simplifications.

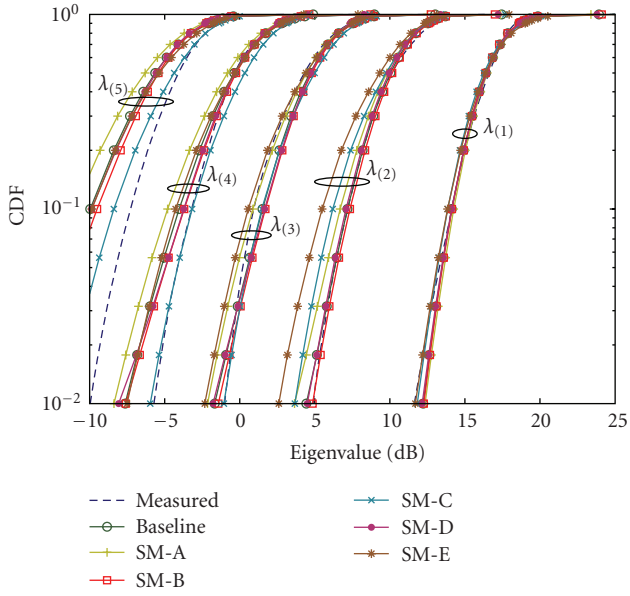

(a) Indoor LOS case

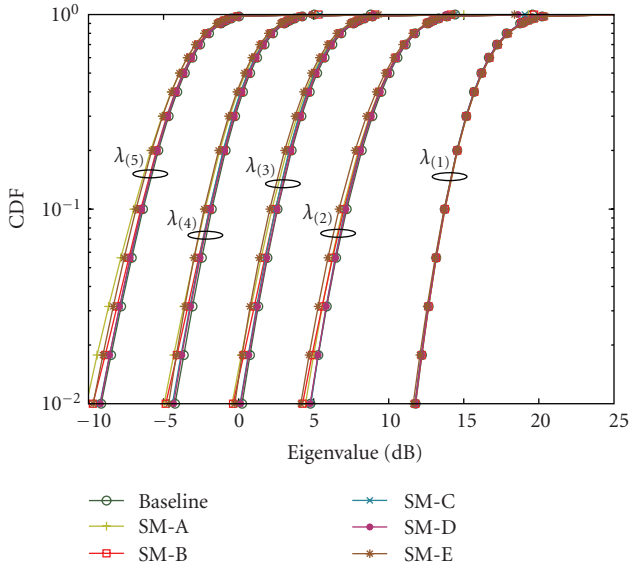

(b) Outdoor NLOS case

Figure 6: CDFs of the first five principal eigenvalues for baseline and simplified cases.

Note that in the measurement-based indoor baseline model, the nonprincipal eigenvalues deviate from the measured results. The relative deviation of the eigenvalue becomes larger for smaller eigenvalues.

5.3.2. Outage Capacity. Broadband capacity are obtained by integrating the narrowband capacity over the entire bandwidth as in (5). The CDFs of MIMO capacity for the baseline and simplified models are depicted in Figure 7. There are three different SNR levels which represent the marginal, medium, and high SNR cases. We see that the baseline and simplified models always underestimate the MIMO capacity

Table 4: Assumptions of channel reconstruction.

Parameter	Description
Carrier frequency	5.25 GHz
Bandwidth	100 MHz
BS antenna array	7-element UCA, vertical polarized
MS antenna array	9-element UCA, $\pm 45^\circ$ dual polarized
MS velocity	1.5 km/h (indoor) and 120 km/h (outdoor)
Sample density	2 samples per half wavelength
No. of drops	1000
No. of time samples per drop	200
Delay sampling density	5 ns
No. of frequency bins	1024

with respect to the measured result. This underestimation comes from several aspects such as measurement errors and possibly the lack of elevation spread in the models, which was theoretically analyzed in [34]. For the indoor LOS case, the variations in MIMO capacity due to the proposed simplifications increase as the SNR increases. With SM-E, the relative deviation of the capacity for an outage of 5% at high SNR ($\rho = 20$ dB) is 4.23%. Since the use of SM-E will lead to the maximum deviation in outage capacity, the relative deviation of the capacity for outages of 5% due to the application of any proposed simplified model will not exceed 5% in the high SNR regime. For the outdoor NLOS case, the relative deviation is always less than 5%.

As shown in Figure 7(a), there is a deviation of the baseline model from the measurements in the high SNR case. This deviation is mainly caused by the deviation of nonprincipal eigenvalues. For a given frequency f, denote the measured and model generated $U \times S$ channel matrix as $\mathbf{H}(f)$ and $\mathbf{H}'(f)$, respectively. Let $\lambda_{(n)}$ and $\lambda'_{(n)}$ be the ordered eigenvalues of $\mathbf{H}(f)\mathbf{H}(f)^\dagger$ and $\mathbf{H}'(f)\mathbf{H}'(f)^\dagger$, respectively, where $\lambda_{(1)} \geqslant \lambda_{(2)} \geqslant \cdots \geqslant \lambda_{(U)}$ and $\lambda'_{(1)} \geqslant \lambda'_{(2)} \geqslant \cdots \geqslant \lambda'_{(U)}$. Assume the eigenvalues can be divided into two sets: the well fitted principal eigenvalues in $\mathcal{L}_1 = \{(\lambda_{(n)}, \lambda'_{(n)}) : n = 1, 2, \ldots, r'\}$ with negligible relative deviation; and small eigenvalues in $\mathcal{L}_2 = \{(\lambda_{(n)}, \lambda'_{(n)}) : n = r'+1, r'+2, \ldots, U\}$ with large deviations. When the SNR $\rho \to \infty$, the capacity deviation tends to

$$\begin{aligned} \epsilon_C &= \lim_{\rho \to \infty} \sum_{n=1}^{U} \log_2 \frac{1 + (\rho/S)\lambda'_{(n)}}{1 + (\rho/S)\lambda_{(n)}} \\ &= \sum_{n=1}^{r'} \log_2 \left(1 + \frac{\Delta\lambda_{(n)}}{\lambda_{(n)}}\right) + \sum_{n=r'+1}^{U} \log_2 \left(1 + \frac{\Delta\lambda_{(n)}}{\lambda_{(n)}}\right), \end{aligned} \tag{15}$$

where $\Delta\lambda_{(n)} = \lambda'_{(n)} - \lambda_{(n)}$. The first term in (15) approximates to zero as the relative deviation $\Delta\lambda_{(n)}/\lambda_{(n)}$ is very small. For the eigenvalues in $\mathcal{L}_2$, the nonnegligible relative deviation $\Delta\lambda_{(n)}/\lambda_{(n)}$ causes the capacity deviation. In Figure 6(a), we can take $r' = 4$. For the probability of 0.5, we have $\lambda_{(5)} = -4.0$ dB $= 0.40$ and $\lambda'_{(5)} = -5.6$ dB $= 0.28$. Thus, $\Delta\lambda_{(5)}/\lambda_{(5)} = -0.43$, and $\log_2(1+\Delta\lambda_{(n)}/\lambda_{(n)}) = -0.81$ bit/s/Hz.

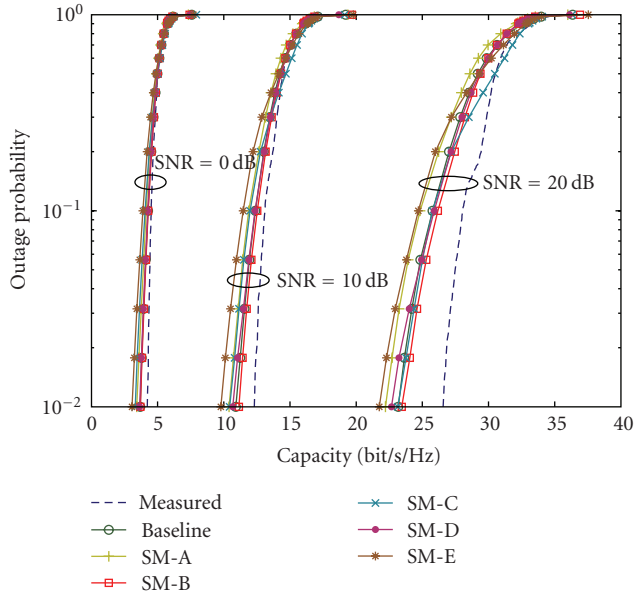

(a) Indoor LOS case

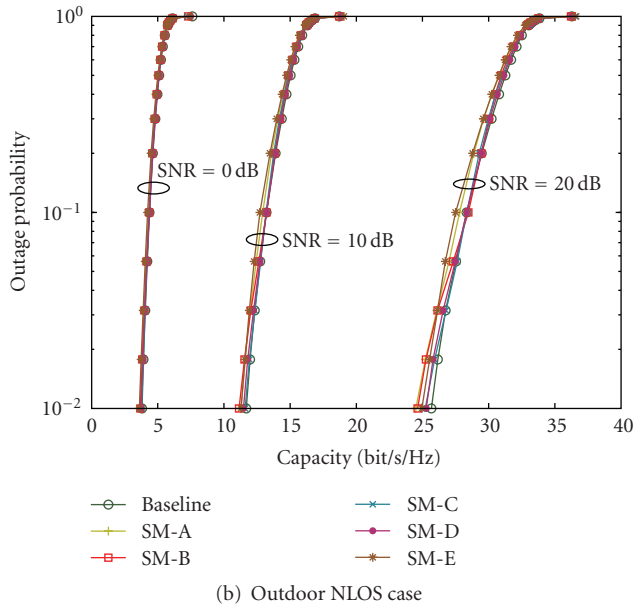

(b) Outdoor NLOS case

Figure 7: CDFs of MIMO capacity for baseline and simplified cases.

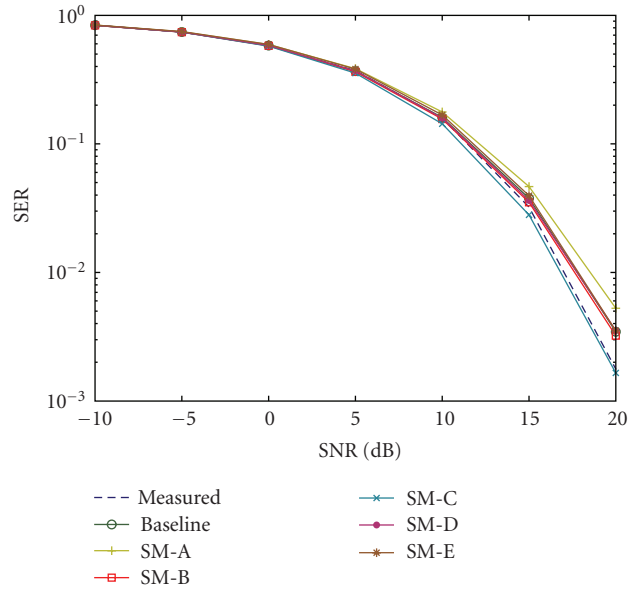

(a) Indoor LOS case

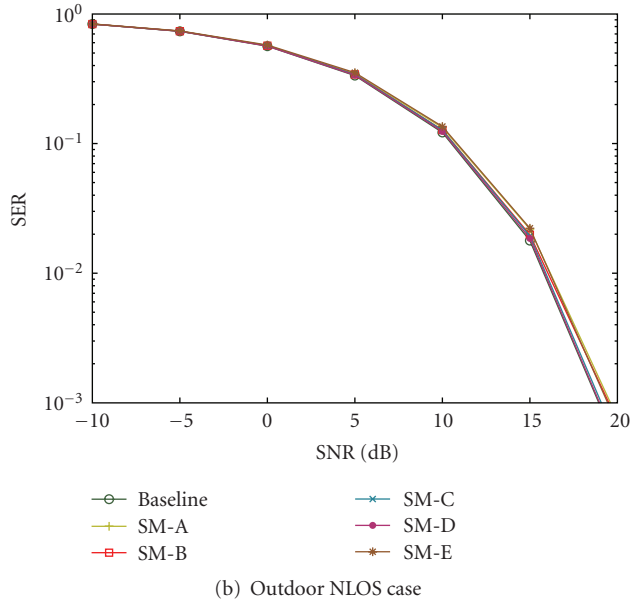

(b) Outdoor NLOS case

Figure 8: SVD symbol error probabilities for baseline and simplified cases.

For $n = 6$ and $n = 7$, larger deviations of eigenvalues can be expected, which finally lead to the gap between the measurements and the baseline model as shown in Figure 7(a).

5.3.3. Symbol Error Probability. For the indoor case, consider the baseline model extracted from the measurements conducted in the LOS environment. The gain of the last three MIMO eigenmodes is limited due to the presence of the LOS ray. Consequently, we consider the SVD transmission over the first four principal eigenmodes. The symbol error rates for the baseline and simplified models are shown in Figure 8(a). In the low SNR regime, all simplified models perform almost identically to the baseline model. However, in the high SNR regime, there is an approximate shift of 1 dB in SNR for an SER of 10^{-2} due to both SM-A and SM-C

Table 5: Designators for simplified models.

Designator	Simplification
SM-A	Clip out clusters with a 25 dB (for indoor LOS case) or 15 dB (for outdoor NLOS case) threshold.
SM-B	Fix the RMS DS as the mean value μ_{DS} in Table 3.
SM-C	Fix the XPR as the mean value μ_{XPR} in Table 3.
SM-D	Remove cross-correlations between all LSPs.
SM-E	All simplifications in SM-A, SM-B, SM-C, and SM-D.

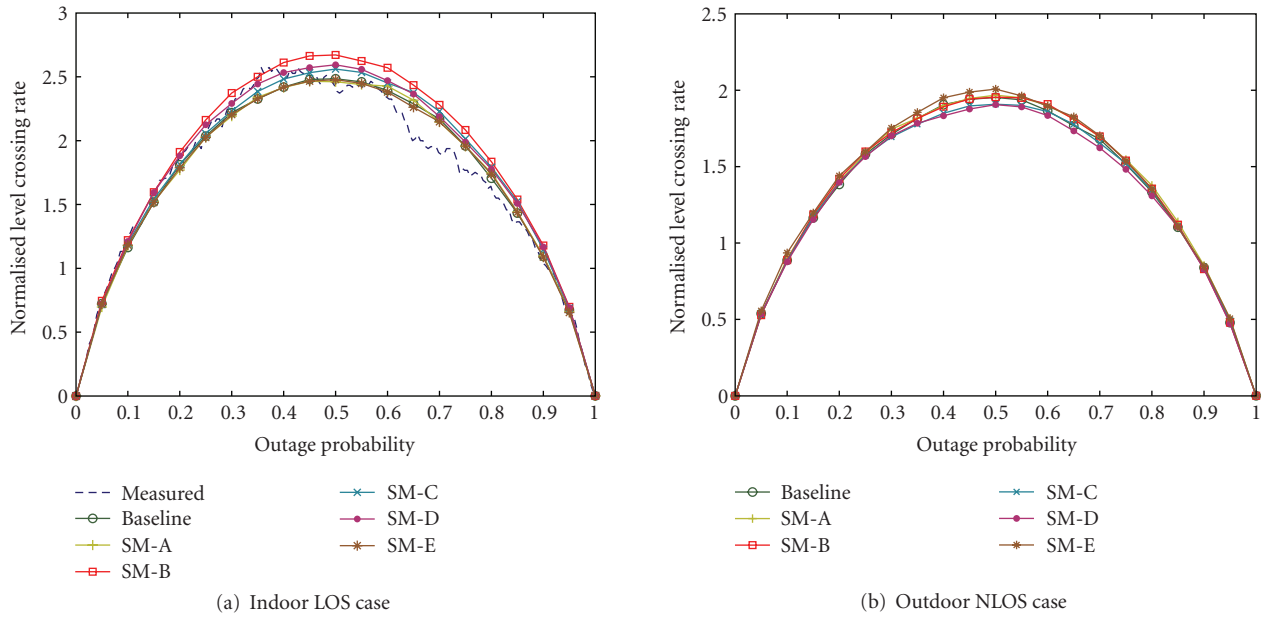

(a) Indoor LOS case (b) Outdoor NLOS case

Figure 9: Level crossing rates of standardized MIMO capacity for baseline and simplified cases when $\rho = 20$ dB.

Table 6: Comparisons between the baseline model and SM-E model.

Item		Indoor LOS		Outdoor NLOS	
		Baseline	SM-E	Baseline	SM-E
Complexity	No. of parameters	26	14	20	12
	No. of RVs	6	4	5	3
	NCT per drop	100%	57%	100%	85%
Accuracy	Relative deviation of $C_{5\%}$	0	<5%	0	<5%
	SNR shift for SER of 10^{-2}	0	<1 dB	0	<0.5 dB
	LCR for outage below 10%	Approximately equal			

for the indoor LOS case. Again, the performance variation due to both SM-B and SM-D is negligible. It is worth noting that the performance of SM-E is nearly the same as the baseline model across the whole SNR range. Although conventional wisdom says that large delays will result in higher error rates due to frequency-selective fading. However according to (8), the frequency-selective channel is effectively decomposed into a series of flat-fading channels, hence the SER result here does not show any sensitivity to the delay randomness. The symbol error rates for the outdoor case are plotted in Figure 8(b) which shows negligible deviations of all simplified models from the baseline model.

5.3.4. LCR for the Standardized MIMO Capacity. The normalized LCR of standardized MIMO capacity at 20 dB SNR is given in Figure 9 which shows that all simplified models cross-capacity thresholds for outage levels below 10% at nearly same rate. It means that all simplified models exhibit a similar temporal behavior for MIMO capacity as the baseline model for both indoor- and outdoor cases.

5.3.5. Comparisons. We compare the baseline model and the simplified model, SM-E, from an accuracy and complexity point of view in Table 6. The complexity of a channel model is two fold: (a) the time for generating channel coefficients; and (b) the time for convolution of the transmitted signal and the channel [26]. Since the real computational time depends on many factors such as the implementation of the model and the computational power of the simulation platform, we employ some indirect metrics and evaluate the complexity. The number of parameters used is related to the time of coefficient generation and is referred to as the number of parameters required to describe a model. For the baseline model, it equals the number of items listed in Table 3, that is, 26 for the indoor LOS scenario and 20 for the outdoor NLOS scenario. For SM-E, the following parameters are not required: σ_{DS}, σ_{XPR}, and 10 (for LOS) or 6 (for NLOS) cross-correlation coefficients. Hence, only 14 or 12 parameters are required to describe the SM-E model. The number of RVs is another value of interest, since the metrics of interest in simulation (e.g., bit error rate) require less time to converge when the number of RVs in the model is reduced. For the baseline model, there are 6 (for LOS) or 5 (for NLOS) RVs, that is, 5 (for LOS) or 4 (for NLOS) random LSPs and the random XPR. With SM-E, both DS and XPR are fixed as constants and only 4 or 3 RVs remain. Recall that the NCT measure can reflect the convolution reduction. The NCT is

obtained by approximating (11) through simulation. The results show that the SM-E is an acceptable tradeoff between accuracy and complexity with respect to the baseline model.

6. Conclusion

In this paper, we have studied the simplification of the GBSM by several approaches. The double-directional channel model developed under the IST-WINNER project is employed as the baseline model. The parameters for the indoor LOS baseline model are extracted by applying the SAGE algorithm to the data obtained from channel measurements. Four metrics are proposed to evaluate the impact of the simplifications on the behavior of the channel models. These include the MIMO capacity, eigenvalue distributions, symbol error rate of SVD-transmission, and level crossing rate of the MIMO capacity. Five different simplified models are developed based on the baseline model with the following modifications:

(i) SM-A: clipping clusters with a 25 dB (for indoor LOS case) or 15 dB (for outdoor NLOS case) power threshold,

(ii) SM-B: fixing the RMS DS at its mean value,

(iii) SM-C: fixing the XPR at its mean value,

(iv) SM-D: removing cross-correlations between LSPs,

(v) SM-E: all the above modifications.

The simulation results show that all these five simplified models have a minor impact on all proposed metrics. Compared to the baseline model, the SM-E can provide much better computational efficiency with a negligible loss of accuracy. Besides the two scenarios presented in this paper, we have repeated the simulations for all other scenarios in the WINNER model. All these simulation results support our conclusion. However, for reasons of space we cannot present those results in this paper. This means that fixed parameters and fewer random parameters can be used to give similar results. We have shown that simplification is possible and perhaps further simplifications might follow to make the models even more appealing. The simplified models have been far more rigorously tested. Instead of only looking at spatial and temporal correlations, we have looked at full system behavior in terms of many metrics. Furthermore, since the simplifications keep the original structure of the GBSM, the antenna geometries and radiation patterns can still be changed by the users as these parameters remain part of the simplified model. We also find that the baseline model underestimates the outage capacity with respect to the measurements. This might be due to measurement errors, modeling errors of nonprincipal eigenvalues or possibly the neglect of angular spread in elevation. Hence, simplifications of three-dimensional GBSMs will be considered in future work.

Acknowledgments

The authors would like to thank the engineers of Elektrobit Testing Ltd., Finland, for their efforts in the measurement campaign. Discussions with Doctor Guangyi Liu and Weihui Dong from China Mobile have been enlightening. They also appreciate the useful comments from the anonymous reviewers. This work was supported in part by the National 863 High Technology Research and Development Program of China under Grant No. 2006AA01Z258, and by the Research Institute of China Mobile Communications Corporation.

References

[1] J. H. Winters, "On the capacity of radio communication systems with diversity in a Rayleigh fading environment," *IEEE Journal on Selected Areas in Communications*, vol. 5, no. 5, pp. 871–878, 1987.

[2] E. Telatar, "Capacity of multi-antenna Gaussian channels," *European Transactions on Telecommunications*, vol. 10, no. 6, pp. 585–595, 1999.

[3] G. J. Foschini and M. J. Gans, "On limits of wireless communications in a fading environment when using multiple antennas," *Wireless Personal Communications*, vol. 6, no. 3, pp. 311–335, 1998.

[4] P. Kyritsi, D. C. Cox, R. A. Valenzuela, and P. W. Wolniansky, "Effect of antenna polarization on the capacity of a multiple element system in an indoor environment," *IEEE Journal on Selected Areas in Communications*, vol. 20, no. 6, pp. 1227–1239, 2002.

[5] C. Oestges and B. Clerckx, "Modeling outdoor macrocellular clusters based on 1.9-GHz experimental data," *IEEE Transactions on Vehicular Technology*, vol. 56, no. 5, pp. 2821–2830, 2007.

[6] J. W. Wallace, M. A. Jensen, A. Gummalla, and H. B. Lee, "Experimental characterization of the outdoor MIMO wireless channel temporal variation," *IEEE Transactions on Vehicular Technology*, vol. 56, no. 3, pp. 1041–1049, 2007.

[7] M. Landmann, K. Sivasondhivat, J.-I. Takada, I. Ida, and R. Thomä, "Polarization behavior of discrete multipath and diffuse scattering in urban environments at 4.5 GHz," *EURASIP Journal on Wireless Communications and Networking*, vol. 2007, Article ID 57980, 16 pages, 2007.

[8] S. Wyne, A. F. Molisch, P. Almers, G. Eriksson, J. Karedal, and F. Tufvesson, "Outdoor-to-indoor office MIMO measurements and analysis at 5.2 GHz," *IEEE Transactions on Vehicular Technology*, vol. 57, no. 3, pp. 1374–1386, 2008.

[9] P. Almers, E. Bonek, A. Burr, et al., "Survey of channel and radio propagation models for wireless MIMO systems," *EURASIP Journal on Wireless Communications and Networking*, vol. 2007, Article ID 19070, 19 pages, 2007.

[10] D.-S. Shiu, G. J. Foschini, M. J. Gans, and J. M. Kahn, "Fading correlation and its effect on the capacity of multielement antenna systems," *IEEE Transactions on Communications*, vol. 48, no. 3, pp. 502–513, 2000.

[11] W. Weichselberger, M. Herdin, H. Özcelik, and E. Bonek, "A stochastic MIMO channel model with joint correlation of both link ends," *IEEE Transactions on Wireless Communications*, vol. 5, no. 1, pp. 90–100, 2006.

[12] L. M. Correia, Ed., *Wireless Flexible Personalised Communications: COST 259, European Co-Operation in Mobile Radio Research*, John Wiley & Sons, Chichester, UK, 2001.

[13] L. M. Correia, Ed., *Mobile Broadband Multimedia Networks: Techniques, Models and Tools for 4 G*, Academic Press, Oxford, UK, 2006.

[14] G. Calcev, D. Chizhik, B. Göransson, et al., "A wideband spatial channel model for system-wide simulations," *IEEE*

Transactions on Vehicular Technology, vol. 56, no. 2, pp. 389–403, 2007.

[15] "IST-2003-507581 WINNER D5.4 v1.4 Final report on link level and system level channel models," November 2005, http://www.ist-winner.org/DeliverableDocuments/D5.4.pdf.

[16] "IST-4-027756 WINNER II D1.1.2 v1.2 WINNER II channel models," February 2008, http://www.ist-winner.org/WINNER2-Deliverables/D1.1.2.zip.

[17] "Working document towards proposed draft new report [Guidelines for evaluation of radio interface technologies for IMT-Advanced]," ITU-R Document 5D/TEMP/90-E, International Telecommunication Union (ITU), Geneva, Switzerland, June 2008.

[18] M. Failli, Ed., *COST 207: Digital Land Mobile Radio Communications, Final Report*, European Commission, Luxembourg, Belgium, 1989.

[19] "Guidelines for evaluation of radio transmission technologies for IMT-2000," ITU-R Recommendation M.1225, International Telecommunication Union (ITU), Geneva, Switzerland, February 1997.

[20] P. J. Smith and M. Shafi, "The impact of complexity in MIMO channel models," in *Proceedings of IEEE International Conference on Communications (ICC '04)*, vol. 5, pp. 2924–2928, Paris, France, June 2004.

[21] A. Forenza, D. J. Love, and R. W. Heath Jr., "Simplified spatial correlation models for clustered MIMO channels with different array configurations," *IEEE Transactions on Vehicular Technology*, vol. 56, no. 4, part 2, pp. 1924–1934, 2007.

[22] H. Asplund, J. Medbo, B. Göransson, J. Karlsson, and J. Sköld, "A simplified approach to applying the 3GPP spatial channel model," in *Proceedings of the 17th IEEE International Symposium on Personal, Indoor and Mobile Radio Communications (PIMRC '06)*, pp. 1–5, Helsinki, Finland, September 2006.

[23] A. F. Molisch, M. Steinbauer, M. Toeltsch, E. Bonek, and R. S. Thomä, "Capacity of MIMO systems based on measured wireless channels," *IEEE Journal on Selected Areas in Communications*, vol. 20, no. 3, pp. 561–569, 2002.

[24] L. M. Garth, P. J. Smith, and M. Shaft, "Exact symbol error probabilities for SVD transmission of BPSK data over fading channels," in *Proceedings of IEEE International Conference on Communications (ICC '05)*, vol. 4, pp. 2271–2276, Seoul, South Korea, May 2005.

[25] A. Giorgetti, P. J. Smith, M. Shafi, and M. Chiani, "MIMO capacity, level crossing rates and fades: the impact of spatial/temporal channel correlation," *Journal of Communications and Networks*, vol. 5, no. 2, pp. 104–115, 2003.

[26] P. Kyösti and T. Jämsä, "Complexity comparison of MIMO channel modelling methods," in *Proceedings of the 4th IEEE Internatilonal Symposium on Wireless Communication Systems (ISWCS '07)*, pp. 219–223, Trondheim, Norway, October 2006.

[27] P. J. Smith and M. Shafi, "The use of cross-polarized antennas for MIMO systems," in *Proceedings of the Australian Communications Theory Workshop (AusCTW '04)*, Newcastle, Australia, February 2004.

[28] Elektrobit Corporation, "EB Propsound CS: radio channel measurement and research," 2008, http://www.elektrobit.com/index.php?209.

[29] X. Gao, J. Zhang, G. Liu, et al., "Large-scale characteristics of 5.25 GHz based on wideband MIMO channel measurements," *IEEE Antennas and Wireless Propagation Letters*, vol. 6, pp. 263–266, 2007.

[30] X. Zhao, J. Meinilä, L. Hentilä, T. Jämsä, P. Kyösti, and J.-P. Nuutinen, "Effects of noise cut for extraction of wideband channel parameters," in *Proceedings of the 18th IEEE International Symposium on Personal, Indoor and Mobile Radio Communications (PIMRC '07)*, pp. 1–4, Athens, Greece, September 2007.

[31] B. H. Fleury, M. Tschudin, R. Heddergott, D. Dahlhaus, and K. I. Pedersen, "Channel parameter estimation in mobile radio environments using the SAGE algorithm," *IEEE Journal on Selected Areas in Communications*, vol. 17, no. 3, pp. 434–450, 1999.

[32] X. Yin, B. H. Fleury, P. Jourdan, and A. Stucki, "Polarization estimation of individual propagation paths using the SAGE algorithm," in *Proceedings of the 14th International Symposium on Personal, Indoor and Mobile Radio Communications (PIMRC '03)*, vol. 2, pp. 1795–1799, Beijing, China, Sepember 2003.

[33] L. Hentilä, P. Kyösti, M. Käske, M. Narandzic, and M. Alatossava, "MATLAB implementation of the WINNER Phase II Channel Model ver1.1," December 2007, http://www.ist-winner.org/phase_2_model.html.

[34] M. Shafi, M. Zhang, P. J. Smith, A. L. Moustakas, and A. F. Molisch, "The impact of elevation angle on MIMO capacity," in *Proceedings of IEEE International Conference on Communications (ICC '06)*, vol. 9, pp. 4155–4160, Istanbul, Turkey, June 2006.

Hindawi Publishing Corporation
EURASIP Journal on Wireless Communications and Networking
Volume 2009, Article ID 715403, 15 pages
doi:10.1155/2009/715403

Research Article

Polarimetric Kronecker Separability of Site-Specific Double-Directional Channel in an Urban Macrocellular Environment

Kriangsak Sivasondhivat,[1] Jun-Ichi Takada,[2] Ichirou Ida,[3] and Yasuyuki Oishi[3]

[1] *Agilent Technologies Japan, Ltd., Kobe-shi, Hyogo, 651-2241, Japan*
[2] *Department of International Development Engineering (IDE), Graduate School of Science and Technology, Tokyo Institute of Technology, Tokyo 152-8550, Japan*
[3] *Fujitsu, Ltd., Fujitsu Laboratory, Yokosuka-shi, 239-0847, Japan*

Correspondence should be addressed to Kriangsak Sivasondhivat, sivasondhivat.kriangsak@gmail.com

Received 2 August 2008; Revised 22 November 2008; Accepted 7 January 2009

Recommended by Persefoni Kyritsi

This paper focuses on the modeling of a double-directional power spectrum density (PSD) between the base station (BS) and mobile station (MS) based on the site-specific measurements in an urban macrocell in Tokyo. First, the authors investigate the Kronecker separability of the joint polarimetric angular PSD between the BS and MS by using the ergodic mutual information. The general form of the sum of channel polarization pair-wise Kronecker product approximation is proposed to be used to model the joint polarimetric angular PSD between the BS and MS. Finally, the double-directional PSD channel model is proposed and verified by comparing the cumulative distribution functions (CDFs) of the measured and modeled ergodic mutual information.

1. Introduction

It has been shown that the use of multiple antennas at a base station (BS) and a mobile station (MS), called as multiple input multiple output (MIMO) system, can promisingly increase the data rate [1]. However, low correlation between antennas is required in MIMO systems, in order to ensure the data rate improvement [2]. This implies the need of large antenna spacing, resulting in the size increase of the system. As a candidate scheme to achieve the low correlation in compact MIMO systems, the application of multiple polarizations to MIMO systems has been increasingly investigated [3–6].

To evaluate and compare MIMO systems with multiple polarizations, a channel model having the polarimetric information in addition to azimuth and elevation angles at the BS and MS is obviously needed [7, 8]. Recently, for outdoor environments, standard channel models having such information for polarimetric MIMO systems have been defined in the spatial channel model (SCM), which was presented in the 3rd Generation Partnership Project (3GPP) standard body [9], and in the European co-operation in the field of scientific and technical research (COST) actions 273 [10]. The further analytical extension of the SCM to the 3D case has been recently done by Shafi et al., in [11].

Since the degree of depolarization of a propagation channel directly affects the performance of the MIMO systems with multipolarizations [12], a channel model must accurately reproduce the polarization behavior of the channel. However, due to the lack of reliable tools to reproduce polarization mechanisms, the derivation of the polarimetric channel model from measurements is still of great significance [13–15].

Moreover, it is also important that a channel model is applicable to any arbitrary array antennas under development, the channel model must thus be independent of the measurement antennas, which is known as the double-directional channel model [16, 17]. It should be noted that double-directional channel models aim to present the physical channel propagation alone by describing the parameters

of multipaths. They are different from conventional channel models, which mainly aim to present the statistics of a transfer function between the BS and MS and thus the effect of measurement antennas are included. Independent and identically distributed (i.i.d.) Rayleigh and correlation matrices-based MIMO channel models such as Kronecker [2, 18] and Weichselberger et al., [19] MIMO channel models are good examples of conventional channel models.

In [20], the authors have proposed an angular-delay power spectrum density (PSD) channel model at the MS based on a 3D double-directional measurements in a residential urban area in Tokyo. The PSD channel model was shown to be able to predict the eigenvalue distributions of a diversity system assumed for the MS. In this paper, the authors focus on a site-specific double-directional PSD channel model by extending the directional PSD channel model at the MS.

To do so, the following contributions are done.

(i) First, to motivate the study of channel modeling for multiple polarized MIMO systems, the polarization characteristics of the measured channel are investigated. The benefit of exploiting a polarization diversity is next shown by using the measurement antennas.

(ii) Then, the separability of the joint polarimetric angular PSD between the BS and MS of the measured propagation channel, which is a necessary assumption for the angular-delay PSD channel model in [20] when extended to the double-directional PSD channel model, is investigated. This is done by investigating the Kronecker separability of a joint correlation matrix of reference polarized antennas at the BS and MS.

The standard antenna configurations of a 3GPP LTE channel model are used as reference in the evaluations of the Kronecker separability, which are based on the ergodic mutual information.

(iii) It should be noted that in the conventional Kronecker product [2, 18], when single polarized antennas are used at the BS and the MS, the validity of the Kronecker separability of the joint correlation matrix shows how well the joint angular PSD between the BS and MS can be modeled as the product of the marginal angular PSDs [21].

However, for multiple polarized MIMO systems, the conventional Kronecker product is not suitable to be used for evaluating the separability of the joint angular PSD since the propagation channel polarizations are mixed with the antenna polarizations. Moreover, the angular-delay PSD channel model at the MS in [20] was proposed for each channel polarization-pair, so the Kronecker separability of the joint correlation matrix must be investigated for each channel polarization-pair as well.

The authors propose a general form of the sum of channel polarization pair-wise Kronecker product approximation, which is shortly called "sum of Kronecker products" herewith, to investigate the separability of the joint polarimetric angular PSD. By using the proposed sum of Kronecker products, the error of the assumption that the joint correlation matrix can be separated for each polarization-pair is investigated. Also, its validity is compared with the following Kronecker product approximations:

(a) conventional Kronecker product,

(b) 3GPP long-term evolution (3GPP LTE) Kronecker product [22].

(iv) Next, the polarimetric angular PSD models at the BS are studied and their best-fit parameters are derived. Then, by using the proposed sum of Kronecker products, a double-directional PSD channel model is presented. Finally, this double-directional PSD channel model is evaluated by comparing the ergodic mutual information of 3GPP LTE system scenario.

It should be noted that even though the validation of Kronecker separability based on the proposed sum of Kronecker products is done by using the standard antenna configurations of a 3GPP LTE channel model, the term "double-directional PSD channel model" is used here for the presented PSD channel model due to the fact that extracted channel parameters are independent of the measurement antennas since the beam patterns of the measurement antennas are taken into account in the multipath parameters extraction [20].

This paper is organized as follows. Section 2 explains the measurement system, measurement environment, and the extraction of multipaths parameters. In Section 3, the mathematical expression of a polarimetric MIMO channel matrix is first given. Following this, the polarization characteristics of the measured channel are investigated and then the effect of exploiting a polarization diversity is studied. In Section 4, the concepts of different Kronecker product approximations, that is, conventional Kronecker product, 3GPP LTE Kronecker product, and sum of Kronecker products proposed by the authors are explained. The comparison among Kronecker product approximations is done in Section 5. Based on the validity of sum of Kronecker products shown in Section 5, the double directional PSD channel model is presented in Section 6. Section 7 presents the result of the evaluation of the double directional PSD channel model. Finally, the conclusion is given in Section 8.

2. Measurement and Channel Parameters Extraction

The double-directional measurements were carried out in a residential urban area in Minami-Senzoku, Ota-ku, Tokyo. The measurement site consists of 4 streets, which were divided into the measurement segments of about 10 m. The MS was moved continuously to collect consecutive snapshots. The BS antenna used was a 2×4 polarimetric uniform rectangular antenna array of dual-polarized patch antenna elements. At the MS side, a 2×24 polarimetric circular

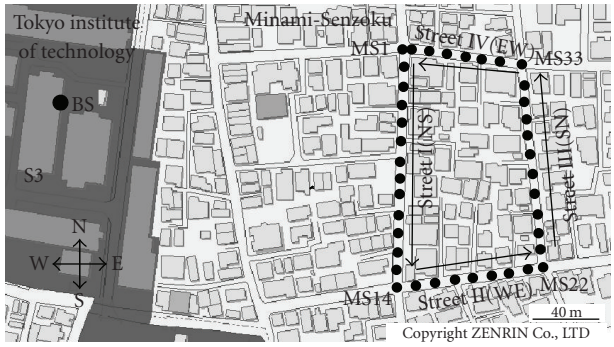

Figure 1: Measurement site map.

Table 1: Measurement parameters.

Center frequency	4.5 GHz
Bandwidth	120 MHz
Excess delay window	3.2 μs
Transmitting power	10 W
BS antenna height	30 m
MS antenna height	1.65 m
Total measurement length	380 m
Total measurement snapshots	872
Distance to the BS	186 m –276 m

antenna array was used. The measurement was explained in detail in [20]. Figure 1 shows the measurement map. Note that the arrows in the figure show the moving direction of the MS. The important parameters are summarized in Table 1.

By using a multidimensional gradient-based maximum-likelihood estimator [23], multipath parameters were extracted. A path is modeled as an optical ray with the azimuth at BS (ABS), elevation at BS (EBS), azimuth at MS (AMS), elevation at MS (EMS), delay, and a matrix of polarimetric complex path weights, respectively. For the kth multipath, it is modeled by

$$\begin{bmatrix} \gamma_{\mathrm{VV},k} & \gamma_{\mathrm{VH},k} \\ \gamma_{\mathrm{HV},k} & \gamma_{\mathrm{HH},k} \end{bmatrix} \delta(\phi^{\mathrm{BS}} - \phi_k^{\mathrm{BS}})\delta(\vartheta^{\mathrm{BS}} - \vartheta_k^{\mathrm{BS}})\delta(\phi^{\mathrm{MS}} - \phi_k^{\mathrm{MS}}) \times \delta(\vartheta^{\mathrm{MS}} - \vartheta_k^{\mathrm{MS}})\delta(\tau - \tau_k), \tag{1}$$

where $\gamma_{\mathrm{VV},k}$, $\gamma_{\mathrm{HV},k}$, $\gamma_{\mathrm{VH},k}$, and $\gamma_{\mathrm{HH},k}$ are the polarimetric complex path weights. The first and the second subscripts show polarizations at the MS and BS, respectively. In this paper, vertical and horizontal polarizations are defined as ϑ and ϕ components of electric field. It is assumed that the vertically placed infinitesimal electric and magnetic dipoles as the reference vertically and horizontally polarized antennas. This corresponds to Ludwig's Definition 2 of the polarization [24].

The quantities ϕ_k^{BS}, $\vartheta_k^{\mathrm{BS}}$, ϕ_k^{MS}, $\vartheta_k^{\mathrm{MS}}$, and τ_k denote the ABS, EBS, AMS, EMS, and delay, respectively. The definitions of the angle parameters at the BS and MS are depicted in Figure 2. It should be noted that the extracted polarimetric complex path weights were made independent of the measurement antennas by incorporating the measured beam patterns of the BS and MS antennas in the multipath parameters estimator.

The measurement site is mostly characterized by nonline-of-sight (NLOS) conditions. For some line-of-sight (LOS) measurement snapshots, since their LOS paths are deterministic, they are removed from the extracted multipaths, so that the considered channel becomes zero-mean complex circularly symmetric Rayleigh in order to model the NLOS component.

3. Polarimetric MIMO Channel Matrix, Polarization Characteristics, and Effect of Polarization Diversity

3.1. Polarimetric MIMO Channel Matrix. For wideband MIMO systems having N_{BS} and N_{MS} antennas at the BS and MS, respectively, where $n_{\mathrm{MS}} = 1, \ldots, N_{\mathrm{MS}}$ and $n_{\mathrm{BS}} = 1, \ldots, N_{\mathrm{BS}}$, the $(n_{\mathrm{MS}}, n_{\mathrm{BS}})$ element of a MIMO channel matrix at the frequency f, $\mathbf{H}(f)$, can be expressed as a sum of channel responses of all polarization-pairs, that is,

$$[\mathbf{H}(f)]_{n_{\mathrm{MS}}n_{\mathrm{BS}}} = \sum_{\alpha,\beta=\{\mathrm{V,H}\}} [\mathbf{H}_{\beta\alpha}(f)]_{n_{\mathrm{MS}}n_{\mathrm{BS}}}, \tag{2}$$

where $[\mathbf{H}_{\beta\alpha}(f)]_{n_{\mathrm{MS}}n_{\mathrm{BS}}}$ denotes the $(n_{\mathrm{MS}}, n_{\mathrm{BS}})$ element of single polarization $\mathbf{H}(f)$ of a $\{\beta\alpha\}$ polarization-pair. Note that $[\mathbf{H}(f)]_{n_{\mathrm{MS}}n_{\mathrm{BS}}}$ and $[\mathbf{H}_{\beta\alpha}(f)]_{n_{\mathrm{MS}}n_{\mathrm{BS}}}$ are defined in the downlink direction. Accordingly, β and α show the channel polarization at the MS and BS, respectively.

By using the extracted multipaths in Section 2, $[\mathbf{H}_{\beta\alpha}(f)]_{n_{\mathrm{MS}}n_{\mathrm{BS}}}$ can be expressed as the superposition of all multipaths between the BS and MS as follows:

$$[\mathbf{H}_{\beta\alpha}(f)]_{n_{\mathrm{MS}}n_{\mathrm{BS}}} = \sum_{k=1}^{K} \gamma_{\beta\alpha,k}\, g_{\beta}^{n_{\mathrm{MS}}}(\phi_k^{\mathrm{MS}}, \vartheta_k^{\mathrm{MS}}) g_{\alpha}^{n_{\mathrm{BS}}}(\phi_k^{\mathrm{BS}}, \vartheta_k^{\mathrm{BS}}) \times \exp\left(j[\langle \mathbf{k}_k^{\mathrm{MS}}(f), \vec{r}_{n_{\mathrm{MS}}}\rangle + \langle \mathbf{k}_k^{\mathrm{BS}}(f), \vec{r}_{n_{\mathrm{BS}}}\rangle] - j2\pi f \acute{\tau}_k + j\nu_k^{\beta\alpha}\right), \tag{3}$$

where K = the number of extracted multipaths, $g_{\alpha}^{n_{\mathrm{BS}}}(\cdot)$ = the complex amplitude gain of α component, electric field of the n_{BS}th element, $g_{\beta}^{n_{\mathrm{MS}}}(\cdot)$ = the complex amplitude gain of β component, electric field of the n_{MS}th element, $\mathbf{k}_k^{\mathrm{BS}}(\cdot)$ = the wave vector at the BS, $\mathbf{k}_k^{\mathrm{MS}}(\cdot)$ = the wave vector at the MS, $\vec{r}_{n_{\mathrm{BS}}}$ = the position vector of the n_{BS}th element, $\vec{r}_{n_{\mathrm{MS}}}$ = the position vector of the n_{MS}th element, $\langle\cdot,\cdot\rangle$ = the inner product of two vectors, $\acute{\tau}_k$ = the excess delay, that is, $\tau_k - \tau_0$, τ_0 = the delay of the first arriving multipath at a snapshot, and $\nu_k^{\beta\alpha}$ = a uniformly distributed random phase from 0 to 2π [25, 26].

In general, the vector amplitude gain of an antenna element at either the BS or MS can be expressed as

$$g_{\mathrm{H}}(\phi,\vartheta)\mathbf{u}_{\mathrm{H}}(\phi,\vartheta) + g_{\mathrm{V}}(\phi,\vartheta)\mathbf{u}_{\mathrm{V}}(\phi,\vartheta), \tag{4}$$

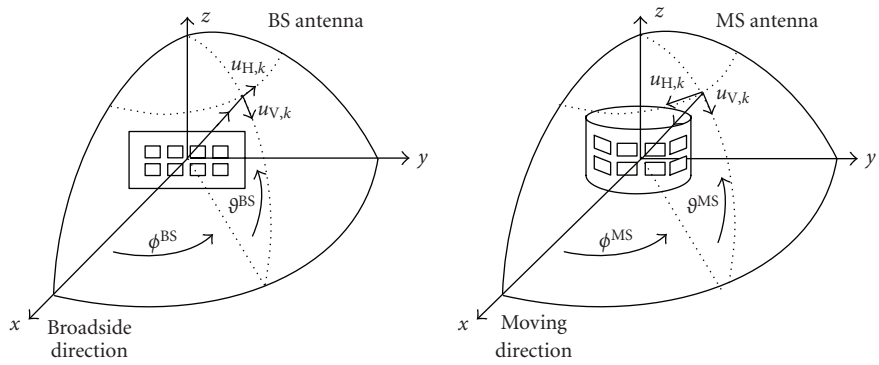

Figure 2: Coordinate systems at the BS and MS.

where $\mathbf{u}_H(\phi, \vartheta)$ and $\mathbf{u}_V(\phi, \vartheta)$ are the H and V polarization vectors in the direction (ϕ, ϑ), respectively. For the kth multipath, $\mathbf{u}_{\alpha,k}(\phi_k^{BS}, \vartheta_k^{BS})$ and $\mathbf{u}_{\beta,k}(\phi_k^{MS}, \vartheta_k^{MS})$ are depicted in Figure 2. It should be noted that $[\mathbf{H}_{\beta\alpha}(f)]_{n_{MS}n_{BS}}$ is normalized with respect to the delay of the first arriving multipath.

Moreover, when synthesizing $\mathbf{H}_{\beta\alpha}(f)$, their realizations are independently generated based on the Monte Carlo simulations of $\nu_k^{\beta\alpha}$. Since in this paper the authors focus on the Kronecker separability of the measured channel, and that the $\mathbf{H}(f)$'s have the same spatial correlation characteristic, $\mathbf{H}(f)$'s can be thus considered as different realizations of the random MIMO channel matrices. Accordingly, $\mathbf{H}(f)$ is simply expressed as $\mathbf{H}$.

3.2. Polarization Characteristics of the Measured Channel. Herein, the term cross-polarization ratio (XPR) is used for the depolarization of each extracted path and can be obtained at both the BS and MS as follows:

$$\begin{aligned}
\mathrm{XPR}_V^{BS}\,[\mathrm{dB}] &= 10\log_{10}\left(\frac{|\gamma_{VV}|^2}{|\gamma_{VH}|^2}\right),\\
\mathrm{XPR}_H^{BS}\,[\mathrm{dB}] &= 10\log_{10}\left(\frac{|\gamma_{HH}|^2}{|\gamma_{HV}|^2}\right),\\
\mathrm{XPR}_V^{MS}\,[\mathrm{dB}] &= 10\log_{10}\left(\frac{|\gamma_{VV}|^2}{|\gamma_{HV}|^2}\right),\\
\mathrm{XPR}_H^{MS}\,[\mathrm{dB}] &= 10\log_{10}\left(\frac{|\gamma_{HH}|^2}{|\gamma_{VH}|^2}\right).
\end{aligned} \tag{5}$$

For a certain path, XPR shows how much the V polarization component changes to the H polarization component, or vice versa. Due to the antenna deembedding, XPR is purely from a propagation channel and does not change with a measurement antenna. It should be noted that when the effects of measurement antennas are also included, the term cross-polarization discrimination (XPD) is often used instead [27].

Table 2: XPRs and CPR.

	Mean [dB] (STD [dB])			
	street I	street II	street III	street IV
XPR_V^{BS}	10.2 (10.6)	6.9 (9.9)	9.6 (10.6)	10.4 (8.8)
XPR_H^{BS}	9.2 (9.0)	6.9 (8.2)	9.1 (9.3)	10.3 (8.5)
XPR_V^{MS}	10.7 (9.2)	8.3 (8.9)	10.8 (9.3)	10.8 (8.7)
XPR_H^{MS}	8.7 (9.4)	5.5 (8.7)	7.9 (9.5)	9.9 (8.8)
CPR	1.5 (8.6)	1.4 (8.7)	1.7 (8.9)	0.5 (7.6)

In addition to XPRs, the copolarization ratio (CPR), which is the power ratio of covertical polarization γ_{VV} to cohorizontal polarization γ_{HH},

$$\mathrm{CPR}\,[\mathrm{dB}] = 10\log_{10}\left(\frac{|\gamma_{VV}|^2}{|\gamma_{HH}|^2}\right) \tag{6}$$

is also necessary to describe the polarization characteristics of a path.

Figure 3 shows the cumulative distribution functions (CDFs) of XPRs and CPR at the BS and MS for all measurement streets. In the normal probability plot of CDFs, if data comes from a normal distribution, the plot will appear linear. Accordingly, the XPRs and CPR can be assumed to be a log-normal distribution. Table 2 shows means and standard deviations (STDs) of XPRs and CPR. As shown in the table, the means of XPRs at the BS and MS have no big difference. Lowest XPRs are found in street II (WE), which is completely NLOS, and thus the more number of scatterings is expected [20]. While, some obstructed LOS (OLOS) by rooftops in the south side of street IV (EW) cause the highest XPRs among all measurement streets.

On the other hand, the mean values of CPRs, which indicate the gainimbalance between V and H transmitting polarizations, are found to be 1.5, 1.4, 1.7, and 0.5 dB for street I (NS) to street IV (EW), respectively. Their positive values suggest that H polarization transmission have on average bigger attenuation compared to that of V polarization. In other words, the propagation in outdoor macrocellular is in favor of vertical transmission [28].

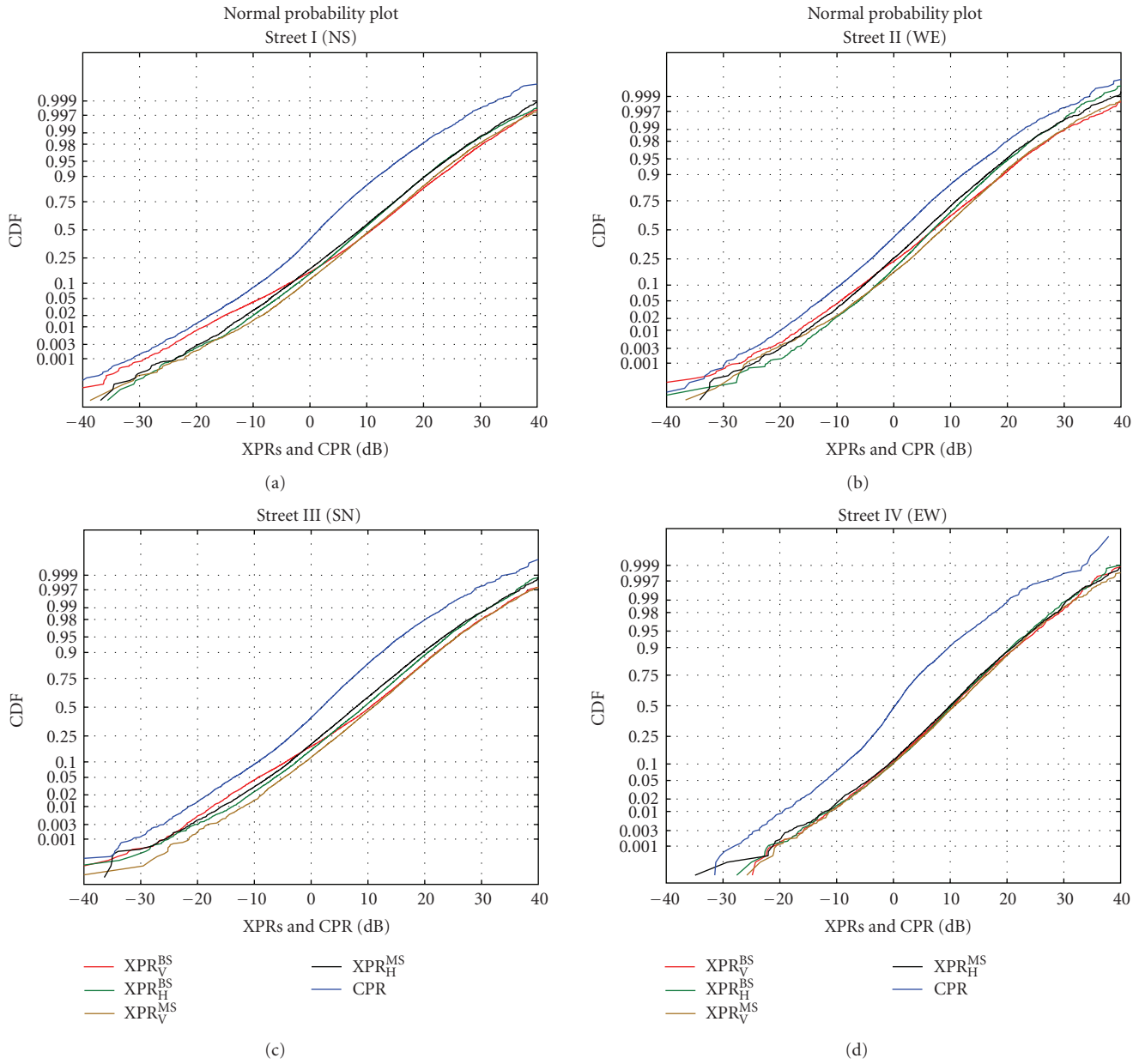

Figure 3: XPRs and CPR.

3.3. Effect of Polarization Diversity. To evaluate the contributions of polarizations, the mutual ergodic information, which is an important criterion from the viewpoint of maximum achievable data rate, of a multiple polarized MIMO system is compared with that of a single polarized MIMO system. 4×4 multiple polarized MIMO antennas are selected from the BS and MS measurement antenna arrays as shown in Figure 4. For a single polarized MIMO system, vertically polarized antenna elements of no. 1, 3, 5, and 7 at both ends are selected. While, the vertically and horizontally polarized antenna elements of no. 2, 3, 6, and 7 at the BS and 2, 3, 5, and 8 at the MS are selected for a multiple polarized MIMO system.

For each measurement snapshot, the authors synthesize measurement-based random MIMO channel matrices, $\mathbf{H}$, according to (2) by Monte Carlo simulations. Each channel realization is generated by the random phase method using (3). The number of the realizations, N_r, is set to 400. The number of the frequency bins, N_f, is set to 25 within a bandwidth of 120 MHz, resulting to a channel separation of 5 MHz at each frequency bin. To take into account the change of the antenna orientation during the movement of the MS, the N_a combinations of antenna array orientation are also considered for each measurement snapshot. N_a is set to 8 with the step of 45°.

In case that the total power is equally allocated to each BS antenna element and assuming that the channel state information is only known at the MS [1], the ergodic mutual information, $\mathcal{I}(n_a)$, of the n_ath MS orientation, where $n_a = 1, \ldots, N_a$, is given by

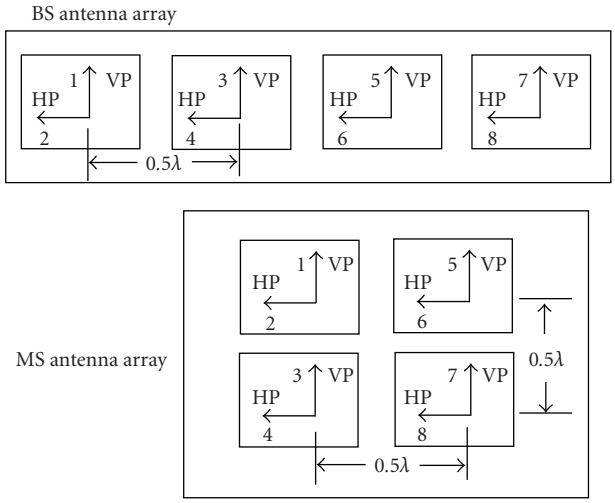

Figure 4: Selected BS and MS antenna arrays.

$$\mathcal{I}(n_a) = E\left[\log_2 \det\left(\mathbf{I}_{N_{\mathrm{MS}}} + \frac{\mathrm{SNR}}{N_{\mathrm{BS}}}\widetilde{\mathbf{H}}(n_a)\widetilde{\mathbf{H}}^H(n_a)\right)\right], \quad (7)$$

where $\mathbf{I}_{N_{\mathrm{MS}}}$ denotes the identity matrix of size N_{MS}, and SNR is the average signal-to-noise ratio at the MS. The expectation is approximated by the sample average of the $N_r \times N_f$ realizations of $\widetilde{\mathbf{H}}(n_a)$.

To appropriately evaluate the use of multiple polarizations, the normalized instantaneous MIMO channel matrices, $\widetilde{\mathbf{H}}^{(n_r,n_f)}(n_a)$s, where $n_r = 1,\ldots,N_r$ and $n_f = 1,\ldots,N_f$, of both single and multiple polarized MIMO systems are obtained with respect to the single polarized MIMO system. In other words, the SNR is defined for the single polarized MIMO system. Thus, for each instantaneous MIMO channel matrix, $\mathbf{H}^{(n_r,n_f)}(n_a)$, $\widetilde{\mathbf{H}}^{(n_r,n_f)}(n_a)$ is obtained as

$$\widetilde{\mathbf{H}}^{(n_r,n_f)}(n_a) = \frac{\mathbf{H}^{(n_r,n_f)}(n_a)}{\sqrt{(1/N_r N_f N_a N_{\mathrm{BS}} N_{\mathrm{MS}}) \sum_{n_r=1}^{N_r}\sum_{n_a=1}^{N_a}\sum_{n_f=1}^{N_f} \left\|\mathbf{H}_{\mathrm{single}}{}^{(n_r,n_f)}(n_a)\right\|_F^2}}, \quad (8)$$

where $\|\cdot\|_F$ is the Frobenius norm and $\mathbf{H}_{\mathrm{single}}{}^{(n_r,n_f)}(n_a)$ is the $\mathbf{H}^{(n_r,n_f)}(n_a)$ of the single polarized MIMO system.

$\mathbf{H}^{(n_r,n_f)}(n_a)$ is obtained by replacing ϕ_k^{MS} with $\{\phi_k^{\mathrm{MS}} - \phi^{\mathrm{MS}}(n_a)\}$ in (3), where $\phi^{\mathrm{MS}}(n_a) = 0^\circ, 45^\circ, \ldots, 315^\circ$ for $n_a = 1,\ldots,8$, respectively. It should be noted that the differences in received power fading among MS antenna orientations are also considered when calculating $\mathcal{I}(n_a)$ in addition to those realizations.

Figure 5 shows the ergodic mutual information of the single and multiple polarized MIMO systems at an SNR of 10 dB. It is clear from the figure that the polarization diversity promisingly increases the ergodic mutual information. When comparing the ergodic mutual information of both systems of each MS antenna orientation at all measurement snapshots, the average increases are 12%, 34%, 18%, and 26% for street I (NS) to street IV (EW), respectively.

4. Reference Scenario and Polarimetric Kronecker Product Approximations

In the previous section, the benefit of exploiting the polarization diversity in a MIMO system has been confirmed. Next, the validity of polarimetric Kronecker separability of the measured channel is investigated in this section. However, in principle, since the validity of polarimetric Kronecker separability depends not only on the characteristics of the channel, but also on the polarized antennas, some standard polarized antennas at the BS and MS have to be assumed in the investigation.

4.1. Reference Scenario. As reference antennas, the standard antenna configurations of the 3GPP LTE channel model are used (see Annex C of [22]). For the BS, an antenna configuration with 4 antenna elements, where 2 elements are dual at slants of $\pm 45^\circ$ is assumed. For the MS antenna, the authors assume *Laptop* scenario, which is shown in Figure 6. The results of the other MS scenarios, i.e., *handheld data* and *handheld talk*, are reported in [29]. Table 3 shows the details of the BS and MS antenna configurations and their parameter values with an azimuth power gain, $G(\phi)$, which is mathematically defined as follows: The vector amplitude gain of an antenna element at the BS and MS in (3) can thus be defined in terms of power gain and the element polarization vector, $\mathbf{p}$, i.e., $\sqrt{G(\cdot)}\mathbf{p}(\cdot)$. It should be noted that $G(\phi)$, which is defined in Annex C of [22], is the normalized power gain, which could cause inappropriate evaluation of the impact of the antennas as it neglects the fundamental fact that the higher the antenna gain is, the narrower is the beamwidth. However, $G(\phi)$ is acceptable for this work since the authors focus on comparing propagation models, not the antennas. Thus, the definition of $G(\phi)$ can be used here for compatibility purposes with the 3GPP LTE channel model.

$$G(\phi) = -\min\left[12\left(\frac{\phi}{\phi_{3\,\mathrm{dB}}}\right)^2, G_{\mathrm{m}}\right], \quad |\phi| \le 180^\circ. \quad (9)$$

For the EBS, it is assumed that multipaths are confined in the same horizontal plane. Note that the assumption is reasonable for the measurement environment as will be discussed in Section 6.2. For the MS antenna configurations, it is assumed that an elevation power gain, $G(\vartheta)$, has the same expression as in (9). The power gain for the MS antenna configuration is then given as

$$G(\phi,\vartheta) = G(\phi)G(\vartheta), \quad |\phi| \le 180^\circ,\ |\vartheta| \le 90^\circ. \quad (10)$$

It should be noted that all element polarization vectors for the BS and MS are assumed to be unchanged over all directions according to [22].

4.2. Polarimetric Kronecker Product Approximations. In zero-mean complex circularly symmetric Gaussian channels, $\mathbf{H}$ is fully described by its second-order fading statistics, that is, by a full channel correlation matrix, $\mathbf{R}$, which is

$$\mathbf{R} = E[\mathrm{vec}(\mathbf{H})\ \ \mathrm{vec}(\mathbf{H})^H], \quad (11)$$

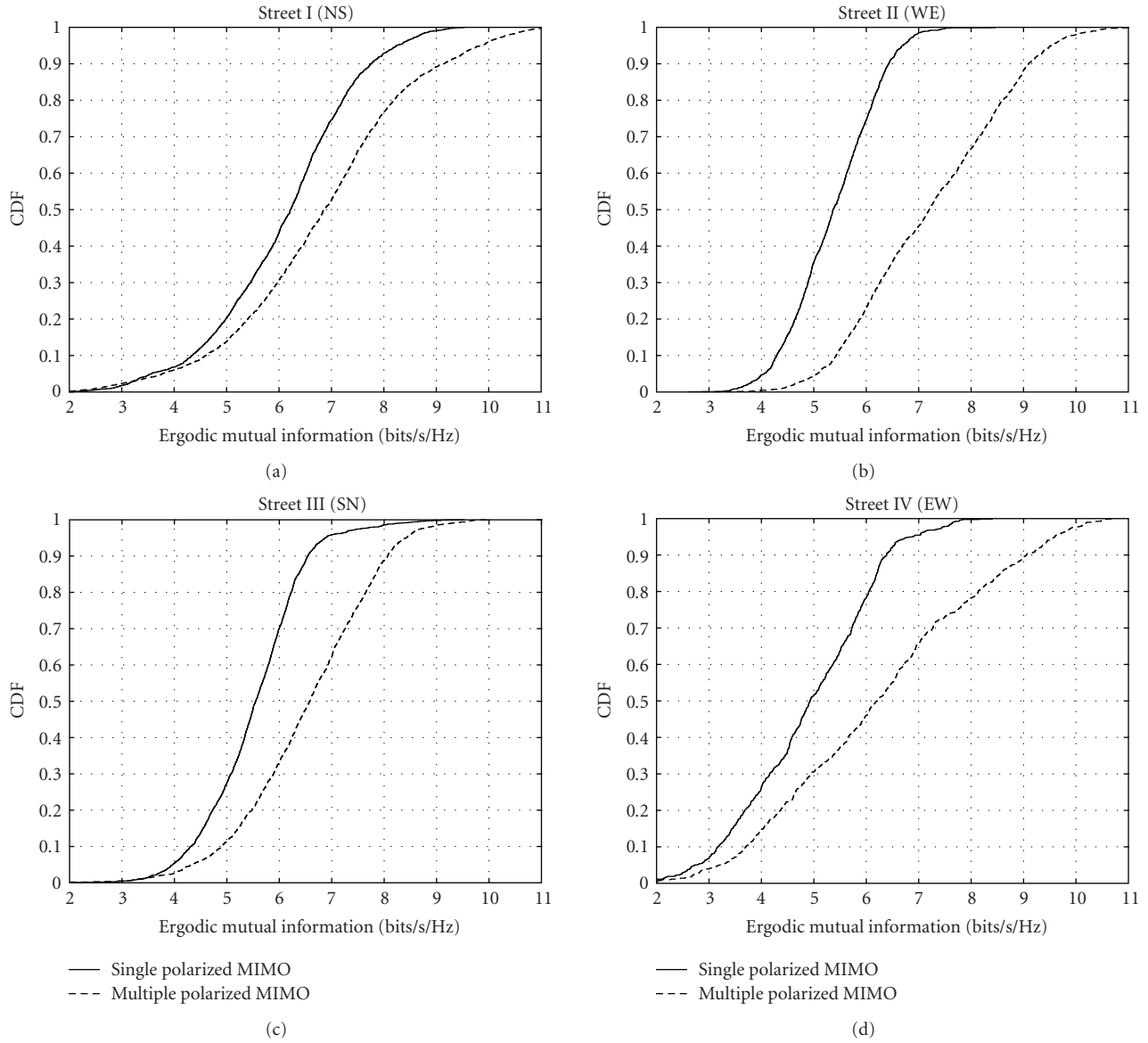

Figure 5: Ergodic mutual information of the single and multiple polarized MIMO systems.

where vec$(\cdot)$ stacks the columns of $\mathbf{H}$ into a column vector, while $E(\cdot)$ and $(\cdot)^H$ are the expectation operator and the Hermitian transpose, respectively.

The conventional Kronecker product approximation [2, 18] models $\mathbf{R}$ by $\mathbf{R}^{\text{Con}}$, which is the Kronecker product of the BS and MS antenna correlation matrices, that is, $\mathbf{R}^{\text{BS}}$ and $\mathbf{R}^{\text{MS}}$, respectively. That is

$$\mathbf{R}^{\text{Con}} = \frac{1}{\text{tr}(\mathbf{R}^{\text{MS}})}\mathbf{R}^{\text{BS}} \otimes \mathbf{R}^{\text{MS}}, \tag{12}$$

where $\otimes$ denotes the Kronecker product,

$$\begin{aligned} \mathbf{R}^{\text{BS}} &= E[\mathbf{H}^T\mathbf{H}^*], \\ \mathbf{R}^{\text{MS}} &= E[\mathbf{H}\mathbf{H}^H]. \end{aligned} \tag{13}$$

$(\cdot)^T$ and $(\cdot)^*$ indicate the transpose and the complex conjugate, respectively. Note that the denominator term, $\text{tr}(\mathbf{R}^{\text{MS}})$, is used to equalize the traces of $\mathbf{R}$ and $\mathbf{R}^{\text{Con}}$.

For single polarization transmission, the conventional Kronecker product approximation was experimentally shown to well predict the ergodic mutual information and ergodic capacity of MIMO systems in [18, 30, 31], in this case, its validity of the performance prediction implies how well the joint angular PSD between the BS and MS can be modeled as the product of the marginal angular PSDs [21].

However, for multiple polarized MIMO systems, the conventional Kronecker product is not suitable to be used for evaluating the separability of the joint angular PSD since the channel polarizations are mixed with the antenna polarizations.

Recently, in the framework of 3GPP LTE, the 3GPP LTE Kronecker product approximation has been proposed to

Table 3: Reference antenna configurations.

Antenna configurations	Value
BS	See Figure 6
Type	2 spatially separated dual polarized antennas
No. of elements	4
Element polarization vectors ($\mathbf{p}$)	$\pm 45^\circ$
Antenna spacing (d_{BS})	4 wavelengths (at 4.5 GHz)
Position vector ($\vec{r}_{n_{\mathrm{BS}}}$)	$-(d_{\mathrm{BS}}/2)\mathbf{u}_y$ for $n_{\mathrm{BS}} = 1, 2$ $(d_{\mathrm{BS}}/2)\mathbf{u}_y$ for $n_{\mathrm{BS}} = 3, 4$
Parameters of $G(\phi)$	$\phi_{3\,\mathrm{dB}} = 70^\circ$, $G_{\mathrm{m}} = 20$ dB
MS: *Laptop* scenario	See Figure 7
Type	2 spatially separated dual polarized antennas
No. of elements	4
Element polarization vectors ($\mathbf{p}$)	$0^\circ, 90^\circ$
Antenna spacing (d_{MS})	2 wavelength (at 4.5 GHz)
Position vector ($\vec{r}_{n_{\mathrm{MS}}}$)	$-(d_{\mathrm{MS}}/2)\mathbf{u}_y$ for $n_{\mathrm{MS}} = 1, 3$ $(d_{\mathrm{MS}}/2)\mathbf{u}_y$ for $n_{\mathrm{MS}} = 2, 4$
Parameters of $G(\phi)$	$\phi_{3\,\mathrm{dB}} = 90^\circ$, $G_{\mathrm{m}} = 10$ dB

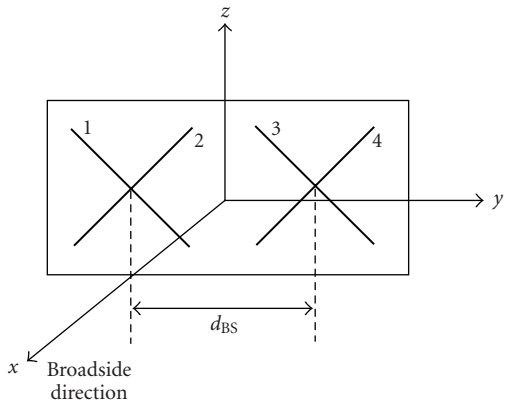

Figure 6: BS antenna configuration [22].

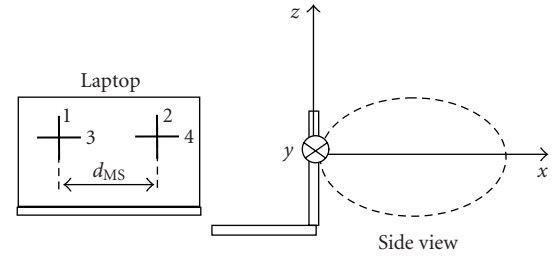

Figure 7: *Laptop* MS antenna configuration [22].

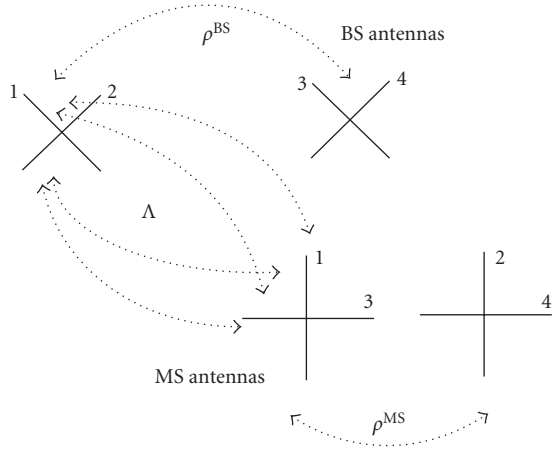

Figure 8: 3GPP LTE Kronecker approximation for the *Laptop* scenario.

model the polarimetric 3GPP LTE channel model [22]. Here, $\mathbf{R}$ is approximated by $\mathbf{R}^{\mathrm{3GPP}}$, which is the Kronecker product of the polarization covariance matrix and the BS and MS spatial correlation matrices as follows:

$$\mathbf{R}^{\mathrm{3GPP}} = \begin{bmatrix} 1 & (\rho^{\mathrm{BS}})^* \\ \rho^{\mathrm{BS}} & 1 \end{bmatrix} \otimes \mathbf{\Lambda} \otimes \begin{bmatrix} 1 & (\rho^{\mathrm{MS}})^* \\ \rho^{\mathrm{MS}} & 1 \end{bmatrix}, \quad (14)$$

where ρ^{BS} and ρ^{MS} are the spatial correlation coefficients between 2 identical omnidirectional antenna elements assumed at the BS and MS, respectively, while $\mathbf{\Lambda}$ is the polarization covariance matrix of the colocated polarization antenna elements, $\mathbf{H}_{\mathrm{pol}}$. It is obtained as follows:

$$\mathbf{\Lambda} = E[\mathrm{vec}(\mathbf{H}_{\mathrm{pol}}) \ \ \mathrm{vec}(\mathbf{H}_{\mathrm{pol}})^H]. \quad (15)$$

In the *Laptop* scenario, $\mathbf{H}_{\mathrm{pol}}$ is vectorized as $[[\mathbf{H}]_{11}, [\mathbf{H}]_{31}, [\mathbf{H}]_{12}, [\mathbf{H}]_{32}]$.

The definitions of ρ^{BS}, ρ^{MS}, and Λ are depicted in Figure 8 for the *Laptop* scenario. Note that (14) is only applicable for the standard antenna configuration of the 3GPP LTE channel model, which was presented in Figure 6.

Interesting work on the polarimetric Kronecker product approximation has been proposed by Shafi et al., in [11]. Based on an analytical derivation by assuming certain PSD models, the use of the sum of channel polarization pair-wise Kronecker products has been proposed to model the full correlation matrix of the 2D SCM model. However, its validity has not been verified or compared with the above mentioned Kronecker product approximations by using real measurement data. Moreover, its extension to 3D case has not been discussed.

By using the similar concept, the authors propose the following general form of the sum of channel polarization pair-wise Kronecker products approximation, which the authors shortly call as the "sum of Kronecker products," to investigate the Kronecker separability of the joint correlation matrix for each channel polarization pair

$$\mathbf{R}^{\mathrm{Sum}} = \sum_{\alpha,\beta=\{\mathrm{V,H}\}} \frac{1}{\mathrm{tr}(\mathbf{R}^{\mathrm{MS}}_{\beta\alpha})} \mathbf{R}^{\mathrm{BS}}_{\beta\alpha} \otimes \mathbf{R}^{\mathrm{MS}}_{\beta\alpha}, \quad (16)$$

where

$$\mathbf{R}_{\beta\alpha}^{\mathrm{BS}} = E[\mathbf{H}_{\beta\alpha}{}^{T}\mathbf{H}_{\beta\alpha}{}^{*}],$$
$$\mathbf{R}_{\beta\alpha}^{\mathrm{MS}} = E[\mathbf{H}_{\beta\alpha}\mathbf{H}_{\beta\alpha}{}^{H}]. \tag{17}$$

$\mathbf{H}_{\beta\alpha}$ is a single polarization MIMO channel matrix for a $\beta\alpha$ polarization pair defined in (3).

The MIMO channel matrix by using the Kronecker product approximations, $\mathbf{H}^{\mathrm{Kron}}$, can be obtained as

$$\mathrm{vec}(\mathbf{H}^{\mathrm{Kron}}) = \hat{\mathbf{R}}^{1/2}\mathrm{vec}(\mathbf{A}), \tag{18}$$

where $\hat{\mathbf{R}}$ is the approximated full correlation matrix. It is replaced by either $\mathbf{R}^{\mathrm{Con}}$, $\mathbf{R}^{\mathrm{3GPP}}$, or $\mathbf{R}^{\mathrm{Sum}}$ in the equation above. $\mathbf{A}$ is an i.i.d. random fading matrix with zero-mean and unity-variance, circularly symmetric complex Gaussian entries. Note that in general once a correlation matrix is given, whether or not it is the Kronecker model, and all entries of the correlation matrix are according to the correlated Rayleigh fading, (18) is always applicable.

5. Evaluation Criterion, Process, and Results

When extending the angular-delay PSD channel model in [20] to the double-directional PSD channel model, it is necessary to know the error of the assumption that the joint correlation matrix can be separated for each polarization pair. By using the proposed sum of Kronecker products, the error is investigated in this section.

5.1. Criterion. The ergodic mutual information introduced in Section 3.3 is used as a criterion to evaluate the Kronecker product approximations. The ergodic mutual information of the Kronecker product approximations, $\mathcal{I}^{\mathrm{Kron}}(n_a)$, can be obtained by replacing the normalized $\mathbf{H}(n_a)$ with the normalized $\mathbf{H}^{\mathrm{Kron}}(n_a)$ in (7). $\mathbf{H}^{\mathrm{Kron}}(n_a)$ is an MIMO channel matrix by applying the Kronecker product approximations to the full correlation matrix of $\mathbf{H}(n_a)$.

However, it should be noted that the normalizations of both measurement and Kronecker product approximations-based instantaneous MIMO channel matrices in this section are done with respect to an MS configuration considered as shown in the following equation for the measurement-based instantaneous MIMO channel matrix, $\tilde{\mathbf{H}}^{(n_r,n_f)}(n_a)$:

$$\tilde{\mathbf{H}}^{(n_r,n_f)}(n_a) = \frac{\mathbf{H}^{(n_r,n_f)}(n_a)}{\sqrt{(1/N_rN_fN_aN_{\mathrm{BS}}N_{\mathrm{MS}})\sum_{n_r=1}^{N_r}\sum_{n_a=1}^{N_a}\sum_{n_f=1}^{N_f}\left\|\mathbf{H}^{(n_r,n_f)}(n_a)\right\|_F^2}}. \tag{19}$$

The absolute percentage of the prediction error is calculated as

$$\varepsilon_{\mathcal{I}^{\mathrm{Kron}}}(n_a) = \frac{\left|\mathcal{I}^{\mathrm{Kron}}(n_a) - \mathcal{I}(n_a)\right|}{\mathcal{I}(n_a)} \times 100\,[\%]. \tag{20}$$

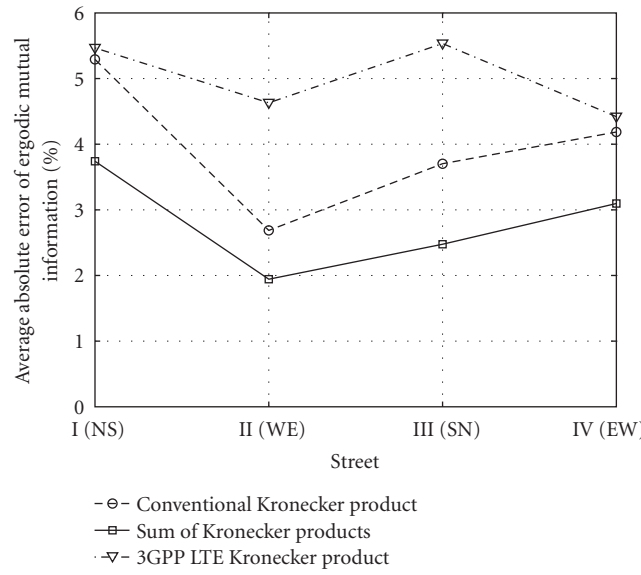

Figure 9: Average absolute errors of ergodic mutual information of the *Laptop* scenario.

5.2. Process. This is how the authors proceed with the evaluation.

(1) Synthesize measurement-based random MIMO channel matrices, $\mathbf{H}$, by using the same values of N_r, N_f, and N_a as explained in Section 3.3.

(2) Obtain $\mathbf{R}^{\mathrm{Con}}$, $\mathbf{R}^{\mathrm{3GPP}}$, and $\mathbf{R}^{\mathrm{Sum}}$ by using (12), (14), and (16). The expectations of the correlation matrices in (13), (15), and (17) are substituted into (18) to synthesize the MIMO channel matrix by using the Kronecker product approximations. This is repeated $N_r \times N_f$ times.

(3) Compare criteria calculated from $\mathbf{H}^{\mathrm{Kron}}$ with $\mathbf{H}$.

5.3. Results. In the evaluation, $\mathcal{I}(n_a)$ and $\mathcal{I}^{\mathrm{Kron}}(n_a)$ are calculated at an SNR of 10 dB. As an example, Figure 10 shows $\mathcal{I}(n_a)$ and $\mathcal{I}^{\mathrm{Kron}}(n_a)$ at MS8 of the *Laptop* scenario. The variation of $\mathcal{I}(n_a)$ and $\mathcal{I}^{\mathrm{Kron}}(n_a)$ with the MS antenna orientation can be clearly seen in the figure. Investigating the accuracy of the predicted $\mathcal{I}^{\mathrm{Kron}}(n_a)$ is done by comparing $\mathcal{I}(n_a)$ and $\mathcal{I}^{\mathrm{Kron}}(n_a)$ of the same MS antenna orientation at a measurement snapshot.

Figure 9 shows the average $\varepsilon_{\mathcal{I}^{\mathrm{Kron}}}$ over the MS antenna orientations and the measurement snapshots in a street, as a function of streets of the *Laptop* scenario. As can be seen, the sum of Kronecker products approximation gives the most accurate prediction of the ergodic mutual information as compared to the others for all measurement streets. While the 3GPP LTE Kronecker product approximation seems to be the worst. This performance degradation could be because of the use of the common correlation coefficients for different colocated polarized antenna elements. Among all streets, street II (WE), where multiple scattering occurs due to its only NLOS characteristic, seems to be most suitable street for applying the Kronecker product approximations.

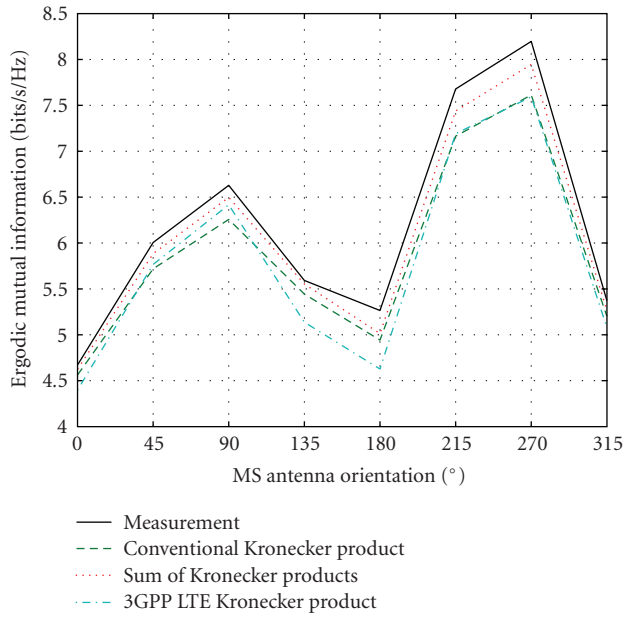

Figure 10: Ergodic mutual information at MS8 of the *Laptop* scenario.

6. Double-Directional Channel Modeling

From the viewpoint of the propagation channel, the validity of the sum of Kronecker product in (16) implies that the joint angular PSD between the BS and MS can be reasonably modeled as the product of the marginal angular PSDs at the BS and MS *when the same single channel polarization-pair is considered*. Mathematically, this can be expressed as

$$P_{\beta\alpha}(\acute{\phi}^{\mathrm{BS}}, \vartheta^{\mathrm{BS}}, \phi^{\mathrm{MS}}, \vartheta^{\mathrm{MS}}) \approx P_{\beta\alpha}(\acute{\phi}^{\mathrm{BS}}, \vartheta^{\mathrm{BS}}) P_{\beta\alpha}(\phi^{\mathrm{MS}}, \vartheta^{\mathrm{MS}}), \tag{21}$$

where $P_{\beta\alpha}(\acute{\phi}^{\mathrm{BS}}, \vartheta^{\mathrm{BS}}, \phi^{\mathrm{MS}}, \vartheta^{\mathrm{MS}})$, $P_{\beta\alpha}(\acute{\phi}^{\mathrm{BS}}, \vartheta^{\mathrm{BS}})$, and $P_{\beta\alpha}(\phi^{\mathrm{MS}}, \vartheta^{\mathrm{MS}})$ are the joint angular PSD, marginal angular PSDs at the BS and MS for a $\{\beta\alpha\}$ polarization-pair, respectively. Note that since measurement snapshots have different ABSs toward the MS, the extracted ABS, ϕ^{BS}, are thus recalculated, so that the ABS of the MS position becomes 0° when obtaining PSDs relating to the ABS. $\acute{\phi}^{\mathrm{BS}}$ denotes the ABS centered at the MS position.

Based on this approximation, the angular-delay PSD channel model at the MS, which has been proposed by the authors in [20], is extended to the double-directional PSD channel model in this paper.

6.1. Angular-Delay PSD Model at MS [20]. In [20], the authors studied the angular-delay channel parameters at the MS in the measurements. The study was carried out for the individual street to clarify the influence of the street direction. By observing the street-based PSDs of AMS (i.e., AMSPSDs), it was clear that they were not ideally uniform. They consist of peak-like components and a residual part, which is the complementary part of the peak-like components. Peak-like components were considered to represent site-specific dominant propagation mechanisms. The peak-like components are identified visually and each is called a class. Table 4 of [20] summarized the identified classes together with their mean EMSs and mean excess delays.

Table 4: Angular-delay PSD model.

Channel parameter	Proposed model
AMSPSD	
$P^{c}_{\beta\alpha}(\phi^{\mathrm{MS}})$	truncated Gaussian PSD
$P^{\mathrm{r}}_{\beta\alpha}(\phi^{\mathrm{MS}})$	uniform PSD
EMSPSD	
$P^{c}_{\beta\alpha}(\vartheta^{\mathrm{MS}})$	general double exponential PSD
$P^{\mathrm{r}}_{\beta\alpha}(\vartheta^{\mathrm{MS}})$	general double exponential PSD
EDPSD	
$P^{c}_{\beta\alpha}(\acute{\tau})$	general double exponential PSD
$P^{\mathrm{r}}_{\beta\alpha}(\acute{\tau})$	general double exponential PSD
Power variation	
$\Gamma^{c}_{\beta\alpha}$	correlated log-normal distribution
$\Gamma^{\mathrm{r}}_{\beta\alpha}$	correlated log-normal distribution

By using their AMSs, mean EMSs, and mean excess delays, the identified classes were connected to the street directions to show their site-specific propagation mechanisms. Table 5 of [20] showed the classification result according the following categorization: *BS-direction*, *street-direction*, *opposite BS-direction*, and *rooftop-diffraction*. The definition of each categorization was described in detail in [20, Section 5].

For the classes and the residual part, the angular-delay PSD channel models were next presented as a product of marginal channel parameter PSDs.

A class or the residual part is considered to exist if its power is larger than zero. While the residual part always exists due to its large occupied AMS, a class can possibly disappear at some measurement snapshots. To take the travel of the MS into account, when a class or the residual part exists, its polarization dependent power variation was modeled by the lognormal distribution with the correlation coefficient matrices between the power values of different polarization pairs of the same multipath component.

In summary, the angular-delay PSD channel model for a $\{\beta\alpha\}$ polarization pair was proposed as

$$P_{\beta\alpha}(\phi^{\mathrm{MS}}, \vartheta^{\mathrm{MS}}, \acute{\tau}) = \sum_{c=1}^{N_c} \Gamma^{c}_{\beta\alpha} P^{c}_{\beta\alpha}(\phi^{\mathrm{MS}}) P^{c}_{\beta\alpha}(\vartheta^{\mathrm{MS}}) P^{c}_{\beta\alpha}(\acute{\tau}) + \Gamma^{\mathrm{r}}_{\beta\alpha} P^{\mathrm{r}}_{\beta\alpha}(\phi^{\mathrm{MS}}) P^{\mathrm{r}}_{\beta\alpha}(\vartheta^{\mathrm{MS}}) P^{\mathrm{r}}_{\beta\alpha}(\acute{\tau}), \tag{22}$$

where $P^{c,\mathrm{r}}_{\beta\alpha}(\phi^{\mathrm{MS}})$, $P^{c,\mathrm{r}}_{\beta\alpha}(\vartheta^{\mathrm{MS}})$, and $P^{c,\mathrm{r}}_{\beta\alpha}(\acute{\tau})$ are the AMSPSD, PSD of EMS (i.e., EMSPSD), and PSD of excess delay (i.e., EDPSD) for a $\{\beta\alpha\}$ polarization pair of the cth class or the

Table 5: Simulation conditions.

Parameters		Value
Number of frequency bins (N_f)		25 in a BW of 120 MHz
Number of antenna azimuth orientations (N_a)		8 with a step of 45°
Number of simulated power variation (N_s)		200
Number of simulated random phase (N_r)		200
Path generation of ABS		
Path number		5
Path spacing		2°
Path generation of AMS		
Path number	of a class	4
	of a residual part	16–21 (varies with streets)
Path spacing	for classes	3°–5° (varies with classes)
	for residual parts	14°
Path generation of EMS		
Path number	of a class	18
	of a residual part	18
Path spacing	for classes	10°
	for residual parts	10°
Path generation of excess delay		
Path number	of a class	80
	of a residual part	80
Path spacing	for classes	8 ns
	for residual parts	8 ns
Path power		Follow a corresponding marginal PSD
Path correlation		0 (independently random path phase)

Table 6: Absolute errors of ergodic mutual information.

	CDF [%]		
Street	10	50	90
I (NS)	10.7	1.7	0.5
II (WE)	4.0	5.1	9.7
III (SN)	4.4	7.0	6.9
IV (EW)	11.3	3.1	2.3

residual part, respectively. The excess delay, $\acute{\tau}$, was obtained as $\acute{\tau} = \tau - \tau_0$, where τ_0 denotes the delay of the first arriving multipath at a measurement snapshot.

$\Gamma_{\beta\alpha}^{c,\mathrm{r}}$ is the power variation of the cth class or the residual part and N_c is the number of classes. All PSDs are normalized to unity. The marginal PSD models are briefly summarized in Table 4. Their best-fit parameters, which were obtained from fitting the PSD models and their corresponding measured PSDs, were listed in the tables in the appendix of [20].

However, since LOS paths traveling through the west side streets were included in the *BS-direction* classes, that is, the 4th class of street I (NS) and the 2nd of street III (SN), the best-fit parameters of the *BS-direction* classes obtained in NLOS environments only are presented in Table 7.

6.2. Angular PSDs at BS. The measured PSD of $\acute{\phi}^{\mathrm{BS}}$, that is, ABSPSD, is found to be well described by the truncated Laplacian PSD [32]. For a $\{\beta\alpha\}$ polarization pair, the truncated Laplacian PSD, $P_{\beta\alpha}(\acute{\phi}^{\mathrm{BS}})$, is expressed as follows:

$$P_{\beta\alpha}(\acute{\phi}^{\mathrm{BS}}) \propto \exp\left[-\frac{\sqrt{2}\,|\acute{\phi}^{\mathrm{BS}} - \acute{\phi}_{0,\beta\alpha}^{\mathrm{BS}}|}{\sigma_{\acute{\phi}_{\beta\alpha}^{\mathrm{BS}}}} \right], \tag{23}$$

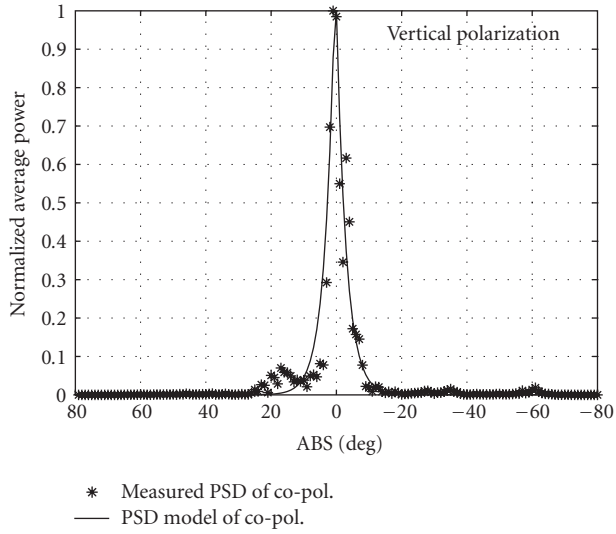

Figure 11: ABSPSDs for a {VV} of street I (NS). 0° is the ABS towards the MS.

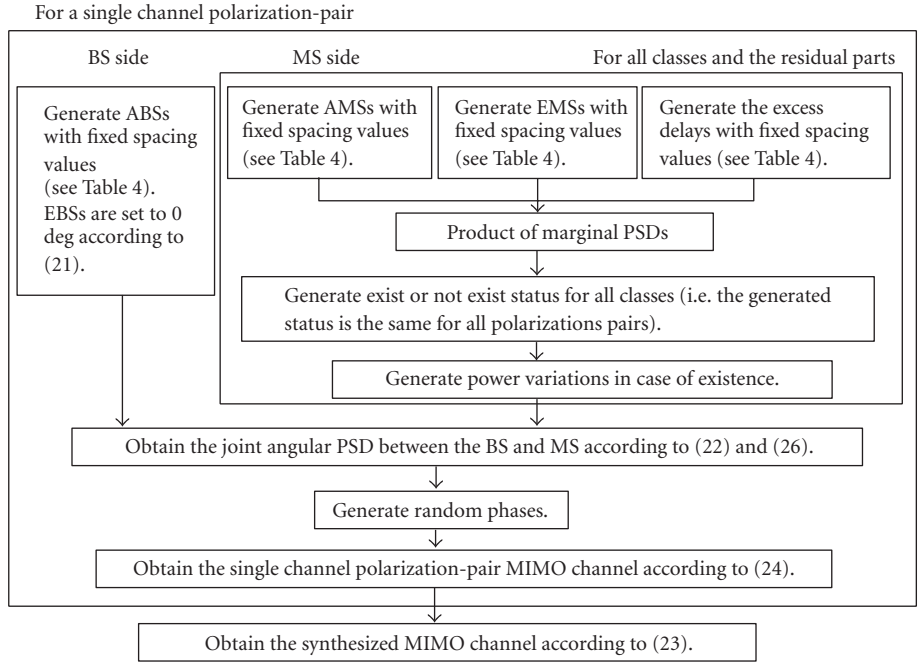

Figure 12: Simulation procedure.

Table 7: Best-fit parameters of *BS-direction* classes for NLOS environments.

		$P^c_{\beta\alpha}(\phi^{\mathrm{MS}})$ VV/HV/HH/VH		
Street	Class no.	$\phi^{c,\mathrm{MS}}_{0,\beta\alpha}$ [°]	$\sigma_{\phi^{c,\mathrm{MS}}_{\beta\alpha}}$ [°]	
I (NS)	4	–102.6/ −104.8/ −103.0/ −92.0	9.2/13.5/9.3/32.5	
III (SN)	2	69.7/69.8/68.9/83.1	11.6/26.3/9.5/36.5	
		$P^c_{\beta\alpha}(\vartheta^{\mathrm{MS}})$ VV/HV/HH/VH		
Street	Class no.	$\vartheta^{c,\mathrm{MS}}_{0,\beta\alpha}$ [°]	$\sigma^{+}_{\vartheta^{c,\mathrm{MS}}_{\beta\alpha}}$ [°]	$\sigma^{-}_{\vartheta^{c,\mathrm{MS}}_{\beta\alpha}}$ [°]
I (NS)	4	10.4/8.0/10.7/13.5	9.8/25.3/10.0/30.4	4.9/3.7/4.6/10.0
III (SN)	2	7.0/7.0/7.0/18.0	8.8/18.7/8.1/16.8	5.6/3.9/5.1/16.0
		$P^c_{\beta\alpha}(\acute{\tau})$ VV/HV/HH/VH		
Street	Class no.	$\acute{\tau}^c_{0,\beta\alpha}$ [ns]	$\sigma^{+}_{\acute{\tau}^c_{\beta\alpha}}$ [ns]	$\sigma^{-}_{\acute{\tau}^c_{\beta\alpha}}$ [ns]
I (NS)	4	4.0/4.0/4.0/4.0	7.6/7.8/7.9/8.8	–/ – / – /–
III (SN)	2	4.8/5.6/4.6/5.6	7.5/5.8/8.1/5.7	–/ – / – /–
		$f(\check{\Gamma}^c_{\beta\alpha})$ VV/HV/HH/VH		
Street	Class no.	Life time	$\check{\Gamma}^{c,\mathrm{r}}_{0,\beta\alpha}$ [dB]	$\sigma_{\Gamma^{c,\mathrm{r}}_{\beta\alpha}}$ [dB]
I (NS)	4	0.98	–116.8/ −127.3/ −116.7/ −128.6	9.9/9.2/10.2/9.0
III(SN)	2	0.96	–117.6/ −128.6/ −117.9/ −129.4	10.4/8.3/9.9/8.3

where $\acute{\phi}^{\mathrm{BS}}_{0,\beta\alpha}$ and $\sigma_{\acute{\phi}^{\mathrm{BS}}_{\beta\alpha}}$ are the mean ABS and spread parameter, respectively. Their best-fit parameters are obtained from fitting $P_{\beta\alpha}(\acute{\phi}^{\mathrm{BS}})$ and the measured ABSPSD, which is calculated by summing the power of a $\{\beta\alpha\}$ polarization pair within a 1° angular bin. Figure 11 shows the measured and modeled ABSPSDs of a {VV} polarization pair of street I (NS). Interestingly, the main peak of the measured ABSPSD is very close to 0° even though the measurements are in NLOS environments. This implies that most multipaths between the BS and MS travel over the rooftop of surrounding buildings around the MS. Table 8 lists the best-fit parameters of the ABSPSD model.

As to the PSD of EBS, for example, EBSPSD, the EBSPSD is confined to its peak of between −9° and −7° depending on streets. The EBSPSD is thus assumed to be a delta function for simplicity, that is,

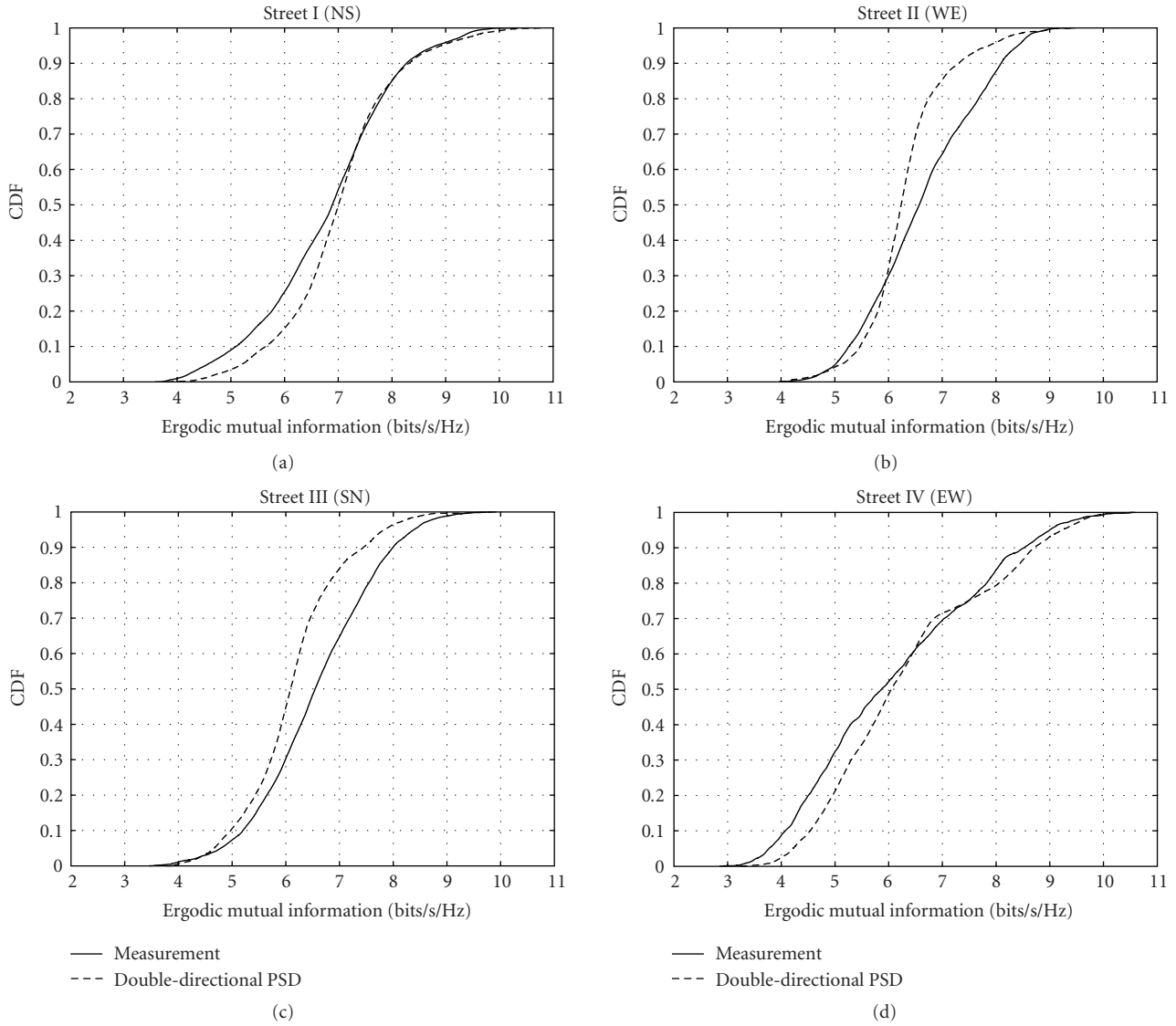

Figure 13: Measured and modeled ergodic mutual information for the *Laptop* scenario.

Table 8: Best-fit parameters of $P_{\beta\alpha}(\acute{\phi}^{\mathrm{BS}})$.

	VV/HV/HH/VH	
Street	$\acute{\phi}^{\mathrm{BS}}_{0,\beta\alpha}$ [°]	$\sigma_{\acute{\phi}^{\mathrm{BS}}_{\beta\alpha}}$ [°]
I (NS)	0.3/0.7/0.7/0.9	4.3/4.9/3.0/2.2
II (WE)	0.4/0.5/0.5/0.6	1.8/1.5/1.8/1.3
III (SN)	1.5/1.4/1.6/1.5	1.7/1.5/1.2/1.1
IV (EW)	1.5/2.5/2.3/1.7	2.5/2.3/2.6/2.0

$$P_{\beta\alpha}(\vartheta^{\mathrm{BS}}) = \delta(\vartheta^{\mathrm{BS}}). \tag{24}$$

In other words, multipaths are assumed to be incident to the horizontal plane. The BS antenna pattern, whose response varies only in the ABS direction, is thus reasonable for the measured environment.

Using (21)–(24), the double-directional PSD for a $\{\beta\alpha\}$ polarization pair is proposed as

$$\begin{aligned} &P_{\beta\alpha}(\acute{\phi}^{\mathrm{BS}}, \vartheta^{\mathrm{BS}}, \phi^{\mathrm{MS}}, \vartheta^{\mathrm{MS}}, \acute{\tau}) \\ &\quad = P_{\beta\alpha}(\acute{\phi}^{\mathrm{BS}}) P_{\beta\alpha}(\vartheta^{\mathrm{BS}}) P_{\beta\alpha}(\phi^{\mathrm{MS}}, \vartheta^{\mathrm{MS}}, \acute{\tau}). \end{aligned} \tag{25}$$

7. Model Evaluation

To evaluate the double-directional PSD channel model, the ergodic mutual information is used. The ergodic mutual information from the synthesized MIMO channel by using the proposed double-directional PSD channel model, that is, $\mathbf{H}^{\mathrm{Model}}(f)$, is compared with the results from the directly synthesized MIMO channel matrix, $\mathbf{H}(f)$. In the model evaluation, the same reference scenario as in the evaluation of the Kronecker separability is assumed.

$\mathbf{H}^{\text{Model}}(f)$ is obtained by using the following equations:

$$\left[\mathbf{H}^{\text{Model}}(f)\right]_{n_{\text{MS}}n_{\text{BS}}} = \sum_{\alpha,\beta=\{\text{V,H}\}} \left[\mathbf{H}^{\text{Model}}_{\beta\alpha}(f)\right]_{n_{\text{MS}}n_{\text{BS}}}, \tag{26}$$

where $\left[\mathbf{H}^{\text{Model}}_{\beta\alpha}(f)\right]_{n_{\text{MS}}n_{\text{BS}}}$ denotes the $(n_{\text{MS}}, n_{\text{BS}})$ element of single polarization $\mathbf{H}^{\text{Model}}(f)$ of a $\{\beta\alpha\}$ polarization pair, that is,

$$\begin{aligned}\left[\mathbf{H}^{\text{Model}}_{\beta\alpha}(f)\right]_{n_{\text{MS}}n_{\text{BS}}} = \sum_{k=1}^{K} \gamma^{\text{Model}}_{\beta\alpha,k} g_{\beta}^{n_{\text{MS}}}(\phi_k^{\text{MS}}, \vartheta_k^{\text{MS}}) g_{\alpha}^{n_{\text{BS}}}(\phi_k^{\text{BS}}, \vartheta_k^{\text{BS}}) \\ \times \exp\left(j\left[\langle \mathbf{k}_k^{\text{MS}}(f), \vec{r}_{n_{\text{MS}}}\rangle + \langle \mathbf{k}_k^{\text{BS}}(f), \vec{r}_{n_{\text{BS}}}\rangle\right]\right. \\ \left. - j2\pi f \tau_k + j\nu_k^{\beta\alpha}\right),\end{aligned} \tag{27}$$

$$\gamma^{\text{Model}}_{\beta\alpha,k} = \sqrt{P_{\beta\alpha}(\phi_k^{\text{BS}}, \vartheta_k^{\text{BS}}, \phi_k^{\text{MS}}, \vartheta_k^{\text{MS}}, \tau_k)}. \tag{28}$$

Multipaths at the BS and MS are generated independently as suggested by (25). That is

$$\gamma^{\text{Model}}_{\beta\alpha,k} = \sqrt{P_{\beta\alpha}(\phi^{\text{BS}})P_{\beta\alpha}(\vartheta^{\text{BS}})P_{\beta\alpha}(\phi^{\text{MS}}, \vartheta^{\text{MS}}, \tau)}. \tag{29}$$

7.1. Simulation Procedure. Figure 12 shows the simulation procedure diagram of multipaths at the BS and MS. All simulation conditions are summarized in Table 5.

For the BS, 5 paths with equal ABS spacing are assigned, so that the magnitude of paths approximately follows the truncated Laplacian PSD of ABSPSD. The EBSs of all multipaths are set to 0° according to (24).

For the MS, multipaths are generated according to the simulation procedures described in [20, Section 7.2].

The generation of multipaths for the MS is briefly summarized as follows.

(1) Generate multipaths for the classes and the residual part. The numbers of multipaths and spacings of the AMS, EMS, and excess delay are set according to the values given in Table 5.

(2) For N_s simulations, generate "exist" or "not exist" status of each class. In general, two-state Markov model is used to generate the status [33]. For the residual part, its status is always set to "exist."

(3) In case of existence, generate power variations, $\Gamma^{c}_{\beta\alpha}$ and $\Gamma^{r}_{\beta\alpha}$.

(4) For a realization of power variation, N_a combinations of antenna array orientation are considered as the evaluation of the Kronecker separability.

After generating multipaths at the BS and MS, the N_r simulations of random phases of polarizations between 0 to 2π are next generated, in order to calculate $\mathbf{H}^{\text{Model}}(f)$ according to (26)–(29). As explained in Section 3.1, $\mathbf{H}^{\text{Model}}(f)$ is simply expressed as $\mathbf{H}^{\text{Model}}$.

For the n_ath MS antenna orientation, the ergodic mutual information of $\mathbf{H}^{\text{Model}}$, $\mathcal{I}^{\text{Model}}(n_a)$, can be obtained by replacing the normalized $\mathbf{H}(n_a)$ with the normalized $\mathbf{H}^{\text{Model}}(n_a)$ in (7). $\mathbf{H}^{\text{Model}}(n_a)$ is a $\mathbf{H}^{\text{Model}}$ when the MS antenna orientation is $\phi^{\text{MS}}(n_a)$. It is obtained by replacing ϕ_k^{MS} with $\{\phi_k^{\text{MS}} - \phi^{\text{MS}}(n_a)\}$ in (27), where $\phi^{\text{MS}}(n_a) = 0^\circ, 45^\circ, \ldots, 315^\circ$ for $n_a = 1, \ldots, 8$, respectively. Similar to the evaluation of the Kronecker separability, all ergodic mutual information are calculated at an SNR of 10 dB.

7.2. Results. Figure 13 shows the CDFs of the measured and modeled ergodic mutual information of all frequencies, antenna array orientations, and power variations for the *Laptop* scenario. In general, there is a close agreement between the measured and modeled results. Table 6 summarizes the absolute percentage errors of modeled results from measured results at 10%, 50%, and 90% CDFs. According to the table, the difference was found to be within around 11%, 7%, and 10% at 10%, 50%, and 90% CDFs, respectively.

8. Conclusion

The improvement in the ergodic mutual information of a multiple polarized MIMO system was first verified. Then, the Kronecker separability of the joint polarimetric angular PSD between the BS and MS of the measured propagation channel was investigated by using the ergodic mutual information. The authors showed that the joint polarimetric angular PSD could be modeled as the product of the marginal angular PSDs at the BS and MS when the same single channel polarization pair is considered. From this result, the extension of the angular-delay PSD model proposed previously by the authors to the double-directional PSD channel model was done. The double-directional PSD channel model was verified by comparing the CDFs of the measured and modeled ergodic mutual information. The results were found to be in a good agreement with those obtained from the measurement.

Acknowledgment

This research is supported by the National Institute of Information and Communications Technology of Japan.

References

[1] E. Telatar, "Capacity of multi-antenna Gaussian channels," *European Transactions on Telecommunications*, vol. 10, no. 6, pp. 585–595, 1999.

[2] D.-S. Shiu, G. J. Foschini, M. J. Gans, and J. M. Kahn, "Fading correlation and its effect on the capacity of multielement antenna systems," *IEEE Transactions on Communications*, vol. 48, no. 3, pp. 502–513, 2000.

[3] T. Svantesson and J. Wallace, "On signal strength and multipath richness in multi-input multi-output systems," in *Proceedings of IEEE International Conference on Communications (ICC '03)*, vol. 4, pp. 2683–2687, Anchorage, Alaska, USA, May 2003.

[4] J. B. Andersen and B. N. Getu, "The MIMO cube—a compact MIMO antenna," in *Proceedings of the 5th International Symposium on Wireless Personal Multimedia Communications*

(WPMC '02), vol. 1, pp. 112–114, Honolulu, Hawaii, USA, October 2002.

[5] C.-Y. Chiu, J.-B. Yan, and R. D. Murch, "24-port and 36-port antenna cubes suitable for MIMO wireless communications," *IEEE Transactions on Antennas and Propagation*, vol. 56, no. 4, pp. 1170–1176, 2008.

[6] T. Wirth, V. Jungnickel, A. Forck, et al., "Polarisation dependent MIMO gains on multiuser downlink OFDMA with a 3GPP LTE air interface in typical urban outdoor scenarios," in *Proceedings of the International ITG Workshop on Smart Antennas (WSA '08)*, pp. 157–161, Darmstadt, Germany, February 2008.

[7] L. Dong, H. Choo, R. W. Heath Jr., and H. Ling, "Simulation of MIMO channel capacity with antenna polarization diversity," *IEEE Transactions on Wireless Communications*, vol. 4, no. 4, pp. 1869–1873, 2005.

[8] G. Calcev, D. Chizhik, B. Goransson, et al., "A wideband spatial channel model for system-wide simulations," *IEEE Transactions on Vehicular Technology*, vol. 56, no. 2, pp. 389–403, 2007.

[9] "Spatial channel model for MIMO simulations," Tech. Rep. TR 25.996 V6.1.0, 3GPP, Valbonne, France, September 2003.

[10] L. M. Correia, Ed., *Mobile Broadband Multimedia Networks: Techniques, Models and Tools for 4G*, Academic Press, New York, NY, USA, 2006.

[11] M. Shafi, M. Zhang, A. L. Moustakas, et al., "Polarized MIMO channels in 3-D: models, measurements and mutual information," *IEEE Journal on Selected Areas in Communications*, vol. 24, no. 3, pp. 514–527, 2006.

[12] C. Waldschmidt, C. Kuhnert, T. Fugen, and W. Wiesbeck, "Measurements and simulations of compact MIMO-systems based on polarization diversity," in *Proceedings of IEEE Topical Conference on Wireless Communication Technology (WCT '03)*, pp. 284–285, Honolulu, Hawaii, USA, October 2003.

[13] V. Erceg, P. Soma, D. S. Baum, and S. Catreux, "Multiple-input multiple-output fixed wireless radio channel measurements and modeling using dual-polarized antennas at 2.5 GHz," *IEEE Transactions on Wireless Communications*, vol. 3, no. 6, pp. 2288–2298, 2004.

[14] M. Landmann, K. Sivasondhivat, J.-I. Takada, I. Ida, and R. Thomä, "Polarization behavior of discrete multipath and diffuse scattering in urban environments at 4.5 GHz," *EURASIP Journal on Wireless Communications and Networking*, vol. 2007, Article ID 57980, 16 pages, 2007.

[15] J. Ling, D. Chizhik, D. Samardzija, and R. A. Valenzuela, "Peer-to-peer MIMO radio channel measurements in a rural area," *IEEE Transactions on Wireless Communications*, vol. 6, no. 9, pp. 3229–3237, 2007.

[16] M. Steinbauer, A. F. Molisch, and E. Bonek, "The double-directional radio channel," *IEEE Antennas and Propagation Magazine*, vol. 43, no. 4, pp. 51–63, 2001.

[17] K. Kalliola, H. Laitinen, P. Vainikainen, M. Toeltsch, J. Laurila, and E. Bonek, "3-D double-directional radio channel characterization for urban macrocellular applications," *IEEE Transactions on Antennas and Propagation*, vol. 51, no. 11, pp. 3122–3133, 2003.

[18] J. P. Kermoal, L. Schumacher, K. I. Pedersen, P. E. Mogensen, and F. Frederiksen, "A stochastic MIMO radio channel model with experimental validation," *IEEE Journal on Selected Areas in Communications*, vol. 20, no. 6, pp. 1211–1226, 2002.

[19] W. Weichselberger, M. Herdin, H. Ozcelik, and E. Bonek, "A stochastic MIMO channel model with joint correlation of both link ends," *IEEE Transactions on Wireless Communications*, vol. 5, no. 1, pp. 90–100, 2006.

[20] K. Sivasondhivat, J.-I. Takada, I. Ida, and Y. Oishi, "Experimental analysis and site-specific modeling of channel parameters at mobile station in an urban macrocellular environment," *IEICE Transactions on Communications*, vol. E91-B, no. 4, pp. 1132–1144, 2008.

[21] M. Bengtsson and P. Zetterberg, "Some notes on the Kronecker model," submitted to *EURASIP Journal on Wireless Communications and Networking*.

[22] "LTE channel models and simulations," Tech. Rep. R4-060334, 3GPP, Valbonne, France, February 2006.

[23] R. Thomä, M. Landmann, and A. Richter, "RIMAX—a maximum likelihood framework for parameter estimation in multidimensional channel sounding," in *Proceedings of the International Symposium on Antennas and Propagation (ISAP '04)*, pp. 53–56, Sendai, Japan, August 2004.

[24] A. Ludwig, "The definition of cross polarization," *IEEE Transactions on Antennas and Propagation*, vol. 21, no. 1, pp. 116–119, 1973.

[25] A. F. Molisch, M. Steinbauer, M. Toeltsch, E. Bonek, and R. Thomä, "Capacity of MIMO systems based on measured wireless channels," *IEEE Journal on Selected Areas in Communications*, vol. 20, no. 3, pp. 561–569, 2002.

[26] S. Takahashi and Y. Yamada, "Propagation-loss prediction using ray tracing with a randomphase technique," *IEICE Transactions on Fundamentals of Electronics, Communications and Computer Sciences*, vol. E81-A, no. 7, pp. 1445–1451, 1998.

[27] K. Kalliola, K. Sulonen, H. Laitinen, O. Kivekäs, J. Krogerus, and P. Vainikainen, "Angular power distribution and mean effective gain of mobile antenna in different propagation environments," *IEEE Transactions on Vehicular Technology*, vol. 51, no. 5, pp. 823–838, 2002.

[28] R. G. Vaughan, "Polarization diversity in mobile communications," *IEEE Transactions on Vehicular Technology*, vol. 39, no. 3, pp. 177–186, 1990.

[29] K. Sivasondhivat, *Analysis and modeling of double-directional polarized channel in urban macrocellular environment*, Ph.D. dissertation, Tokyo Institute of Technology, Tokyo, Japan, 2008.

[30] K. Sivasondhivat, J.-I. Takada, Y. Nakaya, I. Ida, and Y. Oishi, "Verification of kronecker MIMO channel model in a NLOS macrocellular environment," in *Proceedings of the IEICE General Conference*, p. 233, Tokyo, Japan, March 2006, B-1-233.

[31] D. P. McNamara, M. A. Beach, and P. N. Fletcher, "Spatial correlation in indoor MIMO channels," in *Proceedings of the 13th IEEE International Symposium on Personal, Indoor and Mobile Radio Communications (PIMRC '02)*, vol. 1, pp. 290–294, Lisbon, Portugal, September 2002.

[32] K. I. Pedersen, P. E. Mogensen, and B. H. Fleury, "Power azimuth spectrum in outdoor environments," *Electronics Letters*, vol. 33, no. 18, pp. 1583–1584, 1997.

[33] C.-C. Chong, C.-M. Tan, D. I. Laurenson, S. McLaughlin, M. A. Beach, and A. R. Nix, "A novel wideband dynamic directional indoor channel model based on a Markov process," *IEEE Transactions on Wireless Communications*, vol. 4, no. 4, pp. 1539–1552, 2005.